



HAL
open science

Analysis and control of polarization effects in structured semiconductor microcavities

Omblin Lafont

► **To cite this version:**

Omblin Lafont. Analysis and control of polarization effects in structured semiconductor microcavities. Physics [physics]. Université de recherche Paris Sciences et Lettres; Ecole Normale Supérieure (ENS), 2016. English. NNT: . tel-01436954v1

HAL Id: tel-01436954

<https://theses.hal.science/tel-01436954v1>

Submitted on 16 Jan 2017 (v1), last revised 19 Mar 2018 (v2)

HAL is a multi-disciplinary open access archive for the deposit and dissemination of scientific research documents, whether they are published or not. The documents may come from teaching and research institutions in France or abroad, or from public or private research centers.

L'archive ouverte pluridisciplinaire **HAL**, est destinée au dépôt et à la diffusion de documents scientifiques de niveau recherche, publiés ou non, émanant des établissements d'enseignement et de recherche français ou étrangers, des laboratoires publics ou privés.

THÈSE DE DOCTORAT

de l'Université de recherche Paris Sciences et Lettres
PSL Research University

Préparée à l'École Normale Supérieure

Analysis and control of polarization effects in structured
semiconductor microcavities

Ecole doctorale n°564

PHYSIQUE EN ILE-DE-FRANCE

Spécialité PHYSIQUE

Soutenue par **OMBLINE LAFONT**
le 21 octobre 2016

Dirigée par **Philippe**
ROUSSIGNOL

COMPOSITION DU JURY :

M. AMAND Thierry
CNRS/INSA Toulouse,
Rapporteur

M. GIL Bernard
CNRS/Université de Montpellier,
Rapporteur

Mme DELEPORTE Emmanuelle
École normale supérieure de Cachan,
Présidente du jury

M. BRAMATI Alberto
Université Pierre et Marie Curie,
Membre du jury

M. SCHUMACHER Stefan
Universität Paderborn,
Membre invité

M. BAUDIN Emmanuel
École Normale Supérieure,
Membre invité

M. ROUSSIGNOL Philippe
CNRS/École Normale Supérieure,
Directeur de thèse



CONTENTS

INTRODUCTION	9
Index of symbols	15
1 Properties of microcavity exciton-polaritons	19
1.1 Excitons-polaritons confined in structured semiconductor microcavities	21
1.1.1 Properties of excitons confined in quantum wells	22
1.1.2 Properties of microcavities	27
1.1.3 Strong coupling regime	33
1.2 Parametric effects in microcavities	37
1.2.1 Third-order susceptibility	37
1.2.2 Optical Parametric Oscillation	40
1.3 Polarization effects in microcavities	45
1.3.1 Long-range polarization effect: the TE-TM splitting	45
1.3.2 Constraints-induced normal polarization splitting	50
1.3.3 Confinement-induced normal polarization splitting	51
1.3.4 Spin-dependent exciton-exciton interactions	51
2 Experimental methods	53
2.1 Excitation setup	54
2.1.1 Optical path for the pump	54
2.1.2 Small pump tilt	56
2.1.3 Optical path for the probe(s)	57
2.1.4 Properties of the optical pump	58
2.2 Detection setup	64
2.2.1 Momentum space	65
2.2.2 Angle-resolved energy dispersion	66
2.2.3 Real space	67
2.2.4 Polarization control of the exciting and emitted light	71
3 Origins of the normal polarization splitting in microwires	75
3.1 Sample and excitation conditions	76
3.1.1 Sample description	76
3.1.2 Photoluminescence spectrum	77
3.2 Observation and characterization of the polarization splitting	78
3.2.1 Experimental setup and available degrees of freedom	79

3.2.2	Interpretation	85
3.3	Physical origins of the polarization splitting	89
3.3.1	Influence of the constraints linked to the sticking	89
3.3.2	Model of stress relaxation in microwires	90
3.3.3	Lattice mismatch-induced constraints	96
3.3.4	Anisotropic mode confinement	109
3.4	Discussion and conclusion	111
4	Spin-dependent nonlinear effects in a double microcavity	115
4.1	The double microcavity sample	117
4.1.1	Context	117
4.1.2	Description	117
4.1.3	Characterization	118
4.1.4	Scattering processes	122
4.2	Spin- and power-dependent elastic Rayleigh scattering	124
4.2.1	Experiment: influence of the optical pump power	125
4.2.2	Theoretical description	132
4.2.3	Influence of other experimental parameters	137
4.2.4	Conclusion	140
4.3	Spin-dependent parametric scattering	141
4.3.1	First order four-wave mixing	143
4.3.2	Second order four-wave mixing	150
4.3.3	Conclusion	153
4.4	Pattern formation in the Optical Parametric Oscillation regime . . .	154
4.4.1	Key experimental parameters	156
4.4.2	Hexagonal pattern properties	166
4.4.3	Perspectives for further studies on the patterns	169
4.5	Conclusion	170
	GENERAL CONCLUSION	173
	Appendices	177
A1	Angle-resolved energy dispersion: data analysis and calibration	177
A2	Correction of standard errors to take into account heteroscedasticity	181
A3	Growthsheet of the double microcavity	183
	References	185

INTRODUCTION

The optical properties of semiconductors have been a major field of research both in applied and fundamental physics for the last decades. They have led to various important discoveries, such as light-emitting diodes (which were highlighted again in 2014 by the Nobel Prize attribution to Kasaki, Amano and Nakamura for the invention of the blue LED), solar cells and semiconductor laser diodes. The latter are nowadays included in many daily technologies such as barcode readers, laser pointers, CD/DVD/Blu-ray Disc reading and writing, fiber optics communications, *etc.* Amongst the various semiconductor laser technologies, the Vertical-Cavity-Surface-Emitting-Lasers (VCSELs) offer the additional advantages of an improved light collection, a more controllable fabrication process and an easier integration thanks to their emission normal to the surface (hence their name). They are widely used in fiber optics networks.

In these semiconductor lasers, the light and matter excitations must be both confined to enable their interaction. Hence, the VCSEL laser resonator consists of a monolithic semiconductor Fabry-Pérot-like microcavity. The mirrors are formed by Distributed Bragg Reflectors (DBRs). A spacer with a typical thickness of several hundreds of nanometers is placed between the DBRs and defines the accepted wavelengths of the Fabry-Pérot cavity. On the other hand, the active medium consists of a thin quantum well (typically a few nanometers thick) placed at the antinode of the electric field at the center of the cavity. The first excited state of such a quantum well is an electron-hole pair bound by coulombic interaction, called *exciton*. In the regime of weak light-matter coupling, where the light-matter interaction is well described by the Fermi golden rule, a stimulated emission was observed, first at low temperature in 1979 [Soda1979] and later up to room temperature [Koyama1989].

The progress of Molecular Beam Epitaxy (MBE) manufacturing techniques now enable the growth of semiconductor layers at almost the atomic scale. This has opened the door for high-quality DBRs manufacture. The resulting semiconductor microcavities display a large quality factor (typically 10^5) and the light-matter interaction can no longer be considered as a perturbative effect. Instead, the system exhibits new eigenstates which are mixed light-matter quasi-particles called *microcavity exciton-polaritons*. They result from the *strong coupling* between the excitons confined in the quantum well and the photons confined inside the microcavity. An upper and a lower *polaritonic branch* can be defined. They exhibit a quasi-parabolic energy dispersion with the in-plane wavevector near the center of the Brillouin zone, and are separated by a normal-mode energy splitting, often called *Rabi coupling* or Rabi splitting in solid-state physics. The ratio between exciton and photon in a microcavity exciton-polariton depends on the energy difference between the excitonic

transition and the confined cavity mode (called *exciton-photon detuning*), as well as its in-plane wavevector. A thickness wedge in the cavity medium is usually introduced on purpose during the growth, so that the exciton-photon detuning can be adjusted by shifting the excitation spot on the surface of the sample.

Such states were observed for the first time in 1992 by Weisbuch *et al.* [Weisbuch1992]. In certain semiconductors such as GaN or ZnO, microcavity exciton-polaritons can be detected up to room temperature [Christopoulos2007, Schmidt-Grund2008]. The strong light-matter coupling regime has also been reached in solid state physics with other emitters such as cavity-embedded quantum dots [Reithmaier2014, Yoshie2004, Peter2005], artificial atoms based on Josephson junctions in superconducting circuits [Wallraff2004], phonons [Le Gall1997] or plasmons [Craig1983]. Exciton-polaritons also exist in the bulk semiconductor [Fröhlich1971]. Hence, the concept of polariton is very general in condensed matter physics. The excitons considered in this manuscript are confined in quantum wells and the word “polariton” refers specifically to microcavity exciton-polaritons.

Microcavity exciton-polaritons exhibit specific intriguing properties, which make them unique for research in fundamental physics as well as for their applications in photonics.

Photons confined in a cavity acquire a very small effective mass (typically 10^{-4} – 10^{-5} of the free electron mass). Polaritons inherit this small effective mass near the center of the Brillouin zone. Furthermore, they obey to bosonic statistics in the regime of weak excitation. The combination of these two remarkable properties offers the possibility of creating a macroscopically occupied coherent state at relatively large temperatures [Kasprzak2006], analogous to a Bose-Einstein condensate in atomic physics. The superfluidity of such polariton condensates was predicted in 2004 [Carusotto2004] and observed a few years later [Amo2009]. Furthermore, it has been proposed that polariton condensates would give rise to a low-threshold laser emission [Imamoglu1996, Bajoni2008a]. A room temperature electrically injected laser emission was thus recently demonstrated [Bhattacharya2014].

In addition, polaritons experience strong mutual interactions due to their excitonic component, enabling the observation of *Optical parametric amplification* (OPA) [Ciuti2000] and *oscillation* (OPO) [Ciuti2003] processes. In OPA and OPO processes, pump polaritons with frequency ω_p are coherently (and reversibly in the case of OPO) converted in signal and idler polaritons with frequencies ω_s and ω_i , provided phase-matching and energy conservation conditions are fulfilled (such as $\omega_s + \omega_i = 2\omega_p$ for example). This enables the miniaturization and integration of OPOs, which are nowadays typically made with a non linear cristal such as Lithium Niobate in complex optical cavities and pumped by powerful laser light. Additionally, this process produces in theory non-classical states such as quantum-correlated signal and idler polaritons (or “twin polaritons”), raising interest for applications in quantum cryptography and quantum information [Mertz1991].

Hence in 2000 the first experimental observation of stimulated parametric polariton-polariton scattering [Savvidis2000, Stevenson2000] brought about intense research on this

topic. These experiments exploited one specific aspect of the polariton energy dispersion: at large in-plane wavevectors, the lower polariton branch is no longer a parabola but exhibits an inflection point containing a large density of states with longer lifetimes. This feature had been spotted earlier as it is responsible for a *bottleneck* effect: polaritons accumulate in these modes and the phonon-assisted relaxations towards the center of the Brillouin zone are inhibited [Tassone1997, Müller2000]. Thanks to this inflection point, phase-matching conditions can be fulfilled if the pump is sent at a specific large incidence angle (the so-called “Magic Angle”) and parametric processes are possible.

However, the first implementations of micro-OPO using an optical pump at the Magic Angle produced strongly intensity-unbalanced signal and idler beams, which is a serious obstacle to the study of their quantum correlations. The use of a large oblique angle is also a major drawback for an easy device integration. To overcome these problems, our group at the *Laboratoire Pierre Aigrain* (LPA) has proposed to engineer the microcavity dispersion so as to open new scattering channels and isolate these from transitions towards the excitonic reservoir. This is possible when several lower polariton branches are accessible. A degenerate interbranch OPO initiated by a normally-incident pump producing intensity-balanced signal and idler beams has first been observed on coupled microcavities² [Diederichs2006], later in microwires (1D-microcavities obtained by etching a planar microcavity) [Ardizzone2012] and in micropillars (0D-microcavities) [Ferrier2010].

Indeed, when the dimensionality is reduced, a quantization of the cavity mode is induced and several lower polariton states are confined. In the work of Vincenzo Ardizzone [Ardizzone2013a], the presence of a lifting of degeneracy between polarization parallel and perpendicular to the wires was exploited for the study of quantum and classical correlations in a micro-OPO. In this manuscript, a detailed study of this polarization-dependent lifting of degeneracy is presented. The origins of this splitting are manifold and the splitting magnitude can be therefore engineered as a function of various degrees of freedom such as the exciton-photon detuning, the cavity mode index, the angle of the wire with respect to the crystalline axes, *etc.*

Another consequence of the strong polariton-polariton interactions is that they can be assimilated to a fluid [Carusotto2013], exhibiting peculiar effects such as polariton vortices [Lagoudakis2008]. Moreover, analogous to the formation of Rayleigh-Bénard convection cells in hydrodynamics, a pattern formation process was experimentally demonstrated by Vincenzo Ardizzone at the LPA in a double microcavity [Ardizzone2013b], after the proposal of the teams of Stefan Schumacher in Paderborn (Germany) and Rolf Binder in Tucson (USA) [Schumacher2009, Dawes2010, Luk2013]. These patterns are initiated by directional instabilities and stabilized by high-order

²The presence of a second lower polariton branch in a double microcavity also opens new *allowed optical transitions*. We [Huppert2014b] have proposed a design for a double microcavity device able to efficiently detect and potentially generate THz frequencies, taking advantage of bosonic stimulation effects [Kavokin2010, De Liberato2013]. This work will not be treated in this manuscript. A detailed discussion is available in the PhD manuscript of Simon Huppert [Huppert2014a].

non linear processes. They are the optical analog of animal coat patterns such as zebra stripes, or sand ripples, *etc.* They were first described theoretically by A. Turing in the context of chemical reactions and the biological process of morphogenesis (cellular differentiation) [Turing1952]. Other nonlinear optical systems, such as atomic vapours [Maître1994] or macroscopic OPO devices [Ducci2001], display similar behaviours.

The spontaneous breaking of spatial symmetry is worth studying from a fundamental point of view, but also from the perspective of applications in photonics. We will show that the pattern formations can be controlled in many ways, from polarization, to a slight tilt in the pump incidence, paving the way for the development of ultrafast all-optical switches (since the polariton lifetime is typically a few picoseconds [Bloch1997]) and original photonic devices such as microscopic lighthouses.

Finally, polaritons can be attributed a pseudo-spin which is directly connected to the polarization of light absorbed or emitted by the microcavity. This pseudo-spin can be manipulated using several tools such as the presence of a momentum-dependent TE-TM energy splitting, and the spin-dependence dynamics of polariton-polariton interactions. This leads to a variety of phenomena such as the Optical Spin Hall Effect [Kavokin2005, Leyder2007], the formation of polarization vortices [Liew2007] and patterns [Schumacher2008], and skyrmions spin textures [Cilibrizzi2016].

All those exceptional properties open an interesting future for polaritonic devices [Sanvitto2016]. Besides polariton lasers, twin-polaritons generation, and all-optical switches, several theoretical proposals and experimental demonstrations have already been developed, such as electrically-injected light-emitting diodes up to room temperature [Bajoni2008b, Khalifa2008, Tsintzos2008], all-optical gates [Ostatnický2010, Solnyshkov2015, Gao2015], all-optical transistor [Ballarini2013], and exciton-polariton router [Marsault2015].

This work focuses on some polarization-dependent aspects arising in structured semiconductor microcavities, in the perspective of integrated optical devices.

After a detailed description of semiconductor microcavities and the derivation of polariton eigenstates in the strong coupling regime, the **first chapter** describes the consequences of the presence of a $\chi^{(3)}$ susceptibility such as the blueshift of polariton energies and optical parametric amplification and oscillation. Some polarization effects such as the so-called “Optical Spin Hall Effect” and the spin-dependence of polariton-polariton interactions are then introduced.

The **second chapter** is devoted to the description of the various experimental setups and tools: imagery of the momentum space, of the real space, and observation of angle-resolved energy dispersion. The properties of the excitation laser are discussed and compared to an alternative excitation source exhibiting better monochromaticity and stability in the continuous wave regime. The experimental polarization control is exposed in detail.

The **third chapter** presents the detailed study of a normal polarization-dependent energy splitting arising in 1D-microcavities. This splitting exhibits a universal law as a function of exciton-photon detuning. Various origins for this splitting are discussed. Then experimentally-induced parameters are compared to the results of mechanical calculations and simulations.

The **fourth chapter** is devoted to the experimental results obtained in various regimes of excitation power sent on a double microcavity. An all-optical control of the Optical Spin Hall Effect is demonstrated. The interplay between the TE-TM splitting and spin-anisotropic polariton-polariton scattering is explored in the regime of parametric amplification, by using pump-probe(s) scenarios. Lastly, at large pumping powers, the “instability” threshold is reached and the optical parametric oscillation gives rise to unstable off-axis fields, which spontaneously organize into patterns in the far and near field. Various experiments aiming at understanding and controlling the orientation and stability of those patterns are presented.

INDEX OF SYMBOLS

- x proportion of Aluminium in AlGaAs
- DBR Distributed Bragg Reflector
- QW Quantum well
- E_G GaAs direct bandgap energy at the Γ point
- x as subscript or superscript, refers to the exciton
- c as subscript or superscript, refers to the photon
- p as subscript or superscript, refers to the polariton
- m_0 Free electron mass
- E_b Binding energy between the hole and the electron
- $E_k^{x/c/p}$ Exciton/photon/polariton dispersion with in-plane wavevector k
- Δ Exciton-photon detuning ($= E_0^c - E_0^x$)
- $m_{x/c/p}$ Exciton/photon/polariton effective mass
- e Exciton field
- c Electromagnetic field confined in the cavity
- Ψ Polariton field (usually a low polariton mode)
- \mathbf{k}_{\parallel} Exciton, photon or polariton in-plane wavevector, equivalent to the angle of emission θ . Sometimes the symbol \parallel is omitted for simplicity.
- θ Light incidence angle in the air
- θ_c Intracavity angle ($= \arcsin(\frac{1}{n_c} \sin \theta)$)
- α_{PSF} Fermionic phase-space filling, leading to a saturation of the light-matter coupling at large powers
- n_{sat} Saturation exciton density ($= 1/\alpha_{\text{PSF}}$)
- V_{HF} Repulsive Coulombic interaction in the Hartree-Fock approximation

INDEX OF SYMBOLS

- L_{eff} Effective length of the cavity (taking into account the penetration of the electric field inside the DBRs)
- LPB Low polariton branch
- Elastic circle At a given energy, due to the paraboloid form of the energy dispersion with angle, the resonant modes form a circle with a fixed radius in the k_{\parallel} -space
- OPA Optical Parametric Amplification (or parametric scattering)
- OPO Optical Parametric Oscillation
- FWM Four-wave mixing
- \mathbf{E} Electric field
- \mathbf{B} Magnetic field
- k-space Parallel wavevector space/Fourier space/momentum space/angular space/reciprocal space: image of the far field emission
- Real space Image of the near field (surface of the sample)
- H/V Horizontal/vertical linear polarization (see Subsection 2.2.4)
- +/- Left/right circular polarization
- PL Photoluminescence
- j Integer labelling the cavity mode in microwires
- j_n $j = n$ cavity mode in microwires
- (x_0, y_0) Crystalline axes of GaAs
- (X, Y) Short and long axes of the microwires. X corresponds also to the direction of the cavity wedge.
- θ_w Angle between y_0 and Y (wire long axis)
- δE_{pol} Polariton energy splitting between polarizations perpendicular and parallel to the wire long axis Y
- δE_x Heavy-hole exciton energy splitting between polarizations perpendicular and parallel to the wire long axis Y
- δE_c $j = 0$ cavity mode energy splitting between polarizations perpendicular and parallel to the wire long axis Y

$\delta\Omega_R$	Rabi coupling energy splitting between polarization perpendicular and parallel to the wire long axis Y
H	Wire height
W	Wire width
L	Wire length
$\vec{\sigma}$	Stress tensor
C_{ijkl}	Stress-strain tensor
\mathcal{E}	Young's modulus
ν	Poisson's ratio
u_X	Displacement field in the direction X
$\vec{\epsilon}$	Strain tensor
$\vec{\epsilon}^d$	Dielectric permittivity tensor
ϵ	Strain due to the relaxation of the lattice-mismatch induced constraints for $z > H_X$
$H_{X,Y}$	Relaxation length along z due to constraints along X or Y
Λ_m	Relative change in lattice parameter between the layer (m) and GaAs
$h^{(m)}$	Thickness of the DBR layer (m)
n_c	Refractive index of the cavity spacer
n_m	Refractive index of the DBR layer (m)
P_{ijkl}	Photoelastic tensor
ΔE	Energy splitting between the light-hole and the heavy-hole exciton due to their confinement in a QW
ΔE_{SR}	Short-range exciton exchange energy
θ_{eff}	Effective intracavity angle due to the confinement along X in microwires
Ω_c	Cavity-cavity coupling in a double microcavity
ϕ	Azimuthal angle along the elastic circle
TE/TM	Transverse electric/Transverse magnetic

INDEX OF SYMBOLS

- $\Delta_{\mathbf{k}}^{\text{p,TL}}$ Polaritonic TE-TM splitting energy ($= \frac{\hbar^2}{4} (\frac{1}{m_{\text{p}}^{\text{TM}}} - \frac{1}{m_{\text{p}}^{\text{TE}}})$)
- $\Delta_{\mathbf{k}}^{\text{p},\pm}$ Polaritonic TE-TM splitting ($= \Delta_{\mathbf{k}}^{\text{p,TL}} e^{\mp 2i\phi}$)
- ϕ_0 First zero of the degree of linear polarization along the elastic circle
- ϕ_{spatial} Azimuthal angle on the elastic circle where the probe is located
- $\phi_{\text{pol,pump}}$ Direction of the pump linear polarization
- $\Delta\phi$ Angle between the probe location and the direction of the pump polarization
($= \phi_{\text{pol,pump}} - \phi_{\text{spatial}}$)
- OSHE Optical Spin Hall Effect
- $X_{1/2/d}$ Probe 1, 2 or detection is co-polarized to the pump
- $Y_{1/2/d}$ Probe 1, 2 or detection is cross-polarized to the pump
- OPO threshold Also called instability threshold. Above a certain polariton density, OPO and pattern formation processes take place.
- FOFWM First-order first-wave mixing, involving two pump polaritons and two off-axis signal and idler polariton modes
- SOFWM Second-order first-wave mixing, involving one pump polariton and three off-axis polariton modes
- T^{++}, T^{+-} Spin-dependent exciton-exciton interaction strengths
- α^{++}, α^{+-} Spin-dependent polariton-polariton interaction strengths
- φ Azimuthal angle along the elastic circle starting at the polarization of the pump ($= \phi - \phi_{\text{pol,pump}}$)

1

PROPERTIES OF MICROCAVITY EXCITON-POLARITONS

This first chapter introduces the nanostructures of interest and the main properties useful for the next chapters. Planar semiconductor microcavities confine both light (in a Fabry-Pérot-like cavity) and matter excitations (in a quantum well). In the strong coupling regime, the elementary excitations are half light, half matter quasi-particles called microcavity exciton-polaritons. Planar microcavities can be structured to tune the polariton energy dispersion with momentum. First, the introduction of a wedge on the spacer layer allows to modify the wavelength allowed in the cavity with respect to the energy of the matter excitation. Second, the microcavity can be etched so as to form microwires and the reduced dimensionality gives rise to a quantification of the modes allowed in the 1D-microcavity. Finally, multiple microcavities can be superimposed and coupled inducing again new allowed cavity modes.

Thanks to their matter component, polaritons can mutually interact, giving rise to nonlinear effects such as optical parametric scattering and oscillation, depending on the optical power sent on the microcavity. Furthermore, polaritons can be attributed a pseudo-spin directly linked to the polarization of their light component. This pseudo-spin evolves during the polariton propagation by the presence of a momentum-dependent TE-TM splitting. Intrinsic and extrinsic constraints or the reduction of dimensionality can also lead to polarization-dependent liftings of degeneracy. Finally, the polariton-polariton interaction strength exhibits a pseudo-spin dependence as well.

All these properties are detailed in this first chapter, and are essential ingredients for the understanding of various methods which will be used to manipulate polaritons and their pseudo-spin.

The first section is dedicated to the presentation of polaritons in microcavities in the strong coupling regime. The second section is devoted to the consequences of the third order susceptibility in AlGaAs and GaAs, such as optical Kerr effect and parametric effects. The third section presents various polarization-dependent effects, taking into account linear and nonlinear processes.

Chapter content

1.1	Excitons-polaritons confined in structured semiconductor microcavities . . .	21
1.1.1	Properties of excitons confined in quantum wells	22
1.1.1.1	Band structure of GaAs	22
1.1.1.2	The concept of “hole” in a semiconductor	22
1.1.1.3	Excitons in quantum wells	23
1.1.1.4	Dipolar coupling	26
1.1.2	Properties of microcavities	27
1.1.2.1	Distributed Bragg Reflectors	27
1.1.2.2	Fabry-Pérot cavity	28
1.1.2.3	Photons effective mass	29
1.1.2.4	Equivalence between incidence angle and in-plane wavevector	29
1.1.2.5	Simulation : transfer matrix method	30
1.1.2.6	Fabrication: growth by Molecular Beam Epitaxy	31
1.1.2.7	Structured microcavities	32
1.1.3	Strong coupling regime	33
1.1.3.1	Light-matter coupling strength	33
1.1.3.2	Microcavity polaritons	34
1.1.3.3	Transition to the weak coupling regime	36
1.2	Parametric effects in microcavities	37
1.2.1	Third-order susceptibility	37
1.2.1.1	Nonlinear dielectric polarization	37
1.2.1.2	Optical Kerr Effect	38
1.2.1.3	Optical Parametric Amplification	39
1.2.2	Optical Parametric Oscillation	40
1.2.2.1	Generalities	40
1.2.2.2	Phase-matching in microcavities	41
1.2.2.3	Coherence properties	42
1.2.2.4	Quantum treatment	43
1.2.2.5	Pattern formation	44
1.3	Polarization effects in microcavities	45
1.3.1	Long-range polarization effect: the TE-TM splitting	45
1.3.1.1	Origins of the TE-TM splitting	45
1.3.1.2	Consequence: the Optical Spin Hall Effect	47
1.3.2	Constraints-induced normal polarization splitting	50
1.3.3	Confinement-induced normal polarization splitting	51
1.3.4	Spin-dependent exciton-exciton interactions	51

1.1 Excitons-polaritons confined in structured semiconductor microcavities

The semiconductor structures of interest in this manuscript are composed of Aluminium Gallium Arsenide with various proportions of Aluminium (x). The general chemical formula is $\text{Al}_x\text{Ga}_{1-x}\text{As}$. These III-V semiconductor compounds crystallize in a Zinc-Blende-like structure (*cf.* Fig. 1.1).

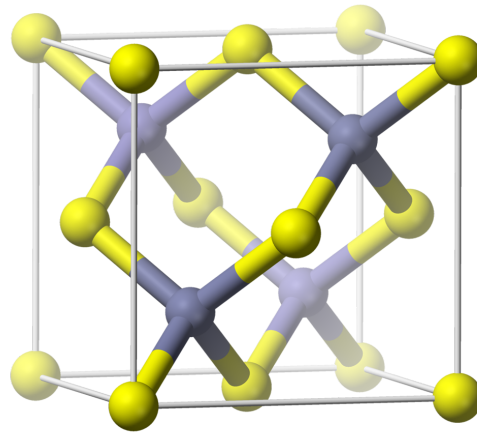


Figure 1.1: Crystalline structure of $\text{Al}_x\text{Ga}_{1-x}\text{As}$ (Zinc-Blende like). The yellow atoms designate the Gallium or Aluminium atoms (as a function of x the Aluminium fraction) and the grey atoms represent the Arsenium atoms. From *Wikimedia Commons*.

The refractive index of $\text{Al}_x\text{Ga}_{1-x}\text{As}$ depends of the Aluminium fraction x , as well as temperature and wavelength. At low temperature (6 K) and in the near-infrared, the refractive index vary approximately between 3 for AlAs ($x = 1$) and 3.58 for GaAs ($x = 0$). Thanks to this property, the realization of efficient Distributed Bragg Reflectors (DBRs) is possible (*cf.* Subsection 1.1.2).

At low temperature, the bandgap energy varies between approximately 1.52 eV for GaAs and 3.04 eV for AlAs. For $x < 0.4$ [Adachi1985], Aluminium Gallium Arsenide is a semiconductor with a direct bandgap, enabling the confinement of direct excitons in quantum wells (*cf.* Subsection 1.1.1).

The lattice constant (typically 5 Å) also varies quasi-linearly with x [Adachi1985]. The lattice mismatch between AlAs and GaAs is very small (less than 0.01 Å [Adachi1985]) such that thin layers of both materials can be superimposed to form stable micrometers-thick structures, containing a small amount of crystalline defects. However, we will see in Chapter 3 that the lattice mismatch between several Aluminium Gallium Arsenide layers having different proportion of Aluminium, despite its small amplitude, plays a key-role for the polarization-anisotropic constraints induced in a 1D-microcavity.

1.1.1 Properties of excitons confined in quantum wells

1.1.1.1 Band structure of GaAs

GaAs is a semiconductor with a direct bandgap E_G lying at the center of the Brillouin zone (the “ Γ ” point, *cf.* Fig. 1.2).

The conduction band contains electronic states of symmetry s , that is, of orbital angular momentum $l = 0$. The valence band is formed by electronic states of type p (orbital angular momentum $l = 1$). Due to spin-orbit coupling, the valence states form two bands of total angular momentum $J^h = \frac{3}{2}$ and $J^h = \frac{1}{2}$, split by an energy Δ_{SO} . At ambient temperature, $E_G \simeq 1.5$ eV and $\Delta_{SO} \simeq 0.3$ eV for GaAs [Fishman].

The $J^h = \frac{3}{2}$ valence band is itself split in two subbands. They are energy-degenerated at the center of the Brillouin zone but do not have the same energy dispersion with the in-plane wavevector k_{\parallel} . We can attribute to each of them a different (negative) effective mass: $\frac{1}{m} = \frac{1}{\hbar^2} \frac{\partial^2 E}{\partial k_i \partial k_j}$. The “heavy hole” band has a angular momentum along z $J_z^{hh} = \pm \frac{3}{2}$ whereas the “light hole” band has angular momentum along z $J_z^{lh} = \pm \frac{1}{2}$.

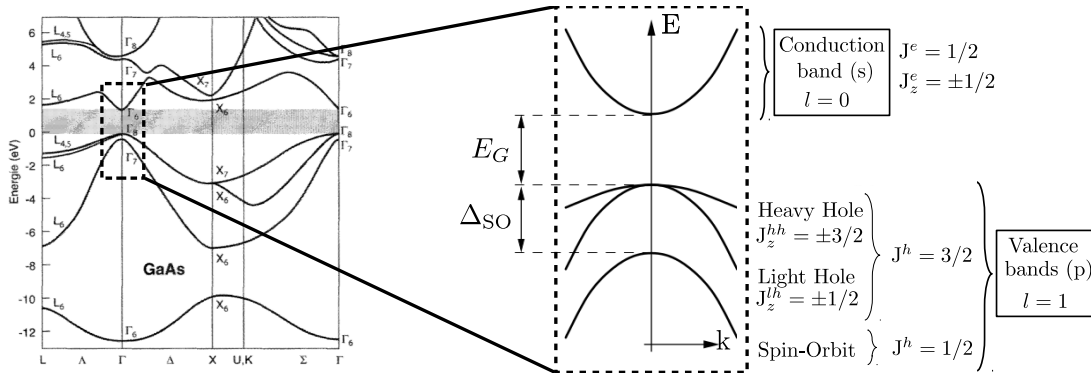


Figure 1.2: Left panel: Complete band structure of GaAs [Fishman]. Right panel : zoom of the GaAs band structure at the vicinity of the Γ point.

The effective mass for electrons in the conduction band is $m_e = 0.0662 m_0$, for electrons in the “heavy hole” valence band $m_{hh} = -0.34 m_0$ and in the light hole valence band $m_{lh} = -0.094 m_0$, where $m_0 = 9.11 \times 10^{-31}$ kg is the free electron mass [Madelung].

1.1.1.2 The concept of “hole” in a semiconductor

In a semiconductor or insulator, the valence band is completely filled with N electrons. If a valence electron is excited, it fills an empty state of the conduction band and leaves behind a “hole” in the valence band.

The hole state is thus defined as the antisymmetric product of the $N-1$ remaining electron states. It can however be easily manipulated using the Kramers conjugate and considering the following properties for the quasi-particle:

1. The hole charge is the opposite of the one of the missing electron: it is therefore positive.
2. The hole effective mass is the opposite of the missing electron: it is positive.
3. The hole spin is the opposite to the spin of the missing electron, defined as the z component of the total angular momentum J_z^e .

1.1.1.3 Excitons in quantum wells

An exciton is a quasi-particle formed by a conduction electron and a hole bound by Coulomb interaction. The exciton energy is therefore the energy of the bandgap E_G to which the *binding energy* E_b is subtracted. Two kinds of excitons are present in the bulk of semiconductors: the Frenkel exciton, which Bohr radius is of the order of magnitude of the lattice parameter, and the Mott-Wannier exciton, which is delocalized over a few unit cells.

In this thesis, we study microstructures in which GaAs nanometers-thick layers are surrounded by $\text{Al}_{0.95}\text{Ga}_{0.05}\text{As}$ barriers, constituting a quantum well. The excitons are confined inside the quantum well in the z direction, or growth axis (see Fig. 1.3).

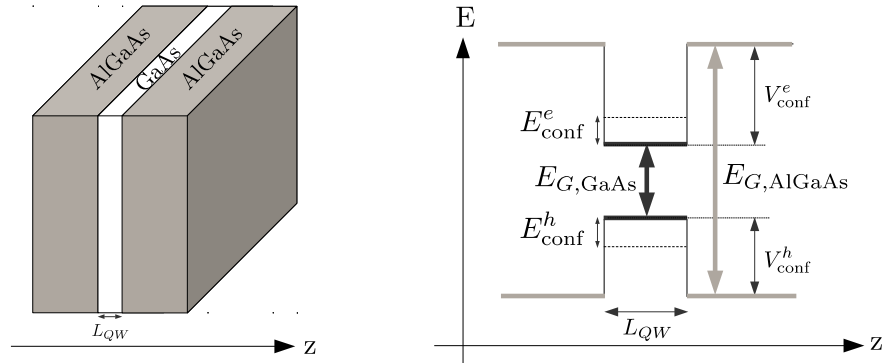


Figure 1.3: Schematic representation of a GaAs quantum well with length L_{QW} . z is the “growth axis”. The plane orthogonal to z is the “layer’s plane”.

In quantum wells, the confinement along z shifts the electron and hole energies by a confinement energy $E_{\text{conf}}^{e/h}$. Due to their different effective masses, the value of this confinement energy differs between light and heavy holes: consequently, it lifts the degeneracy between them (typically several tens of meV). The binding energies of light and heavy hole excitons also differ only by a few meV at most. The next two paragraphs are devoted to calculating the total lifting of degeneracy between heavy and light hole excitons ΔE , which will be useful in Chapter 4.

Calculation of the confinement energy The confinement energy for electron and holes can be calculated solving the finite quantum well problem [Fishman]. We will consider for the calculation a GaAs quantum well of thickness $L_{\text{QW}} = 7 \text{ nm}$ with $\text{Al}_{0.95}\text{Ga}_{0.05}\text{As}$ barriers. The carrier effective masses are m_{GaAs} and m_{AlGaAs} in GaAs and $\text{Al}_{0.95}\text{Ga}_{0.05}\text{As}$, respectively.

The envelope wavefunction for confined electron or hole in the quantum well has the form:

$$\xi(z) = \begin{cases} C_{\text{in}} \cos(kz) & \text{for } |z| < L_{\text{QW}}/2 \\ C_{\text{ext}} e^{-K|z|} & \text{for } |z| > L_{\text{QW}}/2 \end{cases}, \quad (1.1)$$

where C_{in} and C_{ext} are normalization constants. k (resp. K) is the wavevector in the QW (the AlGaAs barrier).

The confinement energy reads:

$$E_{\text{conf}} = \frac{\hbar^2 k^2}{2m_{\text{GaAs}}} = V_{\text{conf}} - \frac{\hbar^2 K^2}{2m_{\text{AlGaAs}}}, \quad (1.2)$$

where V_{conf} is the height of the barrier as defined in Fig. 1.3.

Furthermore, $\xi(z)$ and $\frac{1}{m(z)}\xi'(z)$ must be continuous, which leads to the following condition:

$$k \tan\left(k \frac{L_{\text{QW}}}{2}\right) = K \frac{m_{\text{GaAs}}}{m_{\text{AlGaAs}}} \quad (1.3)$$

for the lowest energy state.

	Light hole	Heavy hole	Electron	Reference
Barrier height V_{conf}	474 meV	474 meV	711 meV	[Bastard]
m_{GaAs} , Effective mass in GaAs	0.094 m_0	0.34 m_0	0.0662 m_0	[Madelung]
m_{AlGaAs} , Effective mass in $\text{Al}_{0.95}\text{Ga}_{0.05}\text{As}$	0.153 m_0	0.409 m_0	0.146 m_0	[Adachi1985]

Table 1.1: Confinement potential and effective masses for electron, light and heavy holes. m_0 is the free electron mass and $x = 0.95$ is the Aluminium fraction in the barrier.

Combining eqs (1.2) and (1.3), E_{conf} can be determined. Using the values ex-

pressed in Table 1.1, we find:

$$\begin{aligned} E_{\text{conf}}^e &\simeq 61 \text{ meV} \\ E_{\text{conf}}^{\text{lh}} &\simeq 46 \text{ meV} \\ E_{\text{conf}}^{\text{hh}} &\simeq 17 \text{ meV}. \end{aligned}$$

The light hole and heavy hole energies are therefore separated by $\simeq 29$ meV due to the confinement in the QW.

Order of magnitude for the binding energies In this paragraph, insight is given on the order of magnitude of the binding energy of heavy and light hole excitons, using Fig. 1.4.b. reproduced from [Bastard].

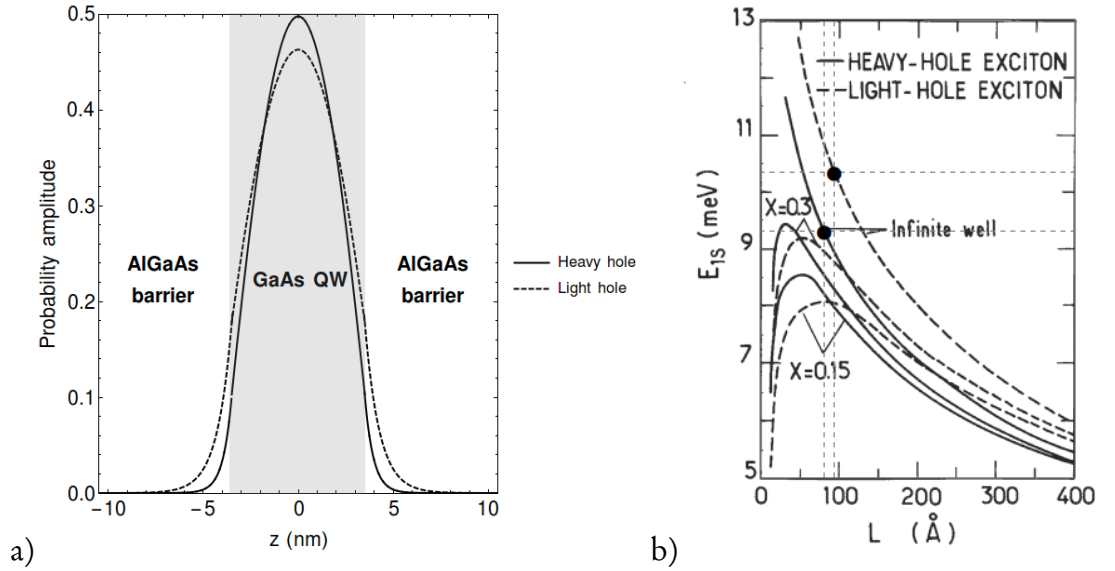


Figure 1.4: a) Probability of presence $\xi(z)$ of the heavy and light holes inside the QW (colored in gray) and in the barriers, computed from eq.(1.1). b) From [Greene1984, Bastard]. Binding energy of a GaAs QW inside various barriers ($\text{Al}_{0.15}\text{Ga}_{0.85}\text{As}$, $\text{Al}_{0.3}\text{Ga}_{0.7}\text{As}$ and infinite barriers) as a function of the QW length. The red dots indicate the binding energy values for the infinite well for an effective length $L_{\text{QW,eff}}^{\text{hh}} = 8.071$ nm for the heavy hole and $L_{\text{QW,eff}}^{\text{lh}} = 9.352$ nm for the light hole.

In Fig. 1.4.b., the finite quantum well is approximated by an infinite quantum well, using effective quantum well thicknesses for the heavy and light holes which take into account the wavefunction penetration in the barrier (Fig. 1.4.a.). This effective thickness $L_{\text{QW,eff}}$ is determined such that the confinement energy for a quantum well with infinite barrier potentials and of thickness $L_{\text{QW,eff}}$ is the same as the confinement energy for a real quantum well of thickness L_{QW} calculated in the

previous paragraph. We find for the electron $L_{\text{QW, eff}}^e \simeq 9.6 \text{ nm}$, $L_{\text{QW, eff}}^{\text{hh}} \simeq 8.1 \text{ nm}$ and $L_{\text{QW, eff}}^{\text{lh}} \simeq 9.4 \text{ nm}$ for the heavy and light holes, respectively.

The binding energy between the electron and the hole is thus slightly different (approximately 1 meV according to the calculation shown in Fig. 1.4.b.). Note that a more accurate calculation of the binding energies, taking into account the Luttinger parameters, can be found in Ref. [Andreani1990].

Conclusion The main contribution to the exciton energy in the typical GaAs quantum wells of interest is therefore the confinement which lifts the degeneracy between light and heavy hole excitons by approximately 29 meV. The difference in the binding energy is only 1 meV. In total, the energy splitting between heavy and light hole excitons is $\Delta E = 28 \text{ meV}$.

The ground state of a quantum well is therefore a 1s exciton formed by an electron in the conduction band and a heavy hole in the valence band. Its energy is expressed by [Fishman]:

$$E_{\mathbf{k}_{\parallel}}^{\text{x}} = E_0^{\text{x}} + \frac{\hbar^2 \mathbf{k}_{\parallel}^2}{2m_{\text{x}}},$$

where $E_0^{\text{x}} = E_{\text{g}} + E_{\text{conf}}^{\text{e}} + E_{\text{conf}}^{\text{hh}} - E_{\text{b}}$, $m_{\text{x}} = m_{\text{e}} + m_{\text{h}} \simeq 0.41 m_0$ is the exciton effective mass ($m_{\text{h}} = -m_{\text{hh}}$ defined in Subsection 1.1.1.1) and \mathbf{k}_{\parallel} is the exciton's in-plane wavevector.

The angular momentum of this first excited state along z is obtained by summing the angular momenta along z of the heavy hole and of the conduction electron (*cf.* Subsection 1.1.1.1):

$$J_z^{\text{exc}} = J_z^{\text{e}} + J_z^{\text{hh}} = \pm 1, \pm 2.$$

1.1.1.4 Dipolar coupling

In the electric dipolar approximation, the interaction between an electron confined in the quantum well and the electromagnetic field reads:

$$\mathbb{H}_{\text{dip}} = -\frac{e}{m_0} \mathbf{p} \cdot \mathbf{A},$$

where \mathbf{p} is the momentum of an electron with charge $-e$ and mass m_0 . \mathbf{A} is the vector potential, defined with the gauge $[\mathbf{p}, \mathbf{A}] = 0$ [Fishman].

The probability of creating an exciton through photon absorption is proportional to the matrix element $\langle \emptyset | \mathbf{p} \cdot \mathbf{A} | e \rangle$, where $|\emptyset\rangle$ is the fundamental state of the crystal, without exciton, and $|e\rangle$ is the first excited state (the heavy hole exciton). The following selection rules apply [Bastard]:

- For spatial symmetry reasons, the exciton must be of type “s” (which is the case for the heavy hole exciton considered),

- The optical excitation of $J_z^{\text{exc}} = \pm 2$ states is forbidden since the angular momentum of a photon is ± 1 , corresponding to left and right circular polarization. The $J_z^{\text{exc}} = \pm 2$ states are therefore called “dark states”.
- Due to translation invariance in the layer’s plane, the in-plane wavevector of excitons must match the photon in-plane wavevector.
- The energy of the photon absorbed or emitted must match the exciton energy.

The radiative lifetime of free QW excitons, given by the Fermi Golden Rule, is approximately 10 ps [Deveaud1991]. The efficiency of the excitonic radiative coupling can be described using an oscillator strength f_{osc} proportionnal to the square modulus of the matrix element of the dipolar interaction corresponding to the creation of an exciton.

In this thesis we will concentrate our study on the bright heavy hole exciton of angular momentum $J_z^{\text{exc}} = \pm 1$ along z .

1.1.2 Properties of microcavities

The coupling between excitons and photons is obtained by inserting the quantum well inside a semiconductor microcavity, the properties of which are detailed in this section. These micrometers-thick monolithic structures are fabricated using Molecular Beam Epitaxy (MBE). The resulting heterostructure has a high quality factor (typically 10^5) and confines photons like a Fabry-Pérot resonator. An important consequence of this confinement is that the photons acquire a (very small) effective mass. The structuration of microcavities through various ways (etching, multiple cavities) as well as the method used to simulate the structure and the fabrication technique are briefly presented.

1.1.2.1 Distributed Bragg Reflectors

The first ingredient of large quality-factor Fabry-Pérot cavities consists of high quality mirrors. In solid-state physics, this is possible using Distributed Bragg Reflectors (DBRs), formed by the alternance of two semiconducting layers with a large refractive index difference. The thickness of each layer is $\lambda/(4n_i)$, where λ is the wavelength of the incoming light and n_i the refractive index of the layer. Under these conditions, an interference takes place which extinguishes transmission on a band of frequencies called stopband, centered on λ .

The reflectivity of such mirrors increases with the refractive index contrast between the two layers and with the number of pairs. Fig. 1.5 presents the reflectivity spectrum of a Bragg mirror with $\text{Al}_{0.95}\text{Ga}_{0.05}\text{As}$ and $\text{Al}_{0.2}\text{Ga}_{0.8}\text{As}$ layers, calculated by the transfer-matrix method (see Subsection 1.1.2.5).

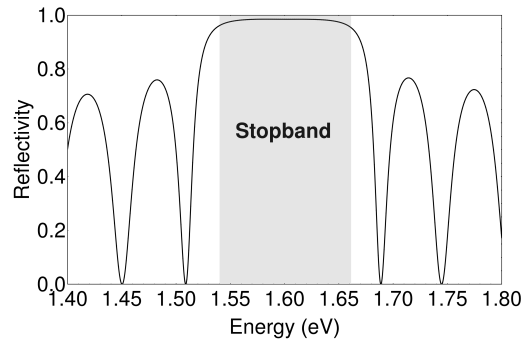


Figure 1.5: Reflectivity spectrum at normal incidence for a Bragg Mirror centered at 1.6 eV with 20 pairs of $\text{Al}_{0.95}\text{Ga}_{0.05}\text{As}/\text{Al}_{0.2}\text{Ga}_{0.8}\text{As}$ surrounded by air, calculated by the transfer-matrix method.

1.1.2.2 Fabry-Pérot cavity

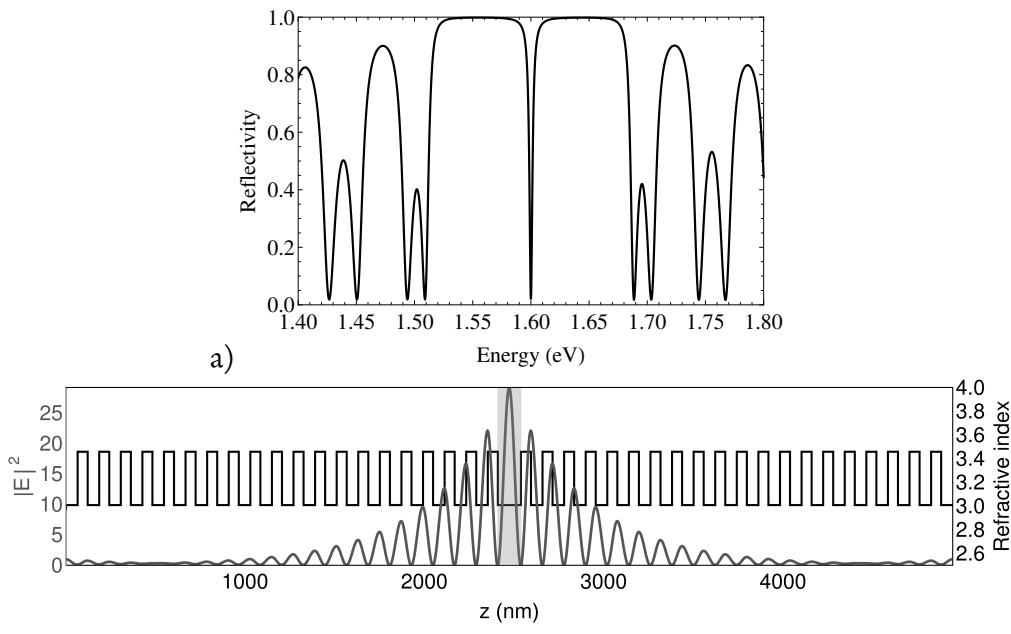


Figure 1.6: a) Reflectivity spectrum at normal incidence of a cavity centered around 1.6 eV surrounded by 20 DBR pairs at each sides, calculated by the transfer-matrix method. b) The corresponding cavity structure is shown in black. In red, the repartition of the squared electric field in the structure. The main antinode is located at the center of the cavity (in gray).

If a spacer of effective thickness $\lambda/(2n_c)$ (where n_c is the refractive index of the spacer) is inserted between two Bragg mirrors, the light of wavelength λ is allowed to penetrate the structure, similarly to Fabry-Pérot cavities. Once inside the structure,

the photons perform a large number of roundtrips (typically 10^5 in the samples presented in this thesis) before being reflected or transmitted.

Fig. 1.6.a. shows an example of the reflectivity spectrum of such structure for normally incident light. The distribution of the electric field intensity corresponding to the cavity mode in the structure is shown in Fig. 1.6.b.

1.1.2.3 Photons effective mass

Due to the confinement along z in the microstructure, the light wavevector k_z is quantized such that $k_{z,p} = \frac{p\pi}{L_{\text{eff}}}$ where $p \in \mathbb{N}^*$ and with L_{eff} the effective length of the half-wavelength ($p = 1$) cavity (taking into account the field penetration into the neighboring DBRs, see Fig. 1.6).

The energy of the admitted mode is therefore:

$$E_{k_{\parallel}}^c = \frac{\hbar c}{n_c} \sqrt{k_{\parallel}^2 + \left(\frac{\pi}{L_{\text{eff}}}\right)^2}, \quad (1.4)$$

where k_{\parallel} is the projection of the wavevector in the layer's plane. The typical photons in-plane wavevectors are small compared to π/L_{eff} , so the cavity mode is a quasi parabolic function of k_{\parallel} . The photon acquires an effective mass $m_c \simeq \frac{n_c \hbar \pi}{c L_{\text{eff}}}$. This effective mass is typically 10^{-5} of the free electron mass, which is several orders of magnitude below the exciton effective mass (*cf.* paragraph 1.1.1.3).

The finesse (which corresponds to the mean number of roundtrips) and quality factor of such half-wavelength cavities coincide:

$$\mathcal{F} = Q = \frac{E_0^c}{\gamma_c},$$

where γ_c corresponds to the linewidth of the cavity mode, or to the cavity losses. The lifetime of the photons in the cavity is typically a few picoseconds.

A large number of DBR pairs reduces the theoretical γ_c , which increases the finesse and the coupling of excitons and photons (see Subsection 1.1.3). However, the number of defects such as dislocations and interface roughness is increased as well, which in turn increases the real photonic losses. In any case, the total thickness must not overcome $\simeq 10 \mu\text{m}$ to ensure the heterostructure mechanical stability.

1.1.2.4 Equivalence between incidence angle and in-plane wavevector

Hence, the energy of the light admitted into the microcavity depends on the effective cavity length L_{eff} and the in-plane wavevector k_{\parallel} of the photons confined in the microcavity.

The intracavity angle of the confined photons θ_c is obtained by the law of refraction: $n_c \sin \theta_c = \sin \theta$, where θ is the light incidence angle on the microstructure

in the air (see Fig. 1.7.a.). For a resonant excitation, this implies that the photons in-plane wavevector is conserved when entering the structure.

k_{\parallel} is related to θ by the following equation:

$$k_{\parallel} = k_{\text{air}} \sin \theta \simeq \frac{E_0^c}{hc} \sin \theta. \quad (1.5)$$

Since the angles considered here are below 30° , $\sin \theta$ can be approximated to θ , such that a one-to-one correspondance between k_{\parallel} and θ is possible.

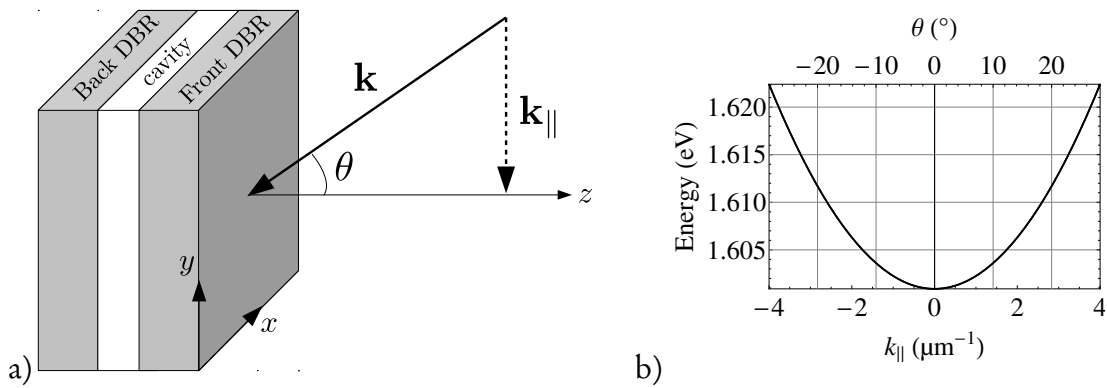


Figure 1.7: a) (x, y) is the “layer’s plane”, orthogonal to the growth direction z . The angle of incidence of the incoming light, θ , is easily related to the in-plane wavevector k_{\parallel} . b) Cavity mode energy dispersion with either k_{\parallel} or θ .

Therefore, energy dispersions as a function of either θ or k_{\parallel} will be presented in this thesis. An example is given in Fig. 1.7.b.

1.1.2.5 Simulation : transfer matrix method

The light acceptance of a 2D-microstructure can be computed using the transfer matrix method [Born&Wolf].

The principle of this method is to calculate the electric and magnetic fields penetrating into the structure layer by layer. In the case of microcavities, this calculation allows:

- To visualize, at a given incident angle, the reflectivity of the structure, and to deduce the admitted wavelength (like in Figs. 1.5 and 1.6).
- By concatenating the reflectivity at several angles, to visualize the cavity angle dispersion which is supposed to follow a quasi-parabolic law (see eq (1.4)). The TE-TM splitting (see Subsection 1.3.1) can be also computed.

- To visualize the electric field repartition in the structure (like in Fig. 1.6.b.). In order to maximize the light-matter coupling, the quantum wells must be placed at the antinodes of the electric field penetrating the structure.

Quantum wells layers can be added in the calculation and modeled as absorbers. The bound exciton resonance is taken into account in the energy-dependent linear susceptibility of the QW layer including an oscillator strength f_{osc} [Khitrova1999]:

$$\chi^{(1)}(E) \propto \frac{f_{\text{osc}} \cdot E_0^x}{E_0^x - E^2 - i\gamma_x E},$$

where E_0^x is the exciton energy (assumed constant considering its large effective mass), γ_x corresponds to excitonic losses.

1.1.2.6 Fabrication: growth by Molecular Beam Epitaxy

The samples are fabricated using Molecular Beam Epitaxy (MBE). This deposition method is done in ultra-high vacuum, by varying the temperature of the Ga, As and Al sources which are deposited on a GaAs wafer. The duration of deposition determines the thickness of each layer. All the samples presented in this manuscript have been grown by Aristide Lemaître at the *Laboratoire de Photonique et Nanostructures* (LPN) in Marcoussis.

For a uniform deposition on the substrate, the wafer can be rotated during the growth. However, the wafer is often kept fixed during the growth of the spacer so that a wedge on the spacer thickness L_c occurs. Consequently, the cavity mode energy has a quasi-linear dependency on position.

The wedge also affects the quantum well thickness inside the spacer. However, for a 7 nm-thick GaAs quantum well, the dominant contribution to the energy variation is the exciton confinement energy of about $E_{\text{conf}} = E_{\text{conf}}^c + E_{\text{conf}}^{\text{hh}} \simeq 80$ meV (see Table 1.1), the exciton binding energy being only a few meV. For infinite barriers, the confinement energy scales as $1/L_{\text{QW}}^2$, where L_{QW} is the quantum well thickness and the normal cavity mode energy E_0^c varies as $1/L_{\text{eff}}$, where L_{eff} is the cavity effective thickness taking into account penetration of the electric field in the neighboring antinodes.

Assuming a similar relative increase in the quantum well thickness and cavity effective length due to the wedge, we deduce that the exciton energy variation compared to the cavity energy variation scales as $2E_{\text{conf}}/E_0^c$, where $E_0^c \simeq 1.6$ eV. This variation is thus approximately 10% of the cavity energy variation and can be safely neglected.

To increase the confined cavity mode energy variation even faster, the rotation of the wafer can be also stopped during the growth of the Bragg mirrors to shift the DBRs stopband as well.

1.1.2.7 Structured microcavities

The structuration of microcavities enables the confinement of several optical modes. Two possible methods are presented in this subsection.

1D microcavity

The microcavity can be engineered so as to break the rotation invariance in the layer’s plane. This is possible by etching the 2D-microcavity so as to form narrow wires. Chapter 3 is devoted to such 1D-microcavities, and the etching was done by Isabelle Sagnes at the *Laboratoire de Photonique et de Nanostructures*.

This breaking of symmetry introduces new boundary conditions and gives rise to a splitting of the 2D optical mode in several photonic modes labelled by $j \in \mathbb{N}$. The confinement along the short axis of the wire X induces boundary conditions for the electric field, which then writes $E_X \propto \cos(k_X X)$ or $E_X \propto \sin k_X X$, where $k_X = \frac{\pi(j+1)}{W}$ and W is the effective wire width [Kuther1998]. The index j corresponds therefore to the number of nodes of the electromagnetic field in the direction X . If j is even (respectively odd), the electromagnetic field has a symmetric (resp. antisymmetric) distribution along X .

With $k_{\parallel}^2 = k_X^2 + k_Y^2$, the new photonic mode energies write:

$$E_{k_Y}^{c,j} = \frac{\hbar c}{n_c} \sqrt{k_Y^2 + \left(\frac{\pi(j+1)}{W}\right)^2 + \left(\frac{\pi}{L_{\text{eff}}}\right)^2}.$$

Some cavity mode energy dependencies on k_Y and their corresponding electric field distribution along the wire short axis, are represented on Fig. 1.8.

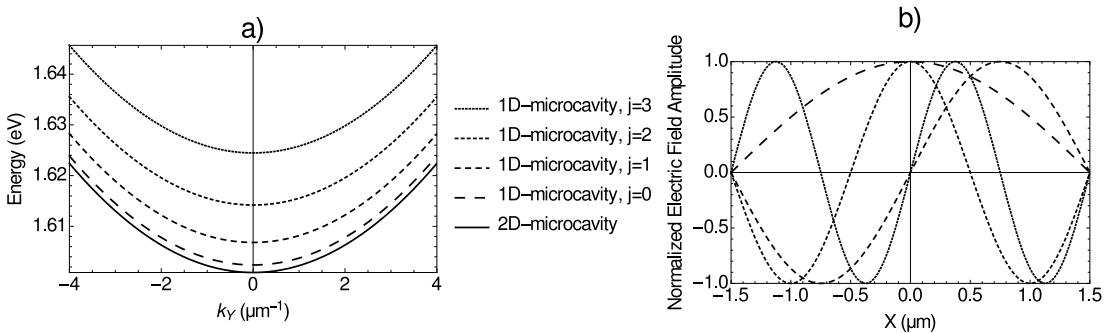


Figure 1.8: a) Energy dispersion for the various cavity modes of a 3 μm -large 1D-microcavity as a function of k_Y (Y is the long axis of the wire). The energy dispersion of the cavity mode of a 2D-microcavity is shown as a plain line, as a function of k_Y (equivalent to any other in-plane wavevector component in a 2D structure). b) Corresponding electric field amplitude along X (short axis of the wire).

Coupled 2D-microcavities

By superimposing two identical 2D-cavities separated by an intermediate Bragg mirror, a coupling can occur between the two cavity modes. Two energy modes are then admitted in the cavity, separated by an energy $2\Omega_C$. The value of this splitting depends on the number of layers constituting the intermediate Bragg mirror and can be computed using the transfer-matrix method (see Subsection 1.1.2.5).

Fig. 1.9 shows the result of the simulations of a structure composed of two identical microcavities having a resonant cavity mode energy at 1.6 eV (such as the one shown in Fig. 1.6). In Fig. 1.9.a., they are separated by 20 DBR pairs. Two optical modes are now allowed separated by 6 meV. In Fig. 1.9.b., the number of DBR pairs is reduced to 10, such that the cavity-cavity coupling increases: the two optical modes are now separated by 25 meV.

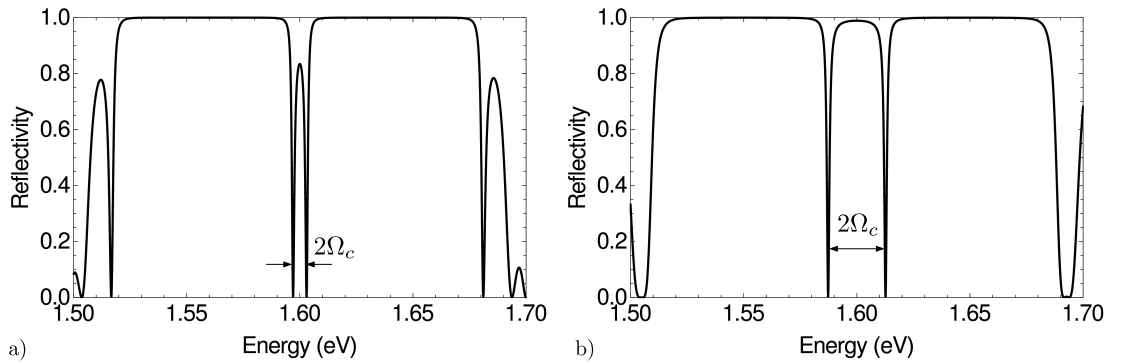


Figure 1.9: Reflectivity spectra of two superimposed microcavities identical to the one of Fig. 1.6. a) Double microcavity with 20 intermediate DBR pairs. b) idem with 10 intermediate DBR pairs.

A such double microcavity will be studied in Chapter 4.

1.1.3 Strong coupling regime

1.1.3.1 Light-matter coupling strength

We consider now the case of quantum wells that are inserted at the antinode of the electric field (at the center of the cavity). When the light-matter coupling is larger than the cavity and exciton losses, the *strong coupling regime* is achieved. A lifting of degeneracy between the excitonic transition and the cavity mode energy takes place with strength $2\Omega_R$, where Ω_R is the normal-mode splitting (also called Rabi coupling or Rabi splitting in solid-state physics), proportionnal to the square root of the oscillator strength f_{osc} and to the overlap integral between the wavefunction of the exciton and the cavity mode.

For N identical quantum wells, this Rabi coupling is increased by a factor \sqrt{N} . In practice, the number of quantum wells coupled to an antinode of the electric

field cannot be increased indefinitely due to its finite size. Moreover, the quantum wells must be well separated so as to avoid any mutual coupling. Given those constraints, in order to increase the light-matter coupling, some quantum wells can also be inserted into the neighboring antinodes of the cavity, that is, inside the first neighboring Bragg mirrors from each side of the cavity.

In the structures presented in this thesis, four quantum wells are inserted in the cavity spacer, and four on the neighboring Bragg mirrors on each side, such that the oscillator strength f_{osc} is increased by $\simeq 12$.

1.1.3.2 Microcavity polaritons

The eigenstates resulting from this strong coupling are mixed exciton-photon states called *microcavity excitons-polaritons*, evidenced for the first time by Weisbuch *et al.* [Weisbuch1992] in 1992. From a general point of view, the term polariton refers to any quasi-particle mixing photon and an elementary excitation of matter, such as phonon [Le Gall1997], plasmon [Craig1983], *etc.* Exciton-polaritons are also observed and well-known in the bulk semiconductors [Fröhlich1971].

Eigenenergies

Let us denote c the cavity field, e the exciton field and Ψ the polariton field. The indices and exponents x (respectively c) refer to excitons (respectively photons). For simplicity, $\mathbf{k} = \mathbf{k}_{\parallel}$ labels the wavevector of excitons and photons in the layer's plane.

When $2\Omega_R$ is larger than γ_x (excitonic losses) and γ_c (cavity losses), the strong coupling regime is achieved and the Schrödinger equation for the exciton and photon fields reads:

$$i\hbar \frac{\partial}{\partial t} \begin{pmatrix} e_{\mathbf{k}} \\ c_{\mathbf{k}} \end{pmatrix} = \begin{bmatrix} E_{\mathbf{k}}^x - i\gamma_x & -\Omega_R \\ -\Omega_R & E_{\mathbf{k}}^c - i\gamma_c \end{bmatrix} \cdot \begin{pmatrix} e_{\mathbf{k}} \\ c_{\mathbf{k}} \end{pmatrix}, \quad (1.6)$$

where $E_{\mathbf{k}}^x = E_0^x + \frac{\hbar^2 k_{\parallel}^2}{2m_x}$ is the exciton energy dispersion with \mathbf{k} . Similarly, $E_{\mathbf{k}}^c = E_0^c + \frac{\hbar^2 k_{\parallel}^2}{2m_c}$ is the cavity energy dispersion with \mathbf{k} .

In this regime, the system can be studied by considering quasi particles half photon half excitons (polaritons) which are eigenstates of the above system of equations:

$$\Psi_{\mathbf{k}}^{\text{LP}} = X_{\mathbf{k}} e_{\mathbf{k}} + C_{\mathbf{k}} c_{\mathbf{k}} \quad (1.7)$$

$$\Psi_{\mathbf{k}}^{\text{UP}} = -C_{\mathbf{k}} e_{\mathbf{k}} + X_{\mathbf{k}} c_{\mathbf{k}}, \quad (1.8)$$

where $X_{\mathbf{k}}$ et $C_{\mathbf{k}}$ are the Hopfield coefficients [Hopfield1958], which determine the exciton and photon weights in the upper (Ψ^{UP}) and lower (Ψ^{LP}) polariton modes. At large in-plane wavevectors, the upper (resp. lower) polariton mode is close to the photonic (resp. excitonic) mode.

The eigenenergies are solution of the two coupled oscillators equation (which

corresponds to the determinant of the matrix 1.6):

$$(E^P - E_{\mathbf{k}}^x + i\gamma_x)(E^P - E_{\mathbf{k}}^c + i\gamma_c) = \Omega_R^2, \quad (1.9)$$

such that:

$$E_{LP}^P(\mathbf{k}) = E_{\mathbf{k}}^x + \frac{\Delta_{\mathbf{k}}}{2} - i\gamma_p - \frac{1}{2}\sqrt{(\Delta_{\mathbf{k}} - i(\gamma_c - \gamma_x))^2 + 4\Omega_R^2} \quad (1.10)$$

$$E_{UP}^P(\mathbf{k}) = E_{\mathbf{k}}^x + \frac{\Delta_{\mathbf{k}}}{2} - i\gamma_p + \frac{1}{2}\sqrt{(\Delta_{\mathbf{k}} - i(\gamma_c - \gamma_x))^2 + 4\Omega_R^2}, \quad (1.11)$$

where $\Delta_{\mathbf{k}} = E_{\mathbf{k}}^c - E_{\mathbf{k}}^x$ is the exciton-photon detuning, and $\gamma_p = \frac{\gamma_c + \gamma_x}{2}$ corresponds to polariton losses at null detuning. In this thesis, we will focus on the lower polariton modes $\Psi_{\mathbf{k}}^{LP}$ with energy $E_{LP}^P(\mathbf{k})$, which will be noted $\Psi_{\mathbf{k}}$ and $E_{\mathbf{k}}^P$ in the following.

The eigenenergies as a function of $\mathbf{k} = \mathbf{k}_{\parallel}$ for various exciton photon detuning at $\mathbf{k}_{\parallel} = 0$, $\Delta = \Delta_0$, are represented on Fig. 1.10 (losses neglected).

In Fig. 1.10.a., the bare exciton and cavity dispersion as a function of in-plane wavevector are displayed for vanishing exciton-photon detuning $\Delta = 0$. The exciton energy is approximated constant considering its much larger effective mass.

In the strong coupling regime, a lifting of degeneracy takes place between the cavity and exciton energy dispersion, leading to two polariton branches (Fig. 1.10.b.). At normal incidence ($k_{\parallel} = 0$), the polariton modes up and down are 50% photon, 50% exciton. At large in-plane wavevectors, the lower polariton branch is very close to the exciton one. This region is called *excitonic reservoir* since the density of these quasi-excitonic states is large. In-between, the low polariton branch exhibits an inflection point which enables the fulfilment of the phase-matching conditions for nonlinear optical processes (see next section).

Fig. 1.10.c. shows the evolution of the normal cavity, exciton, and polariton energies as a function of detuning. At large negative detuning, the lower polariton is almost entirely photonic, whereas at positive detuning it tends towards the exciton.

Figs. 1.10.d. and e. show the polariton dispersion when the cavity energy is shifted out of the exciton resonance. At negative detuning $\Delta < 0$, the minimum of the lower polariton branch becomes more photonic. Inversely, at positive detuning $\Delta > 0$, the lower polariton branch is more excitonic, and its curvature is reduced.

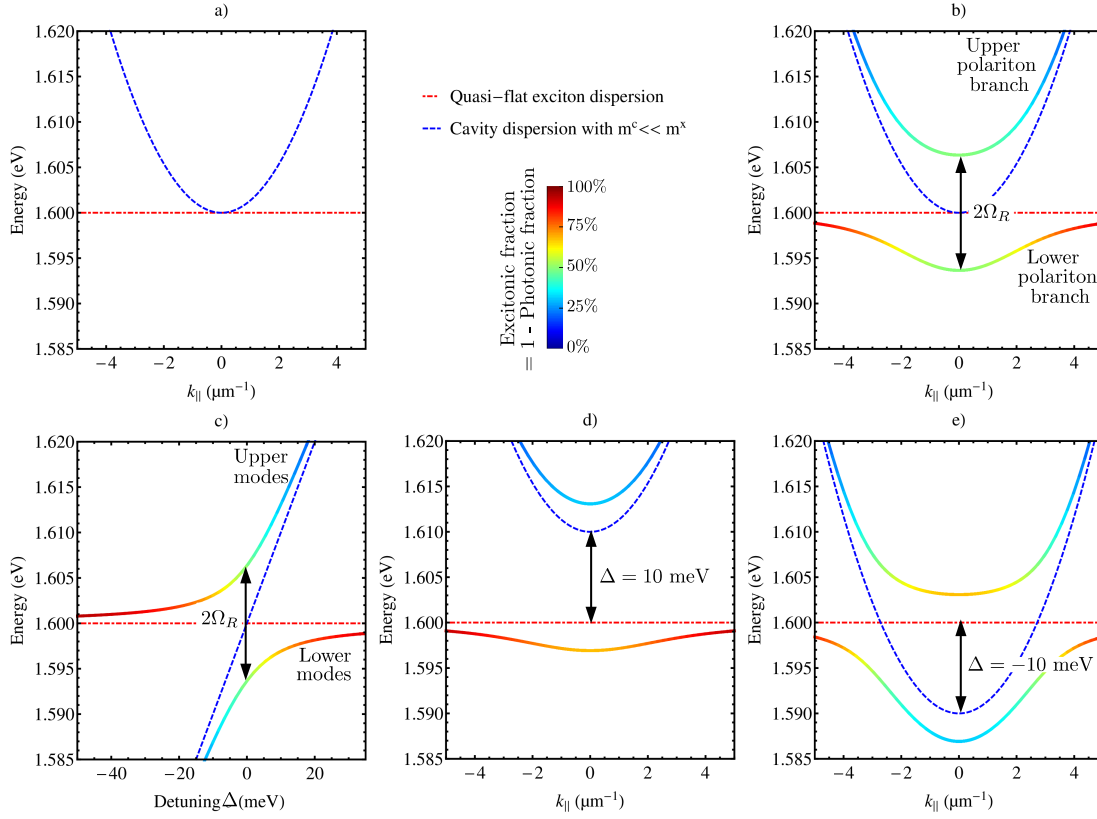


Figure 1.10: (a, b) Energy dispersions with in-plane wavevector k_{\parallel} for vanishing exciton-photon detuning $\Delta = E_0^c - E_0^x = 0$. The cavity effective mass is much smaller than the exciton's. For this reason, the exciton dispersion is approximated by a horizontal line. In b), the strong coupling between excitons and photons induces a lifting of degeneracy of strength $2\Omega_R$ for $k_{\parallel} = 0$, resulting in “up” and “down” polariton branches. The excitonic fraction $|X_{\mathbf{k}}|^2$ (resp. $|C_{\mathbf{k}}|^2$) for the low (resp. up) polaritons (see eqs. (1.8) and (1.7)) is represented via a colorscale. c) Cavity, exciton and polariton energies at $k_{\parallel} = 0$ as a function of exciton-photon detuning, figuring an “anticrossing”. (d, e) Cavity, exciton and polariton energy dispersions for $\Delta = \pm 10$ meV.

1.1.3.3 Transition to the weak coupling regime

At null detuning, the lifting of degeneracy occurs only if $|\gamma^c - \gamma^x| < 2\Omega_R$. If this first condition is fulfilled, then, the lifting of degeneracy is visible only if the splitting strength Ω_R overcomes the polariton loss $\gamma^p = \frac{\gamma^c + \gamma^x}{2}$. Overall, the strong coupling is effective when the photonic and excitonic losses are small compared to $2\Omega_R$. The weak coupling regime is thus described by a perturbative treatment: the cavity modifies the spontaneous emission properties of the quantum well excitons. The exciton desexcites irreversibly and its radiative lifetime is given by the Fermi

Golden rule. The Vertical Cavity Surface Emitting Lasers (VCSEL) operate in this regime at low density.

On the one hand, the Rabi coupling is maximized by using a large numbers of high quality DBR layers, and by increasing the number of quantum wells in the structure, but they are limited by the total size of the structure and the size of the main antinodes of the electric field, as discussed in Subsection 1.1.2.3. On the other hand, the sources of losses for the cavity and exciton are numerous:

- Inhomogeneous broadening due to structural defects, impurities, interface roughness, inhomogeneities between the quantum wells or DBRs,
- Phonon-assisted relaxation. This source of loss is temperature-dependent, and increases the exciton linewidth. For this reason, in this work, all experiments are performed at 6K. This relaxation process is particularly efficient for the upper polariton modes, which are typically located slightly above the *excitonic reservoir*,
- At large polariton densities (above 10^{11} cm^{-2}), saturation of the light-matter coupling occurs (see Subsection 1.2.2.4), which leads to the loss of the strong coupling regime.

Experimentally, the light-matter strong coupling is lost when either the optical power or the temperature is increased. Typically, for III-V semiconductor microcavities containing a single quantum well, the strong coupling is lost above 100K and for excitation densities above $8 \text{ kW} \cdot \text{cm}^{-2}$ [Houdré1995].

1.2 Parametric effects in microcavities

In GaAs/AlGaAs-based semiconductor microcavities, large high-order nonlinearities take place leading to various parametric phenomena analogous to four-wave-mixing processes in nonlinear Optics. In this section the nonlinear equations are presented, with a focus on the third order terms in the electric field. Various nonlinear effects such as the Optical Kerr Effect, responsible for a blueshift of the polariton energies, and the Optical Parametric Amplification are introduced. The second part is devoted to the discussion of the Optical Parametric Oscillation (OPO).

1.2.1 Third-order susceptibility

1.2.1.1 Nonlinear dielectric polarization

The response of a material to an applied electric field is taken into account by a susceptibility tensor $\chi^{(m)}$, where m labels the order of the nonlinearity. The linear susceptibility is related to the refractive index: $n^2 = \Re(1 + \chi^{(1)})$. This susceptibility tensor takes into account anisotropies (for example structural anisotropies aligned

with the crystalline axes of the material). When the optical power is sufficiently strong, the polarization of the medium is a nonlinear function of the electric field such that:

$$\mathbf{P} = \mathbf{P}^{(1)} + \mathbf{P}^{(2)} + \mathbf{P}^{(3)} + \dots,$$

where

$$\mathbf{P}^{(m)}(\omega = \omega_1 + \omega_2 + \dots + \omega_m) = \varepsilon_0 \chi^{(m)}(\omega; \omega_1, \omega_2, \dots, \omega_n) \otimes \mathbf{E}_1(\omega_1) \mathbf{E}_2(\omega_2) \dots \mathbf{E}_m(\omega_m)$$

and ε_0 is the vacuum permittivity.

Assuming an isotropic system, the propagation equation for the electric field reads [Shen]:

$$\Delta \mathbf{E} - \frac{1}{c^2} \frac{\partial^2 \mathbf{E}}{\partial t^2} = \frac{1}{\varepsilon_0 c^2} \frac{\partial^2 \mathbf{P}^{(1)}}{\partial t^2} + \frac{1}{\varepsilon_0 c^2} \frac{\partial^2 \mathbf{P}^{(NL)}}{\partial t^2}, \quad (1.12)$$

where $\mathbf{P}^{(NL)}$ is the nonlinear part of the polarization.

Assuming a plane wave propagating along z , the electric field reads: $\mathbf{E}(z, t) = \Re[\sum_j \mathcal{E}(z, \omega_j) e^{i(\mathbf{k}_j z - \omega_j t)}]$, where $k_j^2 = \omega_j^2 (1 + \chi^{(1)}(\omega_j))/c^2$. In the slow-varying amplitude approximation, eq. (1.12) rewrites:

$$\sum_j 2i k_j \frac{\partial \mathcal{E}(z, \omega_j)}{\partial z} e^{i(\mathbf{k}_j z - \omega_j t)} = \frac{1}{\varepsilon_0 c^2} \frac{\partial^2 \mathfrak{P}^{(NL)}(\omega_j, z)}{\partial t^2}, \quad (1.13)$$

where $\mathfrak{P}^{(NL)}$ is the complex nonlinear polarization.

Due to its crystalline symmetry [Shen], the GaAs second-order susceptibility is null on the growth axis z . Therefore, the following subsections focus on the third order polarization which writes:

$$\mathfrak{P}^{(3)}(z, t) = \sum_{jkl} \varepsilon_0 \chi_{jkl}^{(3)} \mathcal{E}(z, \omega_j) \mathcal{E}^*(z, \omega_k) \mathcal{E}(z, \omega_l) e^{i[(\mathbf{k}_j - \mathbf{k}_k + \mathbf{k}_l) \cdot z - (\omega_j - \omega_k + \omega_l)t]}$$

The linear susceptibility $\chi^{(1)}$ is taken real, such that $k_j = n(\omega_j) \omega_j / c$. The third-order nonlinearity $\chi^{(3)}$ is considered scalar for simplicity.

1.2.1.2 Optical Kerr Effect

Assuming a single incident pump field with wavevector \mathbf{k}_p and frequency ω_p , and keeping only the terms with same phase as the incident field, we get:

$$\mathfrak{P}^{(3)}(\omega_p) = \frac{3\varepsilon_0 \chi^{(3)}}{4} |\mathcal{E}(z, \omega_p)|^2 \mathcal{E}(z, \omega_p) e^{i(\mathbf{k}_p z - \omega_p t)}.$$

With $|\mathcal{E}(z, \omega)|^2 = I$, the propagation equation (1.13) becomes:

$$\frac{\partial \mathcal{E}(z, \omega_p)}{\partial z} = \frac{3i\omega_p \chi^{(3)}}{8nc} \cdot I \cdot \mathcal{E}(z, \omega_p)$$

One possible solution is $\mathcal{E}(z, \omega_p) = \mathcal{E}(0, \omega_p) e^{i\phi_{\text{NL}}(z)}$, where $\phi_{\text{NL}}(z) = \frac{3\omega_p \chi^{(3)}}{8nc} \cdot I \cdot z$. This nonlinear phase depends on the incident power I on the nonlinear medium, phenomenon known as the optical Kerr effect. An effective refractive index n' can be defined: $n' = n + \frac{3\chi^{(3)}}{8n} \cdot I$.

If the nonlinear medium is inserted in an optical resonator, the cavity resonant energy is blueshifted. Experimentally, it implies that when the optical power sent onto the microcavity is changed, the energy must be slightly shifted as well.

This phenomenon leads to a bistability: one can show [Lecomte2011] that the intracavity intensity exhibits an hysteresis behaviour with the incident intensity close to the resonance.

1.2.1.3 Optical Parametric Amplification

Let us consider now a second beam (signal) incident on the material with energy ω_s and wavevector \mathbf{k}_s . The nonlinear polarization rewrites:

$$\mathfrak{P}^{(3)}(\omega) = \frac{\varepsilon_0 \chi^{(3)}}{8} (\mathcal{E}_p e^{i(\mathbf{k}_p z - \omega_j t)} + \mathcal{E}_p^* e^{-i(\mathbf{k}_p z - \omega_j t)} + \mathcal{E}_s e^{i(\mathbf{k}_s z - \omega_j t)} + \mathcal{E}_s^* e^{-i(\mathbf{k}_s z - \omega_j t)})^3,$$

The term $\mathcal{E}_p \mathcal{E}_p \mathcal{E}_s^*$ is responsible for the apparition of a beam with energy $2\omega_p - \omega_s$, called idler beam, which propagates with the wavevector $2\mathbf{k}_p - \mathbf{k}_s$. This phenomenon is a parametric conversion. Assuming a pump beam much more intense than the signal and idler beams, the propagation equations for the signal and idler fields read:

$$\begin{cases} \frac{d\alpha_s}{dz} &= g \cdot \alpha_i^*(z) \\ \frac{d\alpha_i}{dz} &= g \cdot \alpha_s^*(z) \end{cases},$$

with $\alpha_i = \mathcal{E}_i e^{i\phi^{(3)}(z)}$, $\phi^{(3)}(z) = \frac{6i\omega \chi^{(3)}}{8nc} \cdot I \cdot z$, $I = |\mathcal{E}_p|^2$, and

$$g = \chi^{(3)} \frac{3i\omega}{8nc} |\mathcal{E}_p|^2$$

is the parametric gain.

If $\alpha_i(0) = 0$, case where no idler beam is sent onto the material, this system can be solved:

$$\begin{aligned} \alpha_s(z) &= \alpha_s(0) \cosh(gz) \\ \alpha_i(z) &= \alpha_s^*(0) \sinh(gz) \end{aligned} \quad (1.14)$$

The signal beam is amplified by a factor $|\cosh(gz)|^2$. This is optical parametric amplification. An idler beam is furthermore created, with an energy fulfilling $\omega_{\text{idler}} = 2\omega_p - \omega_s$. In terms of photons, this corresponds to a four-wave mixing process: two pump photons are converted into one signal and one idler photon.

Note that this process can occur only if the following phase-matching conditions are fulfilled:

- energy conservation: $\omega_{\text{idler}} = 2\omega_p - \omega_s$
- wavevector conservation: $\mathbf{k}_{\text{idler}} = 2\mathbf{k}_p - \mathbf{k}_s$.

Eq. (1.14) holds as long as $|\alpha_s|, |\alpha_i| \ll |\alpha_p|$. However, the amplification of the signal and idler beams leads to a depletion of the pump beam, such that the pump evolution with time cannot be neglected any longer. Thus, under certain conditions described in the following subsection, a single pump beam can spontaneously and reversibly generate signal and idler beams. This is called Optical Parametric Oscillation (OPO).

1.2.2 Optical Parametric Oscillation

1.2.2.1 Generalities

The nonlinear material is placed in a Fabry-Pérot cavity, resonant for one or several frequencies. A resonant optical pump is sent onto the structure. When the parametric gain of the nonlinear medium is equal to the cavity losses, the system starts to oscillate on the resonant modes. This parametric gain is a function of the pump intensity, as seen in the previous paragraph. This phenomenon appears therefore at large pump intensities (above the “OPO threshold”). When the signal and idler beams intensities increase, the pump intensity decreases (since it is the source for signal and idler beams) and the parametric gain saturates.

The Fabry-Pérot cavity can be resonant with a single mode (signal for example), for two modes (such as signal and idler) or triply resonant (pump, idler and signal). The advantage of doubly and triply resonant OPOs is that the OPO threshold is lowered (from watts to a few milliwatts).

Commercial OPOs are used for the generation of new frequencies in laser cavities. The active medium is usually a nonlinear crystal such as KTP crystals, inserted in complex optical cavities and pumped by an external laser. The advantage of these macroscopic OPO is their tunability (505 - 750 nm range or 1 to 3 μm for the KTP crystal). Besides, OPO devices are potential source of non-classical states such as twin or squeezed states, with large applications in quantum cryptography, teleportation, or information stockage [Heidmann1987, Mertz1991, Teja1998]. Phase-matching or quasi phase-matching [Vodopyanov2004] is obtained using various strategies, such as birefringence [Shen] or crystalline structuration [Myers1995, Vodopyanov2004, Baudrier-Raybaut2004].

In this manuscript, we will only consider degenerate microscopic OPOs created in semiconductor microcavities, meaning that the signal, idler and pump beams all have the same energy. Such OPO processes are the onset of spontaneous pattern formation in a double microcavity, as will be shown in Chapter 4. In this section, the strategies for obtaining the phase-matching for the OPO process in a microcavity are presented. The coherence properties of the signal and idler beams have been extensively studied in our group (V. Ardizzone, T. Lecomte and C. Diederichs) and a brief summary of their work is given. The quantum treatment is presented, followed by a discussion on the pattern formation in micro-OPOs, experimentally demonstrated by V. Ardizzone in 2013 [Ardizzone2013b].

1.2.2.2 Phase-matching in microcavities

The first demonstration of OPO in microcavities was done at large oblique angle for the pump. A pump light injects polaritons near the inflection point (called the "magic angle") of the low energy polariton dispersion with \mathbf{k} . Two pump polaritons can be coherently scattered, giving rise to a signal polariton at $\mathbf{k}_s = 0$ and an idler polariton at $\mathbf{k}_{\text{idler}} = 2\mathbf{k}_p$ on the same polaritonic branch. This process is shown in Fig. 1.11.a. Its first experimental demonstration in 2000 was an optical parametric amplification, where an additional probe sent at $\mathbf{k}_s = 0$ is amplified by two orders of magnitude [Savvidis2000]. Then, the OPO regime was reached [Stevenson2000, Baumberg2000].

The necessary ingredients for this phenomenon are:

1. large $\chi^{(3)}$ nonlinearities,
2. the strong coupling regime to ensure the inflection of the polariton branch and the fulfilment of the phase-matching conditions,
3. injection at a very specific angle which varies with exciton-photon detuning. This is an important limitation in the perspective of integrated micro-OPOs. For example, a VCSEL-type optical pumping is not possible.

Finally, since the idler beam is created on the lower polariton branch with a large in-plane wavevector (see Fig. 1.11.a.), its photonic component is weak. Collecting photons from this mode is particularly inefficient, not to mention the strong imbalance between signal and idler optical intensities, which complicates the measurement of the non-classicity of the emitted beams.

To overcome these limitations, our group at the *Laboratoire Pierre Aigrain* has proposed to structure the microcavities :

- By using multiple microcavities
- By using 1D-microcavities.

In both cases, several low polariton modes exist since several cavity modes can couple to the excitonic transition (see Subsection 1.1.2.7), allowing for interbranch OPOs. In Fig. 1.11.b. for example, the pump is sent at normal incidence resonant with an intermediate low polariton branch, and the signal and idler beams are detected at normal incidence on the neighboring low polariton branches. This process was first demonstrated by C. Diederichs in a triple microcavity [Diederichs2005, Diederichs2006].

In this work we will focus on the degenerate process presented in Fig. 1.11.c.: the pump is sent at normal incidence, and signal and idler beams are detected at opposite angles. Therefore, signal and idler beams have the same Hopfield coefficients so they are well balanced in intensities.

Note that these processes (b. and c.) involve energies situated below the excitonic reservoir, such that the relaxation towards it are reduced.

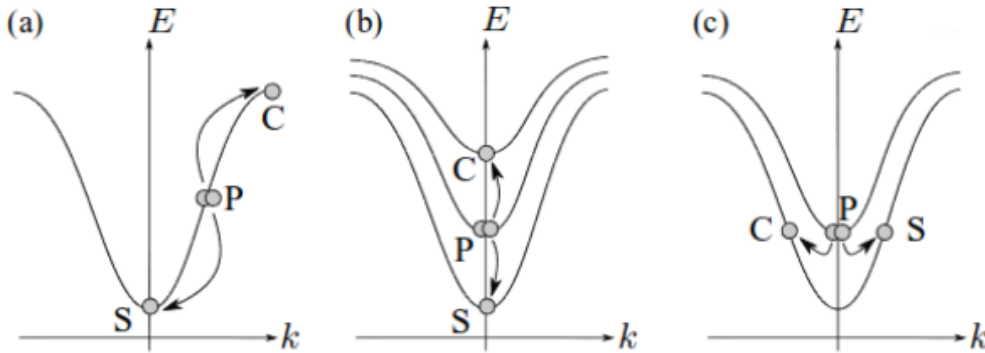


Figure 1.11: Reproduced from [Ardizzone2013a]. a) OPO at the Magic Angle. This process produces strongly intensity-unbalanced signal and idlers due to their different Hopfield coefficients. b) Non-degenerate interbranch OPO at normal incidence in a triple microcavity [Diederichs2005]. This process is not ideal for quantum information applications, since signal and idler beams are not degenerate. However, it is of interest in the prospect of micro-OPO devices. c) Degenerate interbranch OPO.

Note that, similarly to the optical Kerr effect (Subsection 1.2.1.2), the optical parametric oscillation exhibits a bistable behaviour.

1.2.2.3 Coherence properties

In the process represented on Fig. 1.11.c. the signal and idler beams are produced simultaneously, at the same frequency and with opposite angles. This horizontal OPO process is therefore an excellent candidate for the generation of twin polaritons. Theoretically, twin polaritons should violate the following Cauchy-Swchartz

inequality [Ardizzone2013a]:

$$\left[g_{S,I}^{(2)}(0) \right]^2 < g_S^{(2)}(0)g_I^{(2)}(0),$$

where $g_{S,I}^{(2)}(0)$ is the cross-correlation between signal and idler beams, and $g_S^{(2)}(0)$ ($g_I^{(2)}(0)$) is the self-correlation of the signal (idler) beam at zero delay.

However, the violation of this inequality is exalted for small photon fluxes. Indeed, at large powers, the parametric oscillation creates a transition towards a laser-like emission statistics. But, at small powers, parasitic signal such as resonant Rayleigh scattering (see paragraph 1.3.1.2) spoils the parametric signal.

Therefore, no quantum correlation has yet been experimentally demonstrated between signal and idler. Vincenzo Ardizzone has reached in 2013 the classical limit $g_{S,I}(0) \sim g_S(0) \sim g_I(0)$ and detailed in his manuscript the experimental reasons for the saturation of the Cauchy-Schwartz inequality [Ardizzone2013a].

1.2.2.4 Quantum treatment

The third-order nonlinearity is essentially due to a repulsive coulombic interaction between excitons, which can be written in the Hartree-Fock approximation $V_{HF} = 2\pi(1 - \frac{315}{4096}\pi^2)(a_0^{3D})^2 E_b$, where a_0^{3D} is the exciton 3D Bohr radius and E_b is the exciton binding energy.

Additionally, the densities of excitons allowed in the structure saturates due to Pauli-blocking fermionic phase-space filling $\alpha_{PSF} = \frac{4\pi}{7}(a_0^{3D})^2$. The phase-space filling implies that the density of polaritons saturate at a density $n_{sat} = |\Psi^{sat}|^2 = 1/\alpha_{PSF}$. Typically, $n_{sat} = 20 \times 10^{10} \text{ cm}^{-2}$.

Including those two nonlinear terms, and taking into account all the scattering channels in the k-space, the Schrödinger equation for the exciton field $e_{\mathbf{k}}$ rewrites as a *Gross-Pitaevskii equation* [Schmitt-Rink1985]:

$$\begin{aligned} i\hbar \frac{\partial e_{\mathbf{k}}}{\partial t} &= (E_{\mathbf{k}}^x - i\gamma_x)e_{\mathbf{k}} - \Omega_R c_{\mathbf{k}} + \frac{1}{\mathcal{L}^2} \sum_{\mathbf{k}'\mathbf{k}''} e_{\mathbf{k}'+\mathbf{k}''-\mathbf{k}}^* e_{\mathbf{k}'} \alpha_{PSF} \Omega_R c_{\mathbf{k}''} \\ &+ \frac{1}{\mathcal{L}^2} \sum_{\mathbf{k}'\mathbf{k}''} V_{HF} e_{\mathbf{k}'+\mathbf{k}''-\mathbf{k}}^* e_{\mathbf{k}'} e_{\mathbf{k}''}, \end{aligned}$$

where \mathcal{L}^2 is a normalization factor.

The equation for the electric field still writes:

$$i\hbar \frac{\partial c_{\mathbf{k}}}{\partial t} = (E_{\mathbf{k}}^c - i\gamma_c)c_{\mathbf{k}} - \Omega_R e_{\mathbf{k}}.$$

Therefore, for a microcavity in the strong coupling regime, the Gross-Pitaevskii

equation for the lower polariton field rewrites:

$$i\hbar \frac{\partial}{\partial t} \Psi_{\mathbf{k}} = (E_{\mathbf{k}}^{\text{P}} - i\gamma^{\text{P}}) \Psi_{\mathbf{k}} + \alpha \sum_{\mathbf{k}' \mathbf{k}''} \Psi_{\mathbf{k}'+\mathbf{k}''-\mathbf{k}}^* \Psi_{\mathbf{k}'} \Psi_{\mathbf{k}''}, \quad (1.15)$$

where $\alpha \simeq \frac{1}{4}(V_{\text{HF}} + \alpha_{\text{PSF}}\Omega_{\text{R}})$ near null exciton-photon detuning (the dependency of these terms with the Hopfield coefficients and with wavevector is neglected).

The term $\mathbf{k}' = \mathbf{k}'' = \mathbf{k}$ in equation (1.15) can be assimilated to the Optical Kerr Effect (Subsection 1.2.1.2). This term blueshifts the polariton resonance energy by $2\alpha |\Psi_{\mathbf{k}}|^2$. In practice, to remain at resonance, the laser wavelength needs to be adjusted each time the power is changed.

The other terms correspond to $\chi^{(3)}$ nonlinearities due to polariton-polariton interactions.

1.2.2.5 Pattern formation

OPO using $\chi^{(2)}$ nonlinear crystals have been shown to exhibit pattern formation [Vaupel1999, Ducci2001]. A pattern is a self-organized structure, spontaneously arising due to the combination of nonlinearities (to saturate the growth of the unstable modes of the pattern) and spatial coupling terms. Pattern formation is therefore very general in nonlinear physics, from morphogenesis [Turing1952] to hydrodynamics [Cross1993] and chemistry [Kapral&Showalter]. The similarities between the hydrodynamical equations and pattern formation in Optics are detailed in refs. [Arecchi1995, Oppo2008].

Following a proposal from theoretician teams from Paderborn (Germany) and Tucson (Arizona) [Schumacher2009, Dawes2010, Luk2013], V. Ardizzone demonstrated in 2013 [Ardizzone2013b, Ardizzone2013a] the formation of hexagonal patterns in the degenerate OPO regime (process c. of Fig. 1.11) in a double microcavity. Several degrees of freedom for the pattern formation can be exploited such as the polarization, the energy and the (small) wavevector of the pump beam, use of an additional probe beam. Microcavities are thus a unique laboratory for the understanding of the pattern formation physics. From an application point of view, the control of pattern formation offers an excellent candidate for fast all-optical switch devices, easily integrable with other electro-optics components such as VCSELs.

In Chapter 4, I continue the work of V. Ardizzone by a systematic study of the various available degrees of freedom. In particular, a rotation over 360° of a two-point pattern is demonstrated by rotating the pump's linear polarization, paving the way to a potential *microscopic lighthouse* device.

1.3 Polarization effects in microcavities

The polarization effects arising in semiconductor microcavities are numerous, and Ref. [Shelykh2010] gives a detailed review on these aspects. In this thesis, we will concentrate on the polarization effects which affect the propagation of polaritons in various scattering regimes. We will not discuss the polarization effects arising in the regime of Bose condensation.

In the regime of resonant elastic Rayleigh scattering, where the interactions between polaritons can be safely neglected, we first discuss a long-range spin-orbit coupling effect, namely the cavity TE-TM splitting. It gives rise to the so-called “Optical Spin Hall Effect”. Then short-range effects, arising from 1D-confinement or mechanical constraints, are introduced. Finally, we discuss the spin-dependence of exciton-exciton interactions in the nonlinear regime, that is, above the OPO or OPA threshold discussed in the previous section.

1.3.1 Long-range polarization effect: the TE-TM splitting

In this section, the TE-TM splitting, a k -dependent polarization splitting vanishing at $k_{\parallel} = 0$, is detailed. Its origin lies in the photonic, the excitonic or the exciton-photon coupling term of the polariton. The Optical Spin Hall Effect (OSHE) derives from this effect.

1.3.1.1 Origins of the TE-TM splitting

TE and TM polarizations are defined with respect to the direction of the in-plane wavevector k_{\parallel} (see Fig. 1.12.a. and b.).

TE-TM splitting on the cavity mode In 2D microcavities, the TE polarization is always in the layer’s plane, whereas the TM polarization projects with an angle θ in the layer’s plane (see Fig. 1.12.a and b.). The penetration depth of the cavity mode inside the DBRs is therefore different for TE and TM polarization [Panzarini1999]. This effect can be taken into account by a different effective cavity mass for the TM and TE mode (see Fig 1.12.c.).

$$E_{\mathbf{k}}^{c, \text{TE/TM}} = E_0^c + \frac{\hbar^2 k_{\parallel}^2}{2m_c^{\text{TE/TM}}}$$

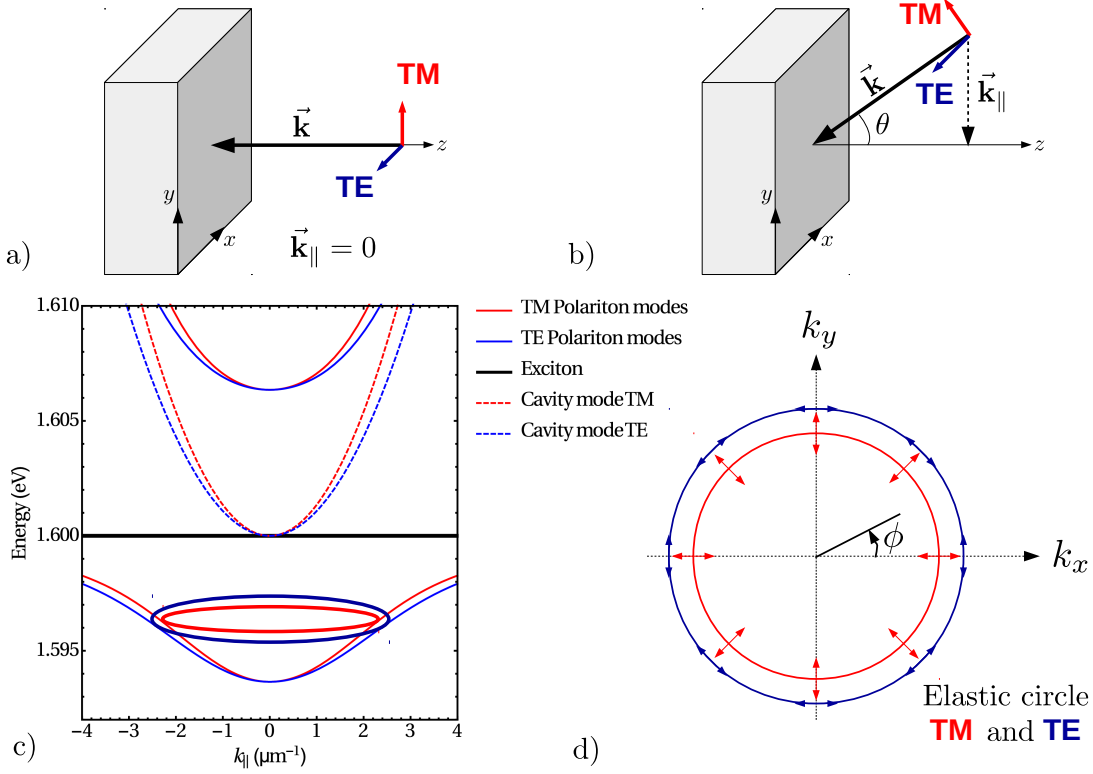


Figure 1.12: TE and TM polarizations for excitation (a) at normal incidence ($k_{\parallel} = 0$) and (b) at oblique incidence ($k_{\parallel} \neq 0$). In (a), TE and TM polarizations are both in-plane, whereas in (b), the TM polarization has an angle θ with the layer’s plane while the TE polarization remains in-plane. c) Energy dispersion with in-plane wavevector. A TE-TM splitting is included here in the cavity mode (exaggerated here with $m_{\text{TE}}/m_{\text{TM}} = 1.25$), and induces in return a TE-TM splitting on the polariton branches. The so-called “elastic circle” at energy 1.596 eV is sketched on the dispersion and represented in (d) in the in-plane wavevector space. ϕ is the azimuthal angle along the elastic circle.

In the basis of circularly-polarized light, the equations for the electric and excitonic field rewrite:

$$i\hbar \frac{d}{dt} \begin{pmatrix} e^+ \\ e^- \\ c^+ \\ c^- \end{pmatrix} = \begin{pmatrix} E_0^x & 0 & -\Omega_R & 0 \\ 0 & E_0^x & 0 & -\Omega_R \\ -\Omega_R & 0 & E_{\mathbf{k}}^c & \Delta_{\mathbf{k}}^{c,+} \\ 0 & -\Omega_R & \Delta_{\mathbf{k}}^{c,-} & E_{\mathbf{k}}^c \end{pmatrix} \begin{pmatrix} e^+ \\ e^- \\ c^+ \\ c^- \end{pmatrix} \quad (1.16)$$

with $E_{\mathbf{k}}^c = E_0^c + \frac{\hbar^2 k_{\parallel}^2}{4} \left(\frac{1}{m_c^{\text{TE}}} + \frac{1}{m_c^{\text{TM}}} \right)$ the mean cavity dispersion and $\Delta_{\mathbf{k}}^{c,\pm} = \frac{\hbar^4}{4} \left(\frac{1}{m_c^{\text{TM}}} - \frac{1}{m_c^{\text{TE}}} \right) (k_x \mp ik_y)^2$ including the cavity TE-TM splitting. This coupling

results in a TE-TM splitting of the polariton modes (Fig. 1.12.c. and d.) on the elastic circle.

N.B.: The losses are neglected in the eq. (1.16), but one can show [Panzarini1999] that the cavity losses γ_c at finite k_{\parallel} also depend on the polarization. Additionally, for multiple microcavities, the cavity-cavity coupling Ω_c defined in paragraph 1.1.2.7 exhibits the same behavior.

TE-TM splitting on the exciton energy There is also a TE-TM splitting of the exciton $\Delta_{\mathbf{k}}^{x,\pm}$ at large k_{\parallel} , coming from the long range part of electron hole exchange interaction. However, its order of magnitude is only a few μeV inside the light cone and can therefore be safely neglected [Shelykh2010].

TE-TM splitting on the exciton-photon coupling Due to the $\cos\theta$ projection on the layer's plane for TM polarization, the exciton-photon coupling is larger for a TE polarization than for a TM one for $k_{\parallel} \neq 0$ (see Fig. 1.12), such that

$$\Omega_{\mathbf{R},\mathbf{k}}^{\text{TM}} \simeq \Omega_{\mathbf{R},\mathbf{k}}^{\text{TE}} \cos\theta_c,$$

where θ_c is the intracavity angle (see Subsection 1.1.2.4) [Panzarini1999].

Conclusion: TE-TM splitting on the polariton energy Whatever the origin of the TE-TM polarization splitting, the equation for the lower polariton in the circular polarization basis close to null exciton-photon detuning can be written:

$$i\hbar \frac{\partial}{\partial t} \Psi_{\mathbf{k}}^{\pm} = (E_{\mathbf{k}}^{\text{p}} - i\gamma_{\text{p}}) \Psi_{\mathbf{k}}^{\pm} + \Delta_{\mathbf{k}}^{\text{p},\pm} \Psi_{\mathbf{k}}^{\mp}, \quad (1.17)$$

$E_{\mathbf{k}}^{\text{p}} \simeq E_0^{\text{x}} - \Omega_{\text{R}} + \frac{\hbar^2 k^2}{2} \frac{1}{2} \left(\frac{1}{m_{\text{p}}^{\text{TE}}} + \frac{1}{m_{\text{p}}^{\text{TM}}} \right)$ is the mean polarization dispersion with \mathbf{k} , where $m_{\text{p}}^{\text{TE/TM}} \simeq 2m_{\text{c}}^{\text{TE/TM}}$ is the polariton effective mass for TE or TM polarizations. $\Delta_{\mathbf{k}}^{\text{p},\pm} = \frac{\hbar^2}{4} \left(\frac{1}{m_{\text{p}}^{\text{TM}}} - \frac{1}{m_{\text{p}}^{\text{TE}}} \right) (k_x \mp ik_y)^2$ takes into account the TE-TM splitting. $\Delta_{\mathbf{k}}^{\text{p},\pm}$ can be rewritten as $\Delta_{\mathbf{k}}^{\text{p,TL}} e^{\mp 2i\phi}$, where $\Delta_{\mathbf{k}}^{\text{p,TL}} = \frac{\hbar^2}{4} \left(\frac{1}{m_{\text{p}}^{\text{TM}}} - \frac{1}{m_{\text{p}}^{\text{TE}}} \right) k^2$ and ϕ is the azimuthal angle along the elastic circle as defined by Fig. 1.12.d.

1.3.1.2 Consequence: the Optical Spin Hall Effect

The Optical Spin Hall Effect is a direct application of this \mathbf{k} -dependent TE-TM splitting. Predicted by Kavokin *et al.* [Kavokin2005] and experimentally observed by Leyder *et al.* in 2007 [Leyder2007], it is similar to the Rashba-Dresselhaus spin-orbit coupling in semiconductors quantum wells. It results from the association of a scattering mechanism (elastic Rayleigh scattering) with the long-range TE-TM splitting

in semiconductors microcavities. In pure photonic cavities an analogue of this effect has also been observed [Maragkou2011].

Consequently, the polariton polarization is rotated as a function of the direction of its propagation, such that opposite polarizations are separated in space.

Resonant elastic Rayleigh scattering The Rayleigh scattering is an elastic scattering on the microcavities defects. It allows to change the polariton wavevector without affecting its energy (provided there is an available polariton state at the new wavevector and energy).

Leyder *et al.* experiment In the original experiment by Leyder [Leyder2007], a pump is sent at an oblique angle resonant with a polariton state. Its polarization is linear. The pump polaritons are scattered by resonant elastic Rayleigh scattering onto the other available states (the so-called elastic circle, see Fig. 1.12). Due to the TE-TM splitting, some eigenstates on the elastic circle are not co-polarized to the pump's polarization. Therefore, the pump polaritons rotate their polarization during propagation. Looking at the circular polarization degree $S_3 = |\Psi^+|^2 - |\Psi^-|^2$, the re-emitted light exhibits four quadrants as a function of polarization.

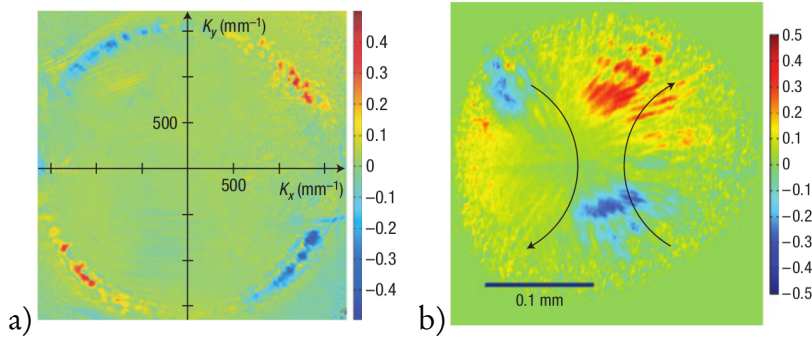


Figure 1.13: First experimental demonstration of the “Optical Spin Hall Effect” from [Leyder2007]. Degree of circular polarization in the far-field (a) and near-field (b) for a “x” (or horizontally) polarized pump sent at oblique incidence and resonant with the elastic circle ($k_x = 1.56 \mu\text{m}^{-1}$). The TE-TM splitting strength is $\Delta_k^{\text{p,TL}} = 0.05 \text{ meV}$.

Direct calculation To account for the experimental result, an “x”-polarized pump term ψ_{pump}^x is added in eq. (1.17), with resonant energy $E_{\text{pump}} = E_{\mathbf{k}}^{\text{p}}$ (elastic Rayleigh scattering). Eq. (1.17) in the steady-state rewrites:

$$\begin{pmatrix} -i\gamma_{\text{p}} & \Delta_{\mathbf{k}}^{\text{p,TL}} e^{-2i\phi} \\ \Delta_{\mathbf{k}}^{\text{p,TL}} e^{2i\phi} & -i\gamma_{\text{p}} \end{pmatrix} \begin{pmatrix} \Psi_{\mathbf{k}}^+ \\ \Psi_{\mathbf{k}}^- \end{pmatrix} + \begin{pmatrix} \psi_{\text{pump}}^+ \\ \psi_{\text{pump}}^- \end{pmatrix} = 0, \quad (1.18)$$

where $\begin{pmatrix} \psi_{\text{pump}}^+ \\ \psi_{\text{pump}}^- \end{pmatrix} = \frac{1}{\sqrt{2}} \begin{pmatrix} \psi_{\text{pump}}^x \\ \psi_{\text{pump}}^x \end{pmatrix}$. Note that the pump term not only includes the pump polaritons at k_x (see Fig. 1.13) but also the x-polarized Rayleigh-scattered polaritons along the whole elastic circle.

We find:

$$\begin{aligned} S_3 &= |\Psi_{\mathbf{k}}^+|^2 - |\Psi_{\mathbf{k}}^-|^2 \\ &= - \frac{2\gamma_p \Delta_{\mathbf{k}}^{\text{p,TL}} |\psi_{\text{pump}}^x|^2 \sin 2\phi}{(\gamma_p^2 + (\Delta_{\mathbf{k}}^{\text{p,TL}})^2)^2}. \end{aligned} \quad (1.19)$$

This $\sin 2\phi$ dependency of the degree of circular polarization is indeed observable in Fig. 1.13.a.

Pseudo-spin evolution Alternatively, the non diagonal terms in eq. (1.18) can be written as the linear combination of the identity matrix and a spin-orbit interaction

$\frac{1}{2}\mathbf{B} \cdot \boldsymbol{\sigma}$, where $\boldsymbol{\sigma} = \begin{pmatrix} \sigma_x \\ \sigma_y \\ \sigma_z \end{pmatrix}$ is the Pauli matrix vector $\sigma_x = \begin{pmatrix} 0 & 1 \\ 1 & 0 \end{pmatrix}$, $\sigma_y = \begin{pmatrix} 0 & -i \\ i & 0 \end{pmatrix}$ and $\sigma_z = \begin{pmatrix} 1 & 0 \\ 0 & -1 \end{pmatrix}$. The modified effective magnetic field is

$$\mathbf{B} = \begin{pmatrix} \Delta_{\mathbf{k}}^{\text{p,TL}} \cos 2\phi \\ \Delta_{\mathbf{k}}^{\text{p,TL}} \sin 2\phi \\ 0 \end{pmatrix}. \quad (1.20)$$

Fig. 1.14 represents the effective magnetic field as a function of ϕ on the elastic circle.

The polariton pseudo-spin is defined using the Stokes parameters:

$$\mathbf{S}_{\mathbf{k},i} = (\Psi^{+*} \quad \Psi^{-*}) \cdot \sigma_i \cdot \begin{pmatrix} \Psi^+ \\ \Psi^- \end{pmatrix}$$

$$\begin{aligned} S_1 &= \Psi^- \Psi^{+*} + \Psi^+ \Psi^{-*} = 2\Re(\Psi^{+*} \Psi^-) \\ S_2 &= -i(\Psi^- \Psi^{+*} - \Psi^+ \Psi^{-*}) = 2\Im(\Psi^{+*} \Psi^-) \\ S_3 &= |\Psi^+|^2 - |\Psi^-|^2 \end{aligned}$$

The evolution of the pseudo spin is given by eq. (1.21):

$$\frac{d\mathbf{S}_{\mathbf{k}}}{dt} = \frac{1}{\hbar} \mathbf{B}_{\mathbf{k}} \wedge \mathbf{S}_{\mathbf{k}} - \frac{\mathbf{S}_{\mathbf{k}}}{\tau} + \frac{\mathbf{S}_0}{\tau_1}, \quad (1.21)$$

where \mathbf{S}_0 is the pump polaritons pseudo-spin (proportional to $(|\psi_{\text{pump}}^x|^2, 0, 0)$), $\tau = \hbar/\gamma_p$ is the polariton lifetime and τ_1 is the Rayleigh scattering time constant. The solution of eq. (1.21) gives the same form for \mathbf{S}_3 than eq. (1.19).

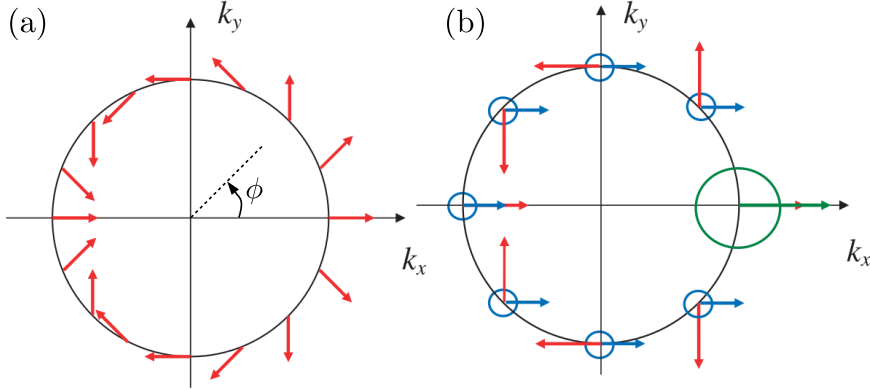


Figure 1.14: Adapted from Ref. [Kavokin2005]. a) Effective magnetic field induced by the TE-TM splitting on the elastic circle. b) The pump location is shown by a green circle, and the direction of its polarization by a green arrow. The Rayleigh-scattered x-polarized pump polaritons are represented by the blue markers. When the pseudo-spin (blue arrows) is not aligned with the direction of the magnetic field, torque occurs on the pseudo-spin inducing its rotation on the Poincaré sphere.

The Optical Spin Hall Effect is therefore a spatial separation of polariton pseudo-spin assisted by resonant elastic Rayleigh scattering, due to the TE-TM splitting and the finite lifetime of polaritons. In Chapter 4, a full optical control of the OSHE is proposed and demonstrated.

In the two next subsections, two possible origins for polarization splittings arising at $k_{\parallel} = 0$ are considered.

1.3.2 Constraints-induced normal polarization splitting

We consider in this subsection polarization splittings arising from mechanical constraints at normal incidence.

Constraints can indeed lead to polarization-anisotropic splitting for the cavity modes via stress-induced birefringence in the microcavity, resulting in a splitting of the bare photon mode into two orthogonally-polarized states [Dasbach2005,Diederichs2007].

An excitonic polarization splitting due to the short-range part of the electron-hole exchange interaction takes also place in GaAs quantum wells and microcavities [Dasbach2002].

Additionally, under anisotropic constraints, a Pikus-Bir deformation Hamiltonian has to be considered, which mixes the heavy-hole and light-hole excitonic states. The diagonalization of the resulting hamiltonian leads to a splitting of the exciton

energy and a difference in the exciton-photon coupling strength of the new states. Such effect has been observed by applying a tip on a microcavity in [Balili2010]. Note that the heavy-light hole mixing is negligible in unstressed samples since light and heavy hole excitons are separated by approximately 30 meV in 7 nm GaAs quantum wells (see Subsection 1.1.1.3).

1.3.3 Confinement-induced normal polarization splitting

In this subsection, we consider polarization splittings arising from additional 1D-confinement (like in microwires, see Subsection 1.1.2.7) at normal incidence. The confinement has an effect on the cavity mode and on the exciton-photon coupling strength [Kuther1998].

First, let us define here the effective confinement angle θ_{eff} : the lateral confinement implies that the cavity modes are plane waves in the lateral direction labelled by the lateral mode index $j = 0, 1, \dots$. Neglecting the contribution of the evanescent field outside of the wire, the lateral wavevector reads $k_X = \frac{\pi(j+1)}{W}$, where W is the wire width (*cf.* Subsection 1.1.2.7).

The internal wavevector is $k = \frac{n_c E_0^c}{\hbar c}$, where n_c is the cavity layer refractive index, E_0^c is the cavity mode energy, and c is the speed of light in the vacuum. We can then define the effective confinement intracavity angle as:

$$\sin \theta_{\text{eff}} = \frac{k_X}{k} \simeq \frac{\hbar c \pi (j+1)}{W n_c E_0^c} \quad (1.22)$$

which is the angle with respect to the normal direction of the virtual propagating plane-wave corresponding to the considered laterally confined mode. This effective angle increases with j and decreases with W . It induces an energy splitting between linear polarizations along X and Y for the cavity mode and for the normal exciton-photon Rabi coupling, which increases with θ_{eff} [Panzarini1999].

1.3.4 Spin-dependent exciton-exciton interactions

Lastly, due to direct and exchange two-excitons correlations [Takayama2002], the exciton-exciton interaction term presented in Subsection 1.2.2.4 is spin-dependent. They are described by the energy-dependent parameters¹ T^{++} and T^{+-} , if the two excitons have the same or opposite spins [Schumacher2007].

¹The system is assumed spin-symmetric such that $T^{++} = T^{--}$ and $T^{+-} = T^{-+}$, where “+” and “-” refer to +1 and -1 exciton spins, which couple to left (“+”) and right (“-”) circularly polarized light (see Subsection 1.1.1.4).

In the polariton basis, the Gross-Pitaevski equation 1.15 rewrites:

$$\begin{aligned}
 i\hbar \frac{\partial}{\partial t} \Psi_{\mathbf{k}}^{\pm} &= (E_{\mathbf{k}}^{\text{p}} - i\gamma_{\text{p}}) \Psi_{\mathbf{k}}^{\pm} + \Delta_{\mathbf{k}}^{\text{p},\pm} \Psi_{\mathbf{k}}^{\mp} \\
 &+ \sum_{\mathbf{k}, \mathbf{k}''} (\alpha^{++} \Psi_{\mathbf{k}'+\mathbf{k}''-\mathbf{k}}^{\pm*} \Psi_{\mathbf{k}'}^{\pm} \Psi_{\mathbf{k}''}^{\pm} + \alpha^{+-} \Psi_{\mathbf{k}'+\mathbf{k}''-\mathbf{k}}^{\mp*} \Psi_{\mathbf{k}'}^{\mp} \Psi_{\mathbf{k}''}^{\pm}), \quad (1.23)
 \end{aligned}$$

where $\alpha^{++} \simeq \frac{1}{4}(T^{++} + \alpha_{\text{PSF}}\Omega_{\text{R}})$ and $\alpha^{+-} \simeq -\frac{1}{4}T^{+-}$. They can be written as a function of the Hopfield coefficients, and depend therefore on detuning and \mathbf{k} . They are analogous to the polariton-polariton interaction potentials V_1 and V_2 sometimes used in polariton theory and experiments [Vladimirova2010, Lecomte2014].

The spin-dependent exciton-exciton interaction parameters affect the efficiency of $\chi^{(3)}$ nonlinear processes. Typically, for the scattering processes and the negative exciton-photon detuning used in this work, $T^{++} > 0$ and $T^{+-} \simeq -\frac{1}{4}T^{++}$. For linear polarization pumping, this implies in particular that the colinear configuration (signal and idler co-polarized to the pump), involving the sum of the two contributions, is less efficient than the cross-polarized configuration, which involves their difference.

Conclusion

In this chapter, the main theoretical tools and concepts have been introduced. Microcavity exciton-polaritons are quasi-particles arising from the strong coupling between quantum well excitons and photons confined in semiconductor microcavities. In single planar microcavities, their energy dispersion with the in-plane wavevector (or, equivalently, with the angle of the incident light, see Subsection 1.1.2.4) exhibit two quasi-parabolic branches (the “lower” and “upper” polariton branches). Microcavities can be structured so as to tune the polaritonic modes allowed in the cavity.

Due to their excitonic component, polaritons can interact. The large $\chi^{(3)}$ susceptibility offered by GaAs/AlGaAs semiconductors induces a blueshift of the polariton energies and leads to Optical Parametric Amplification and Oscillation processes, where two pump polaritons are converted into one signal and one idler polaritons fulfilling phase-matching conditions, similarly to a four-wave mixing process for photons.

Circularly-polarized light couples with excitons with a ± 1 z-component of their total angular momentum. A pseudo-spin corresponding to the Stokes parameter can thus be attributed to polaritons. Various polarization-dependent energy splittings occur, either at large in-plane wavevector, or close to zero incidence angle. Finally, in the nonlinear regime, the polariton-polariton interactions are in fact spin-dependent.

The next chapter is devoted to the experimental tools used to probe the physical phenomena arising in the structured microcavities of interest.

2

EXPERIMENTAL METHODS

In this chapter, the various experimental setups used during this PhD thesis are detailed. The setup is a confocal experiment specially designed for the observation of light emission at large angles. Indeed, the quasi-parabolic polariton dispersion allows to define the so-called elastic circle (see Fig. 2.1): to one excitation energy corresponds a cone of light emission with a specific angle. The typical emission angles observed in this work are between 20° and 30° (depending on the exciton-photon detuning).

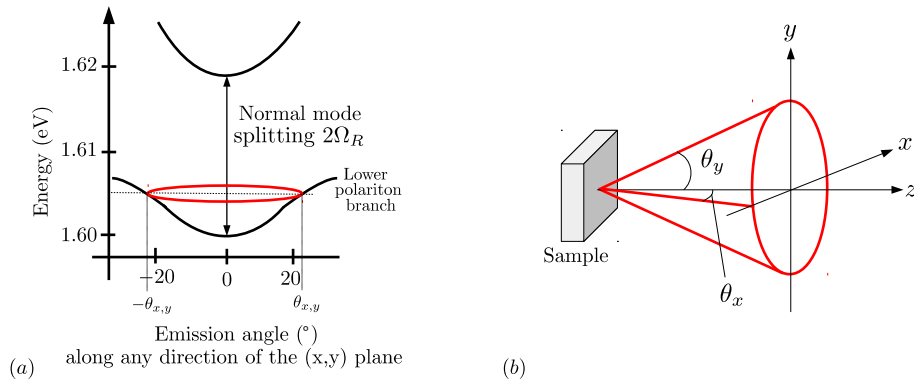


Figure 2.1: *a)* Energy dispersion of a single microcavity. At fixed excitation energy ($\simeq 1.605$ eV) corresponds a fixed angle $\theta_x = \theta_y$, defining a cone of light emission depicted in *(b)*. The so-called “elastic circle” corresponds to the projection of this cone onto the (x, y) plane.

The first section details the various possibilities for the excitation of the sample of interest. The differences between two laser sources are described in detail (the “pump”), as well as the optical path for additional probe beams and the possible ways to tune slightly the angle of incidence of the excitation beam.

In the second section, the various setups used to image and analyze the emitted light from the sample are described, with a specific focus on the polarization control of both excitation beam and emitted light.

Chapter content

2.1	Excitation setup	54
2.1.1	Optical path for the pump	54
2.1.2	Small pump tilt	56
2.1.3	Optical path for the probe(s)	57
2.1.4	Properties of the optical pump	58
2.1.4.1	Intensity fluctuations of the MIRA laser	58
2.1.4.2	Alternative cw tunable laser: the SOLSTIS laser	62
2.2	Detection setup	64
2.2.1	Momentum space	65
2.2.2	Angle-resolved energy dispersion	66
2.2.3	Real space	67
2.2.3.1	Spherical aberrations of the ocular L_f	68
2.2.3.2	Setup for the simultaneous observation of the real space and the momentum space	70
2.2.4	Polarization control of the exciting and emitted light	71

2.1 Excitation setup

The sample is stuck with silver laque on a copper holder inside an Oxford cold finger cryostat. A vacuum of $\simeq 10^{-6}$ mbar is obtained using a turbo pump. The sample is cooled down to 6K, using an Oxford transfer tube with circulating Helium. An ITC503 temperature controller is used to maintain the desired temperature by adjusting the helium flow or by heating the sample holder using a resistance. The cryostat includes a 1 inch optical window for the excitation and collection of the emitted light, and can be shifted along the three space directions.

2.1.1 Optical path for the pump

The optical setup for the excitation of the sample at normal incidence (the “pump”) is shown in Fig. 2.2. The excitation source is a MIRA 900 laser, an infrared tunable Titane:Sapphire laser which can operate either in continuous wave or deliver picosecond or femtosecond pulses in the mode-locking regime. The laser is tunable between 700 and 1000 nm. In most applications, the laser wavelength used is around 775 nm. More details on the laser properties are given in Subsection 2.1.4. The MIRA is pumped by a VERDI laser, a continuous wave frequency doubled Nd:Vanadate laser delivering up to 8W of 532 nm laser light (not represented on Fig. 2.2).

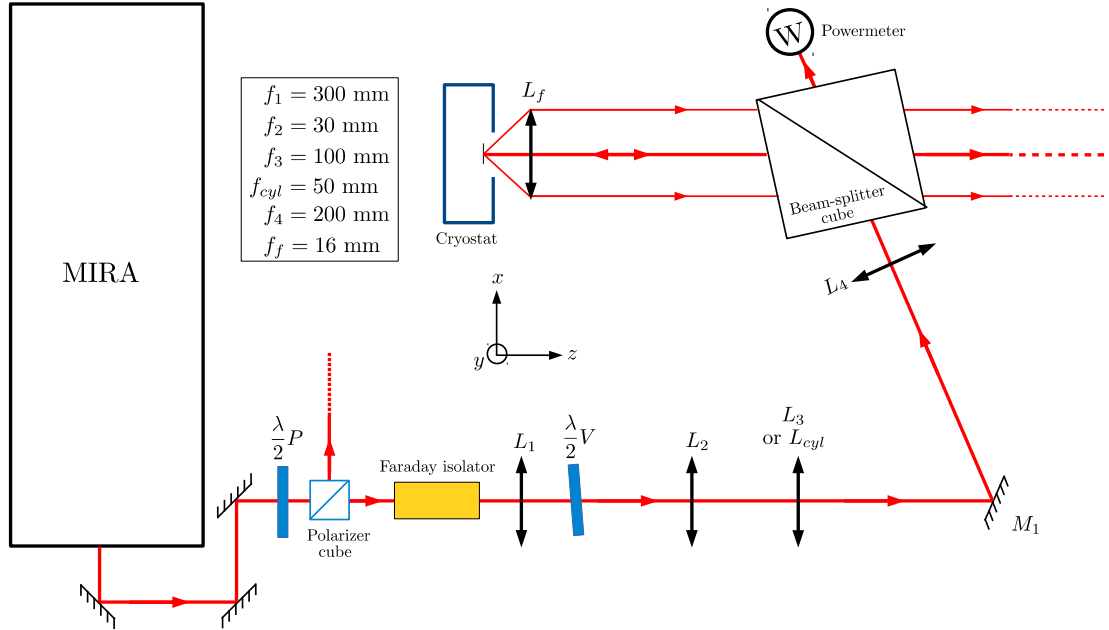


Figure 2.2: Schematic top view of the optical setup for the excitation of the sample with a pump at normal incidence.

The laser is p-polarized at the output (its polarization is “horizontal”, that is, parallel to the optics table plane and perpendicular to the propagation direction). The association of the half-wave plate P and the polarizer cube allows to finely tune the outgoing excitation beam power (Fig. 2.2).

The Faraday isolator ensures that no backreflection from the optical components or from the sample can reenter the MIRA cavity and perturb the laser emission. Its attenuation is 40 dB. The beam-splitter cube is tilted so as to avoid parasitic back-reflections and the lenses L_1 , L_2 , L_3 and L_4 are provided with an anti-reflection coating.

At the output of the Faraday isolator, the polarization of the beam is diagonally linear. The next half-wave plate V rotates the polarization so that the outgoing beam is s-polarized (or vertically-polarized, that is, normal to the optics table plane, or along y). The plate is slightly tilted so as to compensate for a slight remaining elliptical component of the outgoing beam.

The lenses L_1 , L_2 , L_3 and L_4 are placed in order to collimate the beam onto L_f , resulting in a $50 \mu\text{m}$ excitation spot on the sample. The optical path has been calculated using the software GaussianBeam developed by the C.E.A. [Lecomte2011]. The lens L_3 is replaced by a cylindrical lens L_{cyl} for the study of microwires (in Chapter 3). The excitation spot is thus elongated and matches the wire geometry.

The beam-splitter is a 50/50 cube. Half of the incoming beam is reflected and excites the sample, whereas the other half is transmitted through the cube and used to monitor the excitation beam power. The response of the cube under horizontal or vertical polarization has been carefully calibrated and is reported in Table 2.1.

The polarization after reflection and transmission is maintained at more than 95% for both polarization channels.

Polarization of incoming beam	Transmission	Reflection	Losses
Vertical	42%	57%	1%
Horizontal	43%	51%	6%

Table 2.1: Beam-Splitter cube efficiency as a function of the polarization.

The excitation/detection optics is an inverted Wide Scan Type III telescope ocular. The use of a telescope ocular mounted upside-down allows to collect the light emitted at large angles (the numerical aperture is 84°) with reduced aberrations, and with a comfortable working distance (the focal length is 16 mm). However, the spherical aberrations remain quite large and are problematic for the real space imaging, as detailed in Subsection 2.2.3.1.

2.1.2 Small pump tilt

For most measurements, the pump is normally incident onto the sample. To achieve an exact alignment at normal incidence or to study the influence of a small incidence angle, it is useful to be able to slightly modify the pump incidence angle.

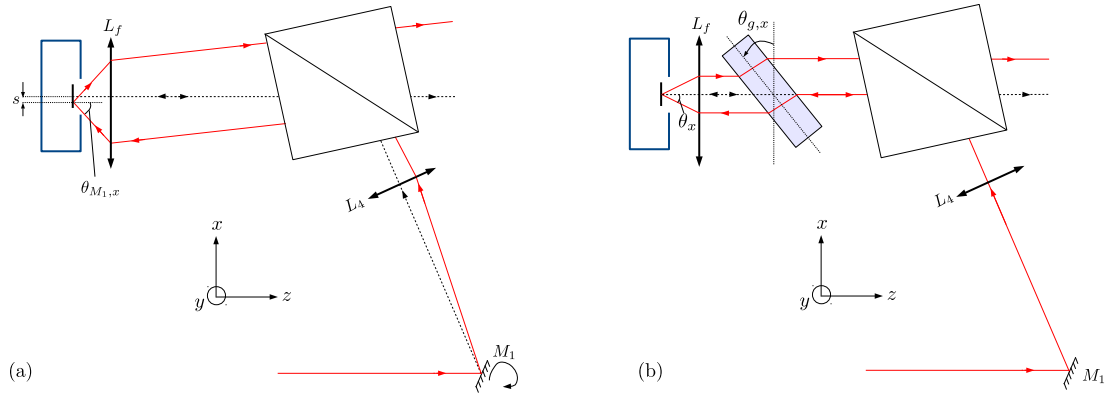


Figure 2.3: Tuning the pump incidence (a) by rotating slightly the mirror M_1 , (b) by rotating a glass plate (which thickness is strongly exaggerated for clarity) by an angle $\theta_{g,x}$. In both drawings, the pump optical path in the normal incident case (mirror M_1 not rotated (a) or $\theta_{g,x} = 0$ (b)) is represented by a black dashed line. In (a), the pump hits the sample at a different spot than when it is normally incident.

A first method consists in a slight rotation of mirror M_1 (see Fig. 2.2). However, this also changes slightly the position of the spot onto the sample. This is a problem since a different position means a different exciton-photon detuning (due to the built-in wedge, *cf.* Subsection 1.1.2.6), as well as a different defect environment, which

both affect the reemission of light. A simple way to shift only the incidence of the pump onto the sample is to use a glass plate between the beam-splitter cube and the telescope ocular L_f . This way, the incoming beam on L_f is not deviated, but only shifted out of the axis of L_f . Fig. 2.3 shows the difference between the two techniques.

In order to scan the influence of a very small pump incidence angle, I have built an automatic stage using two glass slides to vary either the angle along x (θ_x) or along y (θ_y). To automatically rotate the slides, two AGPR100 Agilis Rotation Stage have been used. However, the motor ensuring the automatic rotation is driven by piezoelectrics. Therefore, the absolute position of the rotation stage is not guaranteed, and in particular, the number of steps for a clockwise rotation is different from an anticlockwise rotation for the same angle. Therefore, two AVAGO optical incremental encoders are added to the Agilis automatic rotation stages to precisely monitor the glass plates rotation angles $\theta_{g,x}$ and $\theta_{g,y}$ (Fig. 2.4).

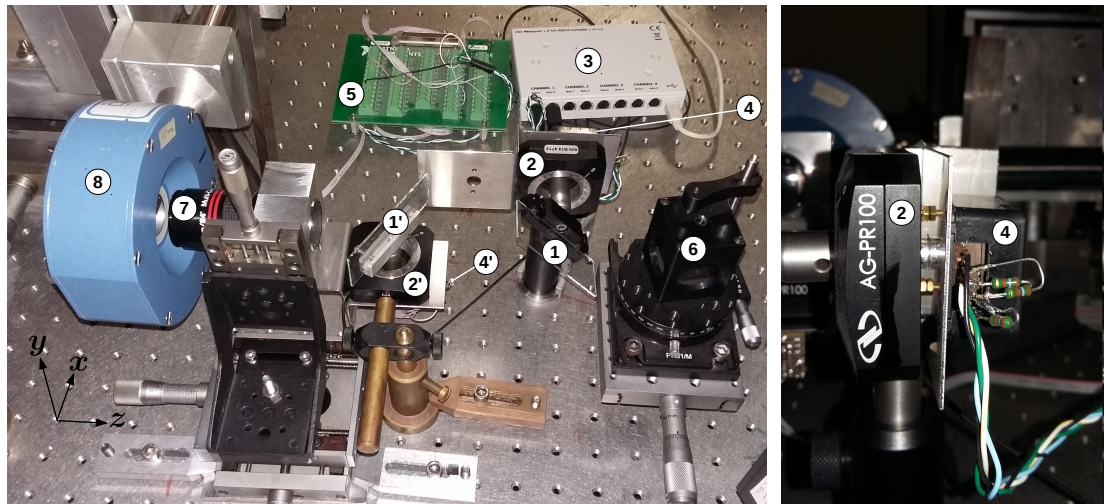


Figure 2.4: Picture of the experimental setup used to vary the pump incidence angle. (1) and (1'): glass plates rotated by angles $\theta_{g,y}$ and $\theta_{g,x}$ respectively, so that the pump incidence is tilted by θ_y and θ_x . (2) and (2'): Agilis automatic rotation stages connected to the Agilis Controller (3). The rotation angles $\theta_{g,y}$ and $\theta_{g,x}$ are determined with precision using AVAGO optical incremental encoders (4) and (4'), electronically controlled by the National Instrument PCI-6320 data acquisition device (5). (6) Beam-splitter cube. (7) Inverted Wide Scan Type III telescope ocular L_f . (8) Oxford Cryostat in which the sample is inserted.

2.1.3 Optical path for the probe(s)

Besides tuning the pump's incidence, one or two probes to seed the Optical Parametric Amplification (see Subsection 1.2.1.3) will be of use in Chapter 4. The optical paths followed by the two probes are depicted in Fig. 2.5. A second polarizer is

added after lens L_p to suppress any remaining circular component to the incoming beam. Then, a beam-splitter divides the beam in two probe beams 1 and 2. Two half-wave plates are inserted in the optical path of each beam to allow the control of their polarization.

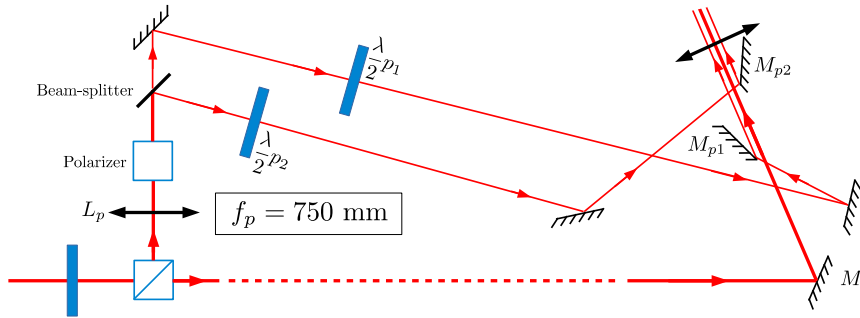


Figure 2.5: Top view for the two probes and pump setup. Mirrors M_{p1} and M_{p2} are used instead of beam-splitter plates in order to keep the pump power as large as possible.

In order to maintain a large pump power, we chose not to use a beam-splitter plate crossing the three beams but mirrors instead (M_{p1} and M_{p2} on Fig. 2.5). However, to reach a resonance condition with the elastic circle, the probes must be sent with a specific incidence angle, and in practice, the respective probe optical paths must be very close to the pump's. Therefore, a delicate optical alignment is needed since the probe beams must hit the very edge of the mirrors M_{p1} and M_{p2} (which, in addition, are stuck on the edge of their optical mount so as to save space).

2.1.4 Properties of the optical pump

2.1.4.1 Intensity fluctuations of the MIRA laser

The MIRA laser is a mode-locked Ti:Sapphire laser able to deliver light pulses while pumped by a VERDI laser. The laser optical cavity is different for the “femto pulsed regime” (plain and dashed line in Fig. 2.6), and for the “pico pulsed regime” (plain line in Fig. 2.6). The birefringent filter (BRF) is also different in the pico and femto configurations. The pulses are obtained by closing the output slit and initiated thanks to the oscillation of the starter.

The MIRA is therefore designed to be multimode, so the “continuous wave” (cw) regime may not allow light emission at a stable wavelength and cannot be finely tuned. To improve the properties of the cw emission, the laser cavity may be set in an third alternative configuration: the “alignment” one, that is, the “pico cavity”, where the mirror M_{10} is removed and the laser is reflected by mirror M_9 .

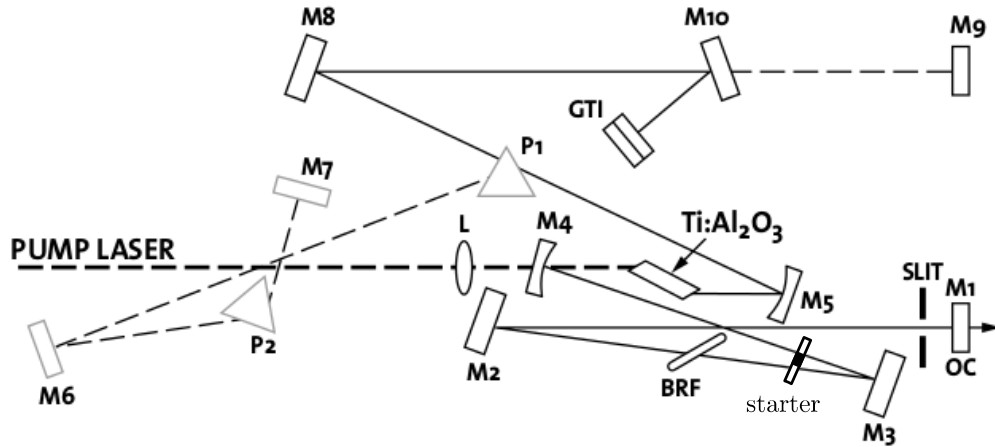


Figure 2.6: Reproduced from the MIRA 900 operator’s manual. The solid line represents the picosecond operation. Solid and dashes lines correspond to a femtosecond operation. The “alignment cavity” is obtained with the pico configuration (P_1 is removed) where M_{10} is removed and M_9 reflects the laser onto M_8 .

In the experiments reported in the next two chapters, the MIRA was operated in the cw mode. Since this is not the usual use of this laser, we have characterized the laser emission in this mode using two techniques:

1. Recording of the voltage of the photodiode included inside the laser cavity,
2. Measurement the autocorrelation of the laser emission. If the laser intensity is stable, the autocorrelation function should be flat.

Characterization with the laser photodiode

Some fluctuations (see Fig. 2.7) are observed on an oscilloscope screen recording the voltage of the intracavity photodiode. These fluctuations appear *only* when the laser hits the sample and their amplitude is even increased when the laser is in resonance with the polariton branch. This indicates that, despite of all the experimental efforts (Faraday isolator, anti-reflection coated lenses, beam-splitter cube tilt), the backreflection from the sample towards the MIRA cavity is not completely suppressed and has a measurable effect on the laser emission.

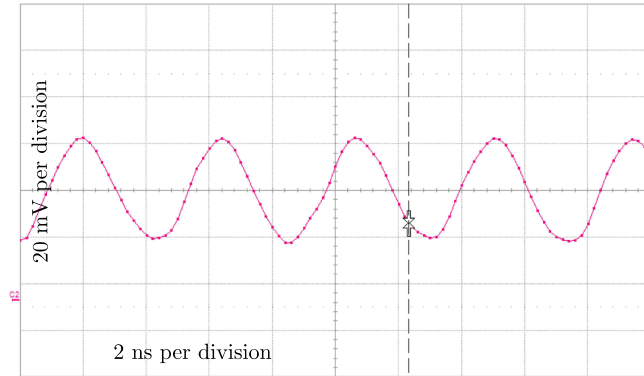


Figure 2.7: Approximately 4 ns fluctuations of the laser emission recorded by the intracavity photodiode. Done with the “pico” cavity. Note that the figure does not show the real amplitude of those oscillations due to the finite photodiode time response.

The absolute amplitude of these oscillations is meaningless since it is dependent on the limited photodiode time response. However, it is direct evidence of the role of the sample backreflection on the laser emission. An autocorrelation measurement on the laser emission must be done so as to get a reliable estimation of the oscillation amplitude and period.

Characterization by autocorrelation

Fig. 2.8 shows the typical autocorrelation setup used to study the MIRA laser emission. The laser is sent to a fibered beamsplitter. Two rapid avalanche photodiodes (ID100 single-photon detectors APD) detect the incoming photons and the Time-Correlated Single Photon Counting PicoHarp module records the delay between the detection of a photon by the two APDs. If the laser emission is continuous, a completely flat response is expected, since the probability of emitting a photon is the same whatever the delay between APD1 and APD2. For other sources such as a single photon source, an antibunching will occur around the zero delay, and on the contrary a bunching in the case of a thermal source.

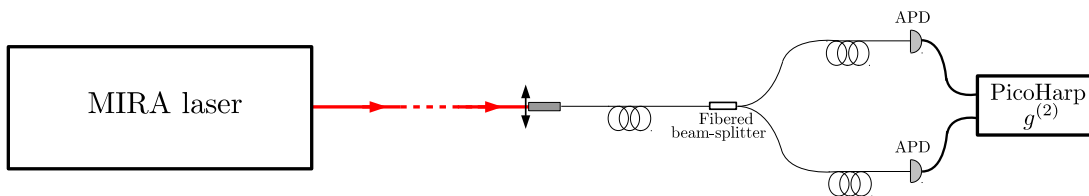


Figure 2.8: Setup for the observation of the MIRA intrinsic autocorrelations. The laser-fiber coupling is achieved using an “Edmund Optics” microscope objective of magnification x20 and working distance 3.3 mm.

Instead of observing a flat response, fast oscillations with period $\simeq 1.45$ ns are observed (see Fig. 2.9). These oscillations are particularly intense when using the pico cavity (60% of the total amplitude). The alignment cavity allowed to decrease the oscillations to 20% of the total amplitude.

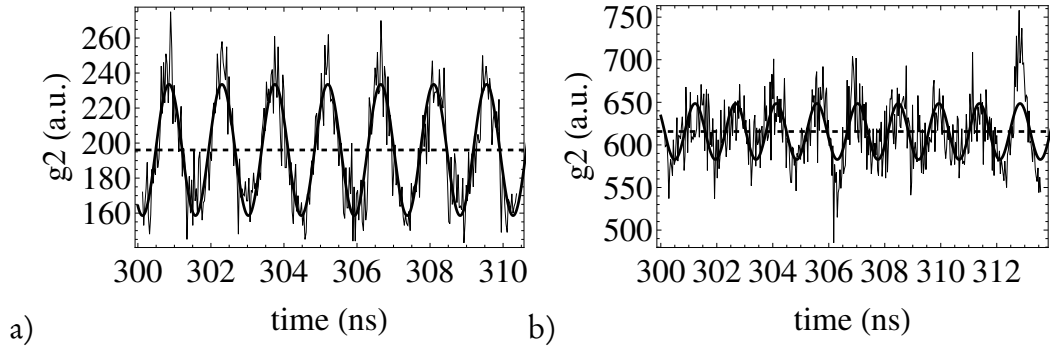


Figure 2.9: Autocorrelation measurements with the MIRA a) for the pico-cavity. b) for the alignment cavity.

These oscillations are present:

- Whatever the excitation intensity of the sample (from 5 mW to 150 mW, tuned by rotating the half-wave plate P shown on Fig. 2.2),
- Whatever the power of the VERDI laser (from 6 W to 8 W),
- Even when a second Faraday isolator is set on the excitation path,
- Even when the laser is slightly disaligned, either by rotating its entrance mirrors (not represented on Fig. 2.6) or translating the output slit,
- Even when a pinhole is added at the laser output so as to make a spatial filter.

Those GHz oscillations corresponds to a distance of $\simeq 45$ cm in the air. This may be the signature of the interference between two mirrors inside the MIRA cavity (see Fig. 2.6). When the laser is resonant with a polariton branch, a secondary oscillation which corresponds to the optical free path (13 ns) is added. This is a sign that the light absorbed by the microcavity reenters the MIRA cavity.

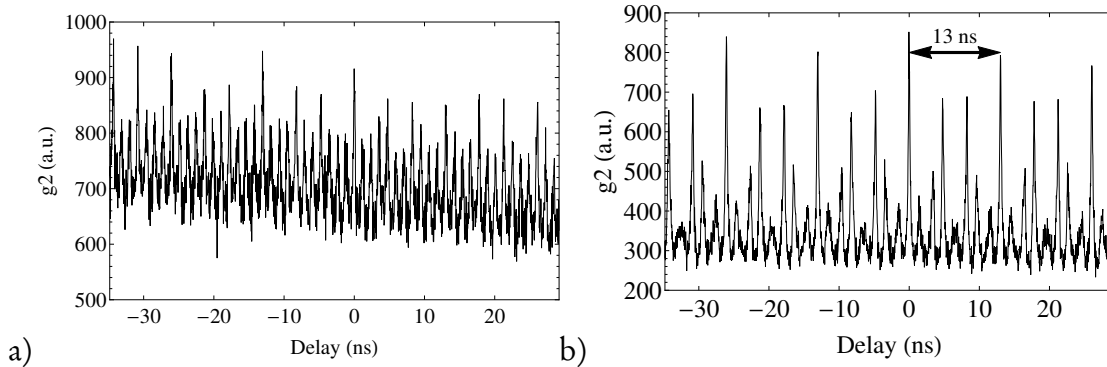


Figure 2.10: Autocorrelation measurements with the MIRA “alignment cavity”. a) Laser out of resonance. b) Oscillations of period $\simeq 13$ ns are added when the laser is resonant with the polariton branch.

In conclusion, the MIRA laser emission has been characterized using two different measurements made by an intracavity photodiode and an autocorrelation setup. The result show that the cw regime is unstable. No experimental method was yet found to suppress or reduce the amplitude of those oscillations below 20%. Indeed, the MIRA laser is not designed to produce a monomode emission, but a pulsed emission with a large spectrum based on the superposition of many longitudinal cavity modes.

To check the influence of this non-ideal cw source, we have also occasionally used another cw tunable Ti:Sapphire laser source which can deliver a much more stable intensity.

2.1.4.2 Alternative cw tunable laser: the SOLSTIS laser

The second laser we explored is the SolsTiS tunable cw Ti:Sapphire Laser. The main differences between the two lasers are summarized in Table 2.2. Mainly, the SolsTiS has a much narrower linewidth than the MIRA.

	MIRA	SolsTiS
Linewidth	10 to 40 MHz	50 kHz
Free spectral range	13 ns	0.7 GHz = 1.4 ns
Tunability	$\simeq 0.5$ nm	< 0.1 nm

Table 2.2: Comparison between the SolsTiS and the MIRA laser emission.

Etalon and cavity lock To achieve this narrow linewidth, an intracavity thin *etalon* is added to the cavity. The etalon introduces a spectral loss into the cavity

that is a much sharper function of the frequency than the birefringent filter. The SolsTiS output frequency is tuned by electronically adjusting the etalon spacing. Additionally, an electronic servo locking of the intracavity etalon can be applied to ensure the stability of the emitted wavelength on long period of time.

To obtain the narrowest possible linewidth, a high stability, high finesse, reference cavity can be added to the SolsTiS. By locking the SolsTiS cavity to this reference cavity, the SolsTiS linewidth can be reduced to less than 50 kHz.

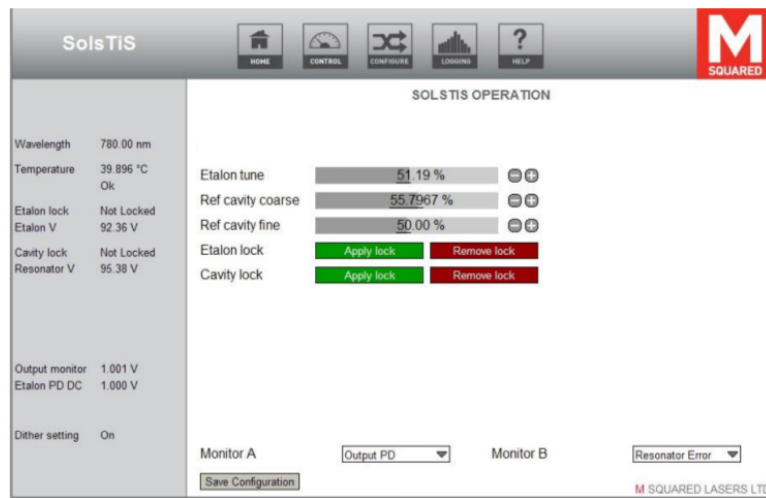


Figure 2.11: Solstis control panel. The “Etalon tune” button allows to finely tune the emitted wavelength with a precision better than 0.1 nm when both etalon and cavity lock are applied.

Experimental setup: high power coupled in a single mode fiber This Solstis laser had been originally bought by our group for the study of carbon nanotubes emission in microcavities [Jeantet2016]. To bring the Solstis laser emission to my optics table, the laser is coupled into a 12 m single mode 780HP fiber. The laser-fiber coupling efficiency must be high in order to get sufficient power (typically 100 mW) onto the sample and observe various regimes of power. To avoid any damage on the fiber end close to the Solstis laser, this very end is first exposed to light illumination, but obliquely cleaved with an angle to deviate the back-reflection and inserted into a ceramic ferrule so as to create a thermal screen shield and reduce any thermal fluctuations. The laser is focused onto the input of the fiber using a Geltech aspheric lens of focal length $f = 8$ mm and numerical aperture $NA = 0.5$. At the output of the fiber, a FC/PC collimator of focal length $f = 4.6$ mm is used to modulate the size and divergence of the outgoing beam. To achieve a 30% coupling between the Solstis laser and the fiber, we use the “beam walking” method by rotating mirrors M_{s1} and M_{s2} (see Fig. 2.12) and shifting slightly the distance of the aspheric lens and the end of the fiber.

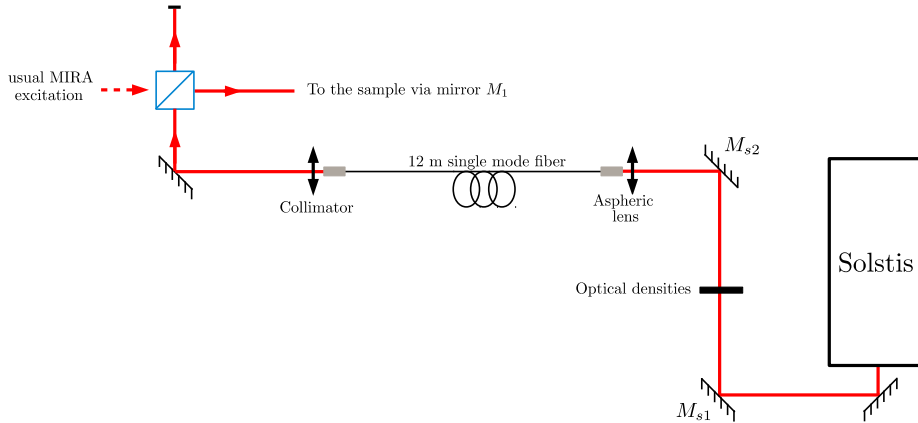


Figure 2.12: Optical path for the SOLSTIS excitation.

Autocorrelation of the SOLSTIS laser Autocorrelation measurements (Fig. 2.8) were also performed on the Solstis laser. If no lock is activated, oscillations with a period of $\simeq 1.29$ ns, corresponding approximately to the laser cavity length, are observed (Fig. 2.13.a.). Those oscillations disappear if both etalon and cavity lock are activated (Fig. 2.13.b.). The cavity lock can be achieved only if optical densities are present between M_{s1} and M_{s2} to attenuate and/or deviate the back-reflection.

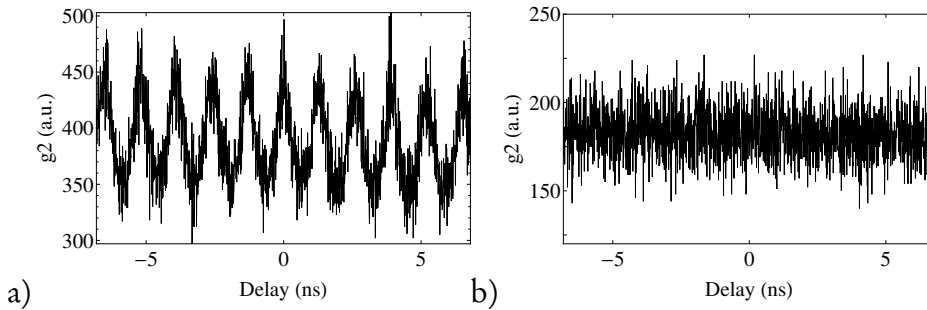


Figure 2.13: a) Autocorrelation measurement on the Solstis laser if no lock is activated. b) Cavity and etalon locked Solstis autocorrelation measurement.

Conclusion The Solstis laser is therefore a useful complementary tool to probe the importance of monochromaticity and intensity fluctuations for the analysis of the physical phenomena of interest. This will be of particular importance in Chapter 4.

2.2 Detection setup

In this section, the various setups used to characterize the light emitted by the sample are described. The detector may either be set to image the surface of the sample (Subsection 2.2.3), or coupled to the Fourier plane of the emitted light. The

influence of the spherical aberrations due to the inverted telescope ocular L_f are discussed. The second option allows to image the angular emission of the microcavity (Subsection 2.2.1) and, by inserting a spectrometer in the optical detection path, to directly image the energy dispersion with angle of the emitted light (Subsection 2.2.2). The experimental setup allowing for the simultaneous observation of the momentum space and real space is detailed in Subsection 2.2.3.2. Finally, the tools used to monitor the polarization of the excitation or emitted beams are detailed in Subsection 2.2.4.

2.2.1 Momentum space

The *far field* of the emitted light is imaged in the focal plane of the ocular L_f , also called *Fourier plane*. Indeed, each point in the Fourier plane is conjugated to one direction of the emitted light, hence the Fourier plane also corresponds to the *angular space* (or, equivalently, the *momentum space* or *parallel wavevector space*, see Subsection 1.1.2.4).

To get an image of the far field at a convenient location, the Fourier plane is imaged on a low noise Charge-Coupled Device (CCD) detector through a lens L_c . The CCD detector (Sony ICX285AL) is composed of 1434×1050 $6.45 \mu\text{m}$ square pixels. The electronic control of the detector was conceived and realized by David Darson at LPA.

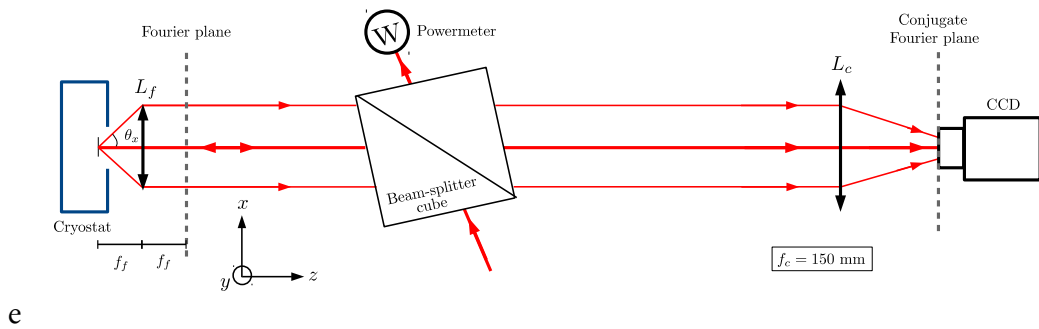


Figure 2.14: Principle of the far field imaging (top view). The Fourier plane, image of the far field emission, is obtained at the focal plane of L_f , and the CCD detector is conjugated to the Fourier plane via the lens L_c .

The distance between L_f and the position of the CCD is fixed experimentally. However, the position of L_c and the distance between the sample and L_f can be slightly adjusted. This alignment is not easy since the precise Fourier plane position is unknown. Indeed,

1. The exact position of L_f compared to the sample is difficult to measure precisely (it should be around 16 mm, the focal length of L_f),

2. The focal length of L_f varies with angle due to spherical aberrations (see Subsection 2.2.3.1),
3. The ocular L_c is a thick optical component: it is not easy to define its center.

The second observation implies in particular that the Fourier plane for the normally incident and reflected pump is located at a different position than the Fourier plane for the light emitted at large angles.

2.2.2 Angle-resolved energy dispersion

The energy dispersion as a function of the angle of emission is easily imaged using a Czerny-Turner type spectrometer which entrance slit is placed at the position of the conjugate Fourier plane of Fig. 2.15).

Set at order 0 with the slit wide open, the grating is a mirror, and the spectrometer simply couples the entrance slit with the output at which the CCD camera is now placed with a 1:1 magnification.

Closing the entrance slit selects the light emitted on the vertical axis y . With the 1200 g/mm grating properly rotated, the portion of the light at a given k_y entering the spectrometer is dispersed by the grating as a function of the wavelength. Thus, we get a picture where one axis corresponds to energy and the other to the angle of emission along y (θ_y), or, equivalently the wavevector along y , k_y .

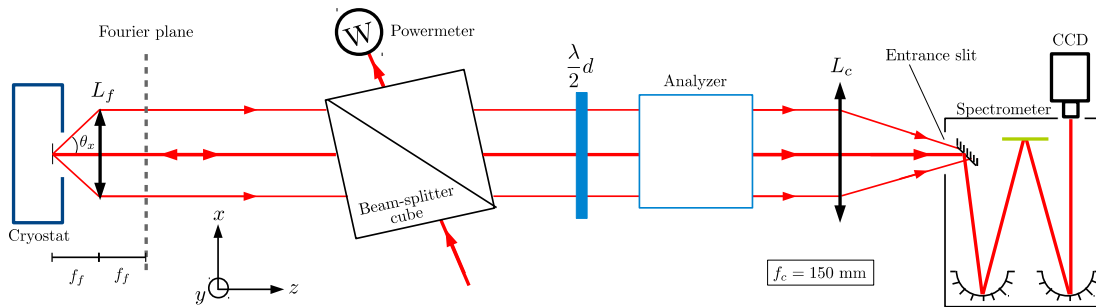


Figure 2.15: Top view of the setup for the observation of the energy dispersion as a function of k_y (or, equivalently θ_y). The entrance slit (represented open on the figure) must be closed to select the light emitted along y .

In this configuration the sample can be excited non resonantly with an blueshifted excitation energy corresponding to a node of the DBRs. Relaxations towards available states at lower energies (photoluminescence or PL) populate the polariton branch(es), and allows to image their dispersion.

Since the spectrometer has an anisotropic response in polarization [Lecomte2011], a polarizer is placed upstream so that the light entering the spectrometer has always the same polarization. The polarization that is best transmitted by the spectrometer

is horizontal, and corresponds to the polarization perpendicular to the pump's (vertical). Therefore the analyzer is set to filtrate only horizontally polarized light. To observe other linearly polarized light, the half-wave plate d can be rotated. However, the stray light of the laser will not be cut anymore.

2.2.3 Real space

An image of the *real space* (sample surface or *near field*) allows to visualize the surface defects, and, for a resonant excitation, the propagation of the polaritons.

A first and simple way to image the near field is to shift the position of the lens L_c until defects (for the double microcavity sample) or wires (for the 1D - microcavities sample) are well defined on the camera. If the sample is located at the focal plane, then the distance between L_c and the entrance slit of the spectrometer must be f_c and the magnification is approximately $-\frac{f_c}{f_f} \simeq -9.3$.

The near-field image allows in principle to measure the spot size of the pump and probes' beams. For the pump, we find a spot size with full width half maximum (FWHM) of about $50 \mu\text{m} \pm 10 \mu\text{m}$. Note that the FWHM value is only indicative: indeed, it is very sensitive to the distance between L_f and the sample since L_f is very convergent.

The laser is a coherent light source which can produce interference patterns (speckle). To avoid this effect, we can also use a red Light-Emitting Diode (LED) source to illuminate the sample surface. A homemade electronic circuit is built to monitor the excitation power. A red LED is preferable to a white light source since its wavelength (635 nm) is close to the laser's, such that the refractive indices of the optical components are almost identical. The scheme for the observation of the near field with the LED is shown on Fig. 2.16. We use a ToUcam Pro Philips webcam to record the near field at the focal plane of the lens L_{rs} . The magnification is approximately $-\frac{f_{rs}}{f_f} \simeq -19$. A pinhole can be placed at the vicinity of L_f to increase the contrast.

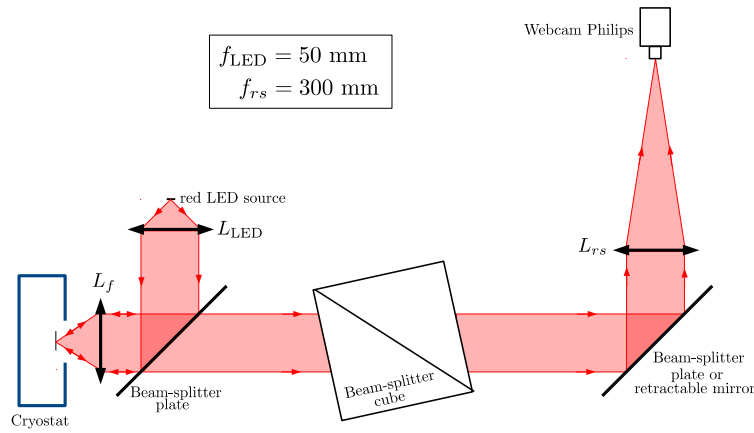


Figure 2.16: Real space imaging using a red LED excitation source.

2.2.3.1 Spherical aberrations of the ocular L_f

Despite the choice of an inverted ocular L_f , in principle corrected for spherical aberrations, the angles of interest in the experiment are so large (between 20 and 30°) than spherical aberrations come into play nevertheless. Practically, it means that the ocular does not have the same focal length for marginal beams (or large angles) and paraxial beams (or small angles). Fig. 2.17 shows the effect of spherical aberrations for various incoming beams.

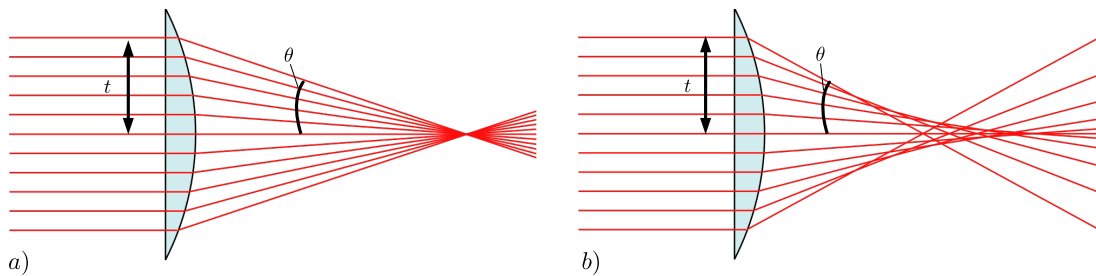


Figure 2.17: (Adapted from Wikimedia Commons). a) Ideal convergent lens. b) Convergent lens with spherical aberrations. Marginal beams (large t or θ) do not have the same focal plane than paraxial beams (small t or θ).

To calibrate the spherical aberration for the ocular L_f , we have measured its focal length as a function of incidence angle. The laser beam is first sent at normal incidence and goes through the center of the ocular L_f . We choose a visible defect at the surface of the sample. The ocular L_f is progressively shifted along x . The sample is then shifted along z to compensate for the spherical aberration so that the defect

is still well-defined. Due to a slight tilt of the cryostat, the sample may need to be shifted also laterally.

However, for distances between the center of the ocular and the laser beam larger than 2 mm, the beam starts to deform along the horizontal axis and the exact z shift necessary to compensate the spherical aberrations is difficult to determine. This method is therefore limited to angles lower than 7° .

To explore larger angles, a second measurement is done, where the sample is replaced by a mirror. L_f is shifted laterally and the distance between L_f and the position of the mirror is adjusted so that the reflected intensity is maximum, meaning that the mirror is located at the focal plane of L_f . The experiment has been done for incoming horizontal and vertical linear polarizations with no significant difference.

Both experiments are represented in Fig. 2.18, and fitted by a parabola:

$$\begin{aligned} f_f(t) &= 16 - 0.02 \cdot t^2 \\ &\simeq 16 - 5.12 \cdot \tan^2 \theta \end{aligned}$$

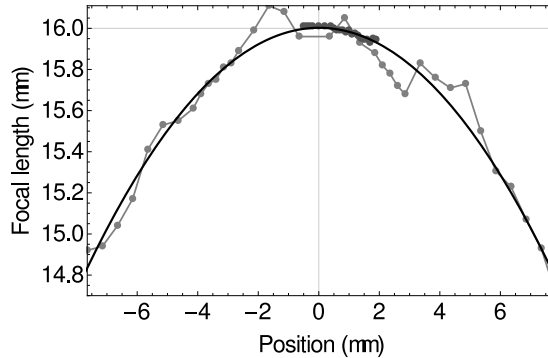


Figure 2.18: Red : Experiment #1. Blue : Experiment #2. The black plain line represents the parabola fit.

The deformation of the beam along the x axis for a shift along x can be understood in the light of Fig. 2.18. Indeed, for $|t| > 2$ mm, the focal length starts to decrease almost linearly with t . Therefore, for a beam waist at the entrance of L_f of about $400 \mu\text{m}$ (calculated using the *GaussianBeam* software), the focal length can differ by more than $30 \mu\text{m}$. The spot on the sample is therefore elongated in the x direction, and undergoes further elongation after reflection and re-transmission by L_f . This phenomenon, which appears only for large t , is present even if the focal length is corrected to account for a mean spherical aberration. It could be also reinforced by a coma aberration (due to a possible slight tilt of L_f).

The focal length for the pump and the elastic circles (or the probes resonant with the elastic circle) are therefore different. This implies in particular that the probe must be sent with a non-normal incidence (approximately 1° angle) onto the ocular L_f , so that the pump and the probe hit the sample at the same point.

Finally, the spherical aberrations strongly affect the near-field image. Indeed, the focal length for the reflected probe beam (or the emitted light on the elastic circle) beams is different from the pump's. So the position of the near-field image for the pump and probe is not the same, as can be seen in Fig. 2.19, where the optical alignment is optimized for the (normally incident) pump. The pump and the probe are not superposed.

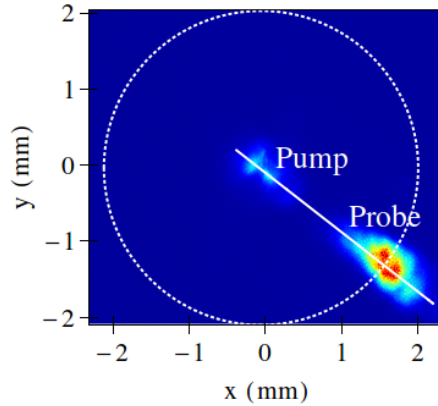


Figure 2.19: Image of the sample surface obtained by shifting the lens L_c of focal length $f_c = 127$ mm closer to the entrance slit of the spectrometer (first method proposed in this subsection). The optical alignment is optimized for normally incident light (the pump). However, the probe is sent at oblique angle in the direction indicated by the plain line (which is also the direction of the probe elongation, in accordance with our interpretation). Pump and probe are superposed on the sample but not in this image due to L_f spherical aberrations. The dashed line represents the effective ring corresponding to the probe incidence angle

2.2.3.2 Setup for the simultaneous observation of the real space and the momentum space

To simultaneously observe the near and far fields created by a normally-incident pump, a beam-splitter can be placed in the detection path, as shown in the scheme of Fig. 2.16. However, the observation of the polaritons propagating with a large in-plane wvector k_{\parallel} in the near field will be blurred by the pump's bare reflection. To hide the pump's bare reflection, spatial filters, made by deposited gold onto glass plates, must be added in an *intermediate* Fourier plane image located *before* the imaging of the near field. Fig. 2.20 shows the corresponding optical setup.

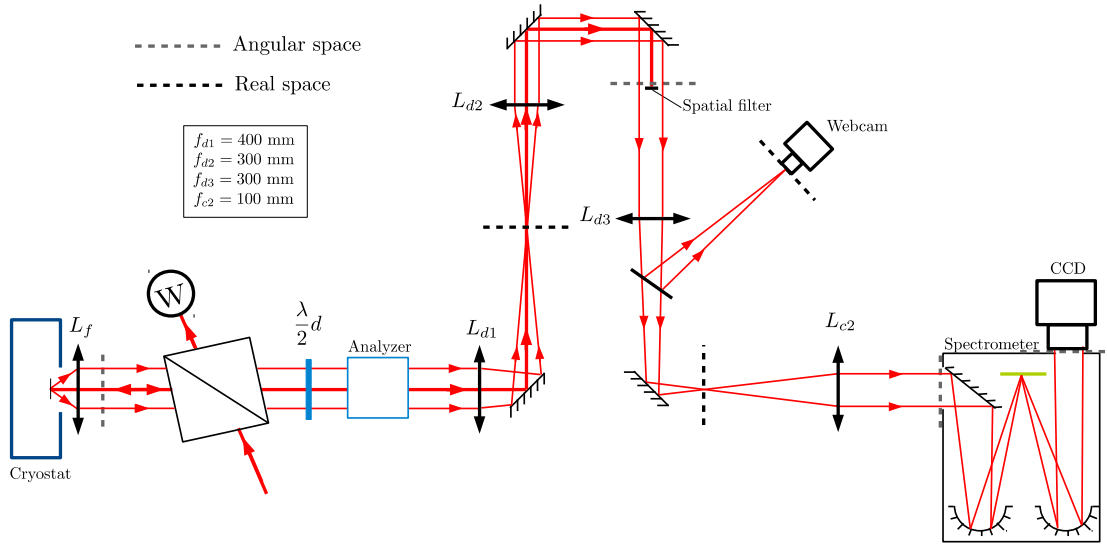


Figure 2.20: Full setup used to observe simultaneously the far and near fields, while selecting the large angle emitted light through the use of a spatial filter in an intermediate Fourier space. The various lenses are positioned in more or less “4-f” configurations.

The lenses L_{d1} , L_{d2} are positioned so as to image the far field in the focal plane of L_{d2} . Since the beams emitted at large angle and the pump reflection are parallel, the pump reflection and the elastic circle are therefore well separated in space, and the spatial filter can be placed with precision to hide only the pump spot. The position of the spatial filter is directly visible on the CCD. The real space is imaged on a webcam at the focal plane of lens L_{d3} .

2.2.4 Polarization control of the exciting and emitted light

In this subsection, the strategy chosen to control the linear polarization of the excitation and reemitted beams are detailed. Table 2.3 summarizes the vocabulary used in this thesis to describe the basis of the linear polarized states.

Vertical	along y	p
Horizontal	In the the optics table's plane	s

Table 2.3: Table of correspondance for the linear polarization basis.

As already mentionned in Subsection 2.2.2, the intensity response of the spectrometer varies as a function of the light polarization. Therefore, the analyzer is fixed to select horizontally-polarized light (cf Fig. 2.21), which corresponds to the most efficient channel for the spectrometer.

As shown in Table 2.1, the beam-splitter also has a small anisotropy between vertical and horizontal polarizations. Therefore, the pump is sent to the beam-splitter with a fixed vertical polarization (selected using the half-wave plate V of Fig. 2.2). This ensures that the power entering the microcavity sample is kept constant during the experiment.

If no other plates are present, this means that the analyzer is by default cross-polarized to the pump. This has several advantages such as avoiding being blinded by the pump’s reflection onto the sample. This configuration also allows to observe pattern formation in the far field of the double microcavity sample (Chapter 4).

If we want to image other linear polarization channels, the half-wave plate d of Fig. 2.15 can be added and rotated out of its fast axis. However, the CCD detector will be saturated by the pump’s reflection.

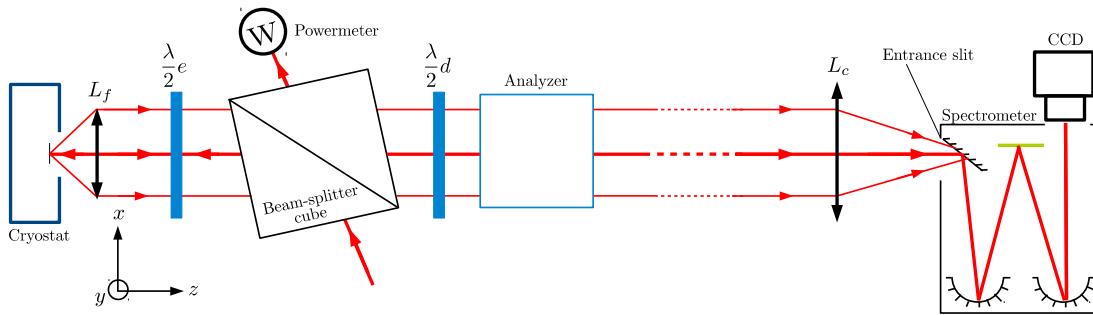


Figure 2.21: Use of an additional half-wave plate ($\lambda/2e$) to rotate the pump’s linear polarization while imaging the pump’s cross-polarized channel. If necessary, the $\lambda/2d$ use can be rotated to image the pump’s co-polarized channel.

To excite the sample with a non-vertical linear polarization, a half-wave plate ($\lambda/2e$) can be placed between the beam-splitter and the ocular L_f . This half wave plate will rotate the polarization of excitation but also the polarization of the re-emitted light in the detection path. However, thanks to the π rotation due to the reflection onto the sample, the reflected pump light’s polarization is rotated back to the vertical direction. An example of the rotation of polarization experienced by the pump light when the $\lambda/2e$ is rotated by an angle $\phi_{\text{pol, pump}}/2$ is given in Table 2.4.

$\lambda/2e$ angle	Pump polarization on the sample after $\lambda/2e$	Pump polarization after reflection on the sample	Reflected pump polarization after $\lambda/2e$
Fast axis	Vertical	Vertical	Vertical
Fast axis + $\frac{\phi_{\text{pol, pump}}}{2}$	$\phi_{\text{pol, pump}}$	$-\phi_{\text{pol, pump}}$	Vertical
Slow axis	Horizontal	Horizontal	Vertical

Table 2.4: Effect of $\lambda/2e$ on the pump polarization.

This allows to study the effect of the rotation of the pump's linear polarization on the far-field emission, while systematically probing the light emitted by the sample cross-polarized to the pump. This avoids being blinded by the pump's bare reflection.

This configuration is also ideal for the study of polarization splitting in microwires between polarizations parallel and orthogonal to the wire axis. In that case, the pump light is blueshifted so as to observe the photoluminescent polariton branches. Whatever the polarization of the incoming pump, the pump polaritons created relax towards both parallel and orthogonally polarized polariton branches. The $\lambda/2d$ could be used to observe both polarizations, but, even if the pump is blueshifted, parasitic pump stray light can blur the branches signal at normal incidence, which is exactly the region of interest for the study of the polarization splitting. Therefore, the rotation of the $\lambda/2e$ instead of the $\lambda/2d$ allows to image either the parallel polarized dispersion, either the orthogonally polarized dispersion, while always cutting the pump's reflection.

Conclusion

I have detailed in this chapter the various experimental methods used in this thesis. The confocal setup is very modular, and therefore can easily be adapted for a large variety of studies: auto and cross-correlations, influence of the excitation beam incidence, influence of the laser source, spontaneous pattern formation...

Three different imagery techniques are available: the momentum space, the real space, and the energy dispersion as a function of angle θ_y , or, equivalently, as a function of the wavevector along y k_y . The momentum space corresponds to an imaging of the far field emission of the microcavity and is very well suited to observe the elastic circle defined in the introduction of this chapter. The real space is useful in positioning the laser spot at the desired location (for example at the center of a 1D-microcavity). The spherical aberrations of the ocular L_f detailed in the present chapter must be taken into account for the precise optical alignment of the real space. This is crucial for the experimental observation of patterns in the near field as discussed in Chapter 4. Finally, the control of the polarization of the pump, probes and emitted beams is necessary for the study of polarization effects in structured semiconductor microcavities.

The next chapter will focus on the study of the energy dispersion of microwires, which exhibits a polarized normal energy splitting. The fourth and last chapter is mainly devoted to the study the far field emission of a double microcavity in various regimes of power.

3

ORIGINS OF THE NORMAL POLARIZATION SPLITTING IN MICROWIRES

In this chapter, we focus on a sample consisting in quasi 1D-microcavities. An energy splitting at normal incidence between polarizations parallel and orthogonal to their long axis is analyzed in detail. Such splitting has been previously observed in 1D-microcavities and attributed to various causes: anisotropic mode confinement [Kuther1998], birefringence in the Bragg mirrors [Diederichs2007], exciton fine structure [Dasbach2002], anisotropic Rabi coupling [Balili2010]. This study provides a comprehensive understanding of this lifting of degeneracy. A model for the mechanical constraints is developed, accounting for the experimental observations. This chapter is the continuation of the work of Vincenzo Ardizzone published in his PhD thesis [Ardizzone2013a].

Chapter content

3.1	Sample and excitation conditions	76
3.1.1	Sample description	76
3.1.2	Photoluminescence spectrum	77
3.2	Observation and characterization of the polarization splitting	78
3.2.1	Experimental setup and available degrees of freedom	79
3.2.1.1	Splitting as a function of detuning	80
3.2.1.2	Influence of the wires width	82
3.2.1.3	Influence of the temperature	83
3.2.2	Interpretation	85
3.3	Physical origins of the polarization splitting	89
3.3.1	Influence of the constraints linked to the sticking	89
3.3.2	Model of stress relaxation in microwires	90
3.3.3	Lattice mismatch-induced constraints	96
3.3.3.1	Calculation of the lattice-mismatch induced strain	97
3.3.3.2	Stress-induced birefringence	101
3.3.3.3	Influence of strain on the exciton energy	105
3.3.3.4	Influence of strain on the light-matter coupling	108
3.3.3.5	Conclusion	109

3.3.4 Anisotropic mode confinement 109
 3.4 Discussion and conclusion 111

3.1 Sample and excitation conditions

The 1D-microcavities of interest have been previously studied by T.Lecomte [Lecomte2011] and V. Ardizzone [Ardizzone2013a] in their PhD, where a full characterization of the sample can be found. We will in this first part quickly describe the main features of the sample that will be useful to understand the origin of the lifting of degeneracy.

3.1.1 Sample description

The microwires are etched out of a 2D-microcavity grown at the *Laboratoire de Photonique et Nanostructures* (Marcoussis, France) by Aristide Lemaître. The Bragg mirrors are formed by 26 (30) periodic alternance of $Al_{0.95}Ga_{0.05}As$ and $Al_{0.2}Ga_{0.8}As$ layers for the top (bottom) mirror. Three group of four 7 nm-thick GaAs quantum wells are embedded in the cavity and in the DBRs at the antinodes of the electric field. The complete growthsheet of the sample is available in Ref. [Wertz2010a].

During the MBE growth, the rotation of the wafer is interrupted in order to introduce a wedge on the cavity thickness. As a consequence, it is possible to tune the cavity mode energies with respect to the excitonic mode energy by simply shifting the excitation spot onto the sample (see Section 1.1.2.6).

The 2D-microcavity has then been etched in 1 mm-long microwires by Isabelle Sagnes at the *Laboratoire de Photonique et de Nanostructures*. The etching was performed down to at least $1\ \mu m$ in the GaAs substrate, and corresponds to an etching depth of at least $7\ \mu m$. The microwires' widths range from 3 to $7\ \mu m$.

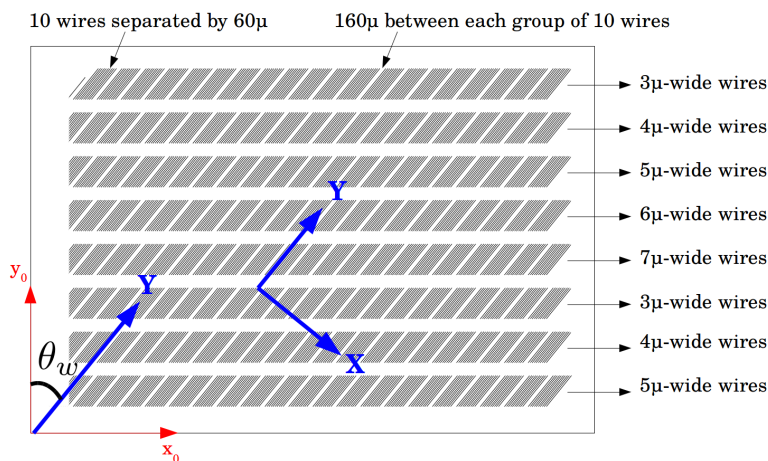


Figure 3.1: Scheme of the available wires on the wafer. The wires are etched perpendicularly to the direction of the cavity wedge X.

Fig. 3.1 displays a map of the final sample in a plane perpendicular to the growth direction ($z = Z$ axis). The wedge is along the X direction. The wires long axis is along Y , orthogonal to X , to ensure that the cavity energy is the same all along the wire. (X, Y) is oriented at about $\theta_w = 39^\circ$ relative to the GaAs crystalline axes (100) and (010) labelled (x_0, y_0) .

3.1.2 Photoluminescence spectrum

Due to the lateral confinement, the microwires exhibit several cavity modes (see section 1.1.2.7). These cavity modes, which are labelled by the integer j , are either symmetric or antisymmetric along the wire width. The distribution of the electric field along X reads [Kuther1998]:

$$\begin{aligned} & \cos\left(\frac{(j+1)\pi}{W}X\right) \quad \text{for } j \text{ even} \\ & \text{and } \sin\left(\frac{(j+1)\pi}{W}X\right) \quad \text{for } j \text{ odd,} \end{aligned} \quad (3.1)$$

with W the lateral width of the wire, X varying between $-\frac{W}{2}$ and $\frac{W}{2}$. For a given mode j , $k_{X,j} = \frac{(j+1)\pi}{W}$ represents the effective wavevector in the X direction.

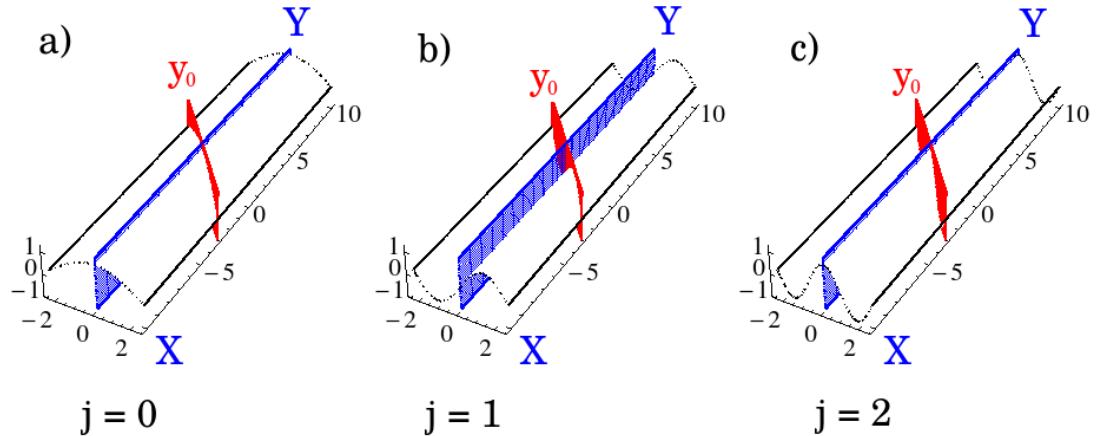


Figure 3.2: Sketch of the mode distribution following Eq. (3.1) wire. The direction of the emitted light selected by the vertical entrance slit of the spectrometer is shown (i) by a blue plane when the sample crystalline axis y_0 is parallel to the slit, and (ii) by a red plane when the sample is tilted such that the long axis of the wire Y is. (a) $j = 0$ mode. (b) $j = 1$ mode. (c) $j = 2$ mode.

To visualize the angle-resolved photoluminescence spectrum, we use the vertical entrance slit of the spectrometer to select the light emitted in the vertical direction y . The spectrometer disperses the vertically incoming light as a function of energy

(see a detailed explanation in section 2.2.2). If the sample is oriented so that the crystalline axis y_0 is parallel to the slit ($y_0 = y$), then the wires are not aligned with the slit, as shown in Fig. 3.2. Due to the cavity mode symmetry, the energy dispersions exhibits several elongated spots instead of a continuous energy branch (Fig. 3.3.a.).

To avoid this situation, the sample is placed with the wires long axis Y parallel to the vertical slit ($Y = y$). In this configuration, the energy dispersion is visualized as a function of k_Y , the wavevector along Y or equivalently, as a function of θ_Y , the corresponding emission angle in the Y direction. This way, the emitted light is collected more efficiently, especially for the mode $j = 0$. This will be particularly useful for the measurement of the energy dispersion at positive detunings, where the polariton branch linewidth is very large. The disadvantage is that to move from one wire to its closest neighbor, the sample must be shifted in a (known) diagonal direction θ_w (which is not very convenient for the experimentalist).

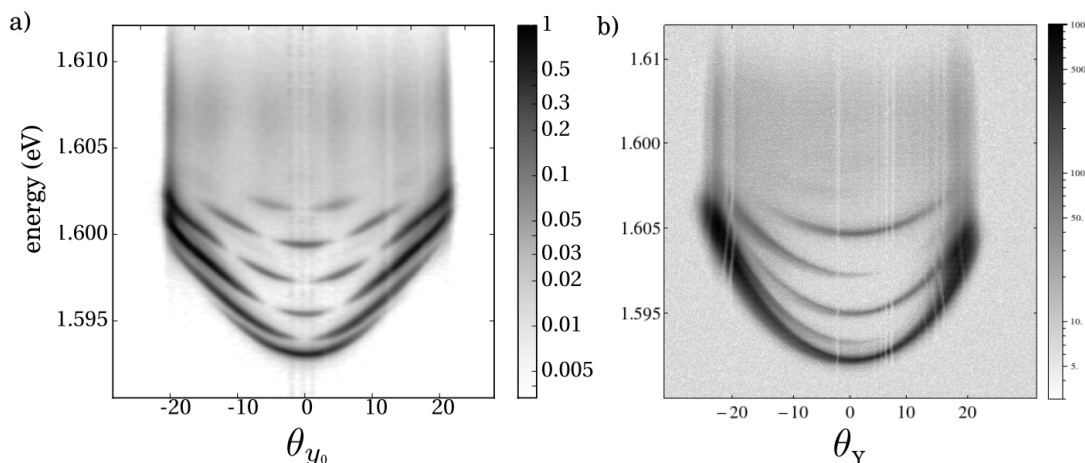


Figure 3.3: (a) From Ref. [Lecomte2011]. Photoluminescence spectrum of a $5\ \mu\text{m}$ -wide wire as a function of θ_{y_0} , that is, when the wire is not aligned to the slit. (b) Photoluminescence spectrum of a $5\ \mu\text{m}$ -wide wire as a function of θ_Y when the wire long axis is aligned with the slit. The even modes exhibit a full parabola. The $j = 0$ mode is very bright. The odd modes are also visible for $\theta_Y < 0$, meaning that the spot is probably not exactly centered on $\theta_Y = 0$ but rather slightly shifted towards negative angles.

3.2 Observation and characterization of the polarization splitting

As noticed by V. Ardizzone during his PhD, the polaritonic branches exhibit an energy splitting between polarizations parallel and orthogonal to the wire. This splitting, which can go up to about 1 meV for the mode $j = 0$, changes its sign and

magnitude as a function of temperature, cavity mode and detuning. In this section, this polarization splitting is investigated using the degrees of freedom experimentally accessible. We observe that the variation of this splitting as a function of cavity-exciton detuning is completely reproducible regardless of the wire width.

3.2.1 Experimental setup and available degrees of freedom

The experimental setup is sketched on Fig. 3.4. A single wire is excited at normal incidence by a laser spot elongated along Y (approximate size: $50\ \mu\text{m} \times 5\ \mu\text{m}$) with an energy lying in the first nodes of the Bragg mirrors (see Section 2.2.2). The order of magnitude of the excitation power density is $0.4\ \text{mW} \cdot \mu\text{m}^{-2}$. Due to non polarization-free relaxation of the electronic excitations, both X- and Y-polarized polaritonic branches are excited regardless of the polarization of the pump.

We record the photoluminescence spectrum for polarizations parallel (Y) or orthogonal (X) to the wire long axis, selected using the half-wave plate e and an analyzer (see Section 2.2.4 for the experimental details).

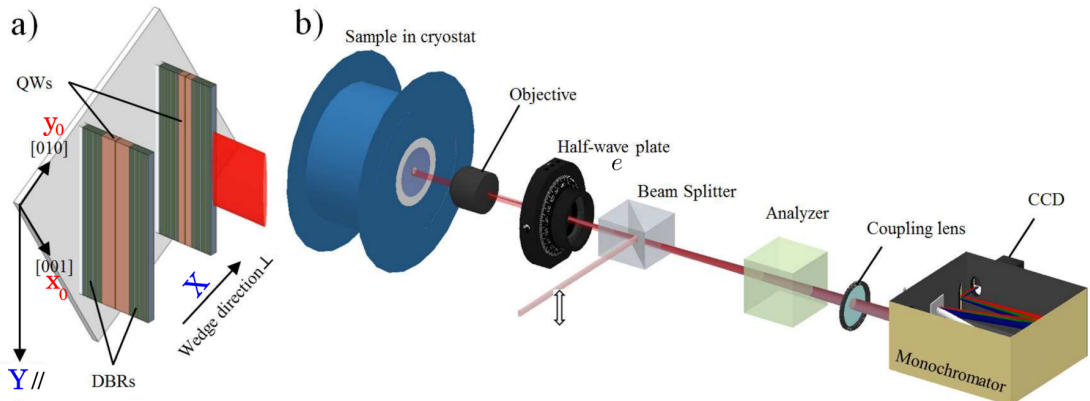


Figure 3.4: a) Schematic representation of the microwires microcavities. QWs in the DBRs have been omitted by sake of simplicity. Wires are etched down to the GaAs substrate in the direction *parallel* to the wire long axis Y. A single wire is excited by an ellipsoidal laser spot in order to match as far as possible its geometry. b) Scheme of the polarization-resolved photoluminescence (PL) setup. The sample is excited non resonantly with laser light blue-shifted with regards to the polaritonic transitions in the first transmission band of the DBR. By using a combination of a half-wave plate and an analyzer, either the X-polarized branch or the Y-polarized branch is selected while always extinguishing the reflection of the pump light.

We observe a splitting between the branches polarized parallel and orthogonal to the long axis of the wire which goes up to $1.33\ \text{meV}$ for the mode $j = 2$ as shown in Fig. 3.5.

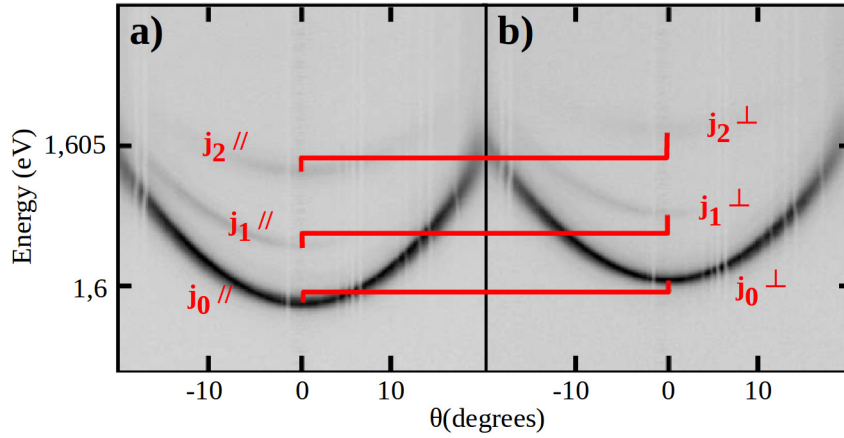


Figure 3.5: Photoluminescence (PL) at 6 K of a 3 μm -large microwire under non resonant excitation observed in the reciprocal space. The cavity-exciton detuning is approximately -7 meV. In this configuration, the dispersion curves of the lower polarization branch of the 1D-confined microcavity polaritons with polarization (a) parallel or (b) orthogonal to the wire axis can be directly observed. The splitting magnitudes for modes $j = 0$ (j_0), $j = 1$ (j_1) and $j = 2$ (j_2) are respectively 0.72 meV, 1.03 meV and 1.16 meV.

Let us now list the various degrees of freedom experimentally accessible to characterize this splitting of degeneracy between the X- and Y-polarized branches:

- The sample exhibits several rows of wires with widths ranging from 3 to 7 μm (see map of the sample in Fig. 3.1). Thus, the splitting can be investigated as a function of wire width.
- On one row, the wedge introduced during the growth of the 2D-microcavity varies quasi linearly. By recording the photoluminescence spectrum on the same row, *i.e.* for the same wire width, the splitting can be measured for various cavity-exciton detunings.
- The temperature control of the cryostat allows to vary the temperature of the sample between 6 K and up to room temperature.
- The splitting for the polaritonic modes with $j > 0$ can be investigated even if their emission intensities are much lower than the one of the fundamental $j = 0$ mode.

3.2.1.1 Splitting as a function of detuning

Since the regularly spaced microwires are etched out of a 2D microcavity possessing a linear cavity energy dependency on the position due to the wedge introduced during the growth step, the cavity-exciton detuning is therefore a linear function of the position on the sample.

3.2. OBSERVATION AND CHARACTERIZATION OF THE POLARIZATION SPLITTING

We first concentrate on the lowest polariton branch (mode $j = 0$ or j_0) which shows the largest PL signal. Measurements have been performed on a set of 82 $5\ \mu\text{m}$ -wide wires. By carefully recording the energy minima of the lowest polariton dispersion curve on each wire, the anticrossing curve between the cavity mode and the excitonic mode can be obtained both for orthogonal and parallel polarization (Fig. 3.6.a.). From these two sets of measurements, the polarization energy splitting is precisely deduced as a function of the cavity-exciton detuning using the data analysis method detailed in Appendix A1.

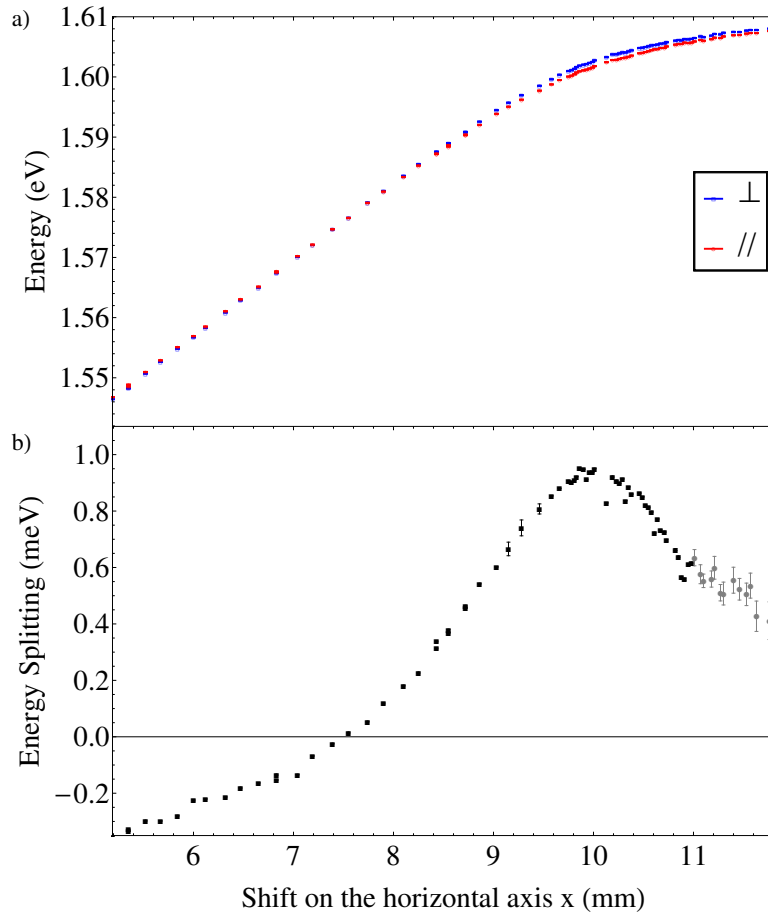


Figure 3.6: a) Energy of the $\theta_Y = 0$ lower polariton for parallel (red) and orthogonal (blue) polarization with respect to the wires axis for 82 $5\ \mu\text{m}$ -wide wires, as a function of a horizontal shift x on the sample. We recognize a typical low-polariton anti-crossing curve, confirming the linear relationship between position and detuning. b) Corresponding polarization splitting. For $x > 11$ mm (gray points), measurements are less accurate due to the broadening of the PL line: a different method of analysis was used (detailed in Appendix A1).

Experimental results Fig. 3.6 shows the result of the experiment as a function of an arbitrary horizontal position x . Figure 3.6.b. represents the energy splitting between parallel (Y) and orthogonal (X) polarized branches. For negative and null detunings, the polarization splittings are large enough with respect to the polariton branches spectral widths and are obtained directly from the energy difference of parallel and orthogonal polarized polariton branches of Fig. 3.6.a. For large positive detuning the polaritonic branch is mainly excitonic and its linewidth becomes large compared to the polarization splitting. In this case, the energy splitting is computed with a second method (see Appendix A1).

Assuming a cavity energy E_0^c varying linearly with position, the cavity-exciton detuning reads:

$$\Delta = E_0^c - E_0^x = a \cdot (x - x_{\text{ref}})$$

and we determine the constants a and x_0 by fitting the energy averaged over the polarization of Fig. 3.6.a. with the equation of the lower polariton branch:

$$E_0^{\text{ave}} = E_0^x + \frac{1}{2}\Delta - \frac{1}{2}\sqrt{\Delta^2 + 4\Omega_R^2}, \quad (3.2)$$

which also gives a calibration for E_0^x and Ω_R .

We find:

	Estimate	Standard Error
E_0^x (eV)	1.6097	0.0002
Ω_R (meV)	8.3	0.2
a (meV.mm ⁻¹)	13.2	0.07
x_{ref} (mm)	9.88	0.01

Table 3.1: Results of the fit of Fig. 3.6.a. using Eq 3.2.

Using this method, the experimental results can be plotted as a function of the cavity-exciton detuning Δ . This reference quantity is independent of the wires' width and will therefore be used to compare different data sets in the following.

3.2.1.2 Influence of the wires width

Figure 3.7 shows the polarization splitting as a function of exciton-photon detuning for various wire widths (3, 4, 5, 6 and 7 μm lateral sizes). No significant difference is observed between the various wire sizes.

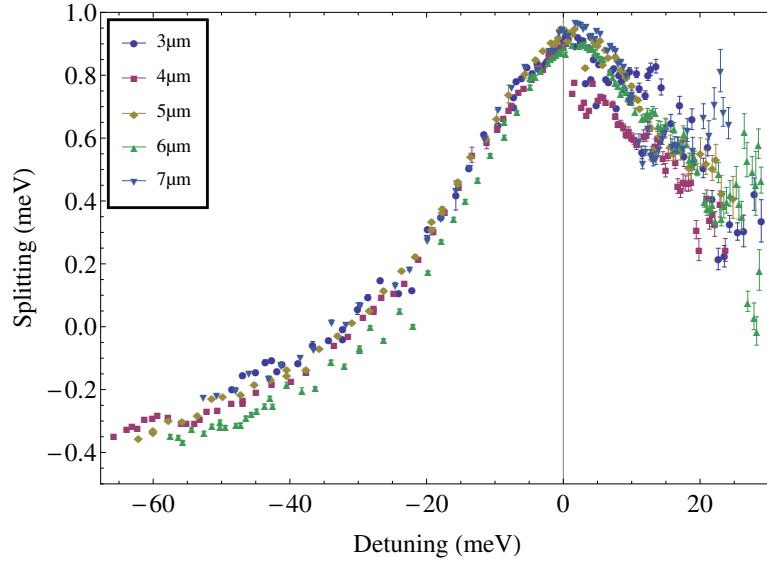


Figure 3.7: Polarization splitting as a function of the cavity-exciton detuning for various wire widths. Each experimental dot corresponds to the measurement of a single wire located at a different position on the sample, i.e. at different cavity-exciton detunings and wire width.

This observation imply that the observed polarization splitting results from local properties of the 1D-microcavities and not from boundary conditions imposed by the wire width.

3.2.1.3 Influence of the temperature

This set of data was recorded by V. Ardizzone. This time, only three wires with the same width are investigated ($3 \mu\text{m}$). They are not located at the same position on the sample, hence their cavity-exciton detunings are different: -63 , -23 and -11 meV at 10 K ¹. For each wire, the temperature is risen, starting from 10 K .

Figure 3.8 displays the polarization splitting δE_{pol} as a function of the temperature for those three wires. These data correspond to the three first lower polariton branches j_0 ($j = 0$), j_1 ($j = 1$) and j_2 ($j = 2$).

¹The detuning is computed for the $j = 0$ mode. The effective detunings for modes $j = 1$ and $j = 2$ are different since $\epsilon_0^{c,j}$ increases with j .

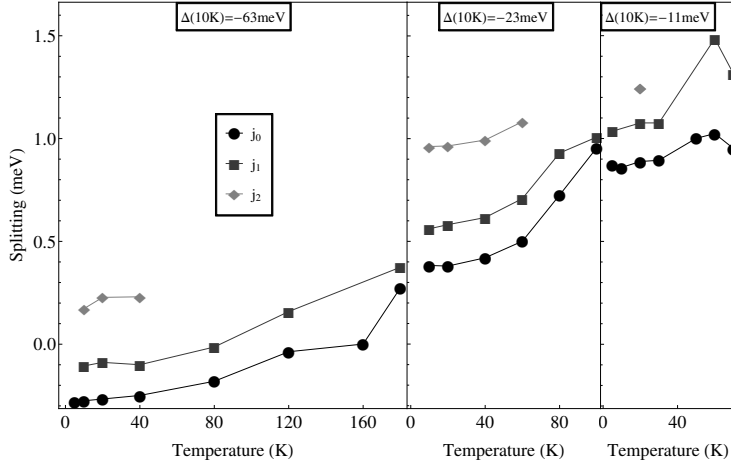


Figure 3.8: Energy splitting as a function of the sample temperature for various detunings at 10 K for 3 μm -wide wires. Disks, squares and triangles refer to the three lower polariton branches j_0 , j_1 and j_2 respectively.

The polarization splitting increases with temperature, mode index and detuning (for $\Delta < 0$). This evolution can be simply understood in the light of the data depicted in Fig. 3.7: when the temperature increases, the GaAs bandgap is reduced and leads to a decrease in the exciton energy. If the cavity is negatively detuned from the exciton energy at low temperature, at high temperature the detuning gets closer to zero, in accordance with the observations of Fig. 3.8. Varying the temperature is thus just another way to vary the cavity-exciton detuning, by shifting the exciton energy instead of the cavity energy.

This interpretation is further confirmed by doing a quantitative comparison between both methods, shown in Fig. 3.9.

Indeed, under the following assumptions:

- the GaAs bandgap varying with temperature T following [Aspnes1976]:

$$E_G(T) = 1.519 - 5.41 \cdot 10^{-4} \frac{T^2}{T + 204},$$

- the exciton energy $E_0^x(T)$ varies like $E_G(T)$ (equivalent to assume constant binding and confinement energies, see paragraph 1.1.1.3),
- the cavity energy E_0^c is quasi constant with temperature,

we can define an equivalent low-temperature detuning for each measurement for the lowest mode $j = 0$:

$$\Delta_{\text{eq}}(T) = \Delta(10\text{K}) - (E_G(T) - E_G(10\text{K}))$$

Using this equivalent detuning, the values of the $j = 0$ splitting with temperature are compatible with the ones of Fig. 3.7:

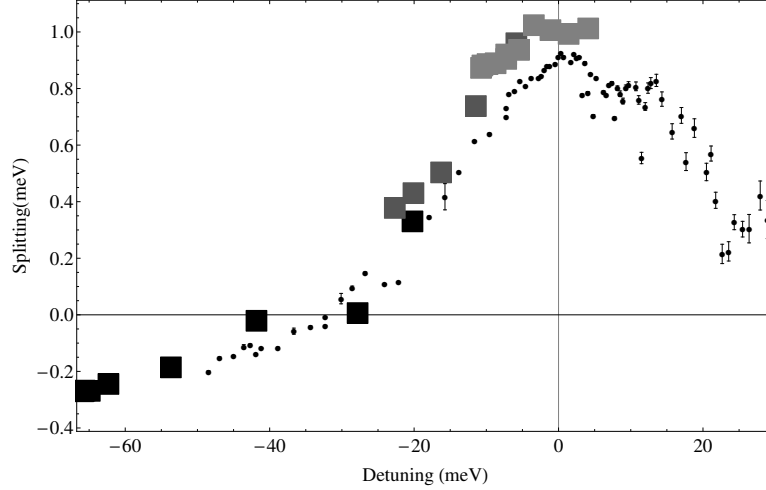


Figure 3.9: Black disks: Energy splitting as a function of detuning for $3 \mu\text{m}$ wires. Black (resp. gray and light gray) squares: equivalent low-temperature detuning for the reference detuning $\Delta(10\text{K}) = -63 \text{ meV}$ (resp. -23 meV and -11 meV).

Note on the influence of the cavity mode j

The different polaritonic modes j correspond to the polaritons arising from different photonic modes. Consequently, at negative detuning, an increase of j is equivalent to an increase of the cavity energy and thus to a reduction of the cavity-exciton detuning. However, we can observe from Fig. 3.8 that the splitting for $j > 0$ goes even beyond the highest reported splitting for $j = 0$ (nearly 1.5 meV at the reference detuning of -11 meV at 50 K). This suggests that the splitting cannot be fully described by an equivalent detuning. The confinement of the electric field along the wire width, which depends on the mode j (see Fig. 3.2), should also come into play.

3.2.2 Interpretation

Gathering all experimental results, the evolution of the $j = 0$ polarization splitting with detuning is highly reproducible. We define this polarization splitting by the following relation:

$$\delta E_{\text{pol}} = E_0^{\text{P},\perp} - E_0^{\text{P},\parallel}$$

Photonic, excitonic and Rabi coupling splittings Let us now comment on the evolution of the observed polarization splitting with the detuning. Polaritons arise from the coupling between photons and excitons. Therefore, three contributions may come into play to account for this polarization splitting: one due to the cavity

mode, one to the excitonic mode, and a last one affecting the exciton-photon coupling strength.

At large negative detuning, the polariton state is mainly photonic and the negative observed splitting is a signature of the presence of a photonic contribution δE_c . At null detuning, the Rabi energy plays an important role in the polariton total energy and the polarization splitting reaches a maximum positive peak. This suggests a contribution of the polarization Rabi splitting $\delta\Omega_R$. Finally, an excitonic one δE_x can also be taken into account.

Each contribution is carefully extracted from experimental data and will contribute to the polarization splitting to a varying degree depending on the cavity-exciton detuning Δ .

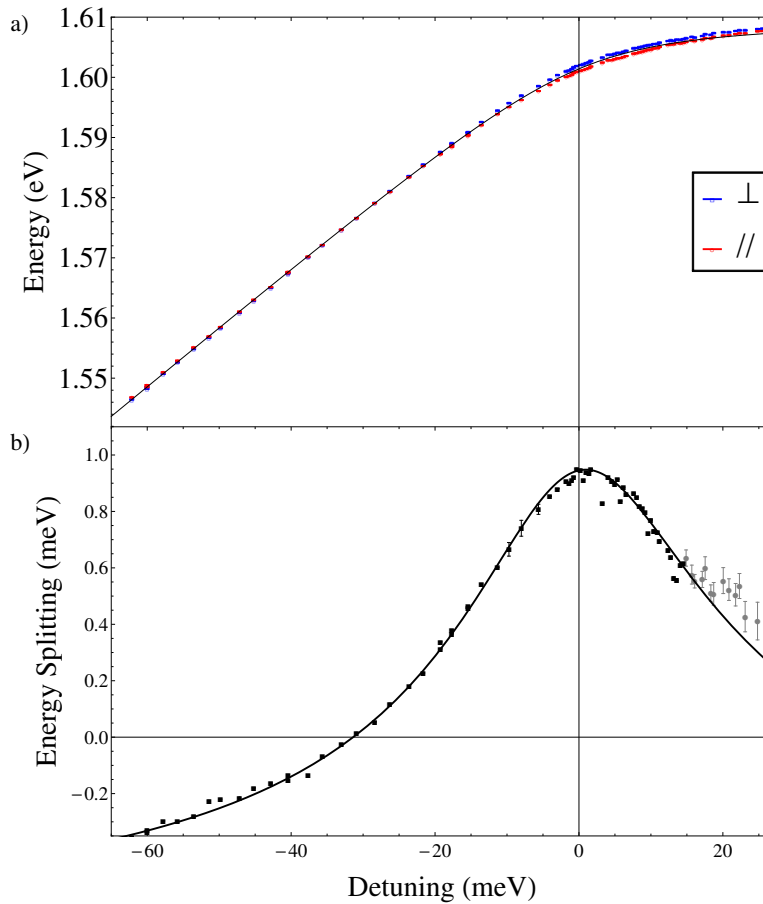


Figure 3.10: a) Data of Fig. 3.6.a. as a function of cavity-exciton detuning, fitted by eq. (3.2) plotted as a plain line. b) Data of Fig. 3.6.b. as a function of cavity-exciton detuning. The best non-linear fit using eq. (3.4) is plotted as a plain line.

The anticrossings observed in Fig. 3.6.a. can be accurately reproduced by the

anticrossing relation:

$$E_0^{p,\parallel} = \frac{1}{2}(E_0^x \pm \frac{\delta E_x}{2}) + \frac{1}{2}(\delta E_c \pm \frac{\delta E_c}{2}) - \frac{1}{2}\sqrt{(\Delta \pm \frac{\delta E_c}{2} \mp \frac{\delta E_x}{2})^2 + 4(\Omega_R \pm \delta\Omega_R)^2} \quad (3.3)$$

However, considering that the Rabi energy is large compared to the polarization splitting terms, we rather fit the mean anticrossing energy averaged over the polarization (eq. 3.2).

Under the same assumption, the polarization splitting expression can be simplified, leading to the following expression:

$$\delta E_{\text{pol}} \simeq \frac{1}{2}(\delta E_x + \delta E_c) - \frac{A}{2}(\delta E_c - \delta E_x) - 2B\delta\Omega_R \quad (3.4)$$

where $A = \frac{\Delta}{\sqrt{\Delta^2 + 4\Omega_R^2}}$ and $B = \frac{2\Omega_R}{\sqrt{\Delta^2 + 4\Omega_R^2}}$.

Data analysis The mean polariton energy $E_0^{p,\text{ave}}$ is first fitted using eq. (3.2) and the obtained value Ω_R is considered as a fixed parameter to fit the polarization splitting data with eq. (3.4). A multilinear fit of δE_{pol} as a function of A and B terms of eq. (3.4) allows to infer the values of the polarization splitting contributions. This simple two-step fitting procedure allows to obtain realistic uncertainties on estimated parameters. A rigorous and complex single-step fitting procedure using the original polarization splitting expression (3.3) has also been used and leads to exactly the same results.

Table 3.2 shows the various contributions to the polarization splitting δE_{pol} inferred from the data fitting procedure.

Contribution	Value (meV)	Standard error (meV)
δE_x	-0.58	0.16
δE_c	-0.76	0.07
$\delta\Omega_R$	-1.62	0.12

Table 3.2: Resulting contribution in meV from the different splitting sources obtained by fitting the data for 5 μm -wide wires with the model equation (3.4).

Justification of the data analysis method The relative uncertainty on Ω_R obtained by eq. (3.2) propagates on $\delta\Omega_R$ due to the induced uncertainty on B. As Ω_R is obtained with a typical 2% standard deviation (see Table 3.1), its effect on $\delta\Omega_R$ is negligible compared to eq (3.4) fitting uncertainties *a posteriori* (about 7%). This

justifies that the fitting procedures for Ω_R (eq. (3.2)) and δE_{pol} (eq. (3.4)) can be done separately.

To estimate the fit quality, the residuals are analyzed (see Appendix A2):

1. Apart from the positive detuning region, residuals are randomly distributed implying that the standard error is not underestimated.
2. p-values are below 1% meaning the null hypothesis for fitting parameters is extremely unlikely.
3. For positive detunings, residuals are significantly larger meaning that the fitting procedure is not able to capture the details of systematic effects of smaller amplitude, probably secondary anticrossings with other levels (excitonic, traps, etc...).

This fitting procedure is done using five² adjustable parameters (Ω_R , E_0^x , δE_x , δE_c , $\delta\Omega_R$), and assuming that the detuning calibration has been previously made. By incorporating the detuning calibration in the fitting procedure, the joint fit uses seven adjustable parameters (the previous ones plus the two coefficients a and x_0 of the linear relationship between position on the sample and detuning). Despite this large number, the results are identical to the simple “separate” fitting procedure both in estimated values and error bars.

Conclusion and numerical results of the fitting procedure Table 3.3 gives the fitting polarization splitting contributions obtained for the various wire widths. On average, the polarization excitonic splitting is $\delta E_x \simeq -0.54 \pm 0.18$ meV the polarization photonic splitting $\delta E_c \simeq -0.73 \pm 0.07$ meV, and the polarization Rabi splitting is $\delta\Omega_R \simeq -1.55 \pm 0.12$ meV. All values in Table 3.3 are compatible within the error bars, confirming that the wire width indeed has no measurable influence on the various sources of splitting.

Wire width (μm)	3	4	5	6	7
δE_x (meV)	-0.56	-0.72	-0.58	-0.49	-0.35
δE_c (meV)	-0.74	-0.73	-0.76	-0.77	-0.66
$\delta\Omega_R$ (meV)	-1.55	-1.61	-1.62	-1.52	-1.46

Table 3.3: Resulting contributions from the different splitting sources obtained by fitting the data for the various wire widths. Typical standard deviations for δE_x , δE_c , and $\delta\Omega_R$ are 0.20, 0.07 and 0.12 meV respectively. As observed on Fig. 3.7, estimated parameters are independent of the wire width.

²We have in fact 3 more adjustable parameters for the calibration of the spectrometer which has a limited spectral range.

3.3 Physical origins of the polarization splitting

Now that we have identified and calibrated the different sources of splitting at stake for the final splitting δE_{pol} , we want to find the physical origin for those liftings of degeneracy.

Quite surprisingly, the splitting does not disappear when the sticking conditions are changed, which is a novelty compared to previous 1D-microcavity samples studied in our group [Diederichs2007].

In fact, in this sample the etching is much deeper (down to $1\ \mu\text{m}$ in the GaAs substrate). We show that the mechanical constraints (whatever their origin) are almost totally relaxed on the short axis X and totally preserved on the long axis Y, resulting in a polarization splitting of degeneracy independent on the wire width.

However, the origin of the splitting must come from some mechanical constraints and we suggest here that the lattice mismatch between the GaAs substrate and the microwire is involved. This hypothesis is developed in a mechanical model and allows to infer an effective strain on the X axis compared to the Y axis due to the GaAs substrate - induced constraints. Using this value and photoelastic coefficients for $\text{Al}_x\text{Ga}_{1-x}\text{As}$, we can then derive the induced photonic polarization splitting δE_c . δE_c and $\delta\Omega_R$ are then obtained by calculating the exchange and Pikus-Bir interactions resulting from this strain (*cf.* Subsection 1.3.2).

3.3.1 Influence of the constraints linked to the sticking

Stress applied to the sample can induce a birefringent behavior of the microcavity and possibly explain the appearance of a polarization splitting for polarization branches. In Ref. [Diederichs2007] the polarization splitting was attributed to the thermal stress applied to the sample by the copper sample holder at low temperature. This origin was verified by observing that the polarization splitting disappeared when the sample stood free from holder in an immersion cryostat. We show here that this external stress is not at stake in the present sample.

Figure 3.11 represents the polarization splitting of the lowest polariton branch (j_0 or $j = 0$) measured on $4\ \mu\text{m}$ -wide wires when the sample is stuck on the cryostat cold finger via its whole surface or when it is stuck only on a small surface far away from the region of interest. This distant sticking (comparable to the size of the sample) ensures that the thermally induced stress is reduced. No substantial difference is observed between the two sticking configurations implying that strain in the sample due to thermal contraction of the sample holder does not significantly contribute to the polarization splitting observed.

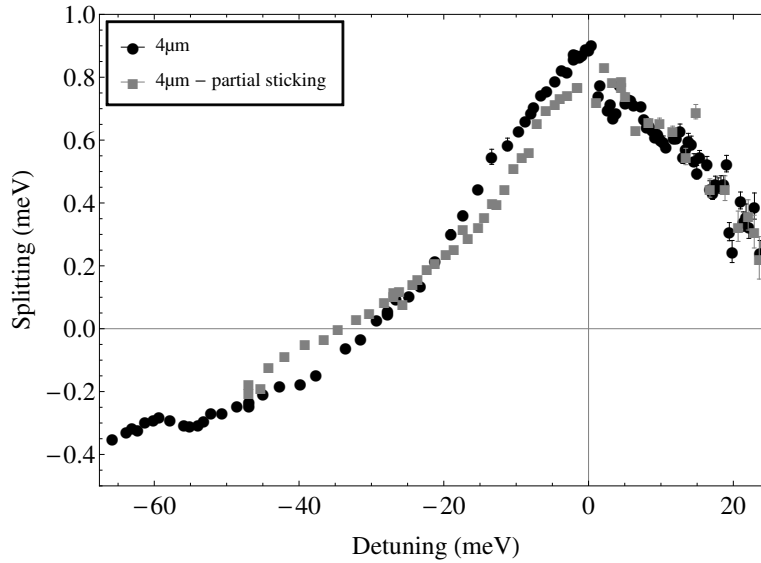


Figure 3.11: Squares correspond to the measurement performed on 4 μm wires when the sample is stuck far away from them to ensure that no thermal strain is induced.

3.3.2 Model of stress relaxation in microwires

In this section we account for the independency of the polarization splitting with the wire widths. Assuming an initial strain at the bottom of the wire, we develop a mechanical model of the stress relaxation in microwires allowing to derive the typical stress relaxation heights H_X and H_Y due to the constraints along X (short axis of the wire) and Y (long axis of the wire). In the range of wires accessible on the sample, we show that $H_X \ll H \ll H_Y$, where H is the wire height (or etching depth), and that this anisotropy is quasi-independent on the wire width.

Useful definitions Let us start by defining the useful mechanical quantities.

The stress tensor $\vec{\sigma}$ (in N.m^{-2}) is related to the strain tensor $\vec{\epsilon}$ (adimensionned) by the Hooke's law:

$$\sigma_{ij} = C_{ijkl}\epsilon_{kl}, \quad (3.5)$$

where $i, j, k,$ and l can take values x, y and z , C_{ijkl} is the stress-strain tensor (also called elastic stiffness tensor, in N.m^{-2}) and Einstein summation conventions are used.

The displacement field \vec{u} is the integral of the strain tensor, such that:

$$\vec{\epsilon} = \begin{pmatrix} \frac{\partial u_x}{\partial x} & \frac{\partial u_x}{\partial y} & \frac{\partial u_x}{\partial z} \\ \frac{\partial u_y}{\partial x} & \frac{\partial u_y}{\partial y} & \frac{\partial u_y}{\partial z} \\ \frac{\partial u_z}{\partial x} & \frac{\partial u_z}{\partial y} & \frac{\partial u_z}{\partial z} \end{pmatrix} \quad (3.6)$$

Mechanical equilibrium The mechanical equilibrium conditions are provided by the Navier equation:

$$\text{div} \vec{\sigma} = \vec{0}, \quad (3.7)$$

since there are no internal volumic forces.

$\text{Al}_x\text{Ga}_{1-x}\text{As}$ is not an isotropic cristal but its stress-strain tensor can be approximately considered as such. Hence the particular form for Hooke's law reads:

$$\vec{\sigma} = \frac{\mathcal{E}}{1+\nu} (\vec{\epsilon} + \frac{\nu}{1-2\nu} \text{Tr}(\vec{\epsilon}) \vec{\mathbb{I}}), \quad (3.8)$$

where \mathcal{E} is the Young's modulus, ν is the Poisson's ratio ($\nu < 0.5$), and $\vec{\mathbb{I}}$ is the identity tensor.

Considering an homogeneous wire we obtain the following mechanical equations:

$$\begin{cases} \alpha \partial_P^2 u_P + \beta \nabla^2 u_P & = -\alpha \partial_P \partial_z u_z \\ \alpha \partial_z^2 u_z + \beta \nabla^2 u_z & = -\alpha \partial_P \partial_z u_x \end{cases} \quad (3.9)$$

where \vec{u} is the displacement field, $P = X$ or Y , $\alpha = \frac{\mathcal{E}\nu}{(1+\nu)(1-2\nu)}$ and $\beta = \frac{\mathcal{E}}{1+\nu}$.

Boundary conditions W is the wire width, L the wire length, H the wire height, H_{sub} the height of the substrate (typically a few hundreds of μm). The origin ($X = Y = z = 0$) is placed at the bottom of the wire in its center. The boundary conditions are:

1. a fixed stress field in the P direction C_{PP} at the bottom of the substrate (H_{sub}):

$$\vec{\sigma}_{PP}(\pm \frac{D}{2}, -H_{\text{sub}}) = C_{PP},$$

where $D = W$ (resp. L) if $P = X$ (resp. Y)

2. a vanishing stress on the free interfaces of the wire:

$$\begin{cases} \vec{\sigma}(\pm \frac{D}{2}, z > 0) & = 0 \\ \vec{\sigma}(P, z = H) & = 0 \end{cases}$$

which leads to

$$\begin{cases} \partial_P u_P(\pm \frac{D}{2}, z) = 0 \\ \partial_P u_P(P, H) = 0 \end{cases}.$$

Since $u_P(0, H) = 0$ (the position of the unit cell located at $P = 0$ does not change), we have: $u_P(P, H) = 0$.

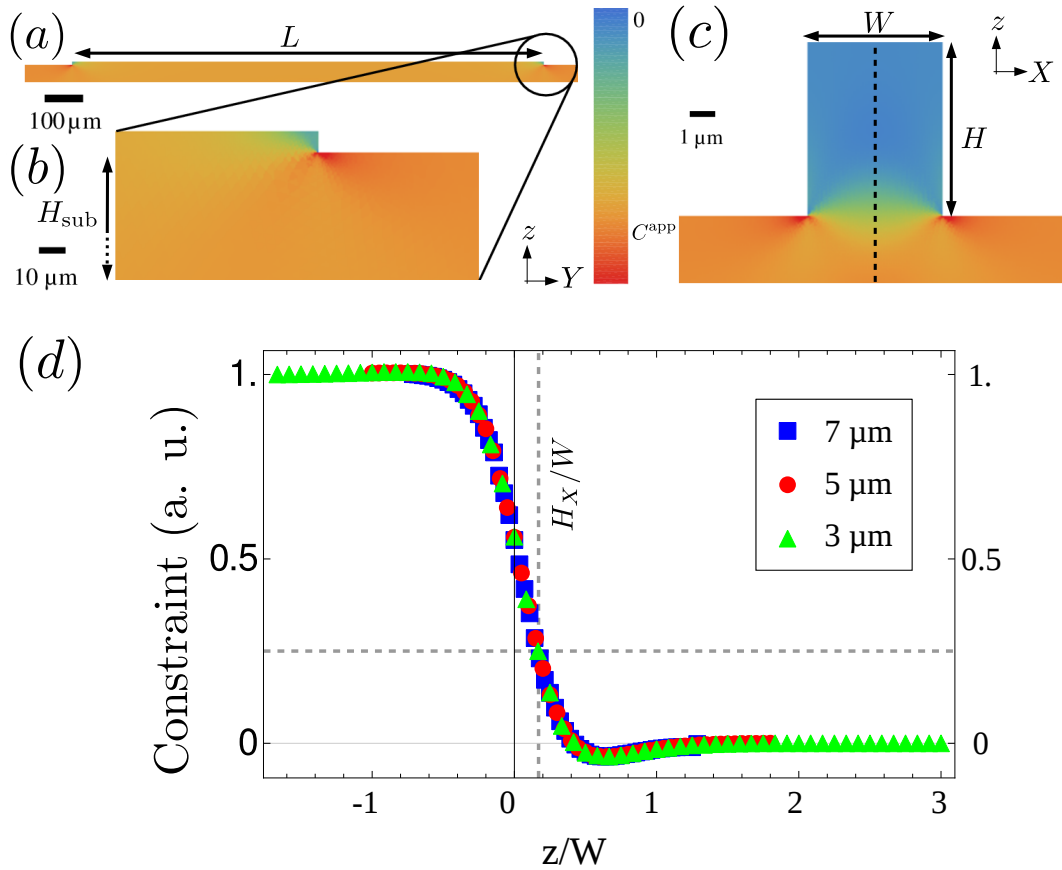


Figure 3.12: (a, b, c): Constraint repartition (in color) in a 7 μm -wide wire. Only a small part of the bulk is represented here. A lateral and longitudinal stresses $C_{XX}^{\text{app}} = C_{YY}^{\text{app}} = C^{\text{app}}$ are applied at the bottom of the bulk. (a) Stress repartition along the wire length (Y). The stress is only relaxed at the very end of the wire (zoomed in (b)). (c) Cut plane on the wire lateral axis (X). Contrarily to (a, b), the lateral stress is completely relaxed on a short lengthscale (approximately 1 μm). (d) The stress is plotted against the reduced vertical position z/W at the center of the wire ($X = 0$, shown by a dashed line in c)) for three wire widths $W = 3, 5$ and 7 μm . The profiles superposition suggests a universal law linking the characteristic stress relaxation height H_X with the wire width.

Result of the simulation The linear set of partial differential equations (3.9) is solved using a finite element method performed by the software Cast3M³. The results are presented on Fig. 3.12.

The constraints are totally relaxed on a short lengthscale in the lateral direction (Fig. 3.12.c.). On the contrary, they are mainly conserved in the longitudinal direction (Fig. 3.12.a. and b.). A plot of the constraint along X as a function of z (Fig. 3.12.d.) for three different wire widths suggests that the stress relaxation height H_X divided by the wire width W is a constant inferior to 1 (dashed vertical on Fig. 3.12.d.). This statement is confirmed by an approximate analytical calculation detailed in the next paragraph.

In the present sample, $L \simeq 1 \text{ mm}$, $W \leq 1 \text{ }\mu\text{m}$ and $L \simeq 7 \text{ }\mu\text{m}$. Therefore,

$$\frac{H}{L} \ll 1 \leq \frac{H}{W},$$

such that the constraints are completely relaxed in the lateral direction regardless of the wire width, but not in the longitudinal direction. This explains why the polarization splitting does not depend on W for this range of wire widths.

Analytical approximate result In this paragraph, an approximate analytical calculation confirm the proportionality between the stress relaxation height along X, H_X , and the wire width W . This method holds also in the Y direction and the result can be therefore easily modified to relate H_Y and L .

For sake of simplicity, the substrate is assumed to be rigid, such that the boundary condition (2) can be rewritten at first order:

$$\partial_X u_X(\pm \frac{W}{2}, 0) = \epsilon_{XX}, \quad (3.10)$$

where ϵ_{XX} is the strain along X at the bottom of the wire induced by the constraints at the bottom of the substrate. In reality, the stress is also partially released in the substrate (see Fig. 3.12.c.). Integration of eq. (3.10) gives $u_X(X, 0) = \epsilon_{XX} \cdot X$.

The set of equations (3.9) is not easily solvable analytically near the connecting edges of the wire due to the singularity of the displacement field. However, in the wire volume the second member can be safely ignored:

$$\gamma^2 \partial_X^2 u_X + \partial_Z^2 u_X = 0 \quad (3.11)$$

which is a Laplace equation in 2 dimensions with $\gamma^2 = \frac{\alpha}{\beta} + 1 = \frac{1-\nu}{1-2\nu}$ ($\gamma^2 > 0$ since $\nu < 0.5$). Assuming a solution in the form $u_X(X, z) = f(X) \cdot g(z)$, eq. (3.11) rewrites:

$$\gamma^2 g(z) \cdot f''(X) + f(X)g''(z) = 0$$

³Cast3M is freely available at <http://www-cast3m.cea.fr>.

If $f(x) = 0$ or $g(z) = 0$, we find the trivial solution $u_X(X, z) = 0$. Therefore we write:

$$\frac{f''(X)}{f(X)} = -\frac{g''(z)}{\gamma^2 g(z)} = -\Lambda$$

with Λ a constant. If $\Lambda \leq 0$, then the boundary conditions impose again the trivial solution for $u_X(X, z)$. If $\Lambda > 0$, we can write $\Lambda = \lambda^2$ and

$$\begin{cases} f(X) &= A \cos(\lambda X) + B \sin(\lambda X) \\ g(z) &= C \cosh(\lambda \gamma z) + D \sinh(\lambda \gamma z) \end{cases}$$

The boundary conditions impose then:

$$\begin{cases} (-A\lambda \sin(\pm \frac{W}{2}\lambda) + B\lambda \cos(\pm \frac{W}{2}\lambda))g(z > 0) &= 0 \\ (A \cos(\lambda X) + B \sin(\lambda X))g(H) &= 0 \\ (A \cos(\lambda X) + B \sin(\lambda X))g(0) &= \epsilon_{XX} \cdot X \end{cases} \quad (3.12)$$

The third equation of the above system of equations imply that $A = 0$ and $C \neq 0$. The second equation allows to relate C and D such that: $\tanh(\lambda \gamma H) = -C/D$, with $D \neq 0$. The first equation of (3.12) imposes then for λ the values $\lambda_n = \pm \frac{n\pi}{W}$, and $n \in \mathbb{Z}^*$. Thus, the general solution $u_X(X, z)$ writes:

$$u_X(X, z) = \sum_{n \in \mathbb{Z}^*} B_n \sin\left(\frac{n\pi}{W} X\right) \cdot g_n(z) = \sum_{n \in \mathbb{N}^*} 2B_n \sin\left(\frac{n\pi}{W} X\right) \cdot g_n(z)$$

where $g_n(z) = C_n \cosh\left(\frac{n\pi}{W} \gamma z\right) \left(1 - \frac{\tanh\left(\frac{n\pi}{W} \gamma z\right)}{\tanh\left(\frac{n\pi}{W} \gamma H\right)}\right)$.

Finally, the third equation of system (3.12) imposes:

$$\sum_{n \in \mathbb{N}^*} 2B_n \sin\left(\frac{n\pi}{W} X\right) \cdot C_n = \epsilon_{XX} \cdot X$$

Hence, $2B_n C_n$ are the sine Fourier series coefficients for $\epsilon_{XX} \cdot X$, such that:

$$2B_n C_n = -\frac{2\epsilon_{XX} W}{\pi} \frac{(-1)^n}{n}$$

The final solution is:

$$u_X(X, z) = -\frac{2\epsilon_{XX} W}{\pi} \sum_{n \in \mathbb{N}^*} \frac{(-1)^n}{n} \sin\left(\frac{n\pi}{W} X\right) \cdot \cosh\left(\frac{n\pi}{W} \gamma z\right) \left(1 - \frac{\tanh\left(\frac{n\pi}{W} \gamma z\right)}{\tanh\left(\frac{n\pi}{W} \gamma H\right)}\right) \quad (3.13)$$

The term $n = 1$ is the main contribution in $u_X(X, z)$:

$$\frac{2\epsilon_{XX}W}{\pi} \sin\left(\frac{\pi}{W}X\right) \cdot \cosh\left(\frac{\pi}{W}\gamma z\right) \left(1 - \frac{\tanh\left(\frac{\pi}{W}\gamma z\right)}{\tanh\left(\frac{\pi}{W}\gamma H\right)}\right) \quad (3.14)$$

It is an increasing exponential function, null for $z = H$ (no displacement at the top of the wire, in accordance with the boundary conditions chosen).

For the discussion, we assume that $H = H_\infty \gg W$, such that the constraints induced by the GaAs substrate are completely relaxed at the top of the wire. We thus have: $\tanh\left(\frac{\pi}{W}\gamma H\right) \approx 1$.

The typical lengthscale H_X for the constraints relaxation is therefore

$$H_X = \frac{W}{\pi\gamma} \ln 2.$$

For GaAs $\nu = 0.31$ so that $\gamma \simeq 1.35$. The maximum value of H_X is $1.2 \mu\text{m}$ for the range of widths explored here (3 to $7 \mu\text{m}$).

The same calculation can be performed for the displacement field on the long axis of the wire u_Y . The typical lengthscale on this axis reads

$$H_Y \simeq \frac{L}{\pi\gamma} \ln 2,$$

where L is the length of the wire (1 mm) so typically a lengthscale of more than $150 \mu\text{m}$. We thus have $H_X < H \ll H_Y$.

Fig. 3.13 shows the displacement fields u_X and u_Y as a function of z (using eq. (3.14)). H_X and H_Y are marked by the red vertical line.

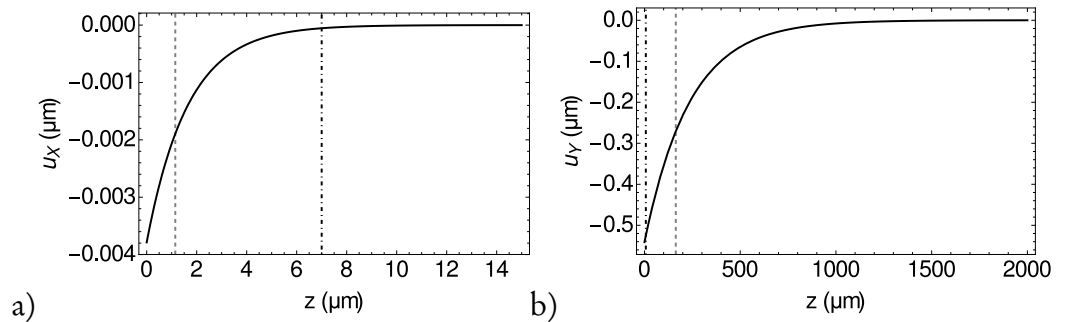


Figure 3.13: Displacement fields (calculated with equation (3.14)) as a function of z for a wire height of 2 mm, along X (a) and Y (b). In each case, the lengthscale for the relaxation of the constraints (H_X and H_Y , respectively) is highlighted by the vertical grey line. The black vertical line indicates the real height of the wire $H = 7 \mu\text{m}$. $\epsilon_{XX} = \epsilon_{YY} = -850 \text{ ppm}$, $W = 7 \mu\text{m}$, and $L = 1 \text{ mm}$.

Since the etching depth is about $H = 7 \mu\text{m}$ (approx. $1 \mu\text{m}$ down in the Bragg mirrors), the constraints are well relaxed on the X axis, regardless of the wire width. However, they are NOT relaxed in the Y direction and are totally relaxed in the X direction regardless of the wire width.

In the sample studied in Ref. [Diederichs2007], the wires were obtained with a much smaller etching depth (slightly below the quantum wells). The thermal constraints were effective because they were not completely relaxed in the lateral direction : changing the sticking procedure would influence the constraints in the lateral direction, and therefore the observed splitting.

Conclusion Stress in the X direction is relaxed on short lengthscales (typically $0.49 \mu\text{m}$ for $3 \mu\text{m}$ wires and $1.15 \mu\text{m}$ for $7 \mu\text{m}$ wires, the wire height being about $7 \mu\text{m}$).

However, along the Y direction, the relaxation length is much longer than the wire height and therefore the bulk stress is preserved through the structure. It is this constraint anisotropy between the directions parallel and perpendicular to the wire axis which is the cause of the polarization splitting δE_{pol} .

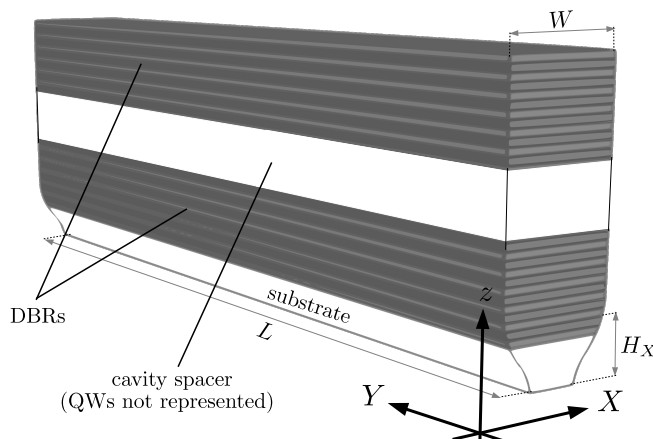


Figure 3.14: Sketch of the microwire. The constraints induced by the bulk GaAs are relaxed on a very short lengthscale in the X direction. On the contrary, they are not relaxed in the Y direction.

This explains why no difference is observed in our sample between wires of various widths and with different sticking methods.

3.3.3 Lattice mismatch-induced constraints

If the sticking conditions do not matter here (see Subsection 3.3.1), another local strain must be responsible for this polarization splitting. In this subsection, we assume that this internal strain is due to the lattice mismatch between the different

layers of Aluminium Gallium Arsenide with various proportion of Aluminum. A mechanical model of the strain distribution in distributed Bragg reflector layers allows to calculate the order of magnitude of this effect.

From the previous subsection we know that the lattice parameter along the wire's long axis Y will be fixed by the lattice parameter of the substrate (GaAs), whereas in the X direction orthogonal to the wire, the average stress is released. Thus, the DBRs lattice parameter is different in the X and Y directions, inducing a birefringence in the cavity mode. Secondly, the lattice parameter of the semiconductor constituting the quantum wells along X is fixed by the mean lattice parameters of the nearby distributed Bragg reflectors, which induces an excitonic splitting. The effect of strain on the Rabi splitting arises due to Pikus-Bir effect [Bir&Pikus].

3.3.3.1 Calculation of the lattice-mismatch induced strain

We assume that the polarization splitting is due to the lattice-mismatch induced constraints, and that those constraints are conserved in the Y direction such that ϵ_{YY} is constant through the structure. On the contrary, the strain along X varies from ϵ_{XX} at the bottom of the wire to 0 at the top (full constraints relaxation). We will consider the strain coefficient $\epsilon = -\epsilon_{XX}$ resulting from the relaxation of the constraints induced by the GaAs substrate for $z > H_X$. Since the GaAs (substrate) has a lower unit cell size than the first DBR layer of AlGaAs, the constraints relaxation induces a dilatation in the X direction (see Fig. 3.14), so we expect $\epsilon > 0$.

Order of magnitude Before starting the full calculation, we want to derive an order of magnitude for ϵ , the strain induced by the relaxation of the lattice-mismatch constraints in the X direction.

In the following, we will refer to $\text{Al}_{0.2}\text{Ga}_{0.8}\text{As}$ layers with index (1) and $\text{Al}_{0.95}\text{Ga}_{0.05}\text{As}$ (intracavity spacer and distributed Bragg reflector layer) with index (2). GaAs (quantum well) will be labelled with index (0).

We define Λ_m as the relative change in lattice parameter between bulk GaAs and the material of layer (m), such that

$$\Lambda_m = \frac{a^{(m)} - a^{(0)}}{a^{(0)}},$$

where $a^{(m)}$ is the lattice parameter of material (m). Using values (at room temperature) of Ref. [Adachi1985], Λ_m is estimated to 270 and 1300 ppm for layers (1) and (2) respectively.

We define $H^{(m)}$ as the total thickness of material (m), such that $H^{(0)} + H^{(1)} + H^{(2)} = H$.

Considering that the Poisson coefficient is null and an equal stiffness for the

various materials, in a first approximation ϵ can be written:

$$\epsilon = \frac{H^{(0)}\Lambda_0 + H^{(1)}\Lambda_1 + H^{(2)}\Lambda_2}{H}$$

As $H^{(1)} \simeq H^{(2)} \gg H^{(0)}$, ϵ can be approximated as the average of Λ_1 and Λ_2 , such that the expected order of magnitude for ϵ is 800 ppm. This small value is expected since the lattice parameter varies slowly with x (*cf.* the first paragraph of Section 1.1).

Note that, since the lattice-mismatch induced constraints follow the crystalline axes x and y , the induced strain ϵ is a function of the angle θ_w between y and the wire axis Y . Since x and y are interchangeable, $\epsilon(\theta_0 + 0) = \epsilon(\theta_0 + \frac{\pi}{2})$ and $\epsilon(\theta)$ must be a periodic function with period $\pi/2$.

Full calculation The full calculation takes into account the strain induced in each layer by its underlying layer. This will also allow us to infer the dependency of ϵ on the orientation of the wire with respect to the crystalline axes.

In the (X, Y, z) basis, the strain tensor $\vec{\epsilon}^{(0)}$ imposed by the relaxation of the constraints induced by the GaAs substrate onto the first layer of the wire reads:

$$\vec{\epsilon}^{(0)} = \begin{pmatrix} \epsilon & 0 & \epsilon_{Xz}^{(0)} \\ 0 & 0 & 0 \\ \epsilon_{zX}^{(0)} & 0 & \epsilon_{zz}^{(0)} \end{pmatrix}$$

The change of basis between (X, Y, z) and (x_0, y_0, z) is performed by the matrix \mathcal{P} :

$$\mathcal{P} = \begin{pmatrix} \cos \theta_w & -\sin \theta_w & 0 \\ \sin \theta_w & \cos \theta_w & 0 \\ 0 & 0 & 1 \end{pmatrix}$$

Thus, in the (x_0, y_0, z) basis $\vec{\epsilon}^{(0)}$ reads:

$$\vec{\epsilon}^{(0)} = \begin{pmatrix} \epsilon \cos^2 \theta_w & -\frac{\epsilon}{2} \sin 2\theta_w & \epsilon_{xz}^{(0)} \\ -\frac{\epsilon}{2} \sin 2\theta_w & \epsilon \sin^2 \theta_w & \epsilon_{yz}^{(0)} \\ \epsilon_{zx}^{(0)} & \epsilon_{zy}^{(0)} & \epsilon_{zz}^{(0)} \end{pmatrix},$$

where the coefficients $\epsilon_{i \neq j}^{(0)}$ are θ_w -dependent. The strain due to the relative lattice mismatch relaxation constraints at the interface change between layer (m) and layer

(m - 1) reads, with $l^{(m)} = \frac{a^{(m)}}{a^{(0)}}$,

$$\vec{\epsilon}^{(m)} = \vec{\epsilon}^{(m-1)} + \begin{pmatrix} -(l^{(m)} - l^{(m-1)}) & 0 & \epsilon_{xz}^{(m)} - \epsilon_{xz}^{(m-1)} \\ 0 & -(l^{(m)} - l^{(m-1)}) & \epsilon_{yz}^{(m)} - \epsilon_{yz}^{(m-1)} \\ \epsilon_{zx}^{(m)} - \epsilon_{zx}^{(m-1)} & \epsilon_{zy}^{(m)} - \epsilon_{zy}^{(m-1)} & \epsilon_{zz}^{(m)} - \epsilon_{zz}^{(m-1)} \end{pmatrix}.$$

Finally:

$$\vec{\epsilon}^{(m)} = \vec{\epsilon}^{(0)} + \begin{pmatrix} -(l^{(m)} - l^{(0)}) & 0 & \epsilon_{x_0z}^{(m)} - \epsilon_{x_0z}^{(0)} \\ 0 & -(l^{(m)} - l^{(0)}) & \epsilon_{y_0z}^{(m)} - \epsilon_{y_0z}^{(0)} \\ \epsilon_{zx_0}^{(m)} - \epsilon_{zx_0}^{(0)} & \epsilon_{zy}^{(m)} - \epsilon_{zy}^{(0)} & \epsilon_{zz}^{(m)} - \epsilon_{zz}^{(0)} \end{pmatrix}$$

The strain being invariant along the y and x direction, $\epsilon_{xz}^{(m)} = \epsilon_{yz}^{(m)} = \epsilon_{zx}^{(m)} = \epsilon_{zy}^{(m)} = 0$. With $l^{(m)} - l^{(0)} = \Lambda_m$, the final expression for $\vec{\epsilon}^{(m)}$ in the (x_0, y_0, z) basis is:

$$\vec{\epsilon}^{(m)} = \begin{pmatrix} \Lambda_m + \epsilon \cos^2 \theta_w & -\frac{\epsilon}{2} \sin 2\theta_w & 0 \\ -\frac{\epsilon}{2} \sin 2\theta_w & \Lambda_m + \epsilon \sin^2 \theta_w & 0 \\ 0 & 0 & \epsilon_{zz}^{(m)} \end{pmatrix} \quad (3.15)$$

ϵ will be obtained in the following by minimizing the free energy of the crystal:

$$F = C_{ijkl}^{(1)} \epsilon_{ij}^{(1)} \epsilon_{kl}^{(1)} h^{(1)} / 2 + C_{ijkl}^{(2)} \epsilon_{ij}^{(2)} \epsilon_{kl}^{(2)} h^{(2)} / 2, \quad (3.16)$$

where $h^{(1)}$ and $h^{(2)}$ are the respective thicknesses of the DBR layers. Since the DBRs constitute the thickest part of the wire, we neglect the contribution of the intracavity spacer and GaAs QWs in the expression of the crystal free energy (3.16).

The only missing parameters of eq. (3.16) are $\epsilon_{zz}^{(m)}$.

Calculation of $\epsilon_{zz}^{(m)}$ The stiffness tensor for a cubic lattice reads:

$$C_{ijkl} = C_{12} \delta_{ij} \delta_{kl} (1 - \delta_{ik}) + C_{11} \delta_{ijkl} \quad (3.17)$$

$$+ C_{44} (\delta_{ik} \delta_{jl} + \delta_{il} \delta_{kj}) (1 - \delta_{ij}) (1 - \delta_{kl}), \quad (3.18)$$

with i, j, k, l standing for x, y or z.

The mechanical equilibrium of the (1)-(2) interface in the vertical direction gives the condition:

$$C_{zzkl}^{(1)} \epsilon_{kl}^{(1)} + C_{zzkl}^{(2)} \epsilon_{kl}^{(2)} = 0 \quad (3.19)$$

The mechanical equilibrium at the edge of the wire in the X direction reads:

$$(C_{ijkl}^{(1)} \epsilon_{kl}^{(1)} h^{(1)} + C_{ijkl}^{(2)} \epsilon_{kl}^{(2)} h^{(2)}) X_i X_j = 0, \quad (3.20)$$

$h^{(1,2)}$ are the respective thicknesses of the layers, $\mathbf{X} = (\cos \theta_w, -\sin \theta_w, 0)$ is the unit vector orthogonal to the wire etching direction in the plane of the DBR, and $\epsilon_{ij}^{(1,2)}$ defined by eq. (3.15).

These two conditions allow to express $\epsilon_{zz}^{(m)}$ as a complex function of the other parameters of the problem.

Calculation of ϵ Consequently, the free energy (eq. (3.16)) can be expressed as a function of the $C_{11}^{(m)}$, $C_{12}^{(m)}$, $C_{44}^{(m)}$, Λ_m , ϵ and θ_w .

The minimization of F gives a complex function of those variables. This allows to derive $\epsilon(\theta)$ as a function of the form:

$$\epsilon \simeq \frac{1}{A + B \cos 4\theta_w}.$$

ϵ is a periodic function with period $\pi/2$ as expected.

Using the room temperature values referenced in [Adachi1985], we obtain:

$$\begin{aligned} C_{11}^{(m)} &= (11.88 + 0.14 \cdot x^{(n)}) \cdot 10^{11} \text{ dyn/cm}^2 \\ C_{12}^{(m)} &= (5.38 + 0.32 \cdot x^{(n)}) \cdot 10^{11} \text{ dyn/cm}^2 \\ C_{44}^{(m)} &= (5.94 + 0.05 \cdot x^{(n)}) \cdot 10^{11} \text{ dyn/cm}^2 \\ \Lambda_m &= \frac{0.0078 \cdot x^{(n)}}{5.6533} \end{aligned}$$

The layer thicknesses are $h^{(1)} = 566 \text{ \AA}$ and $h^{(2)} = 650 \text{ \AA}$ [Wertz2010a] and $x^{(1)} = 0.2$ and $x^{(2)} = 0.95$.

For $\theta_w = 39^\circ$, we find

$$\boxed{\epsilon \simeq 853 \text{ ppm}}$$

in accordance with the order magnitude found in the previous paragraph, though the full calculation also takes into account the stiffness tensor parameters $C_{ijkl}^{(m)}$ and the orientation of the wire with respect to the crystalline axis θ_w in addition to the relative lattice mismatches $\Lambda^{(m)}$.

The dependency of ϵ with θ_w can be seen in the following figure:

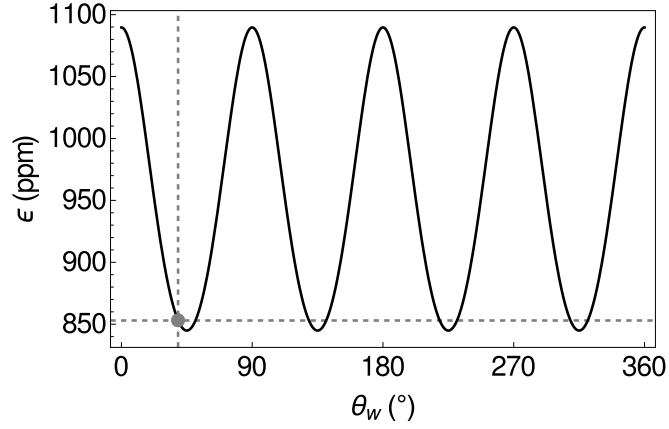


Figure 3.15: ϵ as a function of θ_w , angle between the crystalline axis y_0 and the wire long axis Y . The red spot corresponds to the present situation $\theta_w = 39^\circ$.

3.3.3.2 Stress-induced birefringence

The photonic contribution cannot come from the TE-TM splitting of the cavity mode (refer to Subsection 1.3.1) since it vanishes at normal incidence. The boundary conditions for the electromagnetic field inside the structure may also induce a lifting of degeneracy for the polarization TE and TM of the cavity mode. However, this effect is below $20 \mu\text{eV}$ for the $j = 0$ mode [Kuther1998].

Finally, under an anisotropic constraint, birefringence may take place in the Bragg mirrors, leading to a cavity mode normal splitting which magnitude and polarization eigenbasis depends on the angle between the etching direction and the crystalline axes.

We first calculate the strength and the principal axes of the birefringence-induced photonic splitting, before presenting an experiment which strongly supports this hypothesis.

Calculation of the induced birefringence energy splitting and axes For a given applied strain, the variation of the dielectric impermeability $\delta\eta_{ij}$ writes [Adachi1985]:

$$\delta\eta_{ij}^{(m)} = \sum_{k,l} P_{ijkl} \epsilon_{kl}$$

where P_{ijkl} is the photoelastic tensor, with the same symmetry than C_{ijkl} (eq. (3.17)). Using Voigt notation for ϵ_{kl} and P_{ijkl} , $\delta\eta_{ij}$ is easily computed in the (x_0, y_0, z) basis and reads:

$$\vec{\delta\eta}^{(m)} = \begin{pmatrix} \delta\eta_{11}^{(m)} & -\frac{\epsilon}{2} P_{44}^{(m)} \sin 2\theta_w & 0 \\ -\frac{\epsilon}{2} P_{44}^{(m)} \sin 2\theta_w & \delta\eta_{22}^{(m)} & 0 \\ 0 & 0 & P_{12}^{(m)}(\epsilon - 2\Lambda_m) + P_{11}^{(m)} \epsilon_{zz}^{(m)} \end{pmatrix},$$

where $\delta\eta_{11}^{(m)} = P_{12}^{(m)} \epsilon_{zz}^{(m)} + P_{11}^{(m)}(-\Lambda_m + \epsilon \cos^2 \theta_w) + P_{12}^{(m)}(-\Lambda_m + \epsilon \sin^2 \theta_w)$ and $\delta\eta_{22}^{(m)} = P_{12}^{(m)} \epsilon_{zz}^{(m)} + P_{12}^{(m)}(-\Lambda_m + \epsilon \cos^2 \theta_w) + P_{11}^{(m)}(-\Lambda_m + \epsilon \sin^2 \theta_w)$.

The diagonalization of this matrix gives the eigenvalues and polarization basis of the photonic splitting for the layer (m). We note that the z-axis is an eigenvector for all layers. Since the induced birefringence is between polarization parallel and perpendicular to the wire axis, the component along z is omitted in the following. Secondly, this matrix being symmetric and real, the in-plane eigenvectors of the induced birefringence are orthogonal and the eigenstates are linear polarizations.

The two eigenvalues of interest are

$$\delta\eta_{\pm}^{(m)} = \frac{1}{4} \left(2\epsilon(P_{11}^{(m)} + P_{12}^{(m)}) + 4P_{12}^{(m)} \epsilon_{zz}^{(m)} - 4\Lambda_m(P_{11}^{(m)} + P_{12}^{(m)}) \pm \sqrt{2\epsilon} \sqrt{\Delta_m^2 + P_{44}^{(m)2} + (\Delta_m^2 - P_{44}^{(m)2}) \cos(4\theta_w)} \right),$$

where $\Delta_m = P_{11}^{(m)} - P_{12}^{(m)}$.

The angle between the corresponding eigenvectors $v_{\pm}^{(m)}$ and y reads:

$$\theta_{\pm}^{(m)} = -\arctan \left(\frac{2\Delta_m \cos(2\theta_w) \pm \sqrt{2} \sqrt{\Delta_m^2 + P_{44}^{(m)2} + (\Delta_m^2 - P_{44}^{(m)2}) \cos(4\theta_w)}}{2P_{44}^{(m)} \sin(2\theta_w)} \right)$$

In general, if $\Delta_m = P_{11}^{(m)} - P_{12}^{(m)} \neq P_{44}^{(m)}$ (true for non isotropic materials), the polarization basis for the photonic splitting is not colinear to the wire etching direction, in accordance with experimental observations (see next paragraph and Fig. 3.17).

	Al _{0.2} Ga _{0.8} As	Al _{0.95} Ga _{0.05} As
P ₁₁ - P ₁₂	0.025	-0.005
P ₄₄	-0.030	-0.011
P ₁₁	-0.051	-0.083

Table 3.4: Values of $\Delta_m = P_{11}^{(m)} - P_{12}^{(m)}$ and $P_{44}^{(m)}$ at 10 K and 1.6 eV extrapolated from [Adachi1985]. The value of $P_{11}^{(m)}$ is then deduced from [Goni1990] (isotropic stress-induced birefringence).

Using the values listed in Table 3.4, the deviation angles

$$\xi_{\pm}^{(m)} = \theta_{\pm}^{(m)} - \theta_w$$

between the observed polarization basis and the wire etching basis are shown as a function of θ_w in Fig. 3.16. Note that no deviation is expected for $\theta_w = 0, \pi/4$ and $\pi/2$ (case where the etching is done along the crystalline axes or in a diagonal direction).

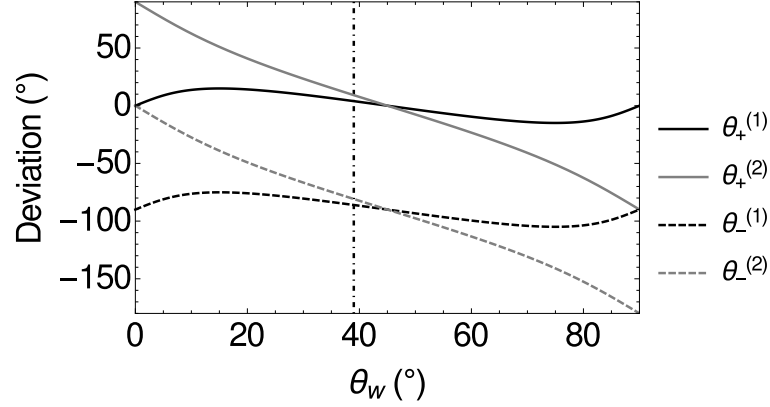


Figure 3.16: Deviation angles $\theta_{\pm}^{(m)} - \theta_w$ as a function of θ_w . The vertical line shows the experimental configuration ($\theta_w = 39^\circ$).

The angle of etching is $\theta_w = 39^\circ$, so we find $\theta_+^{(1)} \simeq 43^\circ$ and $\theta_+^{(2)} \simeq 48^\circ$, which corresponds to a deviation $\xi_+^{(1)} \simeq 4^\circ$ and $\xi_+^{(2)} \simeq 9^\circ$.

Since the dielectric impermeability η corresponds to the inverse of the dielectric permittivity ε , the eigenvalues for the permittivity read:

$$\delta\varepsilon_{\pm}^{(m)} = -n_m^4 \delta\eta_{\pm}^{(m)}, \quad (3.21)$$

where $n_m \simeq 3.578 - 0.6 \cdot x^{(m)}$ is an empirical law linking the refractive index of the unstressed material (m) at low temperature around 1.6 eV to its proportion $x^{(m)}\%$ of Aluminium.

We find:

$\delta\varepsilon_+^{(1)}$	$\delta\varepsilon_-^{(1)}$	$\delta\varepsilon_+^{(2)}$	$\delta\varepsilon_-^{(2)}$
-0.0006	0.0030	0.0071	0.0079

Table 3.5: Correction of the dielectric permittivity due to the stress-induced birefringence, computed using eq. (3.21).

The dielectric permittivity tensor of material (m), $\vec{\delta\varepsilon}^{(m)}$, is diagonal in the $v_{\pm}^{(m)}$ basis. In the (X, Y) basis, they read:

$$\vec{\delta\varepsilon}^{(m)} = \begin{pmatrix} \delta\varepsilon_+^{(m)} \cos^2 \xi_+^{(m)} + \delta\varepsilon_-^{(m)} \sin^2 \xi_+^{(m)} & \frac{\delta\varepsilon_+^{(m)} - \delta\varepsilon_-^{(m)}}{2} \sin 2\xi_+^{(m)} \\ \frac{\delta\varepsilon_+^{(m)} - \delta\varepsilon_-^{(m)}}{2} \sin 2\xi_+^{(m)} & \delta\varepsilon_-^{(m)} \cos^2 \xi_+^{(m)} + \delta\varepsilon_+^{(m)} \sin^2 \xi_+^{(m)} \end{pmatrix}$$

The calculated birefringence $\vec{\delta\varepsilon}^{(m)}$ lifts the energy degeneracy between polarizations. For a symmetric cavity, the cavity mode energy is given by [Panzarini1999]:

$$E_0^c = \frac{L_c E_0^{\text{cav}} + L_{\text{DBR}} E_0^{\text{DBR}}}{L_c + L_{\text{DBR}}}, \quad (3.22)$$

where $L_{\text{DBR}} = \frac{2n_1^2 n_2^2}{n_{\text{cav}}^2 (n_1^2 - n_2^2)} (h^{(1)} + h^{(2)})$ is the cavity field penetration length into the DBR, $n_{\text{cav}} = n_2$ is the cavity refractive index, L_c is the cavity spacer thickness ($\simeq 122$ nm according to Ref. [Wertz2010a]), $E_0^{\text{cav}} = \frac{\hbar\pi c}{n_{\text{cav}} L_c}$ and $E_0^{\text{DBR}} = \frac{\hbar\pi c}{2} \frac{n_1 + n_2}{(n_1^2 h^{(1)} + n_2^2 h^{(2)})}$ is the energy of the center of the stopband.

The energy correction due to birefringence is obtained by using the perturbation theory at first order on eq. (3.22), replacing n_m by $\sqrt{\varepsilon^{(m)}}$:

$$\vec{\delta E}_c = \frac{\partial E_0^c}{2n_1 \partial n_1} \delta\varepsilon^{\vec{z}(1)} + \frac{\partial E_0^c}{2n_2 \partial n_2} \delta\varepsilon^{\vec{z}(2)} + \frac{\partial E_0^c}{2n_c \partial n_c} \delta\varepsilon^{\vec{z}(c)},$$

where $\vec{\delta E}_c$ is the energy matrix in the Stokes space (polarization along x_0 and y_0).

The diagonalization of $\vec{\delta E}_c$ gives two eigenvalues $\delta E_c^+ = -378.3 \mu\text{eV}$, $\delta E_c^- = -510.7 \mu\text{eV}$, detuned from (X, Y) by the deviation angle $\xi_+ = 8^\circ$.

The strain-induced variation of dielectric permittivity is approximately $\delta E_c = \delta E_c^- - \delta E_c^+ = -0.13$ meV, reasonably close from the -0.73 ± 0.07 meV photonic polarization splitting experimentally observed.

Experimental confirmation Hence, this model predicts that the cavity splitting polarization axes are slightly detuned from the (X, Y) basis (typically 8°). Therefore, since the photonic component of the polariton is dominant at large negative detunings, we expect that the polarization axes for the observed splitting are not exactly along X and Y (respectively orthogonal and parallel to the wire axis).

The polarization eigenbasis for the total splitting at low and large negative detuning are compared in Fig. 3.17. A shift of about 21° is observed between the both.

In principle the polarization splitting expression (3.4) considered in Section 3.2.2 has to be corrected to take into account the various linearly polarization bases, but in practice the precisions of the experimental data is insufficient to infer the extra parameters introduced in the fitting model due to vanishingly small corrections.

3.3. PHYSICAL ORIGINS OF THE POLARIZATION SPLITTING

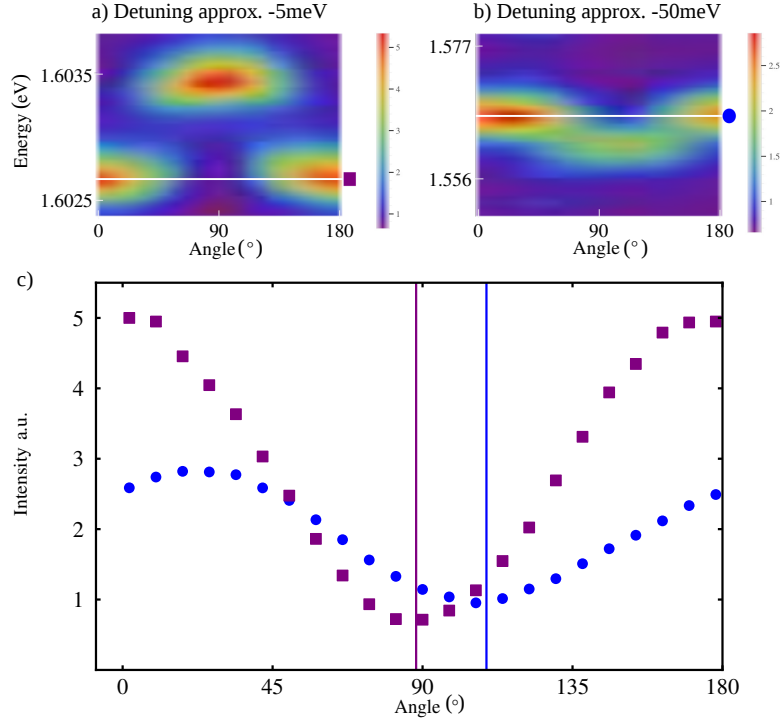


Figure 3.17: (a, b) 2D maps showing the PL intensity at normal incidence of the mode $j = 0$ as a function of the polarization direction: 0° (resp. 90°) polarization angle corresponds to polarization parallel (resp. perpendicular) to the wire's long axis. Measurements were taken each 8° and correspond to vertical stripes. From these maps, the energy splitting is directly accessible and is for (a) $\delta E_{\text{pol}} = 0.77 \text{ meV}$ and for (b) $\delta E_{\text{pol}} = -0.23 \text{ meV}$. (a) The measurements were taken on a wire with low negative exciton-photon detuning (-5 meV). (b) idem at large negative exciton-photon detuning (-50 meV). (c) Intensity profile along the horizontal white lines drawn in (a) and (b) as a function of the polarization angle. The polarization basis at large negative detuning (b) is shifted by an angle of 21° with respect to polarization basis parallel and perpendicular to the wire axis. More generally, angular shifts varies from 13° to 21° depending on the choice of energy cut.

3.3.3.3 Influence of strain on the exciton energy

After having estimated the origin of the photonic polarization splitting we will now consider the excitonic splitting induced by the internal strain ϵ .

The Hamiltonian for the light and heavy hole exciton states is given by

$$H_0 + H_{\text{exch}} + H_{\text{PB}}$$

Here H_0 is the exciton Hamiltonian which is diagonal in the heavy exciton - light exciton basis and associates an energy E_{hh} (E_{lh}) to heavy hole-excited (light hole-excited respectively). It takes the form $H_0 = -\frac{1}{2}\Delta E(J_z^{\text{hh}2} - J_z^{\text{lh}2}/3)$, where $\Delta E =$

$E_{1h} - E_{hh} > 0$, and J^h are angular momentum operators acting on the hole states. $\Delta E \simeq 28 \text{ meV}$ results from the difference between the holes confinement energies and binding energies and is estimated in Subsection 1.1.1.3.

H_{exch} is the short range exchange interaction between the electron and hole of the exciton. We consider the uncoupled hole-electron basis, $|\frac{3}{2}, \uparrow\rangle$, $|\frac{3}{2}, \downarrow\rangle$, $|\frac{1}{2}, \uparrow\rangle$, $|\frac{1}{2}, \downarrow\rangle$, $|\frac{1}{2}, \uparrow\rangle$, $|\frac{1}{2}, \downarrow\rangle$, $|\frac{3}{2}, \uparrow\rangle$, $|\frac{3}{2}, \downarrow\rangle$, where the first index is the magnetic number of the hole state and the second one is the electron spin state in the \hat{z} basis. Neglecting the cubic term in the exchange interaction, H_{exch} reads [Chen1988, Maiale1993]:

$$\frac{3}{4} \frac{\Delta E_{\text{SR}}}{|\phi^{3\text{D}}(0)|^2} \begin{pmatrix} 0 & 0 & 0 & 0 & 0 & 0 & 0 & 0 \\ 0 & I_{hh} & -\frac{I_{hl}}{\sqrt{3}} & 0 & 0 & 0 & 0 & 0 \\ 0 & -\frac{I_{hl}}{\sqrt{3}} & \frac{I_{ll}}{3} & 0 & 0 & 0 & 0 & 0 \\ 0 & 0 & 0 & \frac{2I_{ll}}{3} & -\frac{2I_{ll}}{3} & 0 & 0 & 0 \\ 0 & 0 & 0 & -\frac{2I_{ll}}{3} & \frac{2I_{ll}}{3} & 0 & 0 & 0 \\ 0 & 0 & 0 & 0 & 0 & \frac{I_{ll}}{3} & -\frac{I_{hl}}{\sqrt{3}} & 0 \\ 0 & 0 & 0 & 0 & 0 & -\frac{I_{hl}}{\sqrt{3}} & I_{hh} & 0 \\ 0 & 0 & 0 & 0 & 0 & 0 & 0 & 0 \end{pmatrix}$$

where ΔE_{SR} is the short range exchange splitting in the bulk semiconductor [Maiale1993], $\phi^{3\text{D}}(0)$ is the 3D hydrogenic exciton wave function at zero relative distance, $I_{jj'}$ is a form factor defined by:

$$I_{j'j} = \phi_{1s(j')}(0)\phi_{1s(j)}(0) \int dz |\xi_{1c}(z)|^2 \xi_{1j'h}(z)\xi_{1jh}(z), \quad (3.23)$$

where ϕ_{1s} are the 2D envelope wave-functions of the considered excitons, and ξ_{1c} (ξ_{1jh}) is the conduction envelope wavefunction along the growth axis in the conduction (respectively heavy, or light hole) subband.

Finally, H_{PB} is the Pikus-Bir deformation Hamiltonian given by [Bir&Pikus]:

$$\begin{aligned} H_{\text{PB}} = & a_v(\epsilon_{xx} + \epsilon_{yy} + \epsilon_{zz}) + b[(J_x^{h2} - J^{h2}/3)\epsilon_{xx} + \text{c.p.}] \\ & + \frac{2d}{\sqrt{3}}[\frac{1}{2}(J_x^h J_y^h + J_y^h J_x^h)\epsilon_{xy} + \text{c.p.}], \end{aligned}$$

where a_v , b and d are deformation potentials, ϵ_{ij} are the strain tensor components of the GaAs quantum well material (0), and c.p. stands for cyclic permutations of x , y and z .

Before diagonalizing this Hamiltonian, we first recall that only states with a total magnetic number ± 1 are optically active due to optical selection rules (see Subsection 1.1.1.4). Moreover, bright and dark excitons are not mixed either by the

exchange interaction or the Pikus Bir deformation Hamiltonian since shear is absent. We can consequently restrict ourselves to the bright exciton subspace $\left(\left| \frac{3}{2}, \downarrow \right\rangle, \left| \frac{1}{2}, \uparrow \right\rangle, \left| -\frac{1}{2}, \downarrow \right\rangle, \left| -\frac{3}{2}, \uparrow \right\rangle \right)$ where the total Hamiltonian takes the following form in the axial approximation [?]:

$$\frac{1}{2} \begin{pmatrix} -A & -B & C & 0 \\ -B & A & 0 & C \\ C & 0 & A & -B \\ 0 & C & -B & -A \end{pmatrix},$$

with

$$\begin{aligned} A &= \Delta E + b\epsilon + \left(\frac{I_{ll}}{3} - I_{hh} \right) \frac{3}{4} \frac{\Delta E_{SR}}{|\phi^{3D}(0)|^2} \\ B &= \frac{2}{\sqrt{3}} I_{hl} \frac{3}{4} \frac{\Delta E_{SR}}{|\phi^{3D}(0)|^2} \\ C &= \sqrt{3} b\epsilon. \end{aligned}$$

The symmetry of this Hamiltonian allows to again reduce the dimensionality of the problem by considering the linearly polarized basis $|H, X\rangle, |L, X\rangle, |H, Y\rangle, |L, Y\rangle$. In this basis, the Hamiltonian can be written:

$$\frac{1}{2} \begin{pmatrix} -A & C-B & 0 & 0 \\ C-B & A & 0 & 0 \\ 0 & 0 & -A & -B-C \\ 0 & 0 & -B-C & A \end{pmatrix}, \quad (3.24)$$

and the linearly polarized states are defined as

$$\begin{aligned} |H, X/Y\rangle &= \left| -\frac{3}{2}, \uparrow \right\rangle \pm \left| \frac{3}{2}, \downarrow \right\rangle \\ |L, X/Y\rangle &= \left| \frac{1}{2}, \uparrow \right\rangle \pm \left| -\frac{1}{2}, \downarrow \right\rangle \end{aligned}$$

The eigenstates of those two subsystems correspond to linearly-polarized, mainly heavy-hole excitons ($|H_B, X\rangle$ and $|H_B, Y\rangle$) and linearly-polarized, mainly light-hole excitons ($|L_B, X\rangle$ and $|L_B, Y\rangle$).

We are interested in the mainly heavy-hole excitons which give rise to the polaritons. Their splitting is:

$$\delta E_x \simeq \frac{BC}{A} = \frac{I_{hl} \frac{3}{2} \frac{\Delta E_{SR}}{|\phi^{3D}(0)|^2} b\epsilon}{\Delta E + b\epsilon + \left(\frac{I_{ll}}{3} - I_{hh} \right) \frac{3}{4} \frac{\Delta E_{SR}}{|\phi^{3D}(0)|^2}}.$$

I_{hl} value is found to be $1.18 \times 10^{-3} \text{ nm}^{-3}$ using eq. (3.23). I_{ll} and I_{hh} have similar values $1.12 \times 10^{-3} \text{ nm}^{-3}$ and $1.26 \times 10^{-3} \text{ nm}^{-3}$. $1/|\phi^{3D}(0)|^2 = \pi a_0^{*3} \simeq 9518 \text{ nm}^3$, where a_0^* is the 3D Bohr radius of the GaAs exciton. The deformation potential b is -1.7 eV for GaAs [Adachi1985]. Finally, following [Gilleo1968], we take $\Delta E_{SR} = 0.37 \text{ meV}$. Using these values, δE_x reaches -0.38 meV , compatible with the experimentally inferred value of $-0.54 \pm 0.18 \text{ meV}$.

Note that experimental determination of the short range exchange energy is difficult and experimental values span from 0.02 meV according to Ekardt et al. [Ekardt1979] to 0.37 meV according to Gilleo et al. [Gilleo1968] (see [Chen1988] for a more detailed discussion). However, more direct experimental determinations [Blackwood1994, Amand1997] seem to converge towards a value around $\simeq 100 \mu\text{eV}$.

Inversely, the experimental determination of δE_x obtained in this work can be used to calibrate the bulk short range exchange energy, which would be estimated at $0.50 \pm 0.20 \text{ meV}$.

3.3.3.4 Influence of strain on the light-matter coupling

In this subsection, we evaluate the theoretical strength of the third contribution $\delta\Omega_R$.

Going back to the hamiltonian (3.24), we now express its full (unnormalized) eigenstates at the lowest order in $(B + C)^2/A^2$:

$$|E_B, X/Y\rangle = 2A |H, X/Y\rangle - (C \mp B) |L, X/Y\rangle \quad (3.25)$$

The electric dipole transition $D_{hh/lh}$ for each state is related to the matrix element $\langle H/L, X/Y | \mathbf{p} \cdot \mathbf{A} | \emptyset \rangle$ (see Subsection 1.1.1.4) by [Fishman]:

$$\begin{aligned} \langle H, X | \mathbf{p} \cdot \mathbf{A} | \emptyset \rangle &= D_{hh} \\ \langle H, Y | \mathbf{p} \cdot \mathbf{A} | \emptyset \rangle &= iD_{hh} \\ \langle L, X | \mathbf{p} \cdot \mathbf{A} | \emptyset \rangle &= D_{lh} \\ \langle L, Y | \mathbf{p} \cdot \mathbf{A} | \emptyset \rangle &= -iD_{lh} \end{aligned}$$

The Rabi splitting reads:

$$\begin{aligned} \Omega_R^X &= K |\langle E_B, X | \mathbf{p} \cdot \mathbf{A} | \emptyset \rangle| = K |2AD_{hh} - (C - B)D_{lh}| \\ \Omega_R^Y &= K |\langle E_B, Y | \mathbf{p} \cdot \mathbf{A} | \emptyset \rangle| = K |2AiD_{hh} + i(C - B)D_{lh}| \end{aligned}$$

where K is a common positive constant incorporating the envelope wave-function contribution and the cavity characteristics. The Rabi polarization splitting obtained is

$$\delta\Omega_R \simeq 2\Omega_R C \frac{1}{2 \frac{D_{hh}}{D_{lh}} A - B},$$

where the heavy-hole light-hole exciton dipolar transition ratio $D_{hh}/D_{lh} \sim \sqrt{3}$ is mainly determined by the Clebsch-Gordan coefficients for the heavy- and light-hole composition (while form factors only result in a few percent correction).

As observed from this result, the polarization Rabi splitting does not involve exchange interaction. We also note that the light exciton fraction is almost equal in both eigenstates (3.25) such that $\delta\Omega_R$ does not result from the heavy hole-light hole mixing [Balili2010] but rather from the interference between the light exciton and heavy exciton dipoles.

For the 5 μm -wide wires $\Omega_R \simeq 8 \text{ meV}$, so that $\delta\Omega_R$ is expected to reach -0.5 meV relatively close from the inferred experimental value $\delta\Omega_R = -1.55 \pm 0.12 \text{ meV}$.

3.3.3.5 Conclusion

The presence of a $j = 0$ polarization splitting is therefore consistently explained by the anisotropic relaxation of lattice-mismatch induced constraints. The stress relaxation on a short lengthscale on the short axis of the wire induces a dilatation $\epsilon \simeq 850 \text{ ppm}$ of the lattice parameter, whereas the stress is conserved on the long axis, such that the lattice parameter is fixed by the bulk GaAs unit cell.

This anisotropic stress relaxation leads to birefringence in the Bragg mirrors, accounting for a photonic contribution in δE_{pol} . The presence of a strain ϵ also leads to the emergence of the excitonic and Rabi contributions, through a Pikus-Bir deformation effect. The order of magnitude found for these three contributions by calculation is compatible with their experimental inferred values, obtained by fitting the total polarization splitting variation with exciton-photon detuning.

In the next Subsection, we comment on the magnitude of the splitting for modes $j > 0$.

3.3.4 Anisotropic mode confinement

In this subsection, we focus on the polarization splittings observed for lateral modes $j > 0$. We have seen that these polarization splittings can reach a large magnitude (see for instance Figs. 3.5 or 3.8), beyond the maximal splitting of the $j = 0$ mode.

Figure 3.18 shows the polarization splitting δE_{pol} for the lateral modes $j = 0, 1, \text{ and } 2$ for various wire widths.

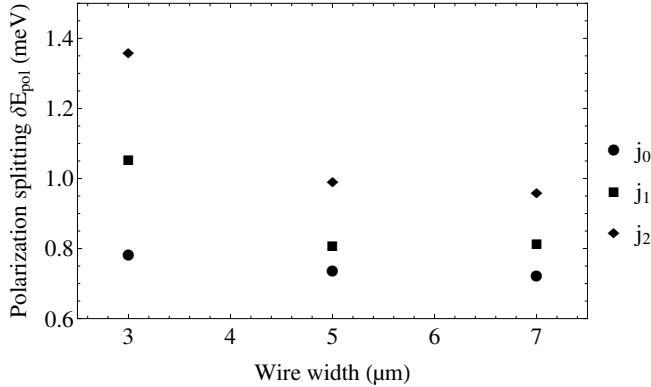


Figure 3.18: Polarization splitting δE_{pol} for wire widths $W = 3, 5,$ and $7 \mu\text{m}$ and for lateral modes $j_0, j_1,$ and j_2 . Measures are done for a reference exciton-photon detuning of the j_0 lateral mode about -13 meV . Note that the effective exciton-photon detuning varies with the lateral mode index for a fixed wire width.

The polarization splitting is larger for narrow wires and large j . The largest polarization splitting observed is -1.36 meV for j_2 and $W = 3 \mu\text{m}$, while the maximum value for j_0 with the same wire at null detuning is $\simeq -0.95 \text{ meV}$ (see Fig. 3.7).

These observations imply that the lateral 1D confinement produces an additional polarization splitting for the modes $j > 0$ with an order of magnitude of -0.4 meV .

We provide here an interpretation of this observation. The confinement along X induces an effective angle incident along X (see Subsection 1.3.3): $\sin \theta_{\text{eff}} = \frac{\hbar c \pi (j+1)}{W n_c E_0^c}$, where E_0^c is the cavity mode energy, W the wire width and j the cavity mode index. For $3 \mu\text{m}$ -wide wires, this angle varies from 2.5° for the cavity ground state ($j = 0$) to 7.5° for the mode $j = 2$.

This effective intracavity angle results in an additional polarization splitting in the cavity mode [Panzarini1999]:

$$\delta E_c^{\text{conf}}(\theta_{\text{eff}}) \simeq \frac{L_c L_{\text{DBR}}(0)}{L_{\text{eff}}^2(0)} \cdot \frac{2 \cos \theta_{\text{eff}} \sin^2 \theta_{\text{eff}}}{1 - 2 \sin^2 \theta_{\text{eff}}} (E_0^{\text{DBR}}(0) - E_0^{\text{cav}}(0)),$$

where E_0^{DBR} is the energy of the center of the stopband, E_0^{cav} the energy defined by the thickness of the intracavity spacer, $L_{\text{eff}}^{\text{TE/TM}}(\theta)$ is the effective cavity length ($L_{\text{eff}}^{\text{TE/TM}}(\theta) = L_c + L_{\text{DBR}}^{\text{TE/TM}}(\theta)$), $\theta_c = \sin^{-1}(\frac{1}{n_c} \sin \theta) = \theta_{\text{eff}}$ is the angle inside the cavity spacer layer, θ being the angle of the incoming field in the air. The sign and magnitude of this contribution is very sensitive to the term $E_0^{\text{DBR}}(0) - E_0^{\text{cav}}(0)$. A calculation using the formulas of eq. 3.22 gives a value of -126 meV for $E_0^{\text{DBR}}(0) - E_0^{\text{cav}}(0)$, which results in a photonic splitting contribution of approximately -0.46 meV for the worst case scenario considered here ($j = 2$ and $W = 3 \mu\text{m}$). This order of magnitude is comparable to our observation. However, the negative

sign should result in a reduction instead of an increase of the total polarization splitting which, close to null detuning, is approximately equal to $\frac{1}{2}(\delta E_x + \delta E_c) - 2\delta\Omega_R$ (see eq. 3.4). However, we stress that the calculation of $E_0^{\text{DBR}}(0) - E_0^{\text{cav}}(0)$ is obtained using parameters defined by transfer-matrix simulation (especially L_c the intracavity spacer thickness, which is essential for the calculation of $E_0^{\text{cav}}(0)$) and not from measurements on the sample grown by MBE. Taking into account the real parameters might reduce the real value of the photonic contribution or even change its sign.

On the other hand, this effective angle also affects the couplings between the cavity modes TE (\parallel) and TM (\perp), and the excitonic mode [Panzarini1999] which read:

$$\begin{aligned}\Omega^{\text{TE}}(\theta) &= \Omega \sqrt{\frac{L_{\text{eff}}(0)}{L_{\text{eff}}^{\text{TE}}(\theta)}} \frac{1}{\cos \theta_c}, \\ \Omega^{\text{TM}}(\theta) &= \Omega \sqrt{\frac{L_{\text{eff}}(0)}{L_{\text{eff}}^{\text{TM}}(\theta)}},\end{aligned}$$

This polarization splitting is negligible for the j_0 lateral mode, but significant for $j > 1$: we find $\delta\Omega_R^{\text{conf}} = -0.2 \text{ meV}$ for the mode $j = 2$ confined in the $3 \mu\text{m}$ -wide wire. This contribution is consistent with the -0.4 meV observed experimentally.

3.4 Discussion and conclusion

According to our experimental calibration, the polarization splitting arising in 1D-microcavities for the ground state $j = 0$ results from three contributions:

$$\text{A photonic contribution: } \delta E_c^{\text{exp}} = -0.73 \text{ meV} \pm 0.07 \text{ meV}$$

$$\text{An excitonic contribution: } \delta E_x^{\text{exp}} = -0.54 \text{ meV} \pm 0.18 \text{ meV}$$

$$\text{A Rabi contribution: } \delta\Omega_R^{\text{exp}} = -1.55 \text{ meV} \pm 0.12 \text{ meV}$$

The resulting polarization splitting δE_{pol} exhibits a universal law as a function of exciton-detuning, independent of the wire width and the sticking conditions on the sample holder.

These three polarization splittings are interpreted as a result of lattice-mismatches induced strain. The constraints induces a birefringence in the structure. Additionally, the induced Pikus-Bir interaction enlarges the excitonic fine structure and produces a polarization splitting in the light-matter interaction. We find:

$$\begin{aligned}\delta E_c^{\text{theo}} &= -0.1 \text{ meV} \\ \delta E_x^{\text{theo}} &= -0.4 \text{ meV} \\ \delta\Omega_R^{\text{theo}} &= -0.5 \text{ meV}\end{aligned}$$

The orders of magnitude of each contribution are compatible with the experimental findings. The underestimation of δE^c is probably due to the use of extrapolated room temperature photoelastic coefficients for the DBR materials. As for the excitonic and Rabi splittings, the discrepancy may come from the poor estimation of the light hole-heavy hole exciton energy splitting which is extremely sensitive to both composition and size of the quantum wells.

These contributions have been independently identified in previous works in various contexts: in Ref. [Dasbach2005,Diederichs2007], a splitting of $\delta E_{\text{pol}} = -280 \mu\text{eV}$ is reported in $5 \mu\text{m}$ -wide wires. It is attributed to a small birefringence induced by thermal stress responsible for the energy splitting δE_c of the photonic modes. In Ref. [Dasbach2002], a splitting of $-130 \mu\text{eV}$ is reported in $3 \mu\text{m}$ -wide wires and attributed to a small excitonic polarization splitting δE_x . The polarization splitting values reported in both studies [Dasbach2005, Dasbach2002] have been obtained while ignoring a possible Rabi polarization splitting. A posteriori, this is partly justified because

1. the samples used in both works were etched from the same microcavity which had a Rabi energy $2\Omega_R = 3.8 \text{ meV}$, whereas, in this work, a Rabi energy of $16.6 \pm 0.4 \text{ meV}$ has been measured.
2. the wire etching in both works was done down to a layer located just below the QW, such that the strain release induced by etching was moderate due to the nearby influence of the bulk material. While the orders of magnitude reported in both papers are compatible with the ones reported in this work, a quantitative comparison is made difficult because of the critical dependence of the polarization splitting values with sample composition and etching depth, which are different from our sample (both samples used in the cited references were based on InGaAs ternary alloys whereas the sample studied in this work is made of AlGaAs ternary alloys).

The Rabi contribution has been identified in Ref. [Balili2010] where an external stress is applied to a 2D microcavity by using a tip. This results in a heavy hole-light hole mixing of the excitonic states. The mixed excitonic states (polarized respectively perpendicular and parallel to the wire axis) have different oscillator strengths and give rise to the polarization Rabi splitting $\delta\Omega_R$. In Ref. [Balili2010], the resulting splitting reached up to $700 \mu\text{eV}$ but it can hardly be compared to the present study (1.55 meV) due to the different origin of the strain.

For modes $j > 0$, in addition to these various sources of polarization splitting, the 1D-confinement induces an extra splitting, which goes beyond the highest total polarization splitting for the $j = 0$ mode (1 meV). Indeed, the presence of a non-vanishing confinement angle θ_{eff} results in an effective TE-TM splitting on the cavity modes and exciton-photon coupling at normal incidence.

Fig. 3.19 summarizes the contribution to the total polarization splitting and their various origins.

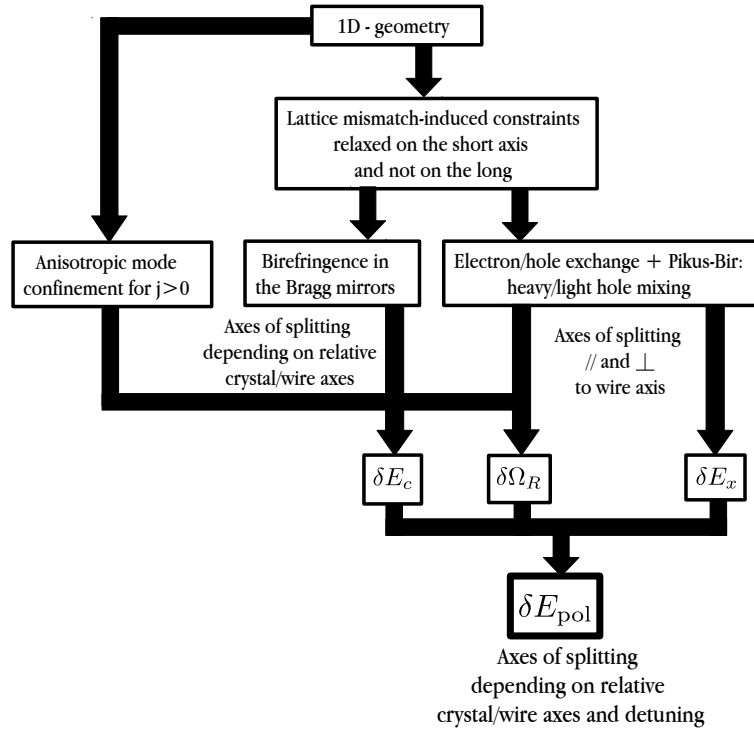


Figure 3.19: Origins of the polarization splitting in microwires

This comprehensive understanding allows to envision an engineering of this splitting magnitude, sign and orientation. The available degrees of freedom are numerous: exciton-photon detuning, wire height, DBR materials, etching axis compared to the crystalline axes and mode symmetry. In the perspective of integrated polaritonics [Liew2008, Espinosa-Ortega2013], the essential building block will consist in microcavity etched optical guides (see [Nguyen2013, Marsault2015] for example). The rotation induced on the polariton pseudo-spin by the 1D-confinement and the induced stress could be used to influence the performances of such devices. For example, in Ref. [Sturm2014], this splitting is exploited to allow a control of the flow of polaritons at the output of a cavity Mach-Zender interferometer. In Refs. [Abbarchi2011, Ardizzone2012], optical parametric oscillation processes are demonstrated using cross-polarized polariton branches in a 1D-microcavity.

Furthermore, more complex microcavity geometries are currently under study such as honeycomb lattices [Nalitov2015, Milićević2015]. In such samples, localized edge states, potentially topologically protected, are confined and also exhibit a longitudinal-transverse splitting that could be interpreted based on the model detailed in this chapter.

In summary, the work presented here could be exploited to interpret and predict the features of polariton propagation in microcavities with reduced dimensionality. The microcavities can be now specifically designed so as to get the required magnitude, sign and orientation of the splitting.

4

SPIN-DEPENDENT NONLINEAR EFFECTS IN A DOUBLE MICROCAVITY

Multiple microcavities are ideal to study interactions between polaritons since phonon-assisted relaxations towards the excitonic reservoir are nearly suppressed for the modes located on the lower polariton branches (two in our case here). In this chapter, we study various nonlinear spin-dependant interactions between polaritons, using the formalism presented in Chapter 1. This chapter is divided in three parts, which correspond to three different scattering regimes under a normally-incident resonant pumping.

First, we demonstrate an all-optical control of the Optical Spin Hall Effect (an anisotropic polarization-dependent polariton propagation) by tuning the pump power. At larger pump powers and low cavity-exciton detuning, strong nonlinear processes occur leading to the appearance of patterns in the far field cross-polarized to the linear polarization of the pump beam. This is the topic of interest in Section 4.4. This regime corresponds to an energy-degenerate Optical Parametric Oscillation (OPO), where two pump polaritons are converted into two off-axis polaritons and vice-versa. The comprehensive understanding of the mechanism leading to the formation of patterns and their orientation is crucial in light of future applications applications such as all-optical switches or “lighthouse” devices.

The intermediate regime of parametric scattering (or parametric amplification) detailed in Section 4.3 is a unique laboratory to investigate nonlinearities involved in pattern formation and orientation. In particular, it allows to probe the interplay between the TE-TM splitting and spin-dependent polariton-polariton interactions by pump-probe(s) experiments.

In the first section, we start by introducing the microcavity of interest.

Chapter content

4.1	The double microcavity sample	117
4.1.1	Context	117
4.1.2	Description	117
4.1.3	Characterization	118
4.1.3.1	Calibrations using the anticrossing curve	118

CHAPTER 4. SPIN-DEPENDENT NONLINEAR EFFECTS IN A DOUBLE MICROCAVITY

4.1.3.2	TE-TM splitting at large in-plane wavevector	120
4.1.3.3	Built-in normal energy splitting	120
4.1.4	Scattering processes	122
4.2	Spin- and power-dependent elastic Rayleigh scattering	124
4.2.1	Experiment: influence of the optical pump power	125
4.2.1.1	Experimental setup	125
4.2.1.2	Analysis method	127
4.2.1.3	Results for various polarization configurations	129
4.2.1.4	Power-dependent OSHE	131
4.2.2	Theoretical description	132
4.2.2.1	Analytical approximate description	133
4.2.2.2	Simulations for a finite pump spot size	135
4.2.2.3	Discussion	137
4.2.3	Influence of other experimental parameters	137
4.2.3.1	Pump resonance with LPB ₂	138
4.2.3.2	Exciton-photon detuning influence	139
4.2.4	Conclusion	140
4.3	Spin-dependent parametric scattering	141
4.3.1	First order four-wave mixing	143
4.3.1.1	Experimental setup	143
4.3.1.2	Experimental results	144
4.3.1.3	Discussion	147
4.3.1.4	Theoretical description	148
4.3.2	Second order four-wave mixing	150
4.3.2.1	Experimental setup	150
4.3.2.2	Experimental and numerical results	152
4.3.3	Conclusion	153
4.4	Pattern formation in the Optical Parametric Oscillation regime	154
4.4.1	Key experimental parameters	156
4.4.1.1	Influence of the exciton-photon detuning	157
4.4.1.2	Effect of a small pump tilt and resonant energy	158
4.4.1.3	Influence of the incident power	160
4.4.1.4	Orientation of patterns with polarization	161
4.4.1.5	Nature of the excitation source	165
4.4.1.6	Conclusion	166
4.4.2	Hexagonal pattern properties	166
4.4.2.1	Observation in the real space	167
4.4.2.2	Presence of a small energy non-degeneracy	168
4.4.3	Perspectives for further studies on the patterns	169
4.5	Conclusion	170

4.1 The double microcavity sample

4.1.1 Context

Our group at LPA was a pioneer for the design and study of multiple microcavities in the Optical Parametric Oscillation regime (OPO). Interbranch OPO was observed in a triple microcavity [Diederichs2007], in a configuration involving polariton modes at the same energy but with opposite in-plane wavevectors (the so-called “horizontal” process), and in a configuration at $k_{\parallel} = 0$ but with different energies (the so-called “vertical” process) [Diederichs2007]. Previous demonstrations of the OPO in single microcavities preferred to use the so-called “Magic angle” (near the inflexion point of the polariton dispersion) [Stevenson2000, Savvidis2000]. However, the “horizontal” parametric process is a unique tool to probe the quantum correlations between the off-axis polaritons, since both states have the same exciton-photon detuning (since they are energy-degenerate and have opposite in-plane wavevectors).

Experiments involving intensity noise measurements [Diederichs2007, Lecomte2011] and Hanbury and Twiss (HBT) setups with pulse laser excitation [Ardizzone2013a] with various detectors have been conducted on triple, double and 1D-microcavities. The conclusion to those experiments was that (i) the inherent optical losses are a strong limitation to observe intensity correlations [Lecomte2011] and (ii) the quantum correlations are enhanced for weak photon fluxes [Ardizzone2013a], which is hardly compatible with the OPO regime arising at large pump powers.

The present sample was designed by Timothée Lecomte in 2011 and grown by Aristide Lemaître at the Laboratoire de Photonique et Nanostructures. Thanks to the improvement of the growth techniques, it is much less disordered than the multiple microcavities previously studied in our group [Ardizzone2013a]. The use of GaAs instead of InGaAs for the QW material also diminishes the density of defects since the lattice mismatch with the AlGaAs barrier is reduced. Finally, a larger number of DBRs and of QWs were introduced so as to maximize the light-matter coupling.

The initial goal of this improved sample was to observe the generation of twin polaritons. However, no classic nor quantum correlation measurements are presented in this chapter for several reasons:

1. I have mainly studied the OPO regime under cw MIRA excitation. The MIRA laser intensity fluctuations in the cw mode presented in Subsection 2.1.4 prevent any reliable HBT measurements.
2. No degenerate OPO process was achieved with the monomode Solstis excitation (see Subsection 4.4.1.5).

4.1.2 Description

The sample of interest in this chapter is composed of two superimposed microcavities: two coupled $\lambda/2$ $\text{Ga}_{0.05}\text{Al}_{0.95}\text{As}$ cavities embedded between three DBRs com-

posed by $\text{Ga}_{0.05}\text{Al}_{0.95}\text{As}$ and $\text{Ga}_{0.8}\text{Al}_{0.2}\text{As}$ with 25 (back), 17.5 (middle), and 17.5 (front) pairs respectively. The back mirror is thicker to ensure a better reflectivity of the total structure. The large number of DBR ensures a nominal Q factor around 10^5 [Ardizzone2013a]. The number of intermediate DBR pairs sets the cavity coupling (see Subsection 1.1.2.7). In each cavity 3 sets of four 7 nm GaAs quantum wells are inserted at the antinodes of the electric field. The detailed growthsheet of the sample is available in Appendix A3. A schematic of the sample structure is shown on Fig. 4.1.

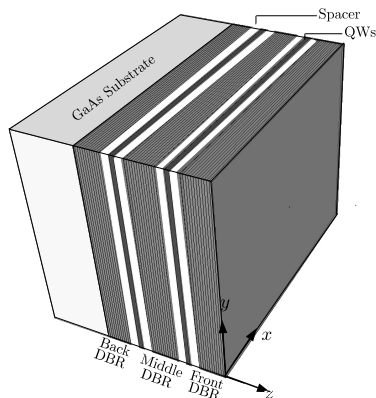


Figure 4.1: Schematic of the double microcavity (not at scale). The QWs inserted inside the first DBR pairs are not represented for simplicity's sake.

A full characterization of this double microcavity sample is available in Ref. [Ardizzone2013a]. Its main properties are presented in the next subsection.

4.1.3 Characterization

4.1.3.1 Calibrations using the anticrossing curve

Due to the presence of two coupled identical cavities containing the same number of quantum wells, the strong light-matter induces two upper and two lower polariton branches. Fig. 4.2.a. shows a typical dispersion curve obtained by photoluminescence, where only the two lower polariton branches (labelled LPB_1 and LPB_2) are visible. In this example, the pump is resonant with the minimum of LPB_2 .

The calibration of the main parameters (exciton energy, Rabi coupling, cavity-cavity coupling, exciton-photon detuning) is obtained by following the method presented Chapter 3. The precise energy minima of LPB_1 and LPB_2 can be obtained by fitting each branch with a fourth order polynomial curve (for more details on this choice of procedure, consult Appendix A1). Then, thanks to the linear wedge introduced during the growth of the sample, the anticrossing curve can be obtained by recording the energy minima of LPB_1 and LPB_2 at several positions on the sample (see Fig 4.2.b.). The points corresponding to the dispersion shown in Fig 4.2.a. are indicated in green in Fig 4.2.b.

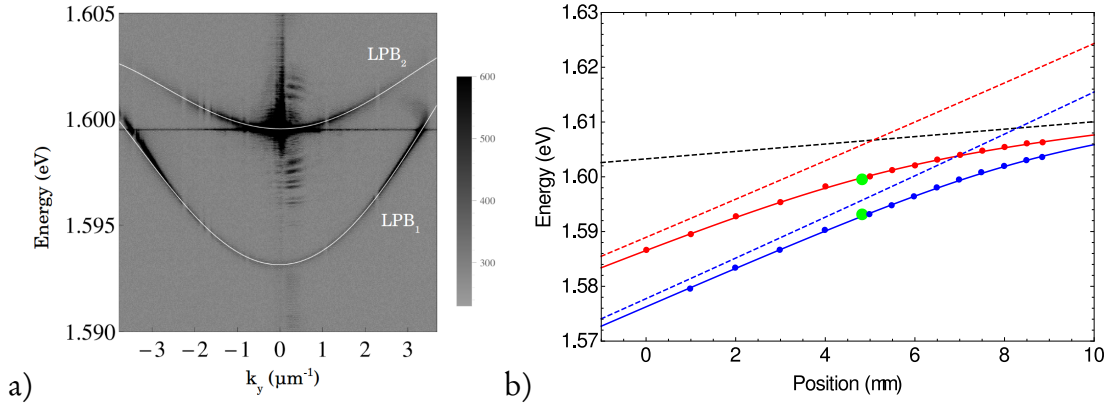


Figure 4.2: a) Typical energy dispersion as a function of k_y for the double microcavity. Only the two lower polaritons branches are visible (LPB_1 and LPB_2). The pump is resonant with the minimum of LPB_2 . The white lines correspond to a fourth order polynomial fit of the branches to obtain as precisely as possible the energy minima of LPB_1 and LPB_2 (*cf.* Appendix A1). b) Reproduced from [Ardizzone2013a]. Anticrossing curve obtained from photoluminescence spectra obtained at various spots onto the sample. The two green points correspond to the position of the energy minima of LPB_1 and LPB_2 branches of (a). The dashed black line corresponds to the exciton energy dependence on their position on the sample. Blue and red dashed lines correspond to the optical cavity modes' energies as a function of the position on the sample.

The energy dispersion (Fig. 4.2.a.) should allow to calibrate all the parameters of interest (exciton-photon detuning, cavity-cavity coupling, Rabi coupling, exciton energy). However, this method is not reliable since the states at large k cannot be determined with enough precision due to possible optical misalignments and spherical aberrations from the inverted telescope (see Chapter 2).

However, assuming a linearly varying wedge with position, the exciton energy and the cavity modes also evolve linearly with position. Therefore, the experimental points of Fig. 4.2.b. allow to calibrate the Rabi coupling, exciton energy, exciton-photon detuning and cavity-cavity coupling corresponding to the position of Fig. 4.2.a, using eq. (1.10). The cavity energy varies quasi linearly with position with a coefficient $3.6 \pm 0.1 \text{ meV}\cdot\text{mm}^{-1}$. Thus, we find:

	fit value	Standard error
Rabi coupling Ω_R	6.4 meV	0.8 meV
Exciton energy E_0^x	1.606 eV	3 meV
Cavity-cavity coupling Ω_c	5.1 meV	0.7 meV
Exciton-photon detuning Δ	-5.8 meV	3 meV

Table 4.1: Parameter values obtained from Fig. 4.2.b. for the dispersion shown in Fig. 4.2.a. using eq. (1.10).

4.1.3.2 TE-TM splitting at large in-plane wavevector

The TE-TM splitting is a well-known phenomenon arising in microcavities at large in-plane wavevector. A full theoretical explanation is given in Section 1.3.1. It consists in a k_{\parallel} -dependent energy splitting between TE and TM-polarized propagating polaritons, and results in different energy dispersion relations for TE and TM polarizations and thus in different effective cavity masses for TE and TM polaritons. The magnitude of m_{TE} and m_{TM} can be computed with a transfer-matrix calculation and we find $m_{\text{TE}}/m_{\text{TM}} \simeq 1.03$.

A polarization-resolved photoluminescence experiment allows to distinguish the two branches TE-TM as a function of k_y , and get an experimental value. We find $m_{\text{TE}}/m_{\text{TM}} \simeq 1.037 \pm 0.006$, which is in fair agreement with the theoretical value.

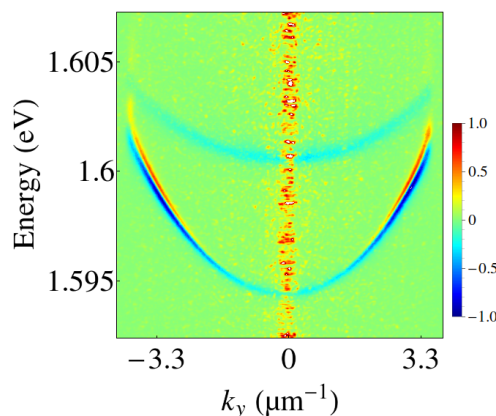


Figure 4.3: Superposition of TE (blue) and TM (red) polariton dispersions. The TE-TM splitting is well visible on the lowest polariton branch (LPB_1). The TE-TM splitting is hidden on LPB_2 due to its larger linewidth and the TM LPB_2 branch's smaller intensity.

Besides the anisotropic dispersion, the TE-TM splitting also induces anisotropic polaritonic losses γ_p between polarizations TE and TM [Panzarini1999]. The experimental calibration for $k_y = 3.3 \mu\text{m}^{-1}$ gives $\gamma_p^{\text{TM}}/\gamma_p^{\text{TE}} = 1.05$.

4.1.3.3 Built-in normal energy splitting

Besides the TE-TM splitting, a small polarization splitting has been observed at normal incidence. To probe this splitting, a reflectivity experiment is performed. The excitation laser is sent onto the sample at a fixed energy with either vertical and horizontal polarization (selected by the half-wave plate e, see Fig. 4.4.a.). Thanks to the wedge, the resonant energy can be varied simply by shifting the sample.

An analyzer is inserted in the detection path to cut the bare reflection of the excitation beam. At low power (5 mW), a drop in the reflectivity is clearly observed for both polarizations (see Fig. 4.4.b.), split by an energy $140 \mu\text{eV}$. This drop results

from the absorption of light when the laser is resonant with the polariton branch. At a larger power (50 mW), a peak is observed for both polarizations (see Fig. 4.4.c.). These peaks are probably due to the partial depolarization of the light reemitted by the microcavity at resonance. Note that, for the same position on the sample, the energies of the polariton branches are blueshifted at large powers next to the resonance due to Coulomb interactions and saturation of the light-matter coupling (*cf.* Subsection 1.2.2.4), effect which also partially reduces the observable splitting below $60 \mu\text{eV}$.

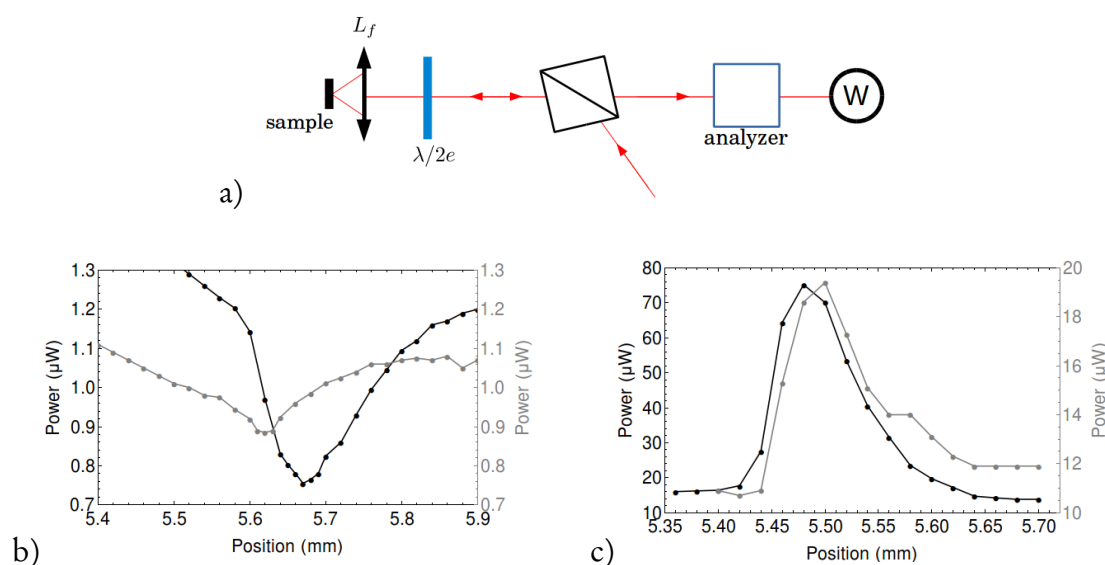


Figure 4.4: (a) Experimental scheme for the observation. (b) Reflectivity as a function of sample position for an excitation power of 5 mW. The position on the sample can be directly related to the polariton energy thanks to Fig. 4.2. Black: vertical polarization. Gray: horizontal polarization. (c) Idem for an excitation power of 50 mW.

These experimental results show that there is a built-in polarization-dependent normal energy splitting, whose order of magnitude is approximately $130 \mu\text{eV}$. Note that the polarization basis for this splitting is not necessarily the vertical and horizontal polarizations. Its origin may lay in the presence of a built-in stress in the structure.

This splitting is unobservable for pump powers larger than 50 mW, due to a polarization-anisotropic blueshift of the polariton branches, and can therefore be neglected for most applications.

However, this shows that the sample is not purely rotationally invariant, in accordance with the experimental observations that will be presented in Subsection 4.4.1.4.

4.1.4 Scattering processes

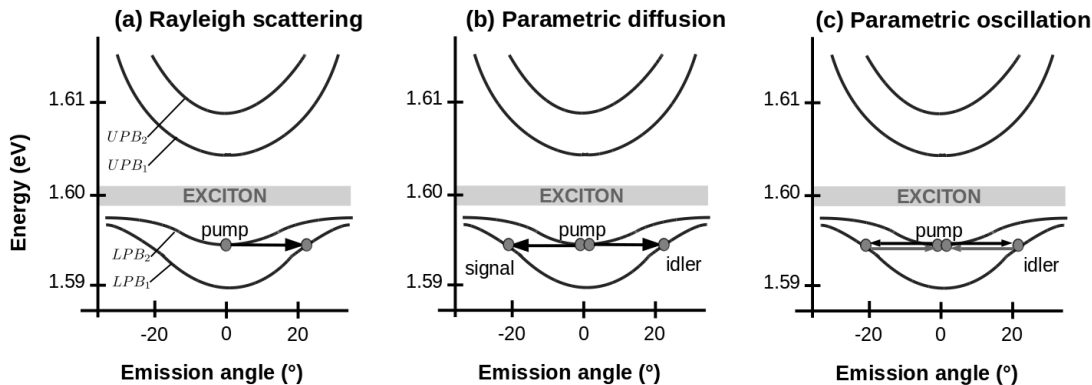


Figure 4.5: The three scattering regimes under a continuous normally incident excitation resonant with the energy minimum of LPB_2 . (a) Elastic Rayleigh scattering regime. (b) Optical parametric scattering regime. (c) Optical Parametric Oscillation regime.

The main experiments detailed in this chapter involve a normally incident pump resonant with the energy minimum of LPB_2 . Depending on the cavity-exciton detuning (which varies the polariton-polariton interaction strength) and the pumping power (which varies the polariton density), three scattering regimes are observed:

1. The linear regime of resonant elastic Rayleigh scattering. In this regime, the pump polaritons are elastically scattered due to the presence of defects and the cavity TE-TM splitting gives rise to the so-called Optical Spin Hall Effect. However, if the pumping is sufficiently strong, we will show that nonlinear interactions between pump polaritons induce a controllable shift of the Optical Spin Hall Effect. This will be the topic of interest of Section 4.2.
2. The Optical Parametric Scattering (or Amplification) regime. This regime is effective when the pumping and nonlinear interactions are sufficiently strong to induce a four-wave mixing process (FWM) initiated by a probe beam sent at oblique angle. We will study in detail the influence of pump/probe polarizations on the efficiency of this process in Section 4.3. A second-order four-wave mixing experiment, involving two probes in a hexagonal geometry in addition to the normally incident pump will be also studied (not shown on Fig. 4.5).
3. The Optical Parametric Oscillation (OPO) regime. In this regime, the nonlinear interactions are so important that the degenerate off-axis signals on LPB_1 become unstable above a certain threshold (the so-called “OPO threshold” or “instability threshold”). Pump as well as off-axis modes are further amplified

by Optical Parametric Oscillation. Due to spatial coupling terms, a pattern arises in the Fourier space (not shown on Fig. 4.5). The phenomenology of this pattern formation is complex and will be detailed in Section 4.4.

All those regimes have in common the scattering of pump polaritons towards off-axis modes at the same energy (*cf.* Fig. 4.5).

Formally, these processes are described by the following system of equations for the excitonic and cavity fields e and c , where third-order ($\chi^{(3)}$) interactions are taken into account [Solnyshkov2007]:

$$\begin{aligned} i\hbar \frac{de_{\mathbf{k}}^{i,\pm}}{dt} = & \overbrace{(E_{\mathbf{k}}^{x,i} - i\gamma_x^i)e_{\mathbf{k}}^{i,\pm}}^1 - \overbrace{\Omega_R c_{\mathbf{k}}^{i,\pm}}^2 \\ & + \sum_{\mathbf{k}'\mathbf{k}''} \overbrace{2\alpha_{\text{PSF}}\Omega_R e_{\mathbf{k}'}^{i,\pm*} e_{\mathbf{k}''}^{i,\pm} c_{\mathbf{k}'+\mathbf{k}''-\mathbf{k}}^{i,\pm}}^3 \\ & + \overbrace{T^{++} e_{\mathbf{k}'+\mathbf{k}''-\mathbf{k}}^{i,\pm*} e_{\mathbf{k}'}^{i,\pm} e_{\mathbf{k}''}^{i,\pm} + T^{+-} e_{\mathbf{k}'+\mathbf{k}''-\mathbf{k}}^{i,\pm*} e_{\mathbf{k}'}^{i,\pm} e_{\mathbf{k}''}^{i,\mp}}^4, \end{aligned} \quad (4.1)$$

$$i\hbar \frac{dc_{\mathbf{k}}^{i,\pm}}{dt} = \underbrace{(E_{\mathbf{k}}^{c,i} - i\gamma_c^i)c_{\mathbf{k}}^{i,\pm}}_{1'} - \underbrace{\Omega_R e_{\mathbf{k}}^{i,\pm}}_{2'} + \underbrace{\Delta_{\mathbf{k}}^{c,\pm} c_{\mathbf{k}}^{i,\pm}}_5 - \underbrace{\Omega_c E_{\mathbf{k}}^{j \neq i,\pm}}_6 + C_{\text{pump}}^{\pm}, \quad (4.2)$$

where

- \pm refers to left and right circular polarizations (or, equivalently, to polaritons with pseudo-spin ± 1),
- i, j refer to the cavity index (since the sample of interest is a double microcavity),
- terms (1) and (1') are the bare exciton and cavity dispersions,
- terms (2) and (2') correspond to the exciton-photon coupling,
- term (3) corresponds to the saturation of the exciton-photon coupling (fermionic phase-space filling α_{PSF} , see Subsection 1.2.2.4),
- term (4) includes the polarization-dependent exciton-exciton interactions T^{++} and T^{+-} in all scattering channels fulfilling the phase-matching conditions (*cf.* Subsection 1.3.4),
- term (5) includes the TE-TM splitting at large k_{\parallel} , which is here assumed to be a pure cavity effect (*cf.* Subsection 1.3.1 for more details). We have: $\Delta_{\mathbf{k}}^{c,\pm} = \frac{\hbar^4}{4} \left(\frac{1}{m_{\text{c}}^{\text{TM}}} - \frac{1}{m_{\text{c}}^{\text{TE}}} \right) (k_x \mp ik_y)^2$,

- term (6) includes the cavity-cavity coupling Ω_c .

An optical pump is included (C_{pump}^\pm).

In the pure elastic Rayleigh scattering regime, all nonlinear terms (3 and 4) are neglected. In the parametric scattering regime, only scattering of $\mathbf{k}_{\text{pump}} = \mathbf{0}$ pump polaritons towards $\mathbf{k}_{\text{signal}} = 2\mathbf{k}_{\text{pump}} - \mathbf{k}_{\text{probe}}$ (or $\mathbf{k}_{\text{signal}} = \mathbf{k}_{\text{pump}} - \mathbf{k}_{\text{probe1}} - \mathbf{k}_{\text{probe2}}$) are taken into account.

In the optical parametric regime (regime of pattern formation), all the terms of eq. (4.2) are taken into account.

4.2 Spin- and power-dependent elastic Rayleigh scattering

In this section we consider the regime where the polariton-polariton interactions are not intense enough to give rise to parametric effects. In the linear regime, a resonant elastic Rayleigh scattering takes place, and is the basis for the Optical Spin Hall Effect (OSHE) [Kavokin2005, Leyder2007] (*cf.* Subsection 1.3.1.2). This phenomenon consists in a spatial separation between “+” and “-” circularly polarized propagating polaritons, similarly to a pseudo-spin-orbit coupling. The effective magnetic field experienced by the propagating polaritons is solely induced by the cavity TE-TM splitting and is confined to the 2D plane in the pseudo-spin space.

No control over the OSHE has been experimentally demonstrated so far, though a theoretical article has recently suggested a control of the OSHE through the use of an external magnetic field [Morina2013]. On the other hand, experimental and theoretical works have shown evidence of the role of a spin-dependent blueshift in polariton condensates [Kammann2012, Cilibrizzi2015, Gao2015, Solnyshkov2015] and in the parametric regime [Shelykh2005, Glazov2005, Flayac2013].

In this chapter, we experimentally demonstrate an optical control over the OSHE. We show that the effective magnetic field can be finely tuned using a strong optical pump beam that induces spin-dependent blueshifts tilting the effective magnetic field vector out of the 2D plane [Renucci2005]. The originality of our approach lies in the fact that:

- The control of the OSHE is fully optical.
- The polariton-polariton spin-dependent interactions responsible for the spin-dependent blueshifts occur independently from other forms of nonlinearities such as parametric effects or condensate formation.

The first part of this section details the main experimental findings. The theoretical description is given in the second part. Finally, other experiments show that additional experimental parameters to the optical pump power must be taken into account to fully control the OSHE.

4.2.1 Experiment: influence of the optical pump power

The experiments presented in this section are similar to the historical one of Leyder *et al.* [Leyder2007]: a pump is sent on the microcavity and the polarization map resulting from the Rayleigh scattering of pump polaritons is analyzed. The main differences are:

1. The use of a double microcavity. The Rayleigh scattering regime can be obtained by pumping on LPB₂ at normal incidence rather than at oblique angle on LPB₁. This allows to spatially separate the pump-induced $k_{\parallel} = 0$ polaritons from the propagating polaritons and observe the full elastic circle in the Fourier space. Moreover, the elastic circle considered has a twice larger k_{\parallel} radius (or, equivalently, a larger angle of emission), such that the TE-TM splitting magnitude is larger.
2. The polarization setup. In Ref. [Leyder2007], the pump is linearly polarized and detection is set to observe the “+” and “-” circularly polarized emitted light from the sample. Here, we do the opposite: pumping with circular polarization and observe the “x” and “y” linearly polarized emitted light. The effect of the spin-dependent blueshifts is indeed more easily measurable in this configuration than in Leyder’s (a theoretical justification will be given in Subsection 4.2.2).

4.2.1.1 Experimental setup

The polarization-resolved far-field spectroscopy is obtained by imaging the Fourier plane of the detection objective on a cooled CCD camera. The pump beam is hidden by a spatial filter (see Fig. 4.6). We have checked that the circular polarization of the incoming pump was not affected by the reflection on the beam-splitter.

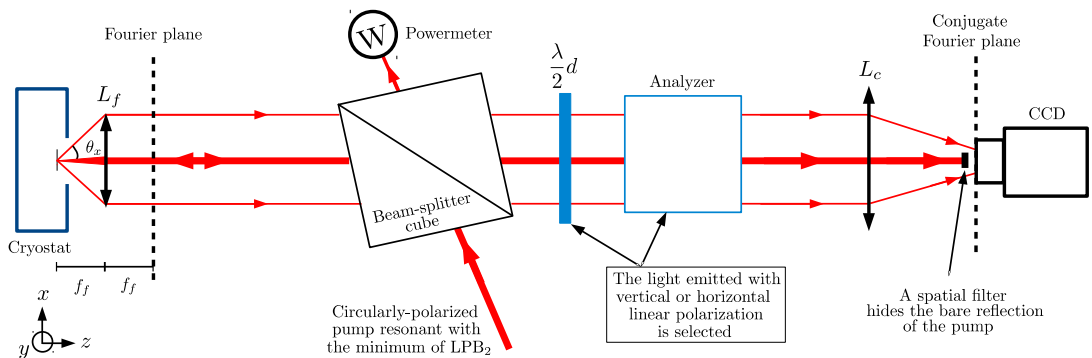


Figure 4.6: Experimental scheme for the observation of the controlled OSHE.

By rotating the half wave plate d , we can select the vertically-polarized (V), the horizontally-polarized (H), right diagonal (rD) and left diagonal (lD) light components of the Rayleigh-scattered polaritons (*cf.* paragraph 1.3.1.2) which evenly

populate the elastic circle in the momentum space. The expected “linear polarization map” (solely resulting from TE-TM splitting) is obtained by performing the operation $\frac{H-V}{H+V}$ under a “+” circularly polarized excitation and shown in Fig. 4.7.b. Note that an inner and outer elastic circle at slightly different in-plane wavevectors are present due to the TE-TM splitting (Fig. 4.7.a), resulting in a slight *polarization overlap* at 0° , 90° , 180° and 270° .

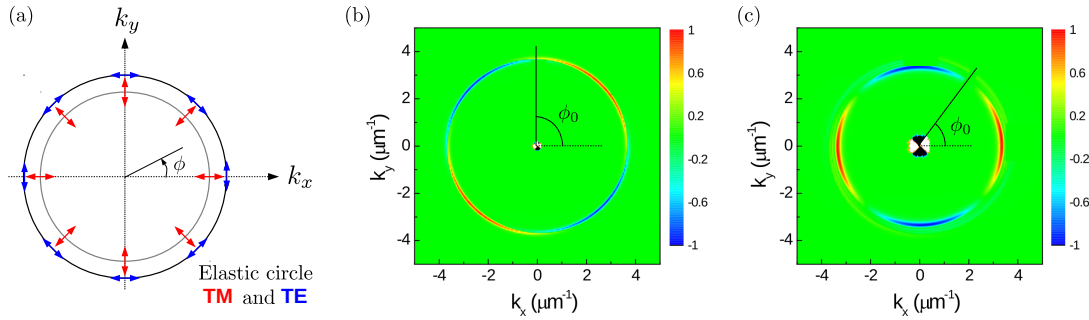


Figure 4.7: (a) TM (inner) and TE (outer) elastic circles. (b) Expected polarization map $\frac{H-V}{H+V}$ for a “+” circularly-polarized excitation in the purely linear regime. The degree of linear polarization along the elastic circle behaves as a sine curve, with its first zero occurring at $\phi_0 = \phi_0^{\text{lin}} = 90^\circ$. (c) With additional polariton-polariton spin-dependent interactions, the polarization map rotates clockwise such that now $\phi_0 < \phi_0^{\text{lin}}$.

Along the azimuthal angle ϕ (defined in Fig. 4.7.a.), the *degree of linear polarization* along the mean elastic circle evolves as a sine curve, $\sin(2\phi)$ in the purely linear regime (Fig. 4.7.b.). We will see in Subsection 4.2.2 that due to additional polariton-polariton spin-dependent interactions, the polarization map is expected to rotate clockwise (resp. anticlockwise) for a “+” or left (resp. “-” or right) circular polarization (Fig. 4.7.c.). To measure the rotation of the polarization map, we perform a precise analysis of the intensity and polarization as a function of ϕ . The rotation of the polarization map is translated into a phase offset ϕ_1 of the sine curve, such that the linear polarization degree along the mean elastic circle is now:

$$\sin(2\phi + \phi_1).$$

In all the experiments presented in this section, the effects of the polariton-polariton spin-dependent interactions will be measured by *the first zero of this function*, labelled ϕ_0 which is:

$$\phi_0 = \phi_0^{\text{lin}} - \frac{\phi_1}{2},$$

where $\phi_0^{\text{lin}} = 90^\circ$ is the value of ϕ_0 in the purely linear regime (*i.e.* polariton-polariton interactions negligible, or $\phi_1 = 0^\circ$).

4.2.1.2 Analysis method

In this subsection, the analysis method used to measure the orientation of the polarization map (the value of ϕ_0) is detailed.

Let us consider a normally-incident 14 mW “+” -circularly polarized excitation (equivalent to “+” circularly polarized), and detection in the channels H (Fig. 4.8.a.) and V (Fig. 4.8.b.).

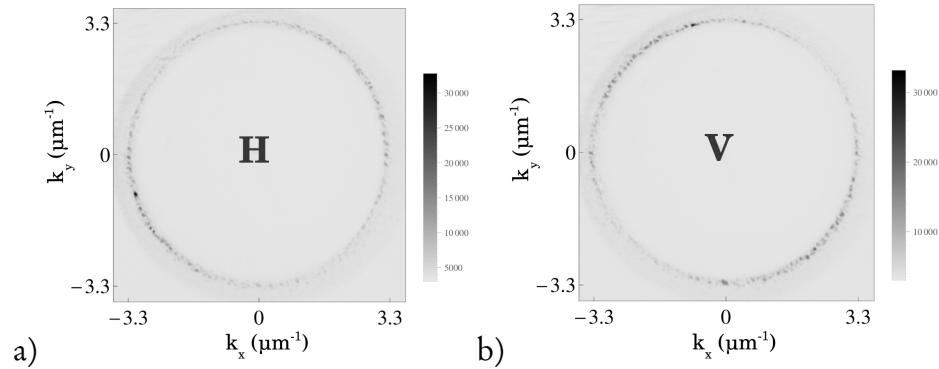


Figure 4.8: a) “+”-circular excitation, horizontally-polarized (H) channel in detection. b) “+”- circular excitation, vertically-polarized (V) channel in detection. The pump (located at the center) is hidden by a spatial filter.

The elastic circles in Fig. 4.8 are populated by Rayleigh scattering. The granularity observed along the elastic circle is a speckle effect due to the disorder in the Bragg mirrors. Additionally, dislocations or parametric scattering effects may create couples of points separated by 180° [Abbarchi2012]. The angular autocorrelation of the intensity along the elastic circle can be used to measure the efficiency of such processes (discussed later in Subsection 4.2.1.3).

The experimental linear polarization map can be directly obtained with the H and V acquisitions (Fig. 4.9).

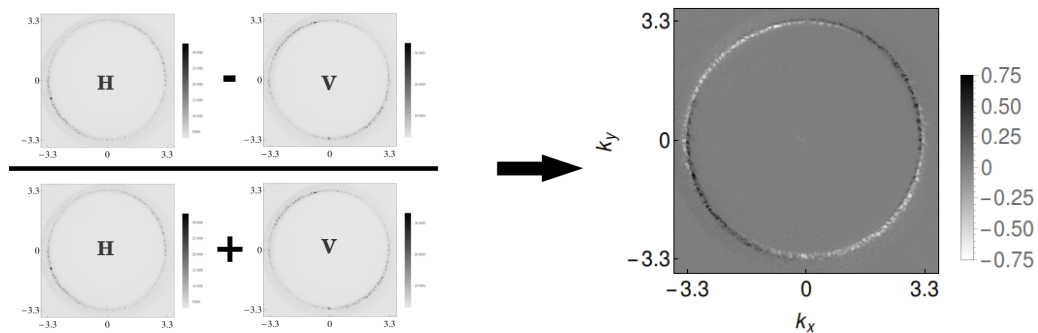


Figure 4.9: Example: Polarization map obtained with the operation $\frac{H-V}{H+V}$ with left-circularly polarized pumping.

A rotation of the polarization map may be directly observable to the naked eye. A *quantitative* measurement of this rotation is obtained by the following method:

1. V and H rings are flattened. (see Fig. 4.10).

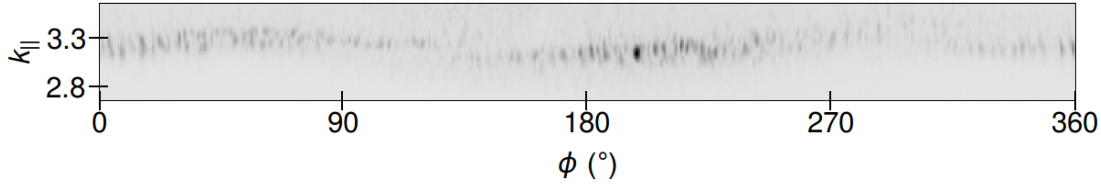


Figure 4.10: H acquisition after flattening.

2. Due to the TE-TM splitting, the result is not a flat line but varies between $k_{\parallel} \simeq 3.0 \mu\text{m}^{-1}$ and $k_{\parallel} \simeq 3.3 \mu\text{m}^{-1}$. Therefore, for each angle, we sum the intensities between a chosen k_1 and k_2 (here $2.54 \mu\text{m}^{-1}$ and $3.55 \mu\text{m}^{-1}$). Let's call V_1 (resp. H_1) the obtained data.
3. The degree of linear polarization $\frac{H_1 - V_1}{H_1 + V_1}$ is plotted as a function of the angle ϕ defined in Fig. 4.7.b. The plot is shown on Fig. 4.11, and follows, as expected, a sine curve.
4. The degree of linear polarization is fitted with the following function:

$$f(\phi) = a \sin(2\phi + \phi_1) + c \sin(\phi + \phi_2) + d \sin(4\phi + \phi_3) + b \quad (4.3)$$

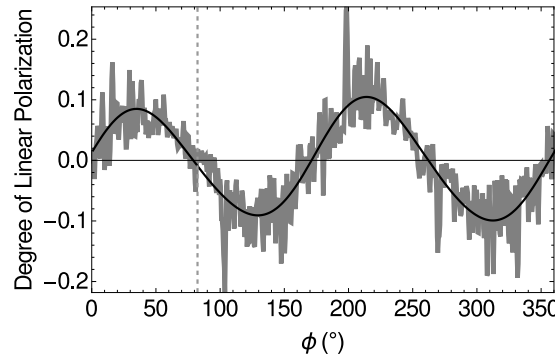


Figure 4.11: Degree of Linear Polarization as a function of ϕ of the momentum space integrated between $k_1 = 2.54 \mu\text{m}^{-1}$ and $k_2 = 3.55 \mu\text{m}^{-1}$. The fit using eq. (4.3) is in black. The vertical dashed line shows the position of ϕ_0 (the first zero of function $\sin(2\phi + \phi_1)$).

The first term is the main contribution, and others are corrections due to various causes such as excitation and detection polarization miscalibration, optical misalignment, or the presence of an additional polarization splitting due to built-in stresses in the structure (see Subsection 4.1.3.3).

As mentioned previously, the parameter chosen to measure the OSHE polarization pattern modification is $\phi_0 = \phi_0^{\text{lin}} - \frac{\phi_1}{2}$, where $\phi_0^{\text{lin}} = 90^\circ$.

In this example, the result of the fit is shown in Fig. 4.11. In this example, we get $\phi_0 = 82.4^\circ \pm 0.9^\circ$. The calculated error for ϕ_0 is a combination of the standard error for ϕ_1 obtained from the fit (4.3) and the autocorrelation length of the fit residuals (*cf.* Appendix A2 for details).

4.2.1.3 Results for various polarization configurations

To check of the effect of power on the degree of linear polarization, we performed several experiments in various polarization configurations for two values of power (labelled HP and LP in the following).

The pump can be switched between “+” and “-”-circular polarization. In this case, the polarization map resulting solely from TE-TM splitting is analogous to Fig. 4.7.b. with up and down reversed¹.

The detection can also be done in the right diagonal and left diagonal channels. In this case, the expected “diagonal linear polarization map”, obtained by performing $\frac{r_{\text{D-ID}}}{r_{\text{D+ID}}}$, is rotated by 45° compared to the one shown in Fig. 4.7.b. For this configuration, the analysis method described above is maintained, except that the phase in the purely linear regime is now $\phi_0^{\text{lin}} = 135^\circ$.

Fig. 4.12 shows the result of eight measurements of ϕ_0 in various excitation and detection configurations.

As already mentioned in Subsection 4.2.1.1, a “+”-circularly polarized excitation is expected to induce a shift to the left of the degree of linear polarization ($\Delta\phi_0 = \phi_0^{\text{HP}} - \phi_0^{\text{LP}}$ is negative) and for a “-”-circularly polarized excitation, the opposite ($\Delta\phi_0 > 0$). The same behaviour is expected for the degree of linear diagonal polarization.

The shift $\Delta\phi_0 = \phi_0^{\text{HP}} - \phi_0^{\text{LP}}$ produced by a strong pump behaves as such in all the various configurations of Fig. 4.12. This gives confidence in the interpretation that this shift is indeed due to the pump polaritons spin-dependent interactions and not induced by other nonlinear effects.

¹Thanks to this geometric transformation, experiments performed with a “-”-circularly polarized pump can easily be compared with simulations performed with a “+”-circularly polarized pump term.

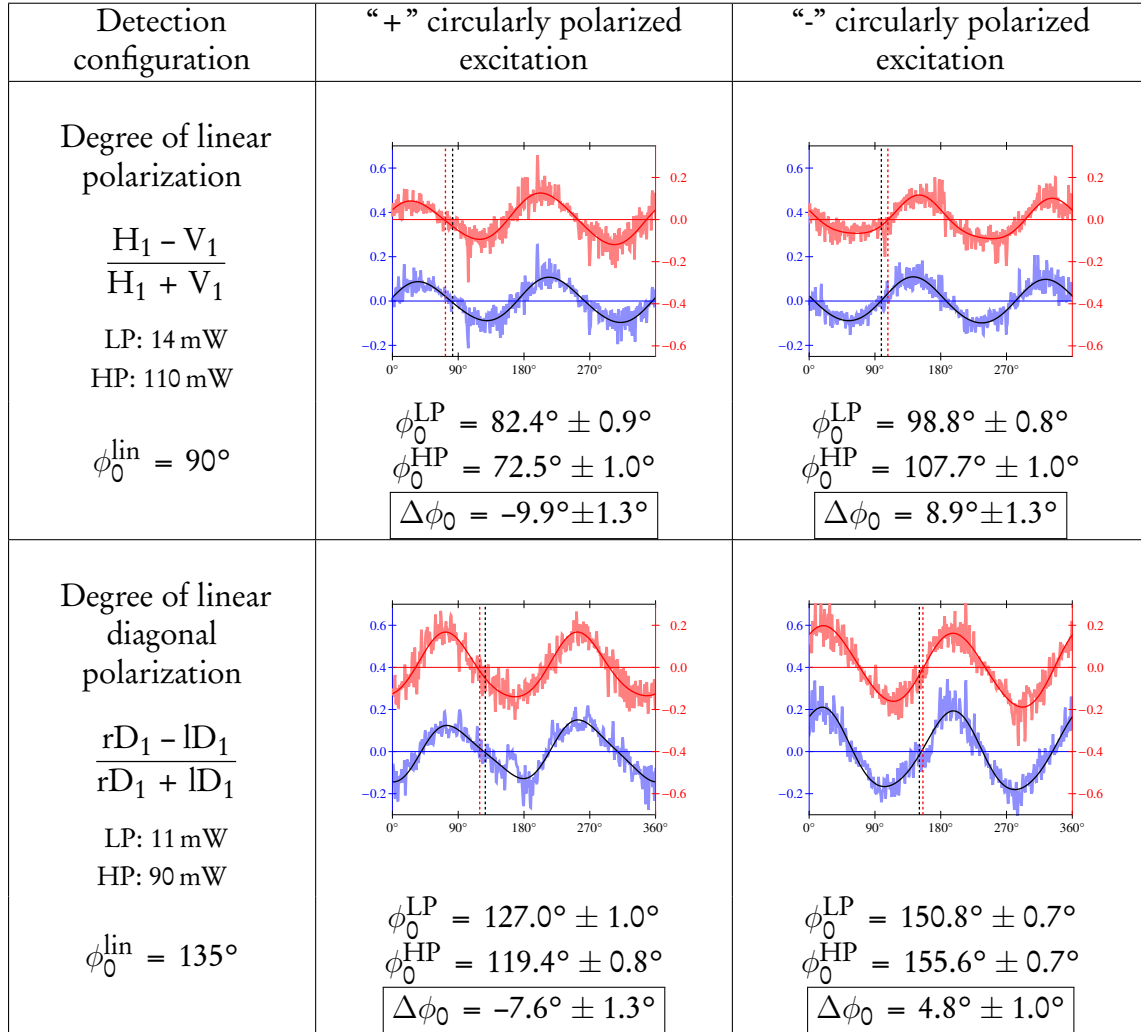


Figure 4.12: Experimental results for two incoming pump powers in various polarization configurations for excitation and detection. The “low power” curves (LP) are plotted in blue and the fit is a plain black line. The “high power” curves (HP) are plotted in red and the fit is a plain red line. The vertical dashed lines indicate ϕ_0 (ϕ_0^{LP} in black, ϕ_0^{HP} in red).

Indeed, parametric scattering of pump polaritons towards the elastic circle would create pairs of polaritons separated by 180° . The sine curve should exhibit twin peaks along certain directions that may influence the phase offset ϕ_1 obtained by the fit equation (4.3). However, this distortion would be nearly the same in all the configurations presented in Fig. 4.12 such that $\Delta\phi_0$ should have the same sign for all configurations. Moreover, intensity correlations along the elastic circle is a direct measure of the strength of parametric scattering. On Fig. 4.13, the autocorrelation of the intensity distribution along the elastic circle is plotted (for more details on autocorrelation calculations, refer to Appendix A2). Since the peak at 180° is rather

weak even at large powers, the intervention of parametric scattering effects can be safely discarded.

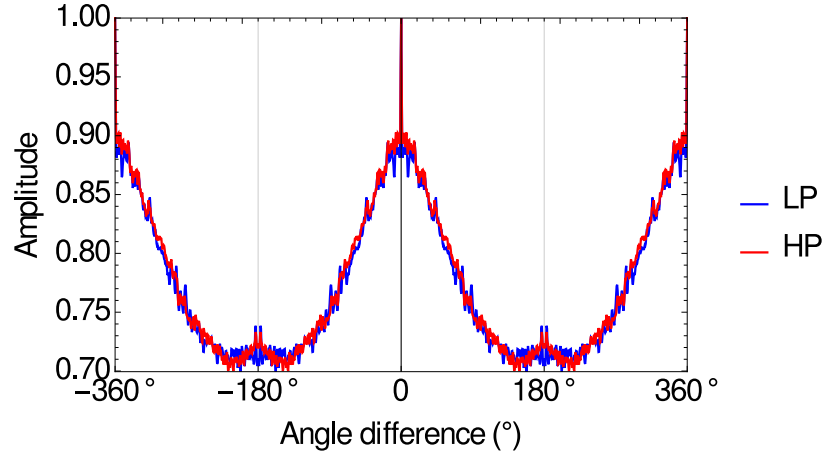


Figure 4.13: Autocorrelation of the intensity distribution (background subtracted) along the elastic circle (namely $V_1 + H_1$ as defined in the previous subsection) for a “+”-circularly polarized pumping at 14 mW (LP) and 110 mW (HP). In both cases, a small correlation is found for the speckle points at 180° . This may come from either dislocations in the DBRs or parametric scattering [Abbarchi2012].

Other parasitic effects such as the presence of a built-in polarization splitting mentioned in Subsection 4.1.3.3 or a small angle error on the pump polarization are taken into account by the monopolar ($\sin \phi$) and octopolar ($\sin 4\phi$) terms of the fit equation (4.3). One can show that they do not affect the quadrupolar term ($\sin 2\phi$), so they also fail to account for the observations of Fig. 4.12.

4.2.1.4 Power-dependent OSHE

The pump power is now slightly tuned from approximately 6 mW to approximately 40 mW. We checked by a reflectivity measurement that on this power range, the pump polariton density increases linearly with power. The pump is “-”-circularly polarized. To compare the results with simulations done with a “+”-circularly polarized pumping term, the geometric transformation proposed in the last subsection is applied. We therefore expect $\phi_0^{\text{HP}} < \phi_0^{\text{LP}}$.

The result of the experiment is shown on Fig. 4.14.a. We observe a decrease of ϕ_0 as a function of power from approximately 95° with a saturation at about 60° . We note, additionally, that the experiment shows no sign of bistable behaviour. The first point at 6 mW does not match the quasi-linear law followed by the other points (before saturation). This may be an effect of the blueshift which is not strong enough to achieve perfect resonance conditions.

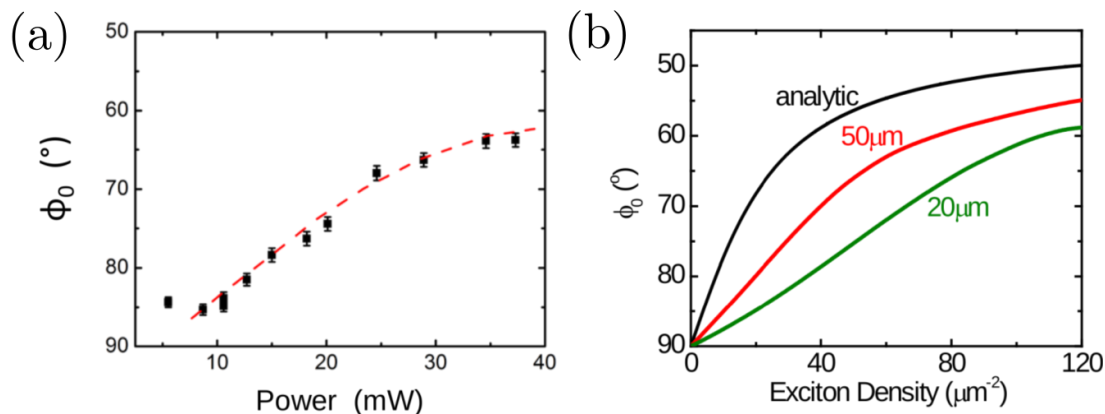


Figure 4.14: (a) Experimental angular orientation in terms of the zero-crossings ϕ_0 vs. incident excitation power. The thin dashed curve is merely a guide for the eye. (b) Theoretical angular orientation ϕ_0 as a function of exciton density for a pump spot spread all over space, in which case an analytic expression (eq. (4.6)) can be derived (black line) and from numerical solutions of the 2-dimensional polariton Gross-Pitaevskii equation for 50 (red) and 20 μm (green) spot sizes. Both methods are detailed in the next subsection 4.2.2.

Fig. 4.14.b. shows the result of theoretical simulations and calculations that will be described in the next subsection. An analytical result can be found if we suppose a plane wave for the optical pump. However, in the experiment, this is not the case and the pump spot size is approximately 50 μm . A direct calculation for the realistic case is not possible, but simulations have been performed by our theoretician collaborators of Tucson, Arizona and Hong-Kong to reproduce the experimental observations. They also find a quasi-linear decrease of ϕ_0 at low exciton densities, and then a saturation plateau close to 60°.

The exciton density in μm^{-2} can be converted into an optical pump power in mW using the value of the recombination rate γ_{rec} (radiative and non-radiative decay) of excitons. With a typical QW light-coupled exciton lifetime of $\simeq 100$ ps in a microcavity [Bajoni2006, Bastard], the scales of Figs. 4.14.a. and b. agree.

4.2.2 Theoretical description

The theoretical description of this experiment was developed by our theoretician collaborators of University of Paderborn, University of Arizona and from the Chinese University of Hong Kong. I reproduce here the main results and relate them to the usual formalism describing the OSHE [Kavokin2005].

Assuming a plane wave for the pump, an analytical form for the phase shift of the sine curve can be derived. Otherwise, numerical methods can be used and will be briefly presented.

4.2.2.1 Analytical approximate description

In this subsection, we derive an equation linking the zero-crossings of the sine curve, ϕ_0 , as a function of the “+”-circularly polarized pump polariton density $|\Psi_0^+|^2$ which is assumed narrowly distributed around $\mathbf{k} = \mathbf{0}$ (plane wave or in the limit of very large spot sizes). To simplify the calculation, we assume here a single cavity and a pump source term populating the elastic circle.

First method: Gross Pitaevskii equation Spinor-valued polaritons are represented by wave functions Ψ^\pm which obey a driven polaritonic Gross Pitaevskii equation. Neglecting the phase space filling, we start with the following equation in the frame rotating at the pump angular velocity ω_{pump} :

$$\begin{aligned} i\hbar \frac{\partial}{\partial t} \Psi_{\mathbf{k}}^\pm &= (E_{\mathbf{k}}^{\text{P}} - i\gamma_{\text{p}} - \hbar\omega_{\text{pump}}) \Psi_{\mathbf{k}}^\pm + \Delta_{\mathbf{k}}^{\text{P},\pm} \Psi_{\mathbf{k}}^\mp + \psi_{\text{pump}}^\pm \\ &+ \sum_{\mathbf{k}', \mathbf{k}''} (\alpha^{++} \Psi_{\mathbf{k}'+\mathbf{k}''-\mathbf{k}}^{\pm*} \Psi_{\mathbf{k}'}^\pm \Psi_{\mathbf{k}''}^\pm + \alpha^{+-} \Psi_{\mathbf{k}'+\mathbf{k}''-\mathbf{k}}^{\mp*} \Psi_{\mathbf{k}'}^\mp \Psi_{\mathbf{k}''}^\pm), \end{aligned} \quad (4.4)$$

where $E_{\mathbf{k}}^{\text{P}} = E_0^{\text{P}} + \frac{\hbar^2 \mathbf{k}^2}{2M}$, $\gamma_{\text{p}} = \gamma_{\text{c}} + \gamma_{\text{x}}$ and $\Delta_{\mathbf{k}}^{\text{P},\pm} = \frac{\hbar^2}{2m} (\mathbf{k}_{\text{x}} \mp i\mathbf{k}_{\text{y}})^2 = \Delta_{\mathbf{k}}^{\text{P},\text{TL}} e^{\mp 2i\phi}$ (cf. Subsection 1.3.1.1), $M = \frac{1}{2} (\frac{1}{m_{\text{p}}^{\text{TE}}} + \frac{1}{m_{\text{p}}^{\text{TM}}})^{-1}$ and $m = \frac{1}{2} (\frac{1}{m_{\text{p}}^{\text{TM}}} - \frac{1}{m_{\text{p}}^{\text{TE}}})^{-1}$. α^{++} , α^{+-} are the interaction strengthes between polaritons with corresponding spins defined in eq. (1.23). ω_{pump} is the pump frequency.

For a strong normally incident pump and in the Rayleigh scattering regime, we successively take ($\mathbf{k}' = \mathbf{0}$, $\mathbf{k}'' = \mathbf{k}$) and ($\mathbf{k}' = \mathbf{k}$, $\mathbf{k}'' = \mathbf{0}$) in the sum and truncate eq. (4.4) below the terms showing a nonlinear dependance in $\Psi_{\mathbf{k} \neq \mathbf{0}}^\pm$. Eq. (4.4) rewrites:

$$i\hbar \frac{\partial}{\partial t} \begin{pmatrix} \Psi_{\mathbf{k}}^+ \\ \Psi_{\mathbf{k}}^- \end{pmatrix} = \begin{pmatrix} \Delta E_{\mathbf{k}}^+ - i\gamma_{\text{p}} & \Delta_{\mathbf{k}}^{\text{P},\text{TL}} e^{-2i\phi} + U^+ \\ \Delta_{\mathbf{k}}^{\text{P},\text{TL}} e^{2i\phi} + U^- & \Delta E_{\mathbf{k}}^- - i\gamma_{\text{p}} \end{pmatrix} \begin{pmatrix} \Psi_{\mathbf{k}}^+ \\ \Psi_{\mathbf{k}}^- \end{pmatrix} + \begin{pmatrix} \psi_{\text{pump}}^+ \\ \psi_{\text{pump}}^- \end{pmatrix} \quad (4.5)$$

where $U^\pm = \alpha^{+-} \Psi_0^{\mp*} \Psi_0^\pm$, $\Delta E_{\mathbf{k}}^\pm = (E_{\mathbf{k}}^{\text{P}} - \hbar\omega_{\text{pump}}) + B^\pm$ and $B^\pm = 2\alpha^{++} |\Psi_0^\pm|^2 + \alpha^{+-} |\Psi_0^\mp|^2$.

The stationary solutions of this equation can be easily computed by inverting the above matrix.

For a “+” circularly polarized pump ($\Psi_0^- = 0$), the degree of linear polarization is

$$\begin{aligned} S_1 &= |\psi_{\text{x}}|^2 - |\psi_{\text{y}}|^2 = 2\Re(\Psi_{\mathbf{k}}^+ \Psi_{\mathbf{k}}^-) \\ &= K(\Delta E_{\mathbf{k}}^- \cos 2\phi - \gamma_{\text{p}} \sin 2\phi) \end{aligned}$$

where K is a real constant depending on $|\psi_{\text{pump}}|^2$, γ_{p} , $\Delta_{\mathbf{k}}^{\text{P},\text{TL}}$ and $\Delta E_{\mathbf{k}}^\pm$.

If $\Delta_{\mathbf{k}}^{\text{p,TL}} < \gamma_{\text{p}}$, the elastic resonant Rayleigh scattering condition for “+” polarized polaritons imposes $\Delta E_{\mathbf{k}}^+ = E_{\mathbf{k}}^{\text{p}} - \hbar\omega_{\text{pump}} + 2\alpha^{++} |\Psi_0^+|^2 = 0$.

Finally

$$S_1 = -K((2\alpha^{++} - \alpha^{+-})|\Psi_0^+|^2 \cos 2\phi + \gamma_{\text{p}} \sin 2\phi)$$

In order to reproduce the shift observed in the experiment, we can rewrite S_1 as a function of $\sin(2\phi + \phi_1)$. The pump power-induced shift of the sine curve is therefore:

$$\phi_1 = \arctan\left(\frac{(2\alpha^{++} - \alpha^{+-})|\Psi_0^+|^2}{\gamma_{\text{p}}}\right), \quad (4.6)$$

Since $2\alpha^{++} - \alpha^{+-} > 0$ (see Subsection 1.3.4), ϕ_1 is positive. Hence the polarization map rotates *clockwise*. Alternatively, for a “-” circularly polarized pump, $\phi_1 = -\arctan\left(\frac{(2\alpha^{++} - \alpha^{+-})|\Psi_0^-|^2}{\gamma_{\text{p}}}\right)$ and the polarization map rotates *anticlockwise*.

Second method: Equation on the pseudospin Alternatively, the hamiltonian (4.5) can be written as the linear combination of identity matrix and a spin-orbit

interaction $\frac{1}{2}\vec{B} \cdot \vec{\sigma}$, where $\vec{\sigma} = \begin{pmatrix} \sigma_x \\ \sigma_y \\ \sigma_z \end{pmatrix}$ is the Pauli matrices vector $\sigma_x = \begin{pmatrix} 0 & 1 \\ 1 & 0 \end{pmatrix}$ and $\sigma_y = \begin{pmatrix} 0 & -i \\ i & 0 \end{pmatrix}$, $\sigma_z = \begin{pmatrix} 1 & 0 \\ 0 & -1 \end{pmatrix}$. The modified effective magnetic field is now:

$$\vec{B} = \begin{pmatrix} 2\Delta_{\mathbf{k}}^{\text{p,TL}} \cos 2\phi + 2\alpha^{+-}\Re(\Psi_0^{+*}\Psi_0^-) \\ 2\Delta_{\mathbf{k}}^{\text{p,TL}} \sin 2\phi + 2\alpha^{+-}\Im(\Psi_0^{+*}\Psi_0^-) \\ (2\alpha^{++} - \alpha^{+-})(|\Psi_0^+|^2 - |\Psi_0^-|^2) \end{pmatrix} \quad (4.7)$$

For a “+” circular-polarized pump, the additionnal terms along x and y vanish. Only $B_3 = (2\alpha^{++} - \alpha^{+-})|\Psi_0^+|^2$ remains, and the equation on the pseudo-spin (1.21) gives:

$$S_1 = \frac{2\Delta_{\mathbf{k}}^{\text{p,TL}} \tau^2 (B_3 \tau \cos 2\phi + \hbar \sin 2\phi) |\Psi_0^+|^2}{(\hbar^2 + (B_3^2 + 4(\Delta_{\mathbf{k}}^{\text{p,TL}})^2)\tau^2)\tau_1},$$

where τ is the polariton lifetime and τ_1 is the Rayleigh scattering time constant.

S_1 can be rewritten such as $\frac{2\Delta_{\mathbf{k}}^{\text{p,TL}} \tau^2 \sin(2\phi + \phi_1)}{(\hbar^2 + (B_3^2 + 4(\Delta_{\mathbf{k}}^{\text{p,TL}})^2)\tau^2)\tau_1}$. The found ϕ_1 is identical to the one found by the previous method (eq. (4.6)).

This shift can therefore be seen as the consequence of the effective magnetic field third component in eq. (4.7) which does not exist in the linear case (see eq. (1.20)), as shown in Fig. 4.15.

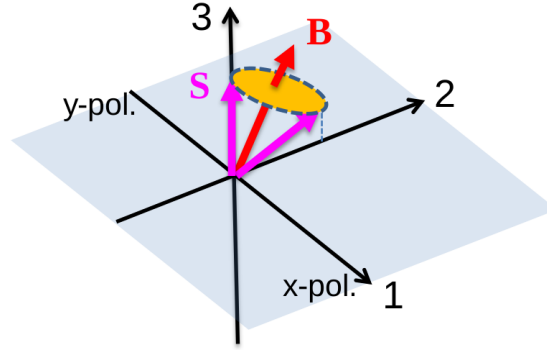


Figure 4.15: Sketch of pseudo-spin space and torque action when \vec{B} has a non zero B_3 component. Courtesy of R. Binder.

Justification of the polarization configuration chosen for the experiment Alternatively, for a “x” linearly polarized pump ([Leyder2007] configuration), the modified effective field is:

$$\vec{B} = \begin{pmatrix} 2\Delta_{\mathbf{k}}^{\text{P,TL}} \cos 2\phi + \alpha^{+-} |\Psi_0^x|^2 \\ 2\Delta_{\mathbf{k}}^{\text{P,TL}} \sin 2\phi \\ 0 \end{pmatrix}$$

The third component of the pseudo-spin S_3 , computed by eq (1.21):

$$S_3 = - \frac{2\hbar\tau^2 \Delta_{\mathbf{k}}^{\text{P,TL}} |\Psi_0^x|^2 \sin 2\phi}{(\hbar^2 + ((\alpha^{+-} |\Psi_0^x|^2)^2 + 4(\Delta_{\mathbf{k}}^{\text{P,TL}})^2 + 4\alpha^{+-} |\Psi_0^x|^2 \Delta_{\mathbf{k}}^{\text{P,TL}} \cos 2\phi)\tau^2)\tau_1}$$

We see that pumping with “+” circularized pump and observing S_1 induces a shift of the sine pattern, whereas doing the experiment in Leyder’s configuration would induce a deformation of the sine, much more difficult to observe experimentally as its signature as a function of ϕ would be more sensitive to perturbations.

4.2.2.2 Simulations for a finite pump spot size

However, this analytical solution has been found under the assumption that the pump is a normally-incident plane wave (truncation of eq. (4.4)).

In order to take into account the finite spot size of the pump, simulations have been made using a Gaussian beam profile (noted $p_{\text{LPB}_2}^+(\mathbf{r})$) for the circularly (“+”)

polarized source, and solving the following real space equations:

$$\begin{aligned} i\hbar \frac{\partial}{\partial t} \Psi_{\text{LPB}_1}^{\pm} &= \mathbb{H}_{\text{LPB}_1}^0 \Psi_{\text{LPB}_1}^{\pm} + \mathbb{H}_{\text{LPB}_1}^{\pm} \Psi_{\text{LPB}_1}^{\mp} + N_{\text{LPB}_1}^{\pm} + P_{\text{LPB}_1}^{\pm} \\ i\hbar \frac{\partial}{\partial t} \Psi_{\text{LPB}_2}^+ &= \mathbb{H}_{\text{LPB}_2}^0 \Psi_{\text{LPB}_2}^+ + N_{\text{LPB}_2}^+ + P_{\text{LPB}_2}^+, \end{aligned}$$

where $\text{LPB}_{1/2}$ label the low polariton branches and \pm is the circular polarization. The branch LPB_2 is solely populated by a “+”-circular polarized pump, with frequency ω_{pump} . The branch LPB_1 is populated by Rayleigh-scattered pump polaritons. The pumping term P is therefore $P_{\text{LPB}_1}^{\pm} = p_{\text{LPB}_1}^{\pm}(\mathbf{r})e^{-i\omega_{\text{pump}}t}$ for the LPB_1 branch whereas $P_{\text{LPB}_2}^+ = p_{\text{LPB}_2}^+(\mathbf{r})e^{-i\omega_{\text{pump}}t}$ and $P_{\text{LPB}_2}^- = 0$ for the LPB_2 branch.

$\mathbb{H}_{\text{LPB}_j}^0 = E_{0,j}^P - \frac{\hbar^2}{4} \left(\frac{1}{m_{\text{P},j}^{\text{TM}}} + \frac{1}{m_{\text{P},j}^{\text{TE}}} \right) \nabla^2 - i\gamma_p$ is the energy dispersion of the polariton branch LPB_j , where $E_{0,j}^P$ is the energy minimum of LPB_j , $m_{\text{P},j}^{\text{TM/TE}}$ are the TE and TM effective polariton masses of branch LPB_j , and γ_p the polariton loss rate.

The term $\mathbb{H}_{\text{LPB}_1}^{\pm} = -\frac{\hbar^2}{4} \left(\frac{1}{m_{\text{P},j}^{\text{TM}}} - \frac{1}{m_{\text{P},j}^{\text{TE}}} \right) \left(\frac{\partial}{\partial x} \mp i \frac{\partial}{\partial y} \right)^2$ includes the TE-TM splitting of the LPB_1 branch (negligible in LPB_2 since we only consider states at vanishing in-plane momentum).

The nonlinear polariton-polariton interactions are included via the terms $N_{\text{LPB}_{1,2}}^{\pm}$ which depend on α^{++} , α^{+-} (taking into account Hopfield coefficients²) and $\Psi_{\text{LPB}_{1,2}}^{\pm}(\mathbf{r}, t)$.

	$m_{\text{p},1}^{\text{TM}}$	$m_{\text{p},1}^{\text{TE}}$
	$6.56 \times 10^{-35} \text{ kg}$	$1.023 m_{\text{p},2}^{\text{TE}}$
	$m_{\text{p},2}^{\text{TM}}$	$m_{\text{p},2}^{\text{TE}}$
	$6.90 \times 10^{-35} \text{ kg}$	$1.031 m_{\text{p},2}^{\text{TE}}$
$E_{0,2}^P - E_{0,2}^P$	Ω_R	T^{++}
7.54 meV	6.35 meV	$5.69 \times 10^{-3} \text{ meV} \cdot \mu\text{m}^{-2}$ [Schumacher2007]
γ_p	α_{PSF}	T^{+-}
0.2 meV	$2.594 \times 10^{-4} \mu\text{m}^{-2}$ [Luk2013]	$-T^{++}/3$ [Schumacher2007]

Table 4.2: Parameter values used for the simulation with finite pump spot sizes.

The simulations using realistic parameters, presented in Table 4.2, can be real-

²Note that the Hopfield coefficient differ for the phase-space filling term $\alpha_{\text{PSF}}\Omega_R$ and the T^{++}/T^{+-} two excitons correlations included in α^{++} and α^{+-} (cf. Subsection 1.3.4)

ized with various gaussian spot sizes. The results for $50\ \mu\text{m}$ (close to experimental conditions) and $20\ \mu\text{m}$ spot sizes are shown in Fig. 4.14.b. (red and green lines).

The simulation exhibits no hysteresis as a function of pump power, in accordance with the experimental findings.

4.2.2.3 Discussion

The result of the model are shown in Fig. 4.14 and reproduces well the experimental results presented in Subsection 4.2.1.4.a. The optical modification of the Optical Spin Hall Effect is therefore demonstrated both theoretically and experimentally.

However, some differences remain between the experiment and the theoretical predictions:

- Under certain conditions yet to be fully understood, the experiment can exhibit Rayleigh scattering for power ranges that are above the OPO threshold predicted by theory. One reason may be that the laser, resonant at low pump powers, gets off resonance at large pump powers due to blueshift effects (*cf.* Subsection 1.2.2.4). The exciton density effectively confined in the structure does not reach the OPO threshold.
- The overlap region between polarizations H and V at $\phi = 0, \pi/2, \pi$ and $3\pi/2$ is much larger in the experiment (see for example Fig. 4.9) than in theory (Figs. 4.7.b. and c.). One possibility is that it is due to the laser intensity instability seen in Subsection 2.1.4, which would result in different shift values as a function of time. The observed polarization map is averaged over time, hence the larger overlap.

In the next subsection, I show additional experiments in order to complete the understanding of this phenomenon. These experiments confirm or go beyond the model and simulations presented.

4.2.3 Influence of other experimental parameters

In this section, I show that *even at fixed pump power*, different shift values ϕ_0 can be obtained. Indeed, the detuning between the excitation laser energy and minimum of LPB₂ branch (neglected in the model and simulation previously presented) plays a role, as well as the exciton-photon detuning. In the first case, the detuning from resonance modifies the exciton density confined in the microcavity, hence the modification of ϕ_0 . Secondly, at large negative exciton-photon detuning, the polariton is almost exclusively photonic, and the polariton-polariton interactions responsible for the shift are thus much reduced.

4.2.3.1 Pump resonance with LPB₂

Two experiments have been conducted to check the significance of the resonant excitation of the minimum of LPB₂: (i) the pump excitation energy is tuned, and (ii) the sample shifted so that the energy of the minimum of LPB₂ varies due to the built-in wedge.

The first experiment is shown in Fig. 4.16.a. The alternative cw Ti:Sapph Solstis laser described in Chapter 2 is used, since its wavelength can be tuned finely using the intracavity etalon while every other parameter is kept fixed. We did the experiment for a “-”-circular excitation on a roundtrip basis (decreasing and then increasing the excitation energy) at two fixed excitation powers: 1 and 50 mW. Note that the polariton branch energy varies during the experiment due to blueshift effects (*cf.* Subsection 1.2.2.4), which depends both on resonance and pump power. The phase shifts behave as expected for a “-”-circularly polarized excitation: $\phi_0^{1\text{ mW}} < \phi_0^{50\text{ mW}}$ (except, surprisingly, for the highest energy point). No hysteresis is observable in accordance with previous experimental findings in either cases. $\phi_0^{50\text{ mW}}$ values span from 98° to more than 108° and exhibit a bell-shaped curve as a function of laser energy. $\phi_0^{1\text{ mW}}$ values are less dispersed (approximately 5° difference between the extrema values) and evolves linearly with energy. These differences can be interpreted as a result of the blueshift of the polariton branch, much more efficient at 50 mW than at 1 mW. Further investigations have shown that the higher values for $\phi_0^{50\text{ mW}}$ corresponds to the situation where the laser is slightly redshifted compared to the LPB₂ minimum (approximately -0.1 meV). .

The result of the second experiment is shown on Fig. 4.16.b. The sample is shifted to achieve different energy values for the minimum of the LPB₂ polariton branch while the laser excitation energy is kept fixed (thick vertical line) at a lower value. The laser excitation power is switched between 12 and 100 mW, and its polarization is “+”-circular polarized, hence we expect $\phi_0^{100\text{ mW}} < \phi_0^{12\text{ mW}}$. The phase shift at 100 mW exhibits again a difference of about 10° between its two extrema. Note that the energy of the polariton branch was measured under the 100 mW excitation, such that the position of the blue points in Fig. 4.16.b. are in reality slightly redshifted.

These two experiments show that the pump-power induced phase shift exhibits different even at fixed power, depending on the detuning between the pump energy and the minimum of LPB₂. This does not undermine the main experimental findings shown in Fig. 4.14 since the laser excitation energy and the position of the sample were kept fixed. However, for a full understanding of the ϕ_0 value, this parameter must not be neglected.

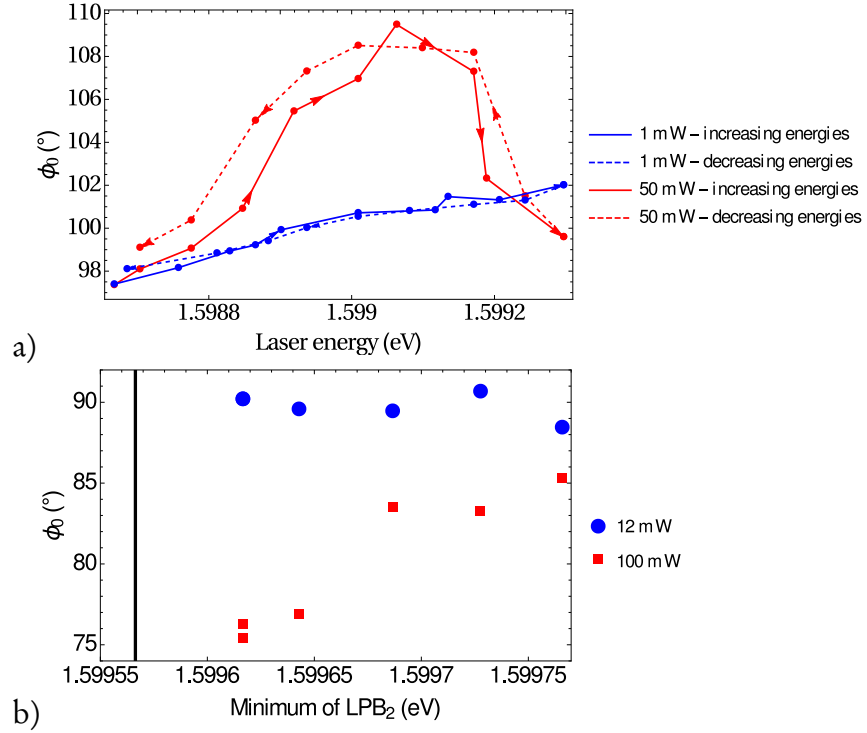


Figure 4.16: a) ϕ_0 as a function of the excitation laser energy at two different pump powers and on a roundtrip basis. The laser is “-” circularly polarized, hence we have $\phi_0^{50\text{ mW}} > \phi_0^{1\text{ mW}}$. b) ϕ_0 as a function of the energy of the polariton branch, the excitation energy being kept fixed for two values of the pump power. The laser is “+” circularly polarized, hence we have $\phi_0^{100\text{ mW}} < \phi_0^{12\text{ mW}}$.

4.2.3.2 Exciton-photon detuning influence

To see the influence of exciton-photon detuning on the zero-crossing value ϕ_0 , experiments have been performed at four different values of the exciton-photon detunings for two excitation powers (12 and 100 mW) and a “-”-circularly polarized excitation. The excitation is resonant with the minimum of the LPB₂, but may vary slightly from one measurement to another (which corresponds to different spots on the sample *and* to different excitation energies). The values found for ϕ_0 at the different detunings must therefore be taken with caution. To simplify the discussion, we will assume here that the excitation energy is optimized such that the peak value of $\phi_0^{100\text{ mW}}$ shown in Fig. 4.16.a. is obtained.

Fig. 4.17 displays the result of such experiment as a function of polariton-exciton detuning ($E_{0,\text{LPB}_2}^{\text{P}} - E_0^{\text{X}}$). As expected for a “+”-circularly polarized pump, we observe that $\phi_0^{100\text{ mW}} < \phi_0^{12\text{ mW}}$ (though the reverse is obtained for the measurement below -17 meV but the phase difference is too small to be significant). The phase difference $|\Delta\phi_0| = |\phi_0^{12\text{ mW}} - \phi_0^{100\text{ mW}}|$ disappears when the polariton branch is far detuned from the exciton. This can be easily interpreted since the shift comes from polariton-

polariton interactions, which are a consequence of the matter (excitonic) component of polaritons.

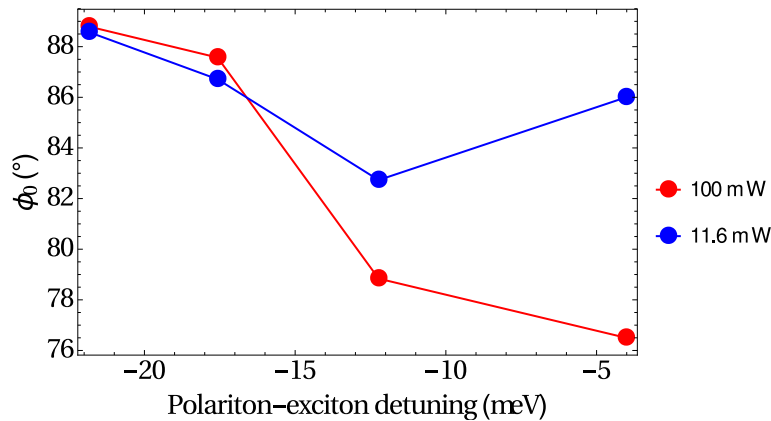


Figure 4.17: ϕ_0 as a function of LPB₂ position for high and low power. The pump is “-”-circularly polarized.

This experiment shows that the optical control of the OSHE is optimized for low exciton-photon detunings, in accordance with our expectations. A more complete study, taking into account the laser detuning with respect to the polariton branch, must be realized to further confirm this preliminary observation.

4.2.4 Conclusion

In conclusion, the optical control of the Optical Spin Hall Effect using a strong optical pump beam is demonstrated in this section.

In the first part, we show that the optical pump power induces a rotation of the OSHE polarization pattern resulting from the elastic Rayleigh scattering of pump polaritons excited by a circularly-polarized pump beam, and a detection of the emitted light in the linear polarization channels. This rotation is clockwise (anticlockwise) for a “+” or left- (“-” or right-) circularly pump. The rotation angle varies linearly below 30 mW and then saturates at approximately 30°. No sign of bistability is found. These experimental results are well reproduced by the inclusion of quadratic nonlinear terms in the pump intensity, without the intervention of any other nonlinear effects such as optical parametric scattering, condensate or pattern formation.

A full experimental characterization of the rotation angle shift as a function of power is yet to be conducted, taking into account other parameters such as the detuning between the pump energy and the minimum of LPB₂, the exciton-photon detuning and the pump size beam, so that a robust correspondence between the incoming power on LPB₂ and the value of the rotation angle is achieved. The two first parameters have been experimentally probed in Subsection 4.2.3, but a more

systematic study is needed. On the other hand, a strong influence of the pump beam size is predicted theoretically: at a fixed exciton density, an increasing pump spot size should correspond to a larger rotation angle (see Fig. 4.14.b.).

This study opens the way towards polariton devices creating pseudo-spin textures and currents that are fully controlled optically. The use of multiple beams and/or sequences of short pulses may in the future allow for an on-demand generation of such polarization patterns. Note that the use of a double microcavity is particularly adequate in a device perspective, since one polariton branch (LPB_1) is here exploited as a *signal channel*, monitored by an optical pump beam resonant with the other polariton branch (LPB_2) which can thus be thought of as the *control channel*.

4.3 Spin-dependent parametric scattering

We have shown that the pump power on the LPB_2 branch minimum influences the propagation of polaritons such that the Optical Spin Hall Effect is fully controllable by optical means.

In this section we go beyond this nonlinearity and study henceforth the influence of the TE-TM splitting in the parametric scattering regime. This regime intervenes when the four-wave mixing is activated, *i.e.* when a pump-probe beam scenario fulfilling the phase-matching conditions leads to the apparition of an idler beam. This regime is reached for sufficiently large pumping intensities ($\simeq 50 \text{ mW}$), when the polariton-polariton interactions are sufficiently efficient to involve several available states on the elastic circle.

This study is motivated towards understanding the formation of formation of spatial hexagonal patterns in the polariton density [Ardizzone2013a] on the elastic circle above the Optical Parametric Oscillation threshold, regime that will be explored in the next section. Here we operate in the nonlinear optical regime, but slightly below the pattern formation threshold so that the spatially homogenous fields are still stable.

Three phase-matched processes are at stake in the hexagonal pattern formation process (Fig. 4.18). The first two (Fig. 4.18.a. and b.) will be studied in this section. The regime of parametric scattering is particularly well-suited to probe the favored processes as well as the influence of linear and nonlinear polarization effects in the patterns organisation mechanisms.

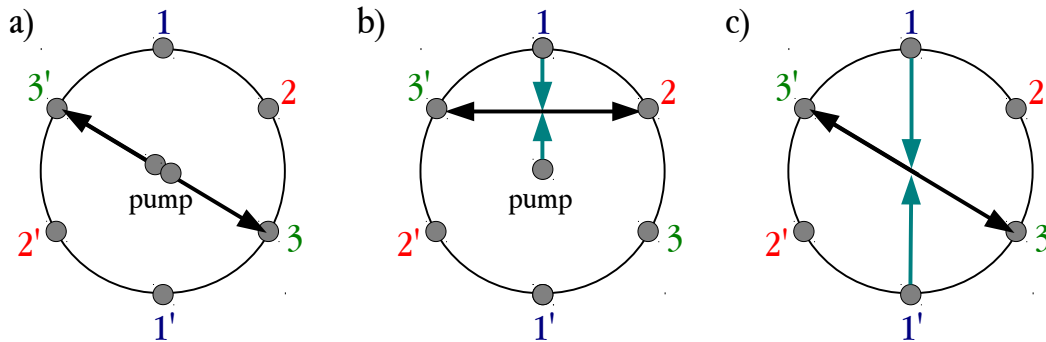


Figure 4.18: Reproduced from [Ardizzone2013a]. Phase-matched processes at stake in the hexagonal pattern formation mechanism involving the pump beam at normal incidence and various states on the elastic circle.

The first scattering mechanism that we will consider involves two pump polaritons photogenerated at zero in-plane momentum and two polaritonic states anywhere on the elastic circle but separated by 180° (for example 1 and $1'$ on Fig. 4.18.a.). Experimentally, a probe is sent at an oblique incidence resonant with the elastic circle, and we study the idler beam, as shown on Fig. 4.19.a. We will refer to this process as *first-order four-wave mixing* (FOFWM).

The second scattering mechanism involves one pump polariton and three polariton states separated by 60° on the elastic circle (for example 1, 2 and 3 on Fig. 4.18.b.). Experimentally, two probe polaritons separated by 120° are sent in resonance with the elastic circle, and the idler beam located in-between is investigated. We will refer to this process as *second-order four-wave-mixing* (SOFWM), illustrated in Fig. 4.19.b.

The third scattering mechanism represented on Fig. 4.18.c. could also in principle be probed using three beams located on the elastic circle (for example 1, $1'$ and 3) *without* the normally-incident pump beam. However, in this work, we will restrict ourselves to the study of FOFWM and the SOFWM processes.

If we go back to eq. (4.2), the processes that are taken into account:

- now includes scattering towards $-\mathbf{k}$ states for the FOFWM,
- and includes as well scattering between \mathbf{k} states separated by 60° for the SOFWM.

Both processes are studied as a function of the linear polarization direction of the pump and probe(s), as represented on Fig. 4.19.

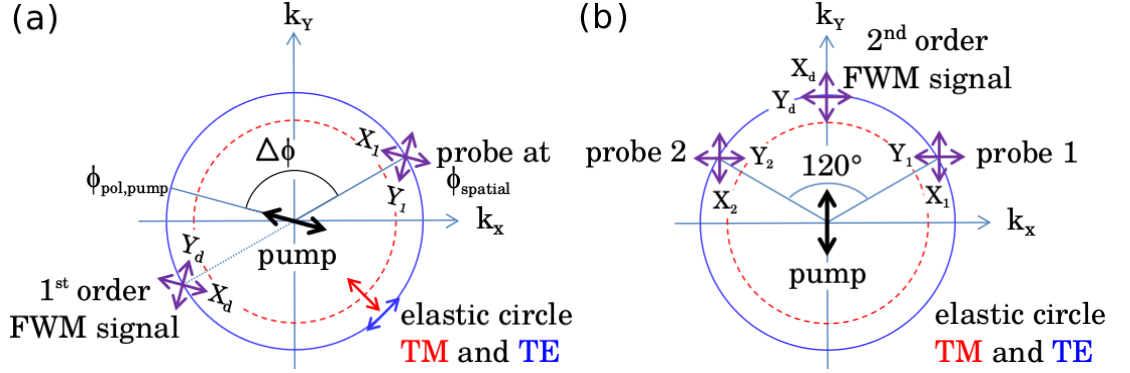


Figure 4.19: Sketch of the two-dimensional transverse momentum space (k -space) plane. The TE and TM elastic circles of LPB₁ are indicated, with TE (TM) polarizations being tangential (orthogonal) to the elastic circle. The pump is normally incident and linearly polarized. In (a) the configuration used to study the FOFWM is illustrated. Probe and FOFWM signals are located on the mean elastic circle respectively at $\mathbf{k}_{\text{probe}}$ corresponding to ϕ_{spatial} and $-\mathbf{k}_{\text{probe}}$ corresponding to $\phi_{\text{spatial}} + 180^\circ$. The pump polarization plane $\phi_{\text{pol,pump}}$ is rotated during the experiment. In (b), the configuration used to study the SOFWM is illustrated. The azimuthal angle ϕ_{spatial} of probe 1 is fixed, and the relative angle between probe 1 and probe 2 is 120° , leading to a SOFWM signal at 90° . In both cases, the linear polarization directions of the probe(s) and of the detection setup are indicated by double arrows.

4.3.1 First order four-wave mixing

First we focus on those four-wave mixing processes that can be interpreted as off-axis scattering of two pump-induced polaritons to finite and opposite momentum \mathbf{k} and $-\mathbf{k}$ on the elastic circle as indicated in Fig. 4.19.a. To selectively analyze these processes, we perform a polarization-resolved pump and probe experiment. In a four-wave mixing context, the dominant contribution to this process is only of linear order in the off-axis probe intensity.

4.3.1.1 Experimental setup

Fig. 4.20 illustrates the optical pump-probe setup used to study the FOFWM: a cw-pump excites the cavity at normal incidence ($k_{\text{pump}} = 0$) resonantly on LPB₂ and gives rise to a coherent polariton field. A cw-probe beam with the same frequency is applied under oblique incidence, resonant on LPB₁, carrying an in-plane momentum k_{probe} . The pump and probe spots on the sample are around $50 \mu\text{m}$ full-width-half-maximum (FWHM)³. For a sufficiently intense pump, the probe

³The probe spot is in reality elongated in real space due to the spherical aberrations induced by the ocular L_f (cf. Subsection 2.2.3.1)

beam at k_{probe} can stimulate a pairwise scattering of pump polaritons into a off-axis mode. The two pump polaritons scatter phase-matched and resonant into the modes k_{probe} (amplifying the probe) and $k_{\text{FOFWM}} = 2k_{\text{pump}} - k_{\text{probe}} = -k_{\text{probe}}$, triggering a FOFWM signal.

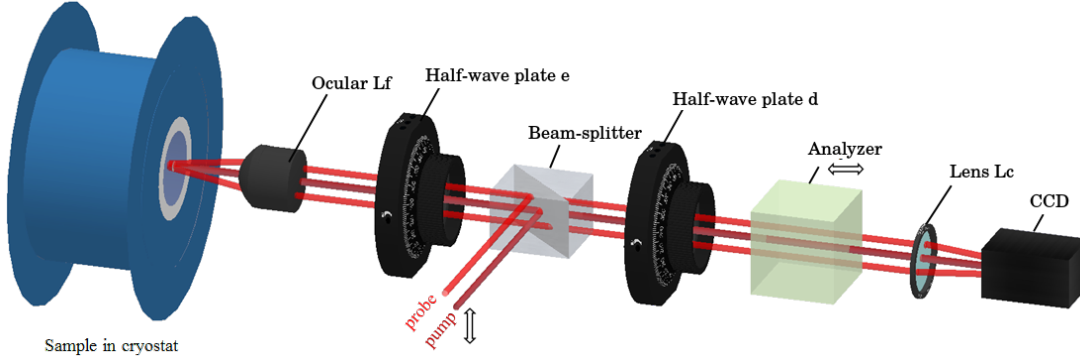


Figure 4.20: Sketch of the optical setup used to study FOFWM. Applying a continuous-wave pump and a continuous-wave probe, the first-order four-wave mixing signal is detected in a reflection geometry. The direction of the pump polarization before entering the beam-splitter cube is indicated by a double arrow. The probe polarization is set either parallel or orthogonal to it.

The pump and probe intensities are fixed during each measurement.

We fix the probe azimuthal angle ϕ_{spatial} and rotate the polarization plane of the linearly polarized pump $\phi_{\text{pol,pump}}$ stepwise using the automatic half-wave plate e. For each $\phi_{\text{pol,pump}}$, the linear polarization of the probe $\phi_{\text{pol,probe}}$ is re-adjusted, either copolarized (X, *i.e.* $\phi_{\text{pol,probe}} = \phi_{\text{pol,pump}}$) or cross-polarized (Y, *i.e.* $\phi_{\text{pol,probe}} = \phi_{\text{pol,pump}} + 90^\circ$) to the pump by rotating the half-wave plate p_1 situated upstream (not represented on Fig. 4.20, refer to Fig. 2.5). We then measure the intensity of the FOFWM signal in X and Y polarization channel by rotating the half-wave plate d. Since the probe polarization matches the TE or TM states only when $\phi_{\text{pol,probe}} = \phi_{\text{spatial}}$ (TM) or $\phi_{\text{pol,probe}} = \phi_{\text{spatial}} + 90^\circ$ (TE), the relevant quantity for this study is the relative angle between the direction of the pump polarization and the azimuthal angle of the probe beam, namely

$$\Delta\phi = \phi_{\text{pol,pump}} - \phi_{\text{spatial}},$$

represented on Fig. 4.19.a.

4.3.1.2 Experimental results

The intensity of the FOFWM signal taken is shown as a function of the in-plane momentum k and for each ϕ between 0 and 360° . Fig. 4.21 shows an example of a

typical measurement in the momentum space. Here $\phi_{\text{spatial}} \simeq 155^\circ$ and the pump is polarized along the orthogonal direction ($\phi_{\text{pol,pump}} \simeq 65^\circ$), such that $\Delta\phi = 90^\circ$. The probe and detection are cross-polarized to the pump. The TE and TM elastic circles are indicated by a plain line and a dashed line.

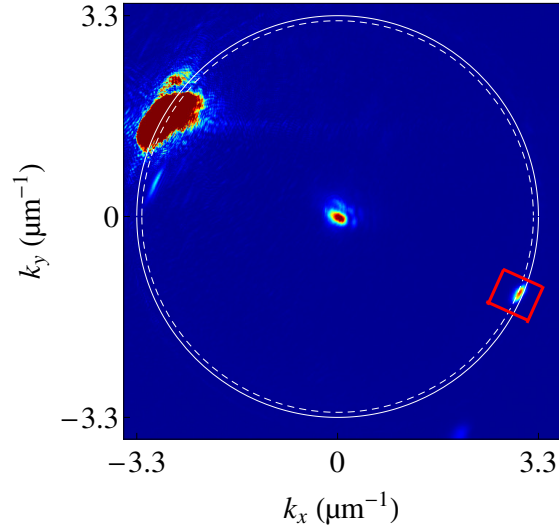


Figure 4.21: The pump at the center is polarized along the arrow, such that $\Delta\phi = 90^\circ$. The probe (large spot on the left) is cross-polarized (Y_1) to the pump. The detection is also done in the cross-polarized channel (Y_d), so that the FOFWM signal, surrounded by a red rectangle, is resonant with the TM elastic circle (dashed). The TE circle is represented with the plain line. The red rectangle figures the typical integration zone for Fig. 4.22.

The experimental and numerical results are shown in Fig 4.22 for four different polarization configurations:

1. probe excitation and FOFWM detection both co-polarized to the pump (X_1X_d , a. and b.),
2. a co-polarized probe and a cross-polarized FOFWM detection to the pump (X_1Y_d , c. and d.),
3. a cross-polarized probe and co-polarized FOFWM detection to the pump (Y_1X_d , e. and f.),
4. a cross-polarized probe and cross-polarized FOFWM detection to the pump (Y_1Y_d , g. and h.).

The FOFWM signal intensity is integrated along the direction orthogonal to ϕ_{spatial} (red rectangle width on Fig. 4.21).

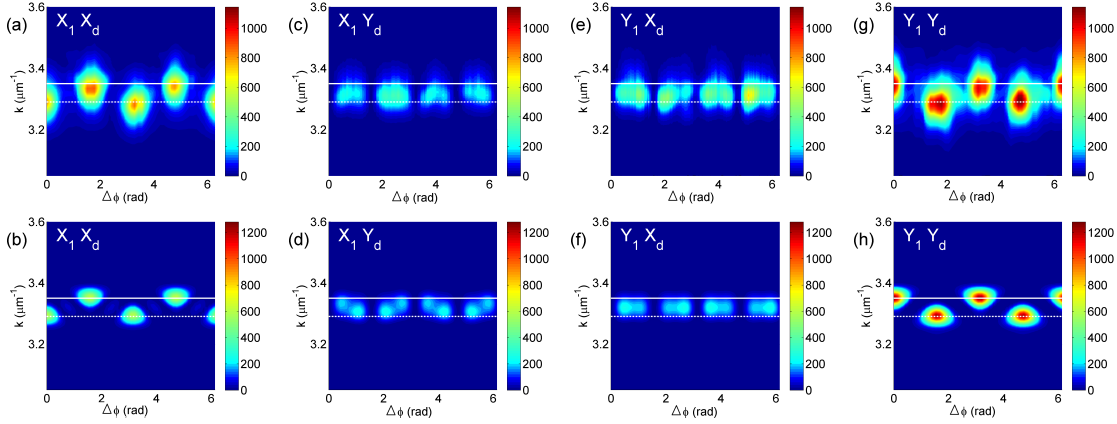


Figure 4.22: Measured (first row) and computed (second row) first-order four-wave mixing intensity in arbitrary units. Results are shown in the two-dimensional transverse momentum space parametrized by the magnitude of the momentum k and angle $\Delta\phi$ which denotes the polar angle between the plane defined by the incident probe and the pump polarization plane (refer to Fig. 4.19a). The X_1X_d (probe and detection co-polarized to the pump) and Y_1Y_d (probe and detection cross-polarized to the pump) experimental pictures a. and g. are each composed of 44 measurements (every 8°) corresponding to vertical stripes. 176 measurements (every 2°) are taken for the experimental pictures Y_1X_d (c.) and Y_1X_d (e.) so that the resolution is large enough to observe the “double-peak” feature expected by simulations. The position of the TM and TE elastic circles is indicated by the dashed and plain white lines.

For each of the polarization configurations, the FOFWM signal exhibits distinct features:

- In the X_1X_d and Y_1Y_d excitation/detection-configuration (probe and detection either both co-polarized, either both cross-polarized to the pump), the FOFWM is strongest if the pump polarization is parallel or orthogonal to the position of the probe ϕ_{spatial} at angles $\Delta\phi = 0$, $\Delta\phi = \pi/2$, $\Delta\phi = \pi$, and $\Delta\phi = 3\pi/2$.
- For X_1X_d , the radius of the FOFWM signal is alternating between $k_{\text{FOFWM}} = 3.29 \mu\text{m}^{-1}$ for parallel and $k_{\text{FOFWM}} = 3.35 \mu\text{m}^{-1}$ for perpendicular excitation (matching the TM and TE elastic circles, respectively). For Y_1Y_d , the roles of parallel and perpendicular excitation are interchanged. The radius reaches a minimum (maximum) for perpendicular (parallel) excitation.
- In contrast, in the X_1Y_d and Y_1X_d configurations the signal vanishes for an excitation of the TE or TM-eigenmode at $\Delta\phi = 0$, $\Delta\phi = \pi/2$, $\Delta\phi = \pi$, and $\Delta\phi = 3\pi/2$, but reaches its maximum for $\Delta\phi = \pi/4$, $3\pi/4$, $5\pi/4$ and $7\pi/4$. Here, the signals are mainly confined in between the TM and TE elastic circle and the variation in radius with varying $\Delta\phi$ is much less pronounced. However, a double-peak structure is observed near each signal maximum.

- Overall, the FOFWM signal is most intense for the Y_1Y_d -configuration, followed by the X_1X_d -configuration, and weakest for X_1Y_d and Y_1X_d configurations.

For all these features, an excellent agreement is found between experiment and theory. The details of the double peak structure (Fig. 4.22.d and f) are not completely identical in the experiment, but they are very sensitive to the exact parameter values chosen for the simulation.

4.3.1.3 Discussion

Before going into the details of the theory, a qualitative understanding of the results can easily be done for some of the features exhibited by Fig. 4.22.

Position of peaks as a function of $\Delta\phi$ and k For angles where the probe polarization matches the TE or TM-eigenmode ($\Delta\phi = 0, \pi/2, \pi,$ and $3\pi/2$), the polarization state of the FOFWM signal matches the probe polarization.

Hence, the configurations where the detection is co-polarized to the probe (X_1X_d and Y_1Y_d) exhibit resonance peaks at $\Delta\phi = 0, \pi/2, \pi,$ and $3\pi/2$, at alternating radii corresponding to the TE- and TM-eigenmodes, and no signal in X_1Y_d and Y_1X_d at angles $\Delta\phi = 0, \pi/2, \pi,$ and $3\pi/2$ is detected.

Instead, the resonance peaks for these configurations are centered near $\Delta\phi = \pi/4, 3\pi/4, 5\pi/4$ and $7\pi/4$, where the TE-TM splitting leads to the strongest rotation of the polarization. The peaks are located in-between the TE and TM elastic circles. They result from a stimulated scattering of two pump polaritons towards one state in the TE and one state in the TM-mode. The scattered polaritons undergo a slight frequency shift (typically $\pm 100 \mu\text{eV}$) to fulfill resonance and phase-matching conditions⁴. The involved LPB₁ modes have a wavevector magnitude in-between the ones of the TE and TM elastic circles, as shown on Fig. 4.23. Additionally, an amplification of the cross-polarized component occurs at the edges of the resonance peaks. This induces a deformation and a slight splitting of these peaks both in experiment and theory.

⁴This interpretation will be further confirmed by an experiment detailed in Subsection 4.4.2.2.

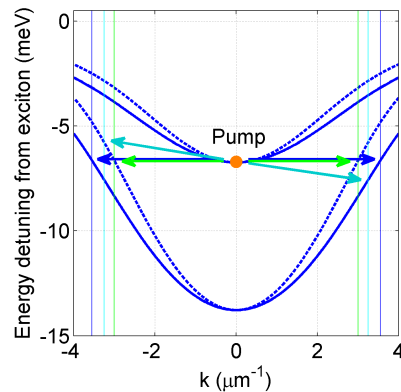


Figure 4.23: Various scattering processes onto LPB₁ involving two pump polaritons photo-created on LPB₂. The TE and TM elastic circles are represented by the plain and dashed lines (the TE-TM splitting is exaggerated here). The fully horizontal processes include scattering towards two opposite states on the TE-branch (blue arrows), or on the TM-branch (green arrows). Additionally, a scattering process of two pump polaritons towards the TE-branch on one side and the TM-branch on the other side (cyan arrows) is possible provided small frequency shifts occur so as to fulfill resonance and phase-matching condition. The corresponding radii for each process are indicated by vertical lines. Courtesy of P. Lewandowski.

Relative intensities The “X₁X_d” process mainly conserves the pseudospin of polaritons (pump, probe and FOFWM signal have the same linear polarization). The “Y₁Y_d” probes processes reverses the pseudospin of polaritons (two X polarized pump polaritons *vs* Y-polarized probe and FOFWM signal). These two processes are spin conservative.

On the contrary, X₁Y_d and Y₁X_d experiment do not conserve the pseudo-spin of polaritons. No signal would even be detected in those configurations if not for the TE-TM splitting. This scattering channel is thus much less efficient than the two others.

Overall, the most “efficient” parametric scattering configuration is the Y₁Y_d, the process that reverses the linear polarization, in accordance with the expected values of the spin-dependent polariton-polariton interactions (*cf.* Subsection 1.3.4).

4.3.1.4 Theoretical description

The simulations to analyze the features of the experiment have mainly been developed by Dr. Przemyslaw Lewandowski and Pr. Dr. Stefan Schumacher at Paderborn Universität (Germany). I will present here the main theoretical results.

The angular, wavevector and polarization dependence of the FOFWM signal shown in Fig. 4.22 is a consequence of the interplay between the TE-TM splitting and a spatially anisotropic polariton amplification resulting from the spin-dependent

exciton-exciton interactions for a linearly polarized pump. The former is present even in the linear optical regime, the latter is a nonlinear optical effect.

The main features of Fig 4.22 can be reproduced using a simplified model to describe the evolution of the following quadruplet:

$$\left(\Psi_{\mathbf{k}_{\text{probe}}}^+, \Psi_{\mathbf{k}_{\text{probe}}}^-, \Psi_{\mathbf{k}_{\text{fofwm}}}^{+*}, \Psi_{\mathbf{k}_{\text{fofwm}}}^{-*} \right),$$

where $\Psi_{\mathbf{k}_{\text{probe}}/\mathbf{k}_{\text{fofwm}}}^{\pm}$ are the polariton wavefunctions of the probe and FOFWM signal. $\mathbf{k}_{\text{probe}} = -\mathbf{k}_{\text{fofwm}}$ is the in-plane wavevector of probe or FOFWM signal polaritons. For simplicity, we use the “+” and “-” circular polarization basis (where the polariton-polariton interactions $\alpha^{+\pm}$ take a simple form).

Assuming a plane wave for the pump and in the rotating frame approximation, the evolution of the quadruplet is given by the sum of three hamiltonians:

$$\mathbb{H} = \mathbb{H}_0 + \mathbb{H}_{\mathbf{k}}^{\pm} + \mathbb{H}_{\text{NL}}.$$

The first term is a diagonal hamiltonian and reads:

$$\mathbb{H}_0 = \begin{pmatrix} \Delta E_{\text{probe}}^+ & 0 & 0 & 0 \\ 0 & \Delta E_{\text{probe}}^- & 0 & 0 \\ 0 & 0 & -\Delta E_{\text{fofwm}}^{+*} & 0 \\ 0 & 0 & 0 & -\Delta E_{\text{fofwm}}^{-*} \end{pmatrix},$$

where $\Delta E_{\text{probe}/\text{fofwm}}^{\pm} = E_0^{\text{p}} + \frac{\hbar^2 \mathbf{k}_{\text{probe}/\text{fofwm}}^2}{4} \left(\frac{1}{m_{\text{p}}^{\text{TE}}} + \frac{1}{m_{\text{p}}^{\text{TM}}} \right) - \hbar \omega_{\text{pump}} - i\gamma_{\text{p}}$ is the pump energy detuning with respect to the polariton energy at the in-plane wavevector $\mathbf{k}_{\text{probe}/\text{fofwm}}$.

$\mathbb{H}_{\text{TE/TM}}$ includes the TE-TM splitting, and following eq. (1.17), can be written:

$$\mathbb{H}_{\mathbf{k}}^{\pm} = \begin{pmatrix} 0 & \Delta_{\mathbf{k}_{\text{probe}}}^{\text{p}+} & 0 & 0 \\ \Delta_{\mathbf{k}_{\text{probe}}}^{\text{p}-} & 0 & 0 & 0 \\ 0 & 0 & 0 & -\Delta_{\mathbf{k}_{\text{fofwm}}}^{\text{p}+*} \\ 0 & 0 & -\Delta_{\mathbf{k}_{\text{fofwm}}}^{\text{p}-*} & 0 \end{pmatrix},$$

where $\Delta_{\mathbf{k}_{\text{fofwm}/\text{probe}}}^{\text{p}+} = \Delta_{\mathbf{k}}^{\text{p,TL}} e^{-2i\phi}$.

Finally, \mathbb{H}_{NL} includes the nonlinear terms introduced in Subsection 1.3.4. Contrarily to the previous section (eq. (4.4)), the scattering processes towards $-\mathbf{k}$ are now taken into account, such that \mathbb{H}_{NL} reads:

$$\mathbb{H}_{\text{NL}} = \begin{pmatrix} B^+ & U^+ & V^+ & W^+ \\ U^- & B^- & W^- & V^- \\ -V^{+*} & -W^{+*} & -B^{+*} & -U^{+*} \\ -W^{-*} & -V^{-*} & -U^{-*} & -B^{-*} \end{pmatrix},$$

where

$B^\pm = 2\alpha^{++} |\Psi_0^\pm|^2 + \alpha^{+-} |\Psi_0^\mp|^2$ includes the pump-induced blueshift of the polariton energies, $U^\pm = \alpha^{+-} \Psi_0^{\mp*} \Psi_0^\pm$ is the coupling between counter-circularly polarized polaritons with the same in-plane wavevector. $V^\pm = \alpha^{++} \Psi_0^{\pm 2}$ and $W^\pm = \alpha^{+-} \Psi_0^\pm \Psi_0^\mp$ include the four-wave-mixing process coupling probe, pump and FOFWM signal.

The variation of $\Psi_{\mathbf{k}_{\text{fofwm}}}^\pm$ as a function of the pump/probe polarizations, \mathbf{k} , and ϕ is easily computed, which must be transformed in the linear polarization basis to reproduce the experimental configurations. The result from this simplified model exhibit a fair agreement with the main features of the experiment.

The numerical results presented in Fig. 4.22, though, were computed with a full theoretical analysis using separate equations for excitons and photons formulated in the real space to take into account the finite pump spot size. The full model and the simulation parameters are detailed in our article [Lewandowski2016].

4.3.2 Second order four-wave mixing

A full experimental and theoretical investigation on the pairwise scattering of two pump polaritons into two off-axis modes (process FOFWM represented on Fig. 4.18.a.) is extensively studied in the last subsection. We now study the second four-wave mixing process shown on Fig. 4.18.b., involving three off-axis modes and one pump polariton (second-order four-wave mixing or SOFWM process). Because of the phase-matching conditions, this scattering mechanism occur *only* in an hexagonal geometry, contrarily to the two other processes represented on Fig. 4.18.

Above the OPO threshold, the off-axis modes are unstable. They lead to the formation and stabilization of patterns in the far field such as hexagons [Ardizzone2013b]. The SOFWM process is therefore worth studying to understand the hexagonal pattern formation mechanism and its pseudo-spin selection rules.

4.3.2.1 Experimental setup

For the SOFWM, a second cw probe with same frequency, intensity, and polar angle of incidence is sent on the cavity (refer to Fig. 4.19.b.). If the azimuthal angle separating the two probes is 120° , phase matching conditions are fulfilled and the two probes can stimulate scattering of one pump polariton into an off-axis mode at $\mathbf{k}_{\text{SOFWM}} = \mathbf{k}_{\text{probe1}} + \mathbf{k}_{\text{probe2}} - \mathbf{k}_{\text{pump}}$, triggering a SOFWM signal on the elastic

circle in-between the two probes. In order to conduct polarization-selective experiments, we again stay below the OPO threshold.

In Fig. 4.24 the measurement configuration in the full momentum space is shown. The pump at normal incidence is at the center of the far-field. The two probes are sent at oblique angle so that they are resonant with the elastic circle. They are separated by 120° on the elastic circle. If pump and probes are correctly aligned and sufficiently intense (typically 50 mW), three idler beams should spontaneously be triggered: the FOFWM processes for pump and probe 1 and 2 each trigger a FOFWM signal (called FOFWM 1 and 2 on the figure), and the SOFWM process populates the elastic circle in-between the two probes (inside the white rectangle). This latter signal only appears if both probes are strictly separated by an azimuthal angle of 120° and vanishes abruptly even for small deviations from this geometry. It disappears when either the pump or the probes are suppressed, giving confidence in the validity of our interpretation in terms of SOFWM process.

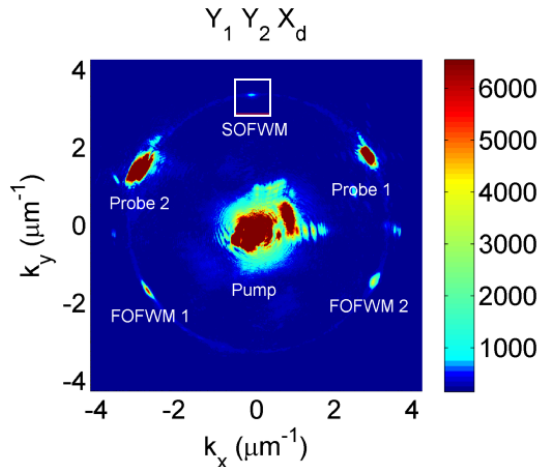


Figure 4.24: Measured second-order four-wave mixing with a pump and two probe beams for two Y-polarized probe beams in X-polarized detection ($Y_1 Y_2 X_d$). A FOFWM process involving the pump and either probe 1 or probe 2 creates FOFWM 1 and FOFWM 2 signals. The SOFWM signal is surrounded by a white rectangle.

In Fig. 4.24, the pump is vertically polarized. The probes are horizontally-polarized (so, cross-polarized to the pump, $Y_1 Y_2$) and the detection is done in the vertical polarization channel (X_d). The FOFWM for probe 1 and probe 2 are distinctly brighter than the SOFWM since each of them involve two pump polaritons and *only* one probe polariton⁵.

In contrast with the FOFWM experiments discussed in the previous section, the pump's polarization will be now *fixed* in the vertical direction.

⁵The probes are sent with a typical optical power and beam waists close to the pump's. However, the density of power on the sample is reduced due to spherical aberrations induced by the ocular L_f (cf. 2.2.3.1).

The probes polarizations can be either vertically polarized (i.e. X, copolarized to the pump's polarization) or horizontally polarized (i.e. Y, cross-polarized to the pump's polarization). We measure the polarization of the resulting SOFWM signal in the X and Y directions.

4.3.2.2 Experimental and numerical results

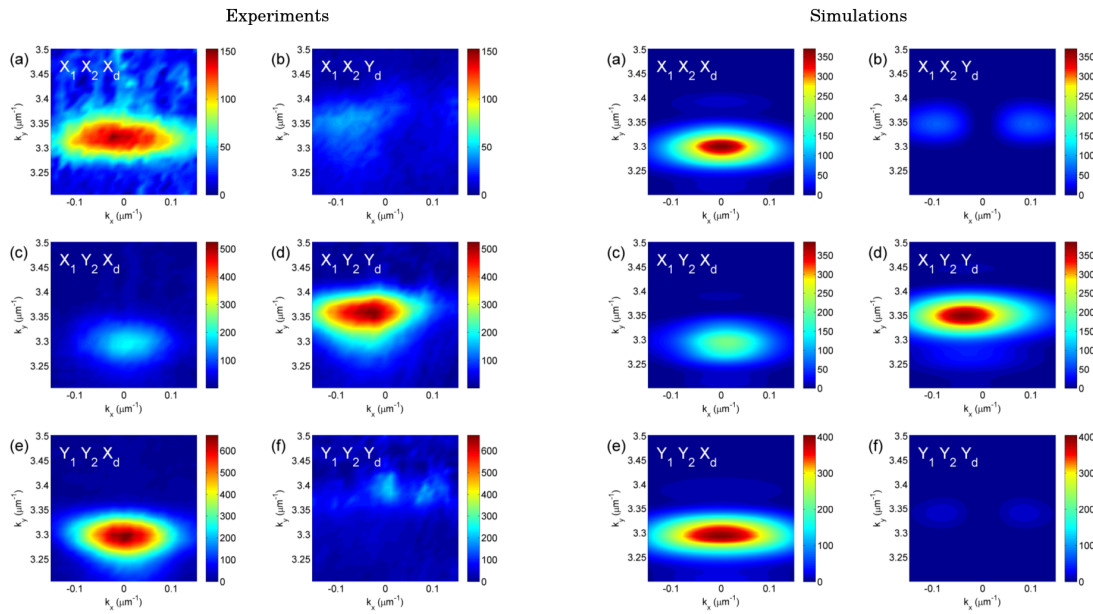


Figure 4.25: Close-up of the k-space region of interest (white rectangle in Fig. 4.24) for the SOFWM signal. Results are shown for the following excitation/detection configurations. The left column (a, c, e) shows the detection in copolarized (X_d), the right column (b, d, f) in cross-polarized (Y_d) detection. Here, either both probes are copolarized (a, b), one probe is co- and the second is cross-polarized (c, d), or both probes are cross-polarized (e, f). Results from the simulations follow the same labelling and are reported in the right panel.

Fig 4.25 shows the result of experiment (left panel) and simulation (right panel) in a zoom in the k-space around the SOFWM signal, for six polarizations configurations:

1. Probe 1, Probe 2 and detection in the vertical polarization channel ($X_1 X_2 X_d$, Figs. 4.25.a.),
2. Probe 1, Probe 2 in the vertical polarization channel and detection in the horizontal polarization channel ($X_1 X_2 Y_d$, Figs. 4.25.b.),
3. Probe 1 and detection in the vertical polarization channel and Probe 2 in the horizontal polarization channel ($X_1 Y_2 X_d$, Figs. 4.25.c.),

4. Probe 1 in the vertical polarization channel and Probe 2, detection in the horizontal polarization channel ($X_1 Y_2 Y_d$, Figs. 4.25.d.),
5. Detection in the vertical polarization channel and Probe 1, Probe 2 in the horizontal polarization channel ($Y_1 Y_2 X_d$, Figs. 4.25.e.),
6. Probe 1, Probe 2 and detection in the horizontal polarization channel ($Y_1 Y_2 Y_d$, Figs. 4.25.f.),

the pump's polarization being fixed in the vertical direction.

The position along k_y of the SOFWM signal matches either the TM (at $3.29 \mu\text{m}^{-1}$) or TE (at $3.35 \mu\text{m}^{-1}$) elastic circles. The same selection rules than the FOFWM are found for the SOFWM:

- The processes which do not conserve polarization ($X_1 X_2 Y_d$, $X_1 Y_2 X_d$ and $Y_1 Y_2 Y_d$, represented on Figs. b., c. and f.) are the weakest.
- The processes that reverses the polarization of two off-axis fields (namely $X_1 Y_2 Y_d$ and $Y_1 Y_2 X_d$, represented on Figs. d. and e.) are more efficient than the one where the polarization is conserved for all fields ($X_1 X_2 X_d$, represented on Fig. a).

The above selection rules mainly arise from the excitonic part of the polariton field, that is, the spin-dependent exciton-exciton interaction parameters $T^{\pm\pm}$ (*cf.* Subsection 1.3.4). In the linear polarization basis, the processes that reverse (conserve) polarization involve the difference (sum) of the two contributions T^{++} and T^{+-} . Since $T^{++} - T^{+-} > T^{++} + T^{+-}$, the strongest signals are found in the configurations $X_1 Y_2 Y_d$ and $Y_1 Y_2 X_d$ rather than in $X_1 X_2 X_d$.

However, due the presence of TE-TM splitting in the cavity field, these purely excitonic selection rules are modified such that weaker SOFWM signals are also found in the “forbidden” polarization channels ($X_1 X_2 Y_d$, $X_1 Y_2 X_d$ and $X_1 Y_2 Y_d$). The simulation presented in Fig. 4.25 are obtained using equation of motions for the excitonic and cavity fields in the real space corresponding to the eight experimental configurations [Lewandowski2016].

Again, the results of the simulation (right panel of Fig. 4.25) reproduce very well the experimental findings. The double structure for the weak signal expected for the $Y_1 Y_2 Y_d$ and $X_1 X_2 Y_d$ configurations (Figs. b. and f.) are hidden in the experiment, probably due to the presence of parasitic pump and probes stray light coming from the pump and probes and/or to remaining elastic Rayleigh scattering effects from the pump or probes towards the elastic circle.

4.3.3 Conclusion

A detailed analysis of the polarization dependence of four-wave mixing processes in a spinor fluid of microcavity polaritons is presented. Numerical simulations per-

formed by our theoretician collaborators well reproduce the experiments for first and second order processes.

In the first order process, the FOFWM signal is largest when probe and detection are cross-polarized to the pump, which is consistent with the fact that exciton-exciton interaction favors scattering of pump polaritons into linearly cross-polarized states. The TE-TM splitting leads to different k -magnitudes for the scattered FOFWM signals. The TE-TM splitting also induce a FOFWM signal in the detection channel that is cross-polarized to the probe. Taken together, these two effects explain the features presented in Fig. 4.22.

In the second order process, two probes separated by 120° on the elastic circle in addition to the normally-incident pump yields a SOFWM signal on a location on the elastic circle defined by the phase-matching conditions, proving that wave mixing processes favoring 60° scattering on the elastic circle are present in the system. The polarization selection rules for the SOFWM process are also investigated. Since the numerical simulations based on two-exciton correlations reproduces well the data, the addition of higher-order nonlinearities is not necessary, even though two-probe experiments are in principle sensitive to them.

We note that these pump-probe(s) experiments offer an optical analogue of the logical AND gate: the FOFWM (SOFWM) signals appears *only* if both pump and probe 1 (and 2) beams are simultaneously sent to the sample.

To conclude, two FWM mechanisms are evidenced and characterized in this section in the parametric scattering regime. They play a key role in the pattern formation mechanism emitted by a double microcavity *above the OPO threshold*, presented in the following section.

4.4 Pattern formation in the Optical Parametric Oscillation regime

In the previous section, one or two probes have been use to seed parametric amplification processes. In this regime, off-axis signals on the elastic circle are amplified by resonant scattering of pump polaritons. When the amplification gain outweighs the polariton loss, exponential growth of off-axis signals happen, and the spatially homogenous polariton field becomes unstable [Ardizzone2013b, Luk2013, Saito2013, Egorov2014]. When this “instability threshold” is reached, the regime of Optical Parametric Oscillation is achieved (refer to Subsection 1.2.2). Furthermore, a spontaneous breaking of spatial symmetry arises, and the polariton fields self-organize to form patterns in the far field and the near field.

Experimentally, this threshold is crossed at large pump powers (typically over 100 mW) at a small negative exciton-photon detuning (typically -5 meV). The pump excitation energy must be resonant with the LPB₂ branch blueshifted due to exciton-exciton interactions and phase-space filling (*cf.* Subsection 1.2.2.4). Furthermore, the pump must be linearly polarized and sent to a spot where the density of defects

4.4. PATTERN FORMATION IN THE OPTICAL PARAMETRIC OSCILLATION REGIME

is reduced. As detailed in the previous section 4.3, the parametric effects that reverse polarization are the most efficient. Therefore, we observe OPO patterns in the channel *cross-polarized* to the pump. In the co-polarized channel, the pump stray light blurs the signal on the elastic circle, hiding any potential pattern formation.

Fig. 4.26 shows various kinds of patterns experimentally obtained above the instability threshold. The pairwise scattering of polaritons imposes indeed a symmetric even pattern such that two, four, six and eight points patterns are observed depending on experimental conditions. The intensity of the off-axis fields forming the pattern are typically a few tens of μW [Ardizzone2013a].

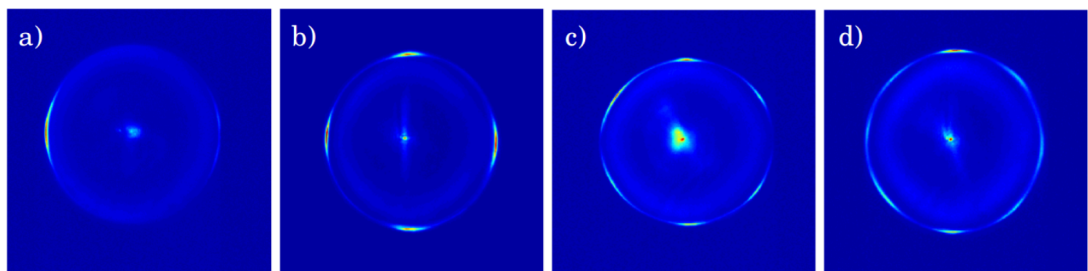


Figure 4.26: Examples of patterns formed by various polariton densities located on the elastic circle obtained in the far field above the instability threshold. The pump, linearly polarized, is at the center of each picture. The detection is done in the cross-polarized channel to the pump. a) Two-points pattern observed in the horizontal direction, b) Four-points pattern, c) Hexagonal pattern, d) Octagonal pattern.

This pattern formation process is formally similar to the formation of Turing patterns on certain animal furs such as zebra or guepars, the convection rolls in hydrodynamics or the famous Salar of Uyuni in Bolivia where the water evaporation creates specific salt patterns on the ground (see Fig. 4.27).



Figure 4.27: In the desert of Uyuni (Bolivia), the evaporation of water in a salt desert creates patterns on the ground.

In optics, similar phenomena have been observed in the far-field of atomic vapours

[Maître1994] and optical parametric oscillators [Ducci2001]. The advantage of microcavities is that they allow coupling between light and matter, such that quasi-particles can indeed have non-linear interactions (which is not possible with bare photons). Turing patterns have been predicted to arise in semiconductor microcavities [Schumacher2009, Dawes2010, Luk2013] and then experimentally demonstrated in our group [Ardizzone2013b]. The control over these patterns has been demonstrated by Vincenzo Ardizzone, either by slightly tilting the pump incidence angle, or by using a second “control” beam (a probe beam resonant with the elastic circle) [Ardizzone2013b].

In this section, I first present the various experiments realized to understand the key parameters responsible for the selection of 2, 4, 6 and 8 points patterns. Until now, only the hexagonal pattern formation mechanism is fully understood by theorists, so this first subsection is almost entirely experimental. The influence of the pump polarization on the *pattern orientation* (defined by the direction formed by its most intense points) is analyzed in detail. In the second part, I discuss the observation of the hexagonal pattern in the near field, and then the possible applications of this pattern formation regime in the perspective of all-optical switch devices.

4.4.1 Key experimental parameters

The main experimental parameters allowing to switch from one pattern to another are:

1. The exciton-photon detuning,
2. A small incident k_{pump} (tilt of the pump out of normal incidence),
3. The energy mismatch between the pump photons and the minimum of LPB_2 ,
4. The pump power,
5. The pump polarization,
6. The density and nature of defects.

The parameter space is therefore quite large and the various degrees of freedom are not easily disentangled.

Additionally, the nature of the excitation source has also revealed to be of particular importance for the observation of patterns. The MIRA laser being intrinsically multimode, we decided to use the cw Soltis laser as the excitation source. Quite surprisingly, no degenerate OPO (necessary condition for the pattern formation on the elastic circle) was observed. This experimental result is discussed in Subsection 4.4.1.5.

The last parameter listed (density and nature of defects) is difficult to estimate from an experimental point of view, but it certainly has a great importance:

the higher the defect density, the more efficient the Rayleigh scattering, which thus compete with the pattern formation process, or can “pin” the OPO in certain directions [Abbarchi2012].

The other degrees of freedom listed above are discussed one by one in the following.

4.4.1.1 Influence of the exciton-photon detuning

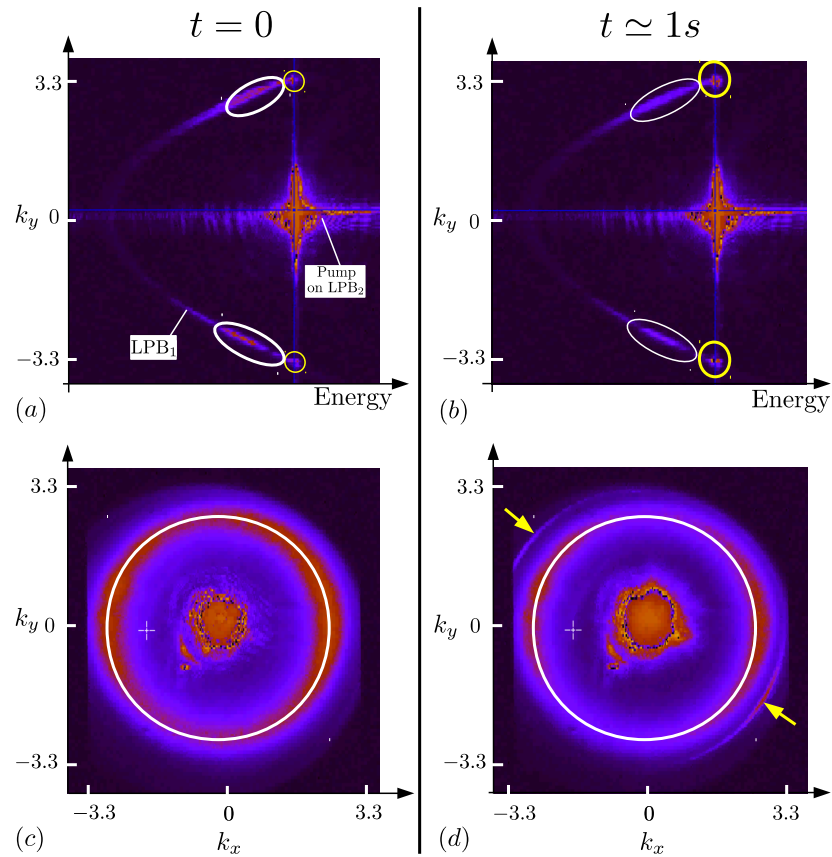


Figure 4.28: Competition between the “relaxation ring” and the pattern formation at low exciton-photon detuning. (a, b) Energy dispersions as a function of in-plane wavevector at $t = 0$ and $t = 1$ s. (c, d) Corresponding far-field images. Left panel (a, c): At $t = 0$, the relaxation ring (white markers) is favored. No pattern is observable on the elastic circle. Right panel (b, d): 1 s later, a pattern appears on the elastic circle (indicated by the yellow arrows and circles) and the relaxation ring intensity is much reduced. Note that the elastic circle is partially hidden by the spectrometer vertical entrance slit.

The exciton-photon detuning (first parameter) plays a rather ambivalent role. A low negative detuning ensures stronger polariton-polariton interactions (since the excitonic fraction of the polariton is larger). However, phonon-assisted relaxations

towards the bottleneck of the LPB₁ branch [Müller2000] creates a *relaxation ring*, visible on the above Figs. 4.26.b., c. and d. This inelastic relaxation process is more efficient at low negative detuning, and an oscillation at large timescales (typically 1 s) between the pattern on the elastic circle and the polaritonic population on the relaxation ring is sometimes observable (see Fig. 4.28). The timescale suggests that the oscillation is due to a warming effect.

4.4.1.2 Effect of a small pump tilt and resonant energy

The influence of a small incident k_{pump} (second parameter) has been probed in the (x, y) space using two glass slides automatically orientable around the x and y axis. Indeed, a glass slide of thickness t and refractive index n tilted by an angle θ_g shifts an optical beam by a distance d (refer to Subsection 2.1.2). The resulting incident angle θ incident onto the sample after a lens of focal f is:

$$\tan \theta = \frac{t}{f} \cdot \frac{\sin(\theta_g - \theta_r)}{\cos \theta_r},$$

where $\theta_r = \arcsin \frac{\sin \theta_g}{n}$ is the refraction angle at the air/glass interface. At the lowest order, we obtain $\theta \simeq \frac{t}{f} (\frac{n-1}{n}) \theta_g$.

This experimental method allows to shift precisely the pump incidence, every other parameters being fixed.

Fig. 4.29 shows the result of two experiments with the same laser energy with an incoming power of 150 mW and a fixed vertical polarization. The two glass slides allow to vary $\theta_{d,x}$ and $\theta_{d,y}$ from -30° to 30° every 3° which corresponds to an angle of incidence varying from -0.65° to $+0.65^\circ$ in the x and y direction (since $t \simeq 1$ mm and $f \simeq 16$ mm), or an in-plane wavevector varying between $\simeq -0.09$ and $0.09 \mu\text{m}^{-1}$ (we recall that $k_{\parallel} \simeq \frac{E_0^c}{\hbar c} \sin \theta$, cf. Subsection 1.1.2.4).

The sample position was slightly shifted between the two experiments so as to tune the resonance conditions between the excitation energy and the energy of the minimum of LPB₂ (third parameter). In the left panel of Fig. 4.29, the minimum of LPB₂ is slightly redshifted (approximately 100 μeV) compared to the laser energy.

4.4. PATTERN FORMATION IN THE OPTICAL PARAMETRIC OSCILLATION REGIME

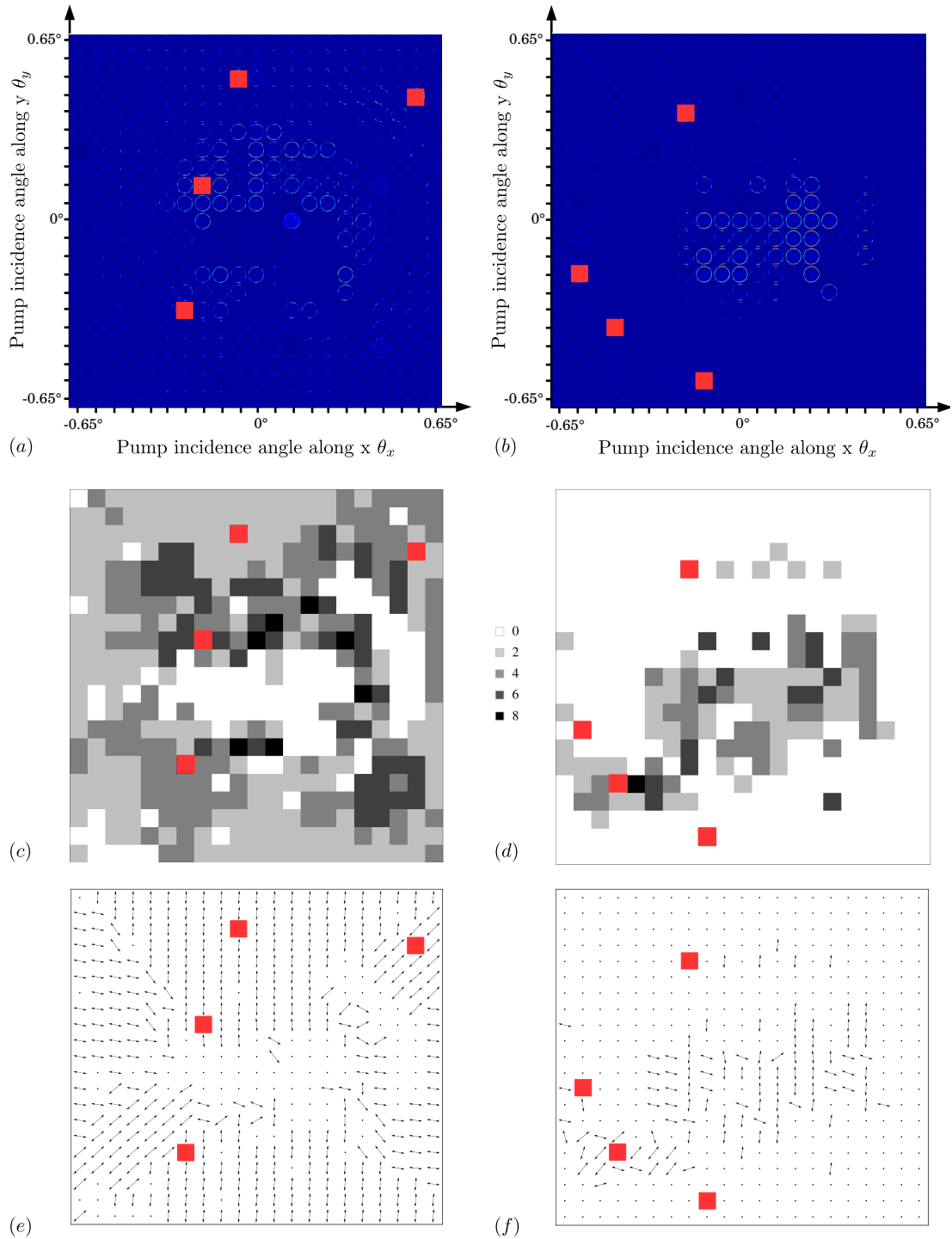


Figure 4.29: The left panel (a, c, e) corresponds to the situation where the minimum of LPB_2 is slightly redshifted with respect to the laser energy, the right panel (b, d, f) where the laser is resonant with the minimum of LPB_2 . (a, b) 21×21 images of the k-space obtained for various values of the incidence angle of the pump θ_x and θ_y . This map allows to visualize the intensity of the far-field emission and the possible presence of patterns as a function of θ_x and θ_y . However, the characteristics of the observed patterns are hardly visible at this scale. Therefore, the number of points defining the patterns are reported on (c, d) and their orientation in (e, f), as a function of θ_x and θ_y . Buggy acquisitions are hidden by red rectangles. 159

Besides the intensity of the far-field emissions, the results presented in Fig. 4.29 give two more facts: the nature of the pattern (2, 4, 6, 8 points points), indicated by a square in different grey levels, and its orientation, indicated by an arrow.

In Fig. 4.29.b., the patterns observed at $\theta_x \simeq \theta_y \simeq 0$ are the most intense, and they are mainly oriented in the direction of the pump polarization (vertical). In Fig. 4.29.a., no pattern is observed at $\theta_x \simeq \theta_y \simeq 0$: close to the normal incidence angles, the excitation is not resonant with the polariton branch. If the excitation beam is slightly tilted, the resonance condition is recovered and a pattern arises. For small pump tilts, high order patterns (4, 6, 8 points) seems to be favored. At higher pump tilts (close to 0.65°), two-points patterns are selected, mainly oriented in the direction of the pump tilt.

Besides these general remarks, no simple and robust law linking the pattern nature or orientation with the tilt angle is exhibited. In particular, the maps presented in Fig. 4.29 are not perfectly centro-symmetric. The fixed polarization of the pump, the presence of a TE-TM splitting of LPB₁ and also, for non-normal incidences, of LPB₂, as well as the presence of a built-in polarization splitting (*cf.* Subsection 4.1.3.3) may cause anisotropies responsible for the breaking of rotational invariance. In addition, other experiments suggest that the pattern formation process depends also on the running direction of the experiment, signature of a bistable behaviour.

4.4.1.3 Influence of the incident power

The incident excitation power (fourth parameter) is explored by shifting the pump power from 29 mW to 100 mW, every other parameters (including the pump linear polarization) being fixed. Since the pump spot has a size of approximately $50 \mu\text{m}$, this corresponds to excitation densities varying from 1160 to 4000 W.cm^{-2} .

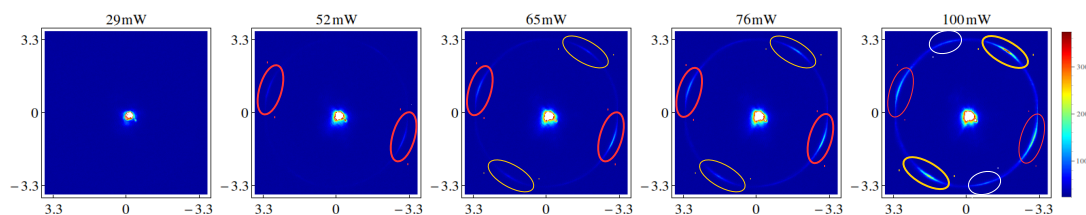


Figure 4.30: Intensity of the far-field emission in arbitrary units for 5 values of the pump power. The pump is on the center. A pattern progressively appears, from two points at 52 mW, to four at 65 mW and six at 100 mW. Each couple of points are surrounded by ellipses as guide to the eyes. At 100 mW, the orientation of the pattern (defined by the two most brilliant points) switches.

A two-points pattern first appears at a pumping power of 52 mW (marked in red in Fig. 4.30). A second and weaker couple of points appears at 65 mW (marked in yellow in Fig. 4.30). At 76 mW, the intensity of the whole four-points pattern

increases. At 100 mW, the two most brilliant points are now the ones marked in yellow, and a third weak couple of points appears in-between the two first directions (marked in white).

Hence, the pattern switches from a two-point pattern to a hexagon within a pump power of 29 and 100 mW, and the two most brilliant points switches from the ones surrounded in red to the ones surrounded in yellow. We conclude that large pump powers tend to induce the formation of high-order patterns, as well as a change in the orientation of the pattern.

4.4.1.4 Orientation of patterns with polarization

At pump powers over 100 mW, the orientation of the pattern (defined by its two most brilliant points) follows the direction of the pump polarization (fifth parameter). This behavior is relatively new in microcavities, in which the OPO is usually pinned to defects-induced specific axes (mainly, the crystalline axes which correspond to favored directions for dislocations) [Lecomte2011, Abbarchi2012].

This new characteristic arises due the relatively low density of defects in our sample, such that it is now the TE-TM splitting which dictates the preferred directions for the OPO. We have shown in Subsection 4.3.1 that the parametric scattering is favored (i) for signal and idler cross-polarized to the pump, and (ii) in the azimuthal directions corresponding either to the direction of the pump polarization or to the direction orthogonal to it, since the states cross-polarized to the pump match either the TE or TM elastic circle respectively in those directions. Theoretically, the pattern orientation should hence be either in the direction of the pump polarization, or orthogonal to it. Experimentally, in the range of $\simeq 100$ to 150 mW pump powers, we will see that it is mainly the former possibility which is observed (though the latter may occur at lower or higher pump powers as suggested by the discussion in the previous subsection). This experimental observation can be explained theoretically if anisotropic TE-TM cavity losses are taken into account (see Subsections 1.3.1.1 and 4.1.3.2).

In this subsection, we first demonstrate the rotation of a two-points pattern with the pump polarization over 360° . This is similar to a microscopic lighthouse device without mechanical parts: the direction of the emitted light can be directly controlled by a simple degree of freedom (the polarization of excitation). Then, the influence of the pump polarization on higher-order patterns is discussed.

Two-point pattern rotation with polarization: the “Lighthouse” experiment

The pump is initially polarized in the vertical direction. The other experimental parameters are chosen such that a stable two-points pattern is favored (see Subsection 4.4.1.2 and 4.4.1.3).

The pump linear polarization is then (automatically or manually) rotated. Fig. 4.31 shows the k-spaces corresponding to four different directions of the pump polarization.

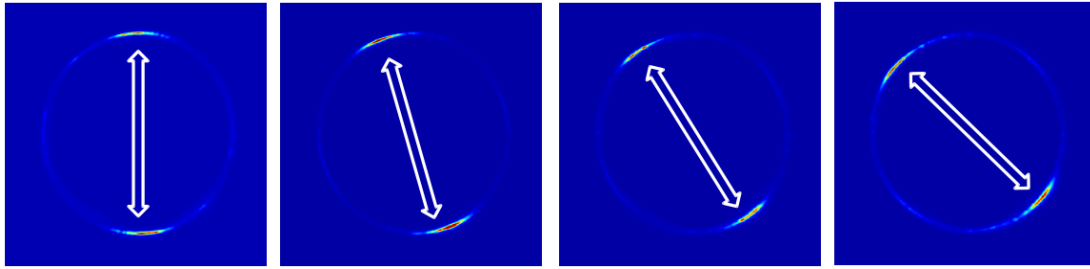


Figure 4.31: Far field image of the light emitted by a double microcavity resonantly pumped on LPB_2 , and cross-polarized to the pump. A two-spot pattern is observed. The orientation of those two points follows the polarization of the pump (white arrow).

Pictures were taken regularly for a pump polarization direction varying between 0 and 360° . For each picture, the variation of the emission along the circumference of the elastic circle is analyzed.

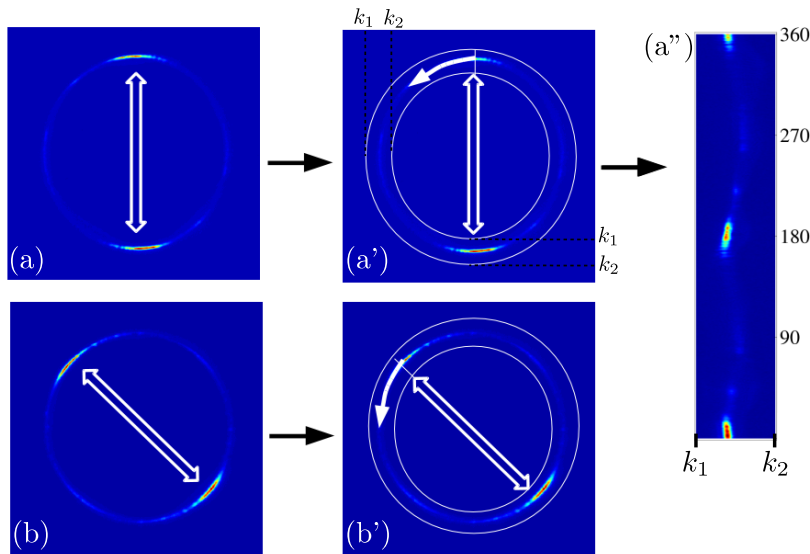


Figure 4.32: (a, b): k -space for two directions of the pump polarization (indicated by the white arrows). (a', b') The elastic circle is opened starting from the direction of the pump polarization, such that 0° corresponds to the direction of the pump polarization. (a'') The intensity along the azimuthal angle of the flattened elastic circle is plotted between chosen k_1 and k_2 . The result does not display a straight line due to the TE-TM splitting and possible optical misalignments, but this does not matter since the intensity is then integrated between k_1 and k_2 such that one single stripe (not represented) is obtained for one value of the pump polarization.

In order to represent the whole set of data in a compact way, for each picture we “open” the elastic circle starting with the angle of the pump polarization angle

(see Fig. 4.32), and then integrate its intensity between chosen k_1 and k_2 (see Subsection 4.2.1.2).

For each pump polarization such a stripe is obtained and we obtain a 2D map of the microcavity emission. The horizontal axis corresponds to the polarization of the pump $\phi_{\text{pol,pump}}$, the vertical axis to the azimuthal angle φ along the elastic circle where 0° correspond to the direction of the pump polarization.

The result for two different sets of experiments are shown in Fig. 4.33, below:

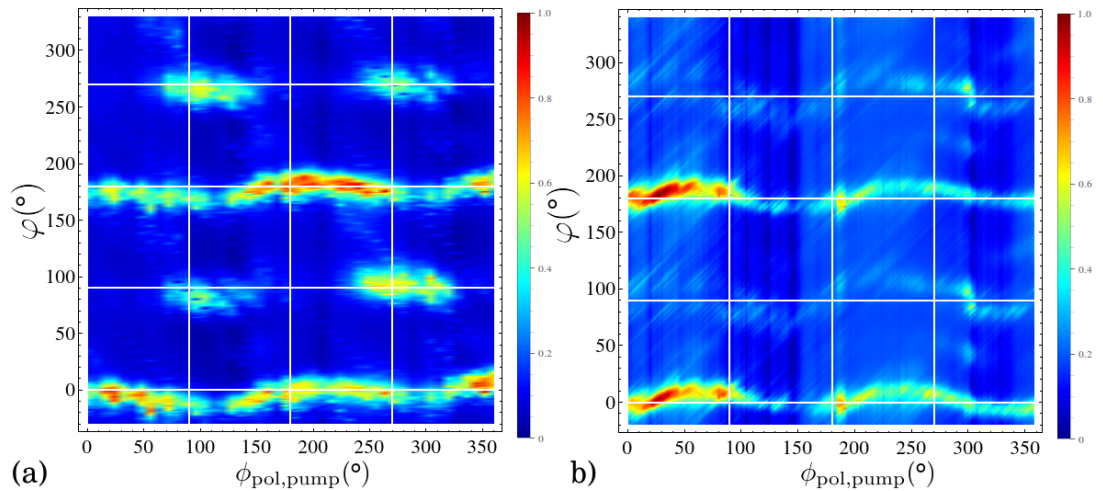


Figure 4.33: Result of two “lighthouse” experiments. The pump polarization is rotated with steps of 8° in (a) and of 1° in (b). One measurement corresponds to a vertical stripe. The continuous lines at 0° and 180° demonstrate that the two point pattern indeed rotates with the pump polarization.

First, looking at the emission at 0° and 180° , we realize that the orientation of the two point pattern follows well the direction of the pump polarization. The rotation of the two-points pattern is therefore demonstrated over 360° .

Note that additional emission is also observed for well defined orientations of the pump polarization in Fig. 4.33.a. Between 90° and 110° , and 250° and 320° , two more spots appear in the direction orthogonal to the pump polarization: a four-points pattern arises. This breaking of rotational symmetry indicates the presence of an extrinsic anisotropy, which might either come from the emission from a defect, the presence of a built-in energy splitting (see Subsection 4.1.3.3), or the presence of anisotropic TE-TM cavity losses (see Subsection 4.1.3.2)... If the experimental conditions are such that the pump is slightly tilted out of the normal incidence, a secondary preferred direction for the light emission might also occur. The presence of the two other points is also visible in Fig. 4.33.b.

In general, the direction of the two most brilliant points in both experiments is parallel to the direction of the pump polarization. This behaviour and its possible applications are discussed in the following paragraph.

Towards a micro-lighthouse device? Such rotation of a two points pattern with the pump polarization is, we believe, the first realization of a *micro-lighthouse device*. Indeed, the continuous control of the light emission direction at the microscopic scale requires three ingredients: (i) a rotational invariance, (ii) a local control degree of freedom α , and (iii) a nonlinear process linking the emission intensity direction I with α . Else, any linear combination of two different values of α would result in a light emission in two different directions, which is incompatible with a lighthouse effect.

The double microcavity resonantly pumped at normal incidence at a large power:

- is planar and therefore in principle rotational-invariant (if we neglect the built-in energy splitting and the presence of various defects),
- reemits light in the direction of the pump's polarization,
- hosts nonlinear processes due to the excitonic component of the polaritons.

This sample is therefore well-adapted for the realization of a microscopic lighthouse device, with potential applications in telecommunications (as an ultra-fast optical switch) or optical microscopy (as an ultra-fast scanning apparatus), provided the time-scale for the pattern formation is indeed of the order of picoseconds as theoretically expected [Ardizzone2013b]. Hence, by an ultra fast modulation of polarization of an optical pump, such device could allow to get very precise temporal informations since the informations received at each time unit can be spatially separated. The functioning is similar, in principle, to a streak camera.

Polarization influence on higher-order patterns Regarding the influence of the pump polarization on higher-order patterns (4, 6 and 8 points patterns), an analogous phenomenon is observed: the two brightest point remain aligned with the polarization of excitation (see Fig. 4.34). However, the pattern switches from an octagonal pattern (visible on the first image of Fig. 4.34.a. which corresponds to a vertical pump polarization) to a two-point pattern (24° pump polarization) and finally a four-point pattern (48° pump polarization). Fig. 4.34.b. shows the analyzed set of experiments for pump polarization directions ranging from 0° (vertical polarization) to 180° . Apart from the two main points aligned in the direction of the pump polarization (horizontal lines at 0° and 180°), some parallel diagonal lines are apparent, corresponding to fixed angles ($\simeq 45^\circ$ and 225° in plain line, $\simeq 148^\circ$ and 328° in dashed lines) angles which may be the signature of built-in dislocations [Abbarchi2012].

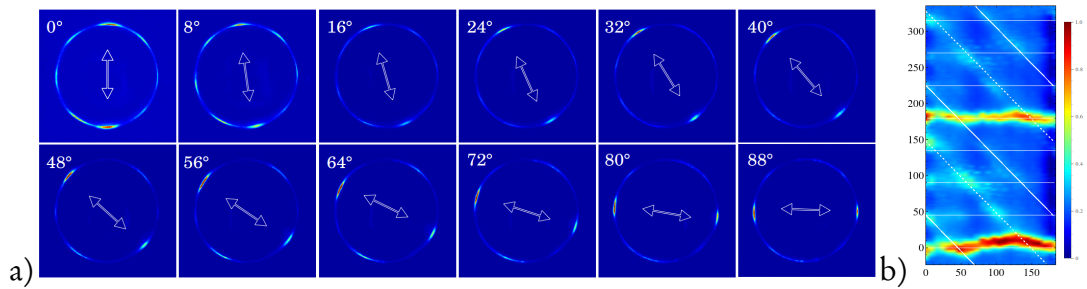


Figure 4.34: a) k-space images for 12 various pump polarization directions (steps of 8°) indicated by the white arrow. The two brightest points stay aligned with the direction of the pump polarization. b) 2D-map showing the microcavity emission along the elastic circle (y axis) for pump polarization directions varying between 0° and 180° (x axis). The data analysis is detailed in the previous paragraph.

The control of the pattern orientation by the pump polarization seems therefore quite robust, even if the nature of the pattern changes, probably because of various built-in anisotropies.

4.4.1.5 Nature of the excitation source

In order to test the resonance between the pump energy with the minimum of LPB₂ (third parameter), we tried to use the Solstis laser instead of the usual MIRA, which wavelength can be finely tuned. Additionally, it exhibits a much better intensity stability than the MIRA as well as a much smaller spectral width (see Subsection 2.1.4). Interestingly, with this laser, no degenerate OPO was observed on the angle-resolved energy dispersion (and, as a result, no pattern in the k-space). The OPO signal and idler beams appeared only when the pump was slightly tilted out of normal incidence and when no feedback loop (ensuring the stability of the emitted wavelength and a narrow spectral width) on the Solstis was activated.

This observation could be explained by two possible mechanisms:

1. The blueshift due to phase-space filling is so strong that a wide excitation spectrum is necessary to remain in resonance conditions.
2. The fast intensity oscillations of the MIRA laser introduce instabilities which are necessary for the pattern formation.

Additionally, when the optical excitation is provided by the MIRA laser, if the Faraday isolator (see Subsection 2.1.1) is removed on the optical path, the OPO threshold goes down to a few mW (compared to the usual threshold around 100 mW). This seems to indicate that a multimode excitation might be requisite for the observation of patterns. This is not included so far in the theory developed by our theoretician collaborators and may need further experimental development to carefully understand the exact process at stake.

4.4.1.6 Conclusion

In conclusion, the comprehensive study of patterns, including the number of points and their relative intensities, involve a large parameter space.

The pattern orientation for a normally-incident pump beam seems to depend quasi entirely on the pump's polarization direction, due to the large magnitude of TE-TM splitting and the relatively small density of defects compared to the previous samples. For usual pump powers (between 100 and 150 mW), the pattern is oriented in the direction of the polarization, such that a micro-lighthouse effect is achieved. On the other hand, if the pump is slightly tilted while the polariton branch energy is slightly tuned to achieve resonance conditions, the high-order pattern switches to a two-point pattern mainly oriented in the direction of the tilt. The nature of the excitation source is an important parameter as well. The degenerate OPO threshold is reached only for a multimode fast-oscillating laser (the MIRA). This may be a result of the strong blueshift or induced instabilities (the OPO threshold being reached only momentarily for example).

Finally, the role of defects, however difficult to probe, may come into play in the formation mechanism of eight and four point patterns. If this interpretation is correct, it means that formally, the eight and four point patterns are not truly Turing patterns, resulting from nonlinear interactions associated with a spatial coupling term, but a combination of nonlinear interactions and defect-driven optical parametric oscillation processes. Besides this defects influence, we note that the formation of a hexagon is theoretically not favored if the "second-order" process shown in Fig. 4.18.b. is suppressed. This may indeed be the case if additional selection rules regarding the symmetries of the two involved cavity modes (which vary as a function of detuning) are taken into account.

The next subsection is devoted to hexagonal patterns, which are well described by the theory of Turing patterns developed by the theoreticians of Tucson, Paderborn and Hong Kong.

4.4.2 Hexagonal pattern properties

The formation of hexagonal pattern is well understood theoretically as a result of a competition between multiple unstable modes. The mechanism driving the hexagon formation is induced by the hexagon-specific higher-order nonlinear interaction process of polaritons illustrated in Fig. 4.18 in the introduction of Section 4.3.

Their formation process is described in detail and probed in references [Ardizzone2013b, Lewandowski2015, Lewandowski2016]. In this manuscript, I focus on two aspects of the hexagonal pattern:

1. The observation of hexagonal patterns in the near-field,
2. The slight energy non-degeneracy of the four less intense points due to the TE-TM splitting.

4.4.2.1 Observation in the real space

A fully energy-degenerate hexagonal pattern in the k -space should result in a grid of hexagonal spots in the real space (Fourier transform of the k -space). Due to spherical aberrations inherent to our experimental setup, the real space is difficult to observe and interpret (*cf.* the discussion in Chapter 2).

Nevertheless, we⁶ observed a pattern in the real space (using the experimental setup shown in Fig. 2.20) that exhibits the correct features:

- it appears and disappears with the hexagon in the k -space (for example when we shift the sample so as to get out of resonance, when the OPO ring is hidden using a pinhole in the intermediate angular space or when the pump polarization is rotated inducing a pattern switch).
- it does not depend on other experimental parameters (e.g. the size of the spatial filters used to hide the pump in the detection path),
- The size of the pattern in the real space has the relatively good order of magnitude. Indeed, due to the properties of Fourier transform, we should get $\Delta k \cdot \Delta R = 2\pi$, where Δk (ΔR) is the size of the hexagon in the k - (real) space (see Fig. 4.35).

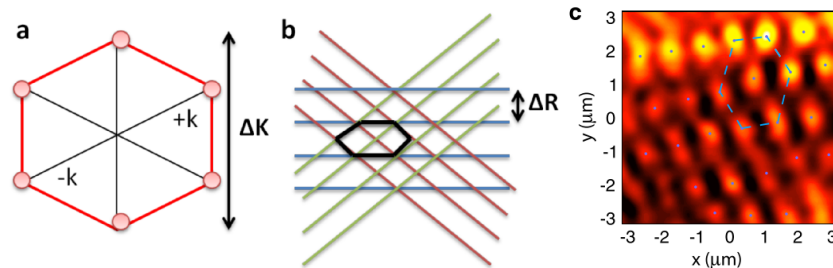


Figure 4.35: Courtesy of T. Champetier. a) Hexagon in the k -space b) Corresponding pattern in the near-field. Due to the properties of the Fourier Transform, $\Delta k \cdot \Delta R = 2\pi$, where $\Delta k \simeq 6.6 \mu\text{m}^{-1}$ d) Experimental near field. We measure $\Delta R_{\text{exp}} \simeq 2 \mu\text{m}$.

However, due to TE-TM splitting, the hexagon is not fully degenerated as will be shown in the next subsection. Therefore, the pattern is supposed to shift with time [Egorov2014] on a nanosecond timescale. If the pattern observed is indeed resulting from the hexagonal pattern in the far field, there must be another mechanism pinning the real-field pattern in time.

⁶This result was achieved by Tatiana Champetier during her master internship in 2013.

4.4.2.2 Presence of a small energy non-degeneracy

The hexagonal pattern exhibits two points brighter than the four others, oriented in the direction of the pump polarization⁷.

The four weaker spots are expected to be slightly detuned from the laser frequency, following the interpretation of the results for the FOFWM process discussed in Subsection 4.3.1.3. In the OPO regime, this statement can be easily tested by observing the energy dispersion of polaritons along y under a resonant pumping on LPB₂. Fig. 4.36 shows the evolution of the y -scattered pump polaritons onto LPB₁ when the polarization of excitation and of detection are rotated together.

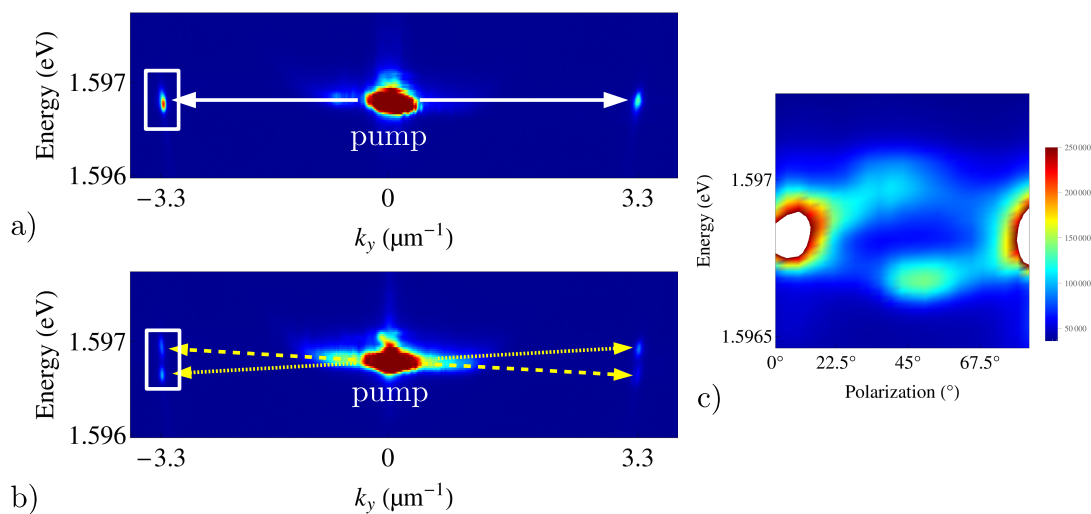


Figure 4.36: a) Energy dispersion as a function of in-plane wavevector. The polarization of excitation is along the vertical direction and the detection is done in the horizontal one. The pump is observed at $k_y = 0$ and the two points of created by Optical Parametric Oscillation are seen at $k_y = \pm 3.3 \mu\text{m}^{-1}$ resonant with LPB₁. b) The polarization of excitation is diagonal and the detection is cross-polarized. Due to the TE-TM splitting, the TE and TM degenerate modes are not populated. Instead, the spots at $\pm 3.3 \mu\text{m}^{-1}$ divide in two spots either on the TM- or the TE- branch, slightly detuned from the pump energy. c) Zoom around the region $k_y = -3.3 \mu\text{m}^{-1}$ (white rectangle on Fig. a. and c.) and polarization of excitation varying between 0° (vertical polarization) and 90° (horizontal polarization). Measurements are taken every 8° and correspond to vertical stripes. The energy splitting is maximum for the diagonal polarization.

⁷Yet, Vincenzo Ardizzone experimentally observed hexagons oriented in the direction orthogonal to the pump polarization during his PhD [Ardizzone2013b, Ardizzone2013a]. This difference may come from the use of a different excitation density. Indeed, the typical excitation powers were kept below 150 mW during this PhD (mainly because of the aging of the VERDI laser), whereas V. Ardizzone had no such limitations and used excitation powers up to 200 mW. The optical path for the excitation has also slightly changed, although, according to our estimations, the pump spot size does not differ.

On Fig. 4.36.a., the pump polarization is vertical (along y) and the detection is done in the cross-polarized channel (so, in the horizontal channel). Two spots corresponding the scattering of pump polaritons towards LPB_1 are observable. They match the TE eigenmode. All the states involved have the same energy. On Fig. 4.36.b., the pump polarization is diagonal, and the detection is done in the opposite diagonal polarization channel. Two spots slightly detuned from the pump energy are created at either side. They result from the scatterings of pump polaritons towards a TM-mode (points at higher energy) and a TE-mode (points at lower energy). This process fulfills phase-matching conditions (see Fig. 4.23).

By varying the pump and cross-polarized detection from 0° (vertical polarization for the pump) to 90° (horizontal polarization) by steps of 8° , a more precise observation of this energy splitting is done. A zoom on the spot(s) emitted at $k_y \simeq 3.3 \mu\text{m}^{-1}$ is realized for each polarization angle. In Fig. 4.36.c., a 2D-map showing the energy of the OPO spot(s) as a function of the pump polarization direction is shown. At 0° and 90° , the detection polarization matches the energy-degenerated TE and TM mode respectively. In-between, the OPO spot splits in two. The blueshifted (respectively redshifted) spot results from the OPO process converting two pump polaritons into one polariton resonant with the TM-branch at $+k_y$ (resp. $-k_y$) at higher energy, and one polariton resonant with the TE-branch at $-k_y$ (resp. $+k_y$) and lower energy. Both processes are highlighted by the dashed and dotted yellow lines on Fig. 4.36.b.

According to these observations, the four weaker points of the hexagonal pattern should therefore be slightly detuned in energy, such that the hexagonal pattern in the near field should not be stable. This disagreement between theory and experiment in the real space suggest the intervention of another effect pinning the hexagon in the real space. More experimental development is needed to understand this discrepancy.

4.4.3 Perspectives for further studies on the patterns

The formation of pattern in the far field results from nonlinear processes fulfilling phase-matching conditions.

In the first part, we have shown that the polarization or a slight tilt of the pump (and the addition of a resonant off-axis probe [Ardizzone2013a]) could be used as control parameters. This result allow to envision various applications such as microcavity-based optical switches and “micro-lighthouses” devices. In this perspective, however, the conversion efficiency from the pump into a far-field pattern in the usual experimental conditions (MIRA laser, optical path described in Fig. 2.2 on page 55), which is at most 0.1%, must be optimized. Several hints suggest that the properties of the excitation source may play an important role. First, we have observed that the OPO threshold was reached at much lower intensities (a few mW instead of a hundred mW) when the multimodal character of the laser was increased (by removing the Faraday isolator on the optical path). Furthermore, no energy-degenerate patterns has been observed when the double microcavity was excited

using the monochromatic and stable Solstis laser.

In the second part, we have discussed the hexagonal pattern properties. Its formation process can be further validated by looking at the classical correlations between each point: classical correlations are expected between dots i and i' (process (a) and (c) of Fig. 4.18 on page 142), between dots 1 and 3 and their circular permutations (process (b) of Fig. 4.18) but *not* between dots 1 and 2 (and their circular permutations). Besides hexagons, the other patterns formation mechanisms can be probed by the same method, allowing to determine whether they arise from defect-induced OPO or by higher-order correlations. Again, this study is possible only if the pump intensity does not fluctuate in the continuous wave regime, to avoid the strong induced correlation background.

To summarize, future studies on patterns will involve the improvement of the light injection efficiency and the clarification of the role of the excitation beam properties in the pattern formation mechanism. If, as we suspect, the present limitations are due to the presence of the bistable blueshift of the polariton branch, another degree of freedom, such as a specific and controllable pump beam-shaping, may be of use to stabilize the pattern formation at lower pump intensities. Finally, in order to confirm the potential of double microcavities in the OPO regime as picosecond-switchable device, we note that the pattern formation dynamics can be investigated by a time-resolved probe experiment.

4.5 Conclusion

We have investigated the polariton-polariton interaction dependence in three different regimes of resonant pumping: the elastic Rayleigh scattering regime, the pattern formation regime, and the intermediate one, the parametric scattering regime which is an excellent way to probe the interplay between the TE-TM splitting of the cavity mode and the spin-dependence of polariton-polariton interactions. The use of a double microcavity allows to perform several scattering mechanisms between the two lower polariton branches LPB₁ and LPB₂.

In the regime of elastic Rayleigh scattering, the TE-TM splitting of the LPB₁ polariton branch induces an Optical Spin Hall Effect (OSHE): a spatial separation in the real and k -space of polaritons with opposite pseudo-spins. We have shown that this phenomenon could be controlled using a strong optical pump beam resonant with with LPB₂ at its minimum since the spin-dependent interactions between pump-polaritons come into play.

In the regime of parametric scattering, experiment involving one or two probe beams have highlighted the important role of the TE-TM splitting to define preferred directions of the idler beam as a function of the polarization of each beam. The first-order four-wave-mixing process (FOFWM) involve two pump polaritons, one probe polariton at $-\mathbf{k}$ and one idler polariton at $+\mathbf{k}$. The second-order four-wave-mixing process (SOFWM) involve one pump polariton, two probe polaritons

separated by 120° on the elastic circle, and one idler polariton in-between. This geometry is specific to fulfil phase-matching conditions, and leads, in the regime of optical parametric oscillation (OPO), to the formation of hexagonal patterns in the far-field.

Besides hexagons, other patterns appear in the far-field such as two-points, four-points and octagonal patterns. Various degrees of freedom allow to switch from one pattern to another. The influence of the various experimental parameters accessible are discussed. Amongst them, the direction of the pump polarization is a robust parameter which dictates the orientation of the pattern. A rotation of a two-points pattern following the pump polarization was hence demonstrated over 360° , similar to a microscopic lighthouse effect.

This work was realized in collaboration with theoretician teams from Paderborn, Tucson and Hong Kong. By extending our understanding and mastering of the mechanisms listed above, it paves the way towards the development of improved application-oriented concepts such as all-optical switches based on semiconductor microcavities or lighthouse devices.

GENERAL CONCLUSION

This work focuses on the polarization properties of excitons-polaritons confined in structured AlGaAs/GaAs microcavities. Microcavity exciton-polaritons are hybrid light-matter quasi-particles arising from the strong coupling between excitons confined in quantum wells and photons confined in the microcavity. The two eigenstates resulting from this light-matter interaction are separated by a normal mode energy splitting of the order of tens of milli-electronvolts. Two kinds of microcavity structuration are studied in this work. Both of them induce at least one additional polariton branch located below the excitonic reservoir. Those polariton modes are therefore well isolated from any relaxation mechanism involving the large density of electronic states of this excitonic reservoir.

In Chapter 3, we have presented the study of the normal energy splitting existing in microwires (1D-microcavities) between polarizations parallel and orthogonal to the wire axis. For the lowest polariton mode, the magnitude of this splitting can reach up to 1 meV, and increases even more with the polariton mode index. Contrarily to previous studies [Diederichs2007], this splitting is found independent of the sticking conditions on the sample holder. It does not depend either on the wire width and its order of magnitude is too large to be solely attributed to an excitonic splitting due to the short-range electron-hole exchange interaction. However, the splitting magnitude follows a universal law as a function of the exciton-photon detuning, which is well reproduced taking into account the interplay of three contributions: a splitting in the cavity mode, of magnitude $-0.73 \text{ meV} \pm 0.07 \text{ meV}$, in the exciton transition ($-0.54 \text{ meV} \pm 0.18 \text{ meV}$) and in the light-matter coupling ($-1.55 \text{ meV} \pm 0.12 \text{ meV}$).

The origin of this splitting is the lattice mismatch between the various layers of Aluminium-Gallium-Arsenide, inducing constraints that are relaxed on the short axis of the wire, but not on the long one. Consequently, a cavity mode normal splitting arises from constraints-induced birefringence in the Bragg mirrors. The basis for this polarization splitting is not strictly along and across the wire axis, but depends also on the crystalline axes, in accordance with the experimental findings. The excitonic and light-matter coupling splittings comes from the combination of the short range electron-hole exchange interaction and constraints-induced Pikus-Bir interaction, which results in a mixing between the light and heavy-hole exciton. Finally, the increase of total splitting magnitude with the polariton mode index is well explained as a result of the presence of an effective confinement angle due to boundary conditions along the wire width, impacting both the cavity mode and the light-matter coupling splitting magnitudes. In each case, the theoretical evaluation well matches the order of magnitude and sign of the three contributions, giving confidence in the validity of this interpretation.

The other structured microcavity presented in this work was a double microcavity (Chapter 4), excited at normal incidence by an optical pump resonant with the highest of the two lower polariton modes. This specific configuration allows an elastic scattering of the pump polaritons towards the lowest polariton branch, either by Rayleigh scattering or by parametric amplification and oscillation.

In the resonant elastic Rayleigh scattering regime, the Optical Spin Hall Effect (OSHE) takes place. Indeed, since circularly-polarized light couples with an exciton with a projection along z (growth direction) of its total angular momentum equal to ± 1 , a polariton pseudo-spin can be defined as a vector of the Poincaré sphere. The presence of a wavevector-dependent TE-TM energy splitting in the polariton states creates an effective magnetic field acting on the polariton pseudo-spin responsible for the so-called OSHE, demonstrated both experimentally and theoretically ten years ago [Kavokin2005, Leyder2007]. This work shows that the presence of spin-dependent polariton-polariton interactions is responsible for a measurable rotation of the TE-TM-induced OSHE polarization pattern. The efficiency of these polariton-polariton interactions can be monitored using a single degree of freedom: the pump optical power. In a device perspective, the lowest polariton branch (populated by Rayleigh-scattered polaritons and splitted in polarization) would be exploited as a signal channel, and the highest (on which the pump is resonant) as a control channel. However further studies are necessary to understand the role of exciton-photon detuning and exact resonance of the pump with the polariton mode.

At larger pump intensities, a degenerate parametric scattering process where two pump polaritons are converted into two polaritons at opposite angles is initiated. At even larger intensities, an instability (or “OPO”) threshold is reached and the off-axis signals become unstable. A stabilization process based on third order nonlinear interactions leads to the emission of light at specific wavevectors forming a hexagon in the k -space. To understand the mechanism responsible for this stabilization, measurements have been performed in the Optical Parametric Amplification regime, using one or two probe beams. The experimental results, which well match the simulations and calculations⁸, highlight the importance of the TE-TM splitting in the formation of patterns as compared to spin-anisotropic polariton-polariton interactions. Moreover, they hint at the mechanism responsible for the orientation of the hexagonal pattern with polarization.

Finally, the far field of the double microcavity microcavity not only exhibits hexagons, but also two points, four points and octagonal patterns. The parameter space of this pattern formation is vast and is discussed in detail in the last part of Chapter 4. Amongst the various degrees of freedom, the direction of the pump linear polarization plays a key role in the pattern orientation mechanism. Hence, the rotation over 360° of a two-point pattern monitored by the pump polarization

⁸This work and the demonstration of the optical control over OSHE were done in close collaboration with theoretician teams from Paderborn (Pr. Dr. Stefan Schumacher and Dr. Przem Lewandowski), Tucson (Pr. Rolf Binder, Pr. Nai Kwong and Samuel Luk), and Hong Kong (Pr. Pui-Tang Leung, Chris Chan).

is demonstrated, paving the way towards a microscopic integrated lighthouse device, with various potential applications such as ultra-fast scanning in optical microscopy or optical switches. All the ingredients necessary for such a device (nonlinearity, rotational invariance, light emission) are combined in their simplest form in this double microcavity in the OPO regime.

These studies open various perspectives for further developments.

1D-microcavities are good candidates for the generation of twin polaritons via Optical Parametric Oscillation, involving scatterings between cross-polarized polariton modes [Abbarchi2011] and are widely used for the generation of polariton condensates [Wertz2010b]. By unveiling the various origins of the normal polarization splitting, the analysis presented in Chapter 3 enables a precise engineering of the 1D-microcavities so as to get the desired splitting magnitude and eigenvectors. Several degrees of freedom are available: the ratios between wire width, length and height, the etching angle relative to the crystalline axes, the exciton-photon detuning and the polariton mode index.

In the double microcavity, if the hexagonal pattern formation mechanism is now rather well understood, this is not the case for the other patterns (especially the octagons). Their stabilization process could be probed by measuring the correlations between the various points forming the pattern. At the moment, this study was hampered by the intrinsic intensity fluctuations of the laser in the continuous wave mode which spoil the self- and cross-correlations signals. Using a stabilized, monochromatic and low-noise laser is thus necessary, but we have experimentally observed in Chapter 4 that such excitation source could not excite any quasi-degenerate pattern in the far field. If this is indeed due to the strong blueshift of the polariton energies at large optical intensities, a specific beam shaping could allow to overcome this limitation. Additionnally, the OPO threshold is expected to be reached at much lower pump intensities.

Finally, the temporal dynamics of the pattern formation could eventually be determined, using a femtosecond pulsed probe excitation to examine how fast the pattern evolves when submitted to a controlled perturbation.

Both studies are essential to evaluate the potential of realistic ultra-fast all-optical switches based on a semiconductor double microcavity operating in the OPO regime.

APPENDIX

Appendix content

A1	Angle-resolved energy dispersion: data analysis and calibration	177
A2	Correction of standard errors to take into account heteroscedasticity	181
A3	Growthsheet of the double microcavity	183

A1 Angle-resolved energy dispersion: data analysis and calibration

In this appendix, the method used to determine with precision the energy minimum of a polariton branch is detailed. The precision offered by this method allows to distinguish even very small normal energy splittings analyzed in detail in Chapter 3. By recording the energy minima on different locations on the sample, and assuming a wedge varying linearly with position, the exciton-cavity detuning, the exciton energy and the normal mode energy splitting (Rabi coupling magnitude) can be determined with precision. This method is used in Chapter 3 and 4.

Other calibration methods which take advantage the inflection of the polariton branch are unreliable here due to the spherical aberrations of the excitation lens L_f (see Subsection 2.2.3.1). Finally, the upper polariton branch(es) do not emit light when excited by photoluminescence in both samples. This is probably due to the fact that the excitonic fraction dominate close to normal incidence, in addition to efficient phonon-assisted relaxations towards the exciton reservoir and lower polariton branches. Therefore, calibrations based on the energy of the upper polariton branch(es) are not possible either.

Precise determination of a polariton branch energy minimum

Energy dispersions are experimentally obtained using the setup described in Subsection 2.2.2. To obtain the energy minimum of the lowest polariton branch energy as precisely as possible, we make use of all the polariton modes located at the vicinity of normal incidence. Each energy spectrum at fixed polariton momentum k_y is first fitted using a free Lorentzian with a background varying linearly in energy. The value of the polariton energy for each k_y along with its uncertainty is obtained from this fitting procedure. The quality of fit also allows to discard lines for which the

parasitic light of the pump laser has been too important, corresponding to maximum 10 – 20% of the data points.

At small in-plane momentums, the polariton branch is a parabola to a good approximation. The resulting data is then fitted using a fourth order polynomial (to take into account possible asymmetries due to optical misalignments) and a weight on data points proportional to the above deduced uncertainties. The caption of Fig. 4.37 details each step of the data analysis.

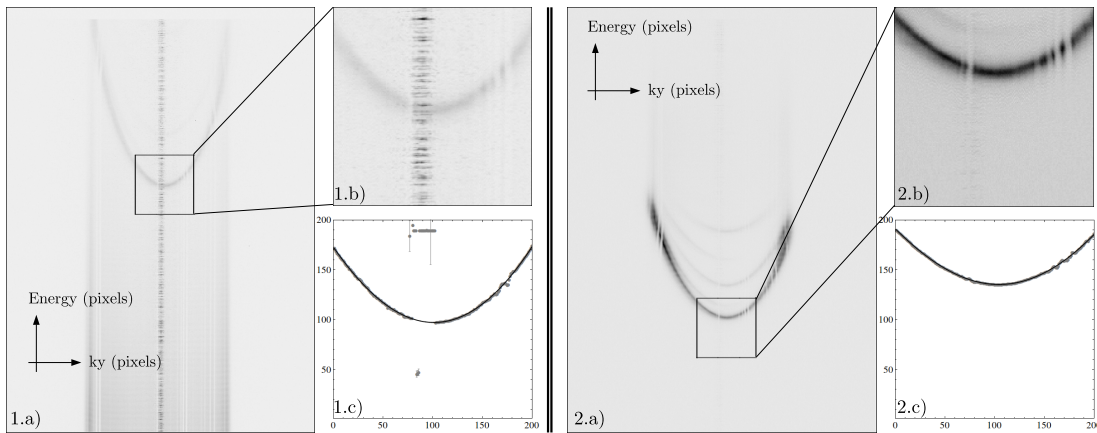


Figure 4.37: Data analysis used to determine the energy minimum of the lowest polariton branch. Two examples on $5\ \mu\text{m}$ -large microwires with different exciton-photon detunings are shown. 1.a) Raw energy dispersion image obtained on the CCD corresponding to a microwire with a large negative detuning. The spectrometer is centered around 785 nm. Parasitic light due to the optical excitation blur the signal close to the minimum of the polariton branch. 1.b) Zone which is exploited for the data analysis (zoom on the raw image). 1.c) The gray points are obtained by 200 lorentzian fits corresponding to each vertical stripe of Fig. 1.b). The points that are too detuned from the polariton branch or have large uncertainties are automatically removed before performing the fourth-order polynomial fit shown as a black line. The y scale is then converted from pixels to wavelength and then electronvolts (not shown), using a calibration of the spectrometer done beforehand. 2.a), b), c): analogous to 1.a), b), c) but for a lower negative detuning. The spectrometer is centered around 775 nm. The zone of interest b) is chosen carefully such that the polariton branches at higher energy do not interfere with the analysis method (especially the lorentzian fits).

In Chapter 3, this data analysis is done for energy dispersion images taken either in the polarization channel parallel to the wire axis or perpendicular to it. Then the energy splitting magnitude is determined simply by subtracting the two obtained energy minima. This method is valid and gives realistic error bars for polariton branches at negative and zero exciton-photon detunings. For positive detunings, another analysis method is used, as described in the following paragraph.

Determination of the normal energy-splitting for microwires at positive detunings

Indeed, for positive detuning, the polariton branch spectral width becomes extremely large (up to 8 times the polarization splitting of interest in Chapter 3) and its curvature nearly vanishes. The error bars given by the fourth order polynomial fitting are therefore highly underestimated. This does not much affect the calibrations of the exciton energy and Rabi coupling since the polariton energy varies slowly with detuning in this region.

However, in Chapter 3, the energy splittings at positive detuning mainly determine the strength of the excitonic contribution δE_x to the total splitting as defined by the model (3.4). The fit based on this model takes into account the uncertainties of the energy splitting magnitudes determined by the data analysis detailed in the previous paragraph.

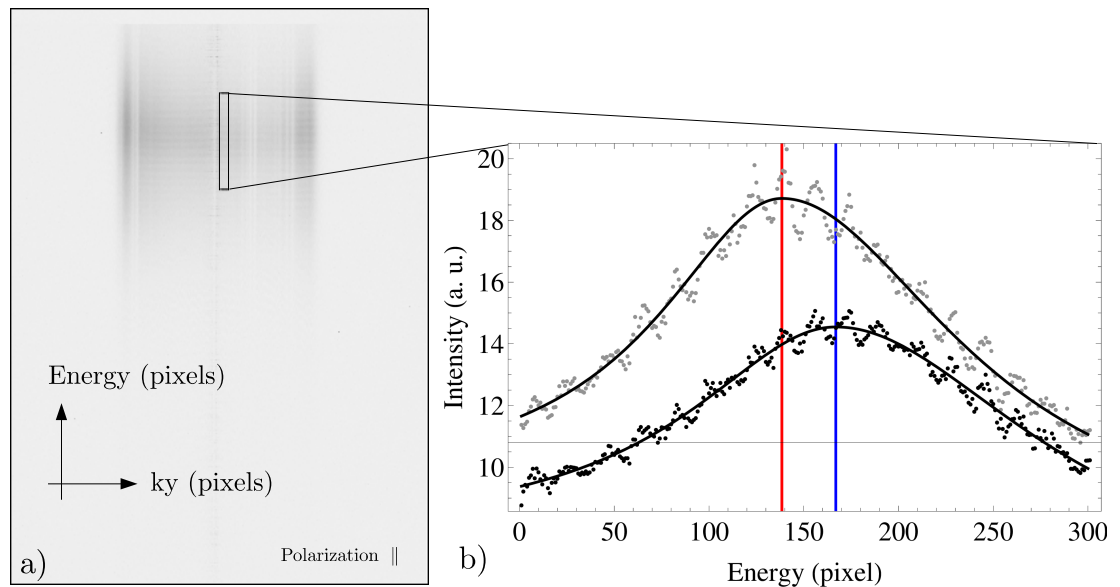


Figure 4.38: a) Raw data obtained at positive detuning for the polarization parallel to the wire axis. The spectrometer is centered at 785 nm. The polariton branch is barely distinguishable, due to its large linewidth and small curvature. The intensity of the twenty lines surrounded by the rectangle are integrated along the vertical axis (energy) and is plotted in b) (gray points). The obtained data is then fitted by an asymmetric Lorentzian function shown as a plain line. The same data analysis is done for the energy dispersion measured in the polarization orthogonal to the wire axis (black points fitted by a plain black line). The position of the peaks is marked by thick red and blue vertical lines.

Hence, in the positive detuning region, we follow a totally different approach to obtain the energy splittings along with realistic error bars. To avoid the parasitic

laser light sometimes apparent close to $k_Y = 0$ (see Fig. 4.37.1.a. for example), the 20 lines at $k_Y > 0$ are integrated and then fitted by an asymmetric lorentzian function, for each of the two polarized branches (see Fig. 4.38).

The energy splitting magnitude is found by subtracting the position of the two lorentzian peaks, and then converting to a electronvolt scale. The uncertainties obtained by this method come from the result of the asymmetric lorentzian fits and are much more reasonable. Note that this method cannot be used to obtain the energy values for the minimum of each branch since the integration zone is not centered around $k_Y = 0$.

A2 Correction of standard errors to take into account heteroscedasticity

In linear regression models, the set of data is assumed *homoscedastic*: the (unknown) *errors* on the observed measures are evenly distributed (or, in other words, the variance of each error ε_i is constant).

This hypothesis can be checked *a posteriori* by looking at the distribution of the *fit residuals*, defined by the difference between the observed values (the data) and their estimates. If the set of data is homoscedastic (and, of course, if the fit model is well adapted), a random distribution of the residuals around 0 is expected. Fig. 4.39 shows the residuals corresponding to the sine fit done in Subsection 4.2.1.2.

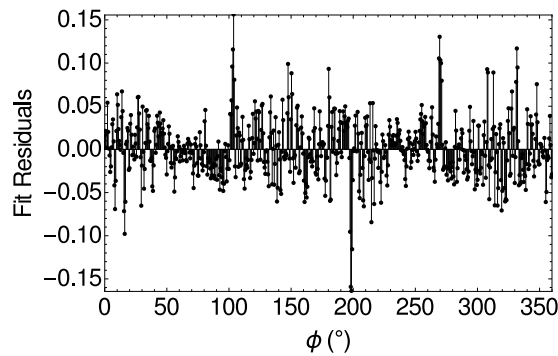


Figure 4.39: Residuals corresponding to the sine fit shown in Fig. 4.11. ϕ is the azimuthal angle along the circumference of the elastic circle.

The residuals as a function of ϕ form a list R of length R_D . To analyze the distribution of the fit residuals in Fig. 4.39, the *autocorrelation* of R , can be calculated by the following operation:

$$A_j = \frac{\sum_{i=0}^{R_D-1} R_i \cdot R_{(i+j) \bmod R_D}}{\sum_{k=0}^{R_D-1} R_k^2},$$

A_j ($j \in \mathbb{Z}$) is the autocorrelation of the fit residuals. If the set of data is perfectly homoscedastic, the fit residuals are totally uncorrelated and $A_{j \neq 0} = 0$. For $j = 0$, there is mathematically a peak: $A_0 = 1$. Fig. 4.40.a. shows the result of this operation done on the fit residuals shown in Fig. 4.39. Apart from the zone close to $j = 0$, the autocorrelation of the fit residuals is close to 0. A zoom on the $j = 0$ peak is then shown on Fig. 4.40.b. The full width half maximum (FWHM) of this peak (highlighted by the red dashed lines) is the *autocorrelation length* of the residuals. This measures the typical lengthscale on which each datapoint is correlated with its neighbors. The autocorrelation length is not zero but 1.4° , indicating a spatial correlation probably due to the granularity observed on the elastic circle

and induced by elastic Rayleigh scattering (see Subsection 4.2.1.2). The dataset is therefore slightly heteroscedastic.

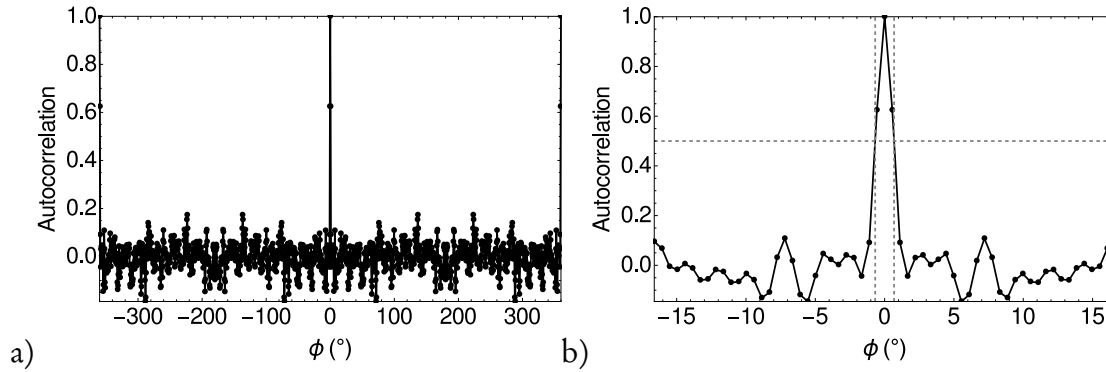


Figure 4.40: a) Autocorrelation of the fit residuals. A peak is observed at zero phase delay. b) Zoom in Fig. a at the vicinity of the main peak. The gray dashed lines mark the FWHM of the main peak and define the autocorrelation length of the fit residuals.

To take into account heteroscedasticity, the standard errors obtained from the sine fit model (4.3) must be corrected by a factor [White1980]

$$\beta = \frac{\phi_c}{\phi_d},$$

where ϕ_c ($\simeq 1.4^\circ$) is the autocorrelation length of the residuals, and ϕ_d ($\simeq 0.6^\circ$) is the discretization step angle of the data.

A3 Growthsheet of the double microcavity

Repetition	Material	Thickness (Å)	Comment
	Al _{0.2} Ga _{0.8} As	561	Front DBR
×16	Al _{0.95} Ga _{0.05} As	647	
	Al _{0.2} Ga _{0.8} As	561	
	Al _{0.95} Ga _{0.05} As	420	
×4	GaAs	70	QWs in DBR
	Al _{0.95} Ga _{0.05} As	30	
	Al _{0.2} Ga _{0.8} As	365	
	Al _{0.95} Ga _{0.05} As	385	Cavity with wedge
×3	GaAs	70	QWs in cavity
	Al _{0.95} Ga _{0.05} As	30	
	GaAs	70	
	Al _{0.95} Ga _{0.05} As	385	Cavity with wedge
×4	Al _{0.2} Ga _{0.8} As	365	QWs in DBRs
	Al _{0.95} Ga _{0.05} As	30	
	GaAs	70	
	Al _{0.95} Ga _{0.05} As	420	
×15	Al _{0.2} Ga _{0.8} As	561	Intermediate DBR
	Al _{0.95} Ga _{0.05} As	647	
	Al _{0.2} Ga _{0.8} As	561	
	Al _{0.95} Ga _{0.05} As	420	
×4	GaAs	70	QWs in DBRs
	Al _{0.95} Ga _{0.05} As	30	
	Al _{0.2} Ga _{0.8} As	365	
	Al _{0.95} Ga _{0.05} As	385	Cavity with wedge
×3	GaAs	70	QWs in cavity
	Al _{0.95} Ga _{0.05} As	30	
	GaAs	70	
	Al _{0.95} Ga _{0.05} As	385	Cavity with wedge
×4	Al _{0.2} Ga _{0.8} As	365	QWs in DBRs
	Al _{0.95} Ga _{0.05} As	30	
	GaAs	70	
	Al _{0.95} Ga _{0.05} As	420	
×25	Al _{0.2} Ga _{0.8} As	561	Back DBR
	Al _{0.95} Ga _{0.05} As	647	
	GaAs		
	GaAs	SUBSTRATE	

Table 4.3: Growthsheet of the double microcavity sample of interest.

REFERENCES

- [Abbarchi2011] M. Abbarchi, V. Ardizzone, I. Sagnes, P. Senellart, J. Bloch & Ph. Roussignol. One-dimensional microcavity-based optical parametric oscillator: Generation of balanced twin beams in strong and weak coupling regime. 201310:2–5, 2011. pp. 113 and 175
- [Abbarchi2012] M. Abbarchi, C. Diederichs, L. Largeau, V. Ardizzone, O. Mauguin, T. Lecomte, A. Lemaître, J. Bloch, Ph. Roussignol & J. Tignon. Discretized disorder in planar semiconductor microcavities: Mosaicity effect on resonant Rayleigh scattering and optical parametric oscillation. *Phys. Rev. B*, 85(4):045316, 2012. pp. 127, 131, 157, 161 and 164
- [Adachi1985] S. Adachi. GaAs, AlAs and Al_xGa_{1-x}As Material parameters for use in research and device applications. *J. Appl. Phys.*, 58(3):R1, 1985. pp. 21, 24, 97, 100, 101, 102 and 108
- [Amand1997] T. Amand, X. Marie, P. Le Jeune, M. Brousseau, D. Robart, J. Barrau & R. Planel. Spin quantum beats of 2d excitons. *Phys. Rev. Lett.*, 78:1355–1358, Feb 1997. p. 108
- [Amo2009] A. Amo, J. Lefrere, S. Pigeon, C. Adrados, C. Ciuti, I. Carusotto, R. Houdré, E. Giacobino & A. Bramati. Superfluidity of polaritons in semiconductor microcavities. *Nat. Phys.*, 5:805–810, 2009. p. 10
- [Andreani1990] Lucio Claudio Andreani & Alfredo Pasquarello. Accurate theory of excitons in gaas-ga_{1-x}al_xas quantum wells. *Phys. Rev. B*, 42:8928–8938, 1990. p. 26
- [Ardizzone2012] V. Ardizzone, M. Abbarchi, T. Lecomte, A. Lemaître, I. Sagnes, P. Senellart, J. Bloch, Ph. Roussignol & J. Tignon. Optical parametric oscillator in 1D semiconductor microcavities. *Phys. status solidi (b)*, 249(5):896–899, 2012. pp. 11 and 113
- [Ardizzone2013a] V. Ardizzone. *Diffusion paramétrique dans les microcavités de semiconducteurs : cohérence du second ordre et formation de motifs transverses*. Theses, Université Pierre et Marie Curie - Paris VI, Sep. 2013. pp. 11, 42, 43, 44, 75, 76, 117, 118, 119, 141, 142, 155, 168 and 169
- [Ardizzone2013b] V. Ardizzone, P. Lewandowski, M. H. Luk, Y. C. Tse, N. H. Kwong, A. Lücke, M. Abbarchi, E. Baudin, E. Galopin, J. Bloch, A. Lemaître,

REFERENCES

- P. T. Leung, Ph. Roussignol, R. Binder, J. Tignon & S. Schumacher. Formation and control of Turing patterns in a coherent quantum fluid. *Sci. Rep.*, 3:3016, Jan. 2013. pp. 11, 41, 44, 150, 154, 156, 164, 166 and 168
- [Arecchi1995] F. T. Arecchi. Optical morphogenesis: pattern formation and competition in nonlinear optics. *Physica D: Nonlinear Phenomena*, 86(1-2):297 – 322, 1995. p. 44
- [Aspnes1976] D. E. Aspnes. GaAs lower conduction-band minima: Ordering and properties. *Phys. Rev. B*, 14:5331–5343, 1976. p. 84
- [Bajoni2006] D. Bajoni, M. Perrin, P. Senellart, A. Lemaître, B. Sermage & J. Bloch. Dynamics of microcavity polaritons in the presence of an electron gas. *Phys. Rev. B*, 73:205344, May 2006. p. 132
- [Bajoni2008a] D.e Bajoni, P. Senellart, E. Wertz, I. Sagnes, A. Miard, A. Lemaître & J. Bloch. Polariton Laser Using Single Micropillar GaAs-GaAlAs Semiconductor Cavities. *Phys. Rev. Lett.*, 100(4):047401, Jan 2008. p. 10
- [Bajoni2008b] D. Bajoni, E. Semenova, A. Lemaître, S. Bouchoule, E. Wertz, P. Senellart & J. Bloch. Polariton light-emitting diode in a GaAs-based microcavity. *Phys. Rev. B*, 77(11):113303, Mar 2008. p. 12
- [Balili2010] R. Balili, B. Nelsen, D. W. Snoke, R. H. Reid, L. Pfeiffer & K. West. Huge splitting of polariton states in microcavities under stress. *Phys. Rev. B.*, 81(12), 2010. pp. 51, 75, 109 and 112
- [Ballarini2013] D. Ballarini, M. De Giorgi, E. Cancellieri, R. Houdré, E. Giacobino, R. Cingolani, A. Bramati, G. Gigli & D. Sanvitto. All-optical polariton transistor. *Nat. Commun.*, 4:QM1D.4, 2013. p. 12
- [Bastard] G. Bastard. *Wave mechanics applied to semiconductor heterostructures*. EDP Sciences, 1992. pp. 24, 25, 26 and 132
- [Baudrier-Raybaut2004] M. Baudrier-Raybaut, R. Haidar, Ph. Kupecek, Ph. Lemasson & E. Rosencher. Random quasi-phase-matching in bulk polycrystalline isotropic nonlinear materials. *Nature*, 432(7015):374–376, 2004. p. 40
- [Baumberg2000] J. Baumberg, P. Savvidis, R. Stevenson, A. Tartakovskii, M. Skolnick, D. Whittaker & J. Roberts. Parametric oscillation in a vertical microcavity: A polariton condensate or micro-optical parametric oscillation. *Phys. Rev. B*, 62(24):R16247–R16250, 2000. p. 41
- [Bhattacharya2014] P. Bhattacharya, T. Frost, S. Deshpande, Md Z. Baten, A. Hazari & A. Das. Room temperature electrically injected polariton laser. *Phys. Rev. Lett.*, 112(23):236802, 2014. p. 10

- [Bir&Pikus] G. L. Bir & G. E. Pikus. *Symmetry and strain-induced effects in semiconductors*. Wiley, 1974. pp. 97 and 106
- [Blackwood1994] E. Blackwood, M. J. Snelling, R. T. Harley, S. R. Andrews & C. T. B. Foxon. Exchange interaction of excitons in gas heterostructures. *Phys. Rev. B*, 50:14246–14254, Nov 1994. p. 108
- [Bloch1997] J. Bloch & J. Y. Marzin. Photoluminescence dynamics of cavity polaritons under resonant excitation in the picosecond range. *Phys. Rev. B*, 56:2103–2108, 1997. p. 12
- [Born&Wolf] M. Born & E. Wolf. *Principles of Optics*. Cambridge University Press, 1959. p. 30
- [Carusotto2004] I. Carusotto & C. Ciuti. Probing microcavity polariton superfluidity through resonant rayleigh scattering. *Phys. Rev. Lett.*, 93:166401, 2004. p. 10
- [Carusotto2013] I. Carusotto & C. Ciuti. Quantum fluids of light. *Rev. Mod. Phys.*, 85(1):299–366, 2013. p. 11
- [Chen1988] Y. Chen, B. Gil, P. Lefebvre & H. Mathieu. Exchange effects on excitons in quantum wells. *Phys. Rev. B*, 37(11):6429–6432, 1988. pp. 106 and 108
- [Christopoulos2007] S. Christopoulos, G. Baldassarri Höger von Högersthal, A. J. D. Grundy, P. G. Lagoudakis, A. V. Kavokin, J. J. Baumberg, G. Christmann, R. Butté, E. Feltn, J.-F. Carlin & N. Grandjean. Room-temperature polariton lasing in semiconductor microcavities. *Phys. Rev. Lett.*, 98:126405, 2007. p. 10
- [Cilibrizzi2015] P. Cilibrizzi, H. Sigurdsson, T. C. H. Liew, H. Ohadi, S. Wilkinson, A. Askitopoulos, I. A. Shelykh & P. G. Lagoudakis. Polariton spin whirls. *Phys. Rev. B*, 92:155308, 2015. p. 124
- [Cilibrizzi2016] P. Cilibrizzi, H. Sigurdsson, T. C. H. Liew, H. Hoadi, A. Askitopoulos, S. Brodbeck, C. Schneider, I. A. Shelykh, S. Höfling & P. Lagoudakis. Skyrmion Spin Textures In Polariton Microcavities. pp. 1–10, 2016. p. 12
- [Ciuti2000] C. Ciuti, P. Schwendimann, B. Deveaud & a. Quattropani. Theory of the angle-resonant polariton amplifier. *Phys. Rev. B*, 62(8):R4825–R4828, 2000. p. 10
- [Ciuti2003] C. Ciuti, P. Schwendimann & A. Quattropani. Theory of polariton parametric interactions in semiconductor microcavities. *Semicond. Sci. Technol.*, 18(10):S279–S293, 2003. p. 10
- [Craig1983] A. E. Craig, G. A. Olson & D. Sarid. Experimental observation of the long-range surface-plasmon polariton. *Opt. Lett.*, 8(7):380–382, 1983. pp. 10 and 34

REFERENCES

- [Cross1993] M. C. Cross & P. C. Hohenberg. Pattern formation outside of equilibrium. *Rev. Mod. Phys.*, 65:851–1112, 1993. p. 44
- [Dasbach2002] G. Dasbach, A. A. Dremin, M. Bayer, V. D. Kulakovskii, N. A. Gippius & A. Forchel. Oscillations in the differential transmission of a semiconductor microcavity with reduced symmetry. *Phys. Rev. B*, 65:1–6, 2002. pp. 50, 75 and 112
- [Dasbach2005] G. Dasbach, C. Diederichs, J. Tignon, C. Ciuti, Ph. Roussignol, C. Delalande, M. Bayer & A. Forchel. Polarization inversion via parametric scattering in quasi-one-dimensional microcavities. *Phys. Rev. B*, 71(16):161308, 2005. pp. 50 and 112
- [Dawes2010] A. M. C. Dawes, D. J. Gauthier, S. Schumacher, N. H. Kwong, R. Binder & A. L. Smirl. Transverse optical patterns for ultra-low-light-level all-optical switching. *Laser Photonics Rev.*, 4(2):221–243, 2010. pp. 11, 44 and 156
- [De Liberato2013] S. De Liberato, C. Ciuti & C. C. Phillips. Terahertz lasing from intersubband polariton-polariton scattering in asymmetric quantum wells. *Phys. Rev. B*, 87:241304, 2013. p. 11
- [Deveaud1991] B. Deveaud, F. Clérot, N. Roy, K. Satzke, B. Sermage & D. S. Katzer. Enhanced radiative recombination of free excitons in GaAs quantum wells. *Phys. Rev. Lett.*, 67:2355–2358, 1991. p. 27
- [Diederichs2005] C. Diederichs & J. Tignon. Design for a triply resonant vertical-emitting micro-optical parametric oscillator. *Appl. Phys. Lett.*, 87(25):251107, 2005. p. 42
- [Diederichs2006] C. Diederichs, J. Tignon, G. Dasbach, C. Ciuti, A. Lemaître, J. Bloch, Ph. Roussignol & C. Delalande. Parametric oscillation in vertical triple microcavities. *Nature*, 440(7086):904–907, 2006. pp. 11 and 42
- [Diederichs2007] Carole Diederichs. *Oscillation paramétrique optique et génération de photons jumeaux dans des microcavités de semiconducteurs*. Theses, Université Pierre et Marie Curie - Paris VI, 2007. pp. 50, 75, 89, 96, 112, 117 and 173
- [Ducci2001] S. Ducci, N. Treps, a. Maître & C. Fabre. Pattern formation in optical parametric oscillators. *Phys. Rev. A*, 64(2):023803, 2001. pp. 12, 44 and 156
- [Egorov2014] O. A. Egorov, A. Werner, T. C. H. Liew, E. A. Ostrovskaya & F. Lederer. Motion of patterns in polariton quantum fluids with spin-orbit interaction. *Phys. Rev. B*, 89:235302, 2014. pp. 154 and 167

- [Ekardt1979] W. Ekardt, K. Lösch & D. Bimberg. Determination of the analytical and the nonanalytical part of the exchange interaction of InP and GaAs from polariton spectra in intermediate magnetic fields. *Phys. Rev. B*, 20(8):3303–3314, 1979. p. 108
- [Espinosa-Ortega2013] T. Espinosa-Ortega & T. C. H. Liew. Complete architecture of integrated photonic circuits based on and not logic gates of exciton polaritons in semiconductor microcavities. *Phys. Rev. B*, 87:195305, May 2013. p. 113
- [Ferrier2010] L. Ferrier, S. Pigeon, E. Wertz, M. Bamba, P. Senellart, I. Sagnes, A. Lemaître, C. Ciuti & J. Bloch. Polariton parametric oscillation in a single micropillar cavity. *Applied Physics Letters*, 97(3), 2010. p. 11
- [Fishman] G. Fishman. *Les bases de la théorie KP*. Éditions de l'École Polytechnique, 2010. pp. 22, 24, 26 and 108
- [Flayac2013] H. Flayac, D. D. Solnyshkov, G. Malpuech & I. a. Shelykh. Parametric inversion of spin currents in semiconductor microcavities. *Phys. Rev. B - Condens. Matter Mater. Phys.*, 87(7):1–6, 2013. p. 124
- [Fröhlich1971] D. Fröhlich, E. Mohler & P. Wiesner. Observation of exciton polariton dispersion in cucl. *Phys. Rev. Lett.*, 26:554–556, 1971. pp. 10 and 34
- [Gao2015] T. Gao, C. Antón, T. C. H. Liew, M. D. Martín, Z. Hatzopoulos, L. Viña, P. S. Eldridge & P. G. Savvidis. Spin Selective Filtering of Polariton Condensate Flow. 011106, 2015. pp. 12 and 124
- [Gilleo1968] M. A. Gilleo, P. T. Bailey & D. E. Hill. Free-carrier and exciton recombination radiation in gaas. *Phys. Rev.*, 174:898–905, 1968. p. 108
- [Glazov2005] M. M. Glazov, I. A. Shelykh, G. Malpuech, K. V. Kavokin, A. V. Kavokin & D. D. Solnyshkov. Anisotropic polariton scattering and spin dynamics of cavity polaritons. *Solid State Commun.*, 134(1-2):117–120, 2005. p. 124
- [Goni1990] A. R. Goni, K. Syassen & M. Cardona. Effect of pressure on the refractive index of ge and gaas. *Phys. Rev. B*, 41:10104–10110, 1990. p. 102
- [Greene1984] Ronald L. Greene, Krishan K. Bajaj & Dwight E. Phelps. Energy levels of wannier excitons in GaAs – $ga_{1-x}al_xAs$ quantum-well structures. *Phys. Rev. B*, 29:1807–1812, Feb 1984. p. 25
- [Heidmann1987] A. Heidmann, R. J. Horowicz, S. Reynaud, E. Giacobino, C. Fabre & G. Camy. Observation of quantum noise reduction on twin laser beams. *Phys. Rev. Lett.*, 59:2555–2557, 1987. p. 40

REFERENCES

- [Hopfield1958] J. J. Hopfield. Theory of the contribution of excitons to the complex dielectric constant of crystals. *Phys. Rev.*, 112(5):1555–1567, 1958. p. 34
- [Houdré1995] R. Houdré, J. L. Gibernon, P. Pellandini, R. P. Stanley, U. Oesterle, C. Weisbuch, J. O’Gorman, B. Roycroft & M. Ilegems. Saturation of the strong-coupling regime in a semiconductor microcavity: Free-carrier bleaching of cavity polaritons. *Phys. Rev. B*, 52:7810–7813, 1995. p. 37
- [Huppert2014a] Simon Huppert. *Nonlinear transport and Terahertz generation in two-dimensional systems under strong optical irradiation*. Theses, Université Pierre et Marie Curie - Paris VI, Sep. 2014. p. 11
- [Huppert2014b] S. Huppert, O. Lafont, E. Baudin, J. Tignon & R. Ferreira. Terahertz emission from multiple-microcavity exciton-polariton lasers. *Phys. Rev. B*, 90:241302, 2014. p. 11
- [Imamog̃lu1996] A. Imamog̃lu, R. J. Ram, S. Pau & Y. Yamamoto. Nonequilibrium condensates and lasers without inversion: Exciton-polariton lasers. *Phys. Rev. A*, 53:4250–4253, Jun 1996. p. 10
- [Jeantet2016] A. Jeantet, Y. Chassagneux, C. Raynaud, Ph. Roussignol, J. S. Lauret, B. Besga, J. Estève, J. Reichel & C. Voisin. Widely tunable single-photon source from a carbon nanotube in the purcell regime. *Phys. Rev. Lett.*, 116:247402, 2016. p. 63
- [Kammann2012] E. Kammann, T. C. H. Liew, H. Ohadi, P. izzi, P. Tsotsis, Z. Hatzopoulos, P. G. Savvidis, a. V. Kavokin & P. G. Lagoudakis. Nonlinear Optical Spin Hall Effect and Long-Range Spin Transport in Polariton Lasers. *Phys. Rev. Lett.*, 109(3):036404, 2012. p. 124
- [Kapral&Showalter] R. Kapral & K. Showalter. *Chemical waves and patterns*, vol. 10. Springer Science & Business Media, 2012. p. 44
- [Kasprzak2006] J. Kasprzak, M. Richard, S. Kundermann, A. Baas, P. Jeambrun, J. M. J. Keeling, F. M. Marchetti, M. H. Szymańska, R. André, J. L. Staehli, V. Savona, P. B. Littlewood, B. Deveaud & L. S. Dang. Bose-Einstein condensation of exciton polaritons. *Nature*, 443:409–414, 2006. p. 10
- [Kavokin2005] A. Kavokin, G. Malpuech & M. Glazov. Optical Spin Hall Effect. *Phys. Rev. Lett.*, 95(13):136601, 2005. pp. 12, 47, 50, 124, 132 and 174
- [Kavokin2010] K. V. Kavokin, M. A. Kaliteevski, R. A. Abram, A. V. Kavokin, S. Sharkova & I. A. Shelykh. Stimulated emission of terahertz radiation by exciton-polariton lasers. *Applied Physics Letters*, 97(20), 2010. p. 11

- [Khalifa2008] A. A. Khalifa, A. P. D. Love, D. N. Krizhanovskii, M. S. Skolnick & J. S. Roberts. Electroluminescence emission from polariton states in GaAs-based semiconductor microcavities. *Appl. Phys. Lett.*, 92(6):061107, 2008. p. 12
- [Khitrova1999] G. Khitrova, H. M. Gibbs, F. Jahnke, M. Kira & S. W. Koch. Nonlinear optics of normal-mode-coupling semiconductor microcavities. *Rev. Mod. Phys.*, 71:1591–1639, 1999. p. 31
- [Koyama1989] F. Koyama, S. Kinoshita & K. Iga. Room-temperature continuous wave lasing characteristics of a GaAs vertical cavity surface-emitting laser. *Applied Physics Letters*, 55(3):221–222, 1989. p. 9
- [Kuther1998] A. Kuther, M. Bayer, T. Gutbrod, A. Forchel, P. A. Knipp, T. L. Reinecke & R. Werner. Confined optical modes in photonic wires. *Phys. Rev. B*, 58:15744–15748, 1998. pp. 32, 51, 75, 77 and 101
- [Lagoudakis2008] K. G. Lagoudakis, M. Wouters, M. Richard, A. Baas, I. Carusotto, R. André, Le Si Dang & B. Deveaud-Plédran. Quantized vortices in an exciton–polariton condensate. *Nature Physics*, 4(9):706–710, 2008. p. 11
- [Le Gall1997] J. Le Gall, M. Olivier & J.-J. Greffet. Experimental and theoretical study of reflection and coherent thermal emission by a sic grating supporting a surface-phonon polariton. *Phys. Rev. B*, 55:10105–10114, 1997. pp. 10 and 34
- [Lecomte2011] T. Lecomte. *Microcavités semiconductrices structurées pour la génération paramétrique optique*. Theses, Université Pierre et Marie Curie - Paris VI, 2011. pp. 39, 55, 66, 76, 78, 117 and 161
- [Lecomte2014] T. Lecomte, D. Taj, A. Lemaître, J. Bloch, C. Delalande, J. Tignon & Ph. Roussignol. Polariton-polariton interaction potentials determination by pump-probe degenerate scattering in a multiple microcavity. *Phys. Rev. B - Condens. Matter Mater. Phys.*, 89(15):155308, 2014. p. 52
- [Lewandowski2015] P. Lewandowski. *Nichtlineare optische Eigenschaften und spontane Musterbildung in Halbleitern Mikro kavitäten*. PhD thesis, Universität Paderborn, 2015. p. 166
- [Lewandowski2016] P. Lewandowski, O. Lafont, E. Baudin, C. K. P. Chan, P. T. Leung, S. M. H. Luk, E. Galopin, A. Lemaître, J. Bloch, J. Tignon, Ph. Roussignol, N. H. Kwong, R. Binder & S. Schumacher. Polarization dependence of nonlinear wave mixing of spinor polaritons in semiconductor microcavities. *Phys. Rev. B*, 94:045308, 2016. pp. 150, 153 and 166
- [Leyder2007] C. Leyder, M. Romanelli, J. Ph. Karr, E. Giacobino, T. C. H. Liew, M. M. Glazov, a. V. Kavokin, G. Malpuech & A. Bramati. Observation of the optical spin Hall effect. *Nat. Phys.*, 3(9):628–631, 2007. pp. 12, 47, 48, 124, 125, 135 and 174

REFERENCES

- [Liew2007] T. C. H. Liew, A. V. Kavokin & I. A. Shelykh. Excitation of vortices in semiconductor microcavities. *Phys. Rev. B*, 75:241301, 2007. p. 12
- [Liew2008] T. C. H. Liew, A. V. Kavokin & I. A. Shelykh. Optical circuits based on polariton neurons in semiconductor microcavities. *Phys. Rev. Lett.*, 101:016402, Jul 2008. p. 113
- [Luk2013] M. H. Luk, Y. C. Tse, N. H. Kwong, P. T. Leung, P. Lewandowski, R. Binder & S. Schumacher. Transverse optical instability patterns in semiconductor microcavities: Polariton scattering and low-intensity all-optical switching. *Phys. Rev. B - Condens. Matter Mater. Phys.*, 87(20):1–22, 2013. pp. 11, 44, 136, 154 and 156
- [Madelung] O. Madelung. *Semiconductors: Data Handbook*. Springer Berlin Heidelberg, Berlin, Heidelberg, 2004. pp. 22 and 24
- [Maialle1993] M. Z. Maialle, E. A. de Andrada e Silva & L. J. Sham. Exciton spin dynamics in quantum wells. *Phys. Rev. B*, 47:15776–15788, 1993. p. 106
- [Maître1994] A. Maître. *Instabilités créées par mélange à quatre ondes dans une vapeur atomique. Chaos et morphogénèse*. Theses, Ecole Polytechnique X, 1994. pp. 12 and 156
- [Maragkou2011] M. Maragkou, C. E. Richards, T. Ostatnický, A. J. D. Grundy, J. Zajac, M. Hugues, W. Langbein & P. G. Lagoudakis. Optical analogue of the spin Hall effect in a photonic cavity. *Opt. Lett.*, 36(7):1095–7, 2011. p. 48
- [Marsault2015] F. Marsault, H. S. Nguyen, D. Tanese, A. Lemaître, E. Galopin, I. Sagnes, A. Amo & J. Bloch. Realization of an all optical exciton-polariton router. *Applied Physics Letters*, 107(20), 2015. pp. 12 and 113
- [Mertz1991] J. Mertz, T. Debuisschert, A. Heidmann, C. Fabre & E. Giacobino. Improvements in the observed intensity correlation of optical parametric oscillator twin beams. *Opt. Lett.*, 16(16):1234–1236, 1991. pp. 10 and 40
- [Milićević2015] M. Milićević, T. Ozawa, P. Andreakou, I. Carusotto, T. Jacqmin, E. Galopin, A. Lemaître, L. Le Gratiet, I. Sagnes, J. Bloch & A. Amo. Edge states in polariton honeycomb lattices. *2D Mater.*, 2(3):34012, 2015. p. 113
- [Morina2013] S. Morina, T. C. H. Liew & I. A. Shelykh. Magnetic field control of the optical spin Hall effect. *Phys. Rev. B*, 88(3):035311, 2013. p. 124
- [Müller2000] M. Müller, J. Bleuse & R. André. Dynamics of the cavity polariton in cdte-based semiconductor microcavities: Evidence for a relaxation edge. *Phys. Rev. B*, 62:16886–16892, 2000. pp. 11 and 158

- [Myers1995] L. E. Myers, W. R. Bosenberg, G. D. Miller, R. C. Eckardt, M. M. Fejer & R. L. Byer. Quasi-phase-matched $1.064\text{-}\mu\text{m}$ -pumped optical parametric oscillator in bulk periodically poled LiNbO₃. *Opt. Lett.*, 20(1):52–54, 1995. p. 40
- [Nalitov2015] A. V. Nalitov, D. D. Solnyshkov & G. Malpuech. Polariton Z Topological Insulator. *Phys. Rev. Lett.*, 114(11):116401, 2015. p. 113
- [Nguyen2013] H. S. Nguyen, D. Vishnevsky, C. Sturm, D. Tanese, D. Solnyshkov, E. Galopin, A. Lemaître, I. Sagnes, A. Amo, G. Malpuech & J. Bloch. Realization of a double-barrier resonant tunneling diode for cavity polaritons. *Phys. Rev. Lett.*, 110:236601, Jun 2013. p. 113
- [Oppo2008] G.-L. Oppo. Formation and control of Turing patterns and phase fronts in photonics and chemistry. *J. Math. Chem.*, 45(1):95–112, 2008. p. 44
- [Ostatnický2010] T. Ostatnický, I. a. Shelykh & a. V. Kavokin. Theory of polarization-controlled polariton logic gates. *Phys. Rev. B*, 81(12):125319, 2010. p. 12
- [Panzarini1999] G. Panzarini, L. Andreani, A. Armitage, D. Baxter, M. Skolnick, V. Astratov, J. Roberts, A. Kavokin, M. Vladimirova & M. Kaliteevski. Exciton-light coupling in single and coupled semiconductor microcavities: Polariton dispersion and polarization splitting. *Phys. Rev. B*, 59(7):5082–5089, 1999. pp. 45, 47, 51, 104, 110, 111 and 120
- [Peter2005] E. Peter, P. Senellart, D. Martrou, A. Lemaître, J. Hours, J. M. Gerard & J. Bloch. Exciton-Photon Strong-Coupling Regime for a Single Quantum Dot Embedded in a Microcavity. *Physical Review Letters*, 95(6):067401+, 2005. p. 10
- [Reithmaier2014] J. P. Reithmaier, G. Sek, A. Löffler, C. Hofmann, S. Kuhn, S. Reitzenstein, L. V. Keldysh, V. D. Kulakovskii, T. L. Reinecke & A. Forchel. Strong coupling in a single quantum dot-semiconductor microcavity system. *Nature*, 432:197–200, 2014. p. 10
- [Renucci2005] P. Renucci, T. Amand, X. Marie, P. Senellart, J. Bloch, B. Sermage & K. V. Kavokin. Microcavity polariton spin quantum beats without a magnetic field: A manifestation of coulomb exchange in dense and polarized polariton systems. *Phys. Rev. B*, 72:075317, Aug 2005. p. 124
- [Saito2013] H. Saito, T. Aioi & T. Kadokura. Order-disorder oscillations in exciton-polariton superfluids. *Phys. Rev. Lett.*, 110:026401, 2013. p. 154
- [Sanvitto2016] D. Sanvitto & S. Kéna-Cohen. The road towards polaritonic devices. *Nature Materials*, 2016. p. 12

REFERENCES

- [Savvidis2000] P. G. Savvidis, J. J. Baumberg, R. M. Stevenson, M. S. Skolnick, D. M. Whittaker & J. S. Roberts. Angle-resonant stimulated polariton amplifier. *Phys. Rev. Lett.*, 84(7):1547–1550, 2000. pp. 10, 41 and 117
- [Schmidt-Grund2008] R. Schmidt-Grund, B. Rheinländer, C. Czekalla, G. Benndorf, H. Hochmuth, M. Lorenz & M. Grundmann. Exciton-polariton formation at room temperature in a planar ZnO resonator structure. *Applied Physics B: Lasers and Optics*, 93:331–337, 2008. p. 10
- [Schmitt-Rink1985] S. Schmitt-Rink, D. S. Chemla & D. A. B. Miller. Theory of transient excitonic optical nonlinearities in semiconductor quantum-well structures. *Phys. Rev. B*, 32:6601–6609, Nov 1985. p. 43
- [Schumacher2007] S. Schumacher, N. Kwong & R. Binder. Influence of exciton-exciton correlations on the polarization characteristics of polariton amplification in semiconductor microcavities. *Phys. Rev. B*, 76(24):245324, 2007. pp. 51 and 136
- [Schumacher2008] S. Schumacher. Spatial anisotropy of polariton amplification in planar semiconductor microcavities induced by polarization anisotropy. *Phys. Rev. B*, 77:073302, 2008. p. 12
- [Schumacher2009] S. Schumacher, N. H. Kwong, R. Binder & A. L. Smirl. Low intensity directional switching of light in semiconductor microcavities. *Phys. status solidi - Rapid Res. Lett.*, 3(1):10–12, 2009. pp. 11, 44 and 156
- [Shelykh2005] I. A. Shelykh, M. M. Glazov, D. D. Solnyshkov, N. G. Galkin, A. V. Kavokin & G. Malpuech. Spin dynamics of polariton parametric amplifiers. *Phys. Status Solidi*, 2(2):768–778, 2005. p. 124
- [Shelykh2010] I. A. Shelykh, A. V. Kavokin, Y. G. Rubo, T. C. H. Liew & G. Malpuech. Polariton polarization-sensitive phenomena in planar semiconductor microcavities. *Semicond. Sci. Technol.*, 25(1):013001, 2010. pp. 45 and 47
- [Shen] Y. R. Shen. *The Principles of Nonlinear Optics*. Wiley, 2002. pp. 38 and 40
- [Soda1979] H. Soda, K. Iga, C. Kitahara & Y. Suematsu. GaInAsP/InP Surface Emitting Injection Lasers. *Japanese Journal of Applied Physics*, 18(12):2329, 1979. p. 9
- [Solnyshkov2007] D. D. Solnyshkov, I. A. Shelykh, M. M. Glazov, G. Malpuech, T. Amand, P. Renucci, X. Marie & A. V. Kavokin. Nonlinear effects in spin relaxation of cavity polaritons. *Semiconductors*, 41(9):1080–1091, 2007. p. 123
- [Solnyshkov2015] D. D. Solnyshkov, O. Bleu & G. Malpuech. All optical controlled-NOT gate based on an exciton-polariton circuit. *Superlattices Microstruct.*, 83:466–475, 2015. pp. 12 and 124

- [Stevenson2000] R. M. Stevenson, V. N. Astratov, M. S. Skolnick, D. M. Whittaker, M. Emam-Ismail, a. I. Tartakovskii, P. G. Savvidis, J. J. Baumberg & J. S. Roberts. Continuous wave observation of massive polariton redistribution by stimulated scattering in semiconductor microcavities. *Phys. Rev. Lett.*, 85(17):3680–3683, 2000. pp. 10, 41 and 117
- [Sturm2014] C. Sturm, D. Tanese, H. S. Nguyen, H. Flayac, E Galopin, A Lemaître, I Sagnes, D. Solnyshkov, A. Amo, G. Malpuech & J. Bloch. All-optical phase modulation in a cavity-polariton Mach-Zehnder interferometer. *Nat. Commun.*, 5:3278, 2014. p. 113
- [Takayama2002] R. Takayama, N.H. Kwong, I. Romyantsev, M. Kuwata-Gonokami & R. Binder. T-matrix analysis of biexcitonic correlations in the nonlinear optical response of semiconductor quantum wells. *Eur. Phys. J. B*, 25(4):445–462, 2002. p. 51
- [Tassone1997] F. Tassone, C. Piermarocchi, V. Savona, A. Quattropani & P. Schwendimann. Bottleneck effects in the relaxation and photoluminescence of microcavity polaritons. *Phys. Rev. B*, 56:7554–7563, 1997. p. 11
- [Teja1998] J. Teja & N. C. Wong. Twin-beam generation in a triply resonant dual-cavity optical parametric oscillator. *Opt. Express*, 2(3):65–71, 1998. p. 40
- [Tsintzos2008] S. I. Tsintzos, N. T. Pelekanos, G. Konstantinidis, Z. Hatzopoulos & P. G. Savvidis. A GaAs polariton light-emitting diode operating near room temperature. *Nature*, 453(7193):372–5, 2008. p. 12
- [Turing1952] A. M. Turing. The chemical basis of morphogenesis. *Philosophical Transactions of the Royal Society B: Biological Sciences*, 237(641):37–72, 1952. pp. 12 and 44
- [Vaupel1999] M. Vaupel, A. Maître & C. Fabre. Observation of Pattern Formation in Optical Parametric Oscillators. *Phys. Rev. Lett.*, 83(25):5278–5281, 1999. p. 44
- [Vladimirova2010] M. Vladimirova, S. Cronenberger, D. Scalbert, K. V. Kavokin, a. Miard, a. Lemaître, J. Bloch, D. Solnyshkov, G. Malpuech & a. V. Kavokin. Polariton-polariton interaction constants in microcavities. *Phys. Rev. B - Condens. Matter Mater. Phys.*, 82(7):1–9, 2010. p. 52
- [Vodopyanov2004] K. L. Vodopyanov, O. Levi, P. S. Kuo, T. J. Pinguet, J. S. Harris, M. M. Fejer, B. Gerard, L. Becouarn & E. Lallier. Optical parametric oscillation in quasi-phase-matched GaAs. *Opt. Lett.*, 29(16):1912–1914, 2004. p. 40
- [Wallraff2004] A. Wallraff, D. I. Schuster, A. Blais, L. Frunzio, R.-S. Huang, J. Majer, S. Kumar, S. M. Girvin & R. J. Schoelkopf. Strong coupling of a single photon to a superconducting qubit using circuit quantum electrodynamics. *Nature*, 431:162–197, 2004. p. 10

REFERENCES

- [Weisbuch1992] C. Weisbuch, M. Nishioka, A. Ishikawa & Y. Arakawa. Observation of the coupled exciton-photon mode splitting in a semiconductor quantum microcavity. *Phys. Rev. Lett.*, 69(23):3314–3317, 1992. pp. 10 and 34
- [Wertz2010a] E. Wertz. *Formation spontanée de condensats de polaritons dans des microcavités à base de GaAs*. PhD thesis, Université Paris - Sud 11, 2010. pp. 76, 100 and 104
- [Wertz2010b] E Wertz. Spontaneous formation and optical manipulation of extended polariton condensates. *Nature Physics*, (6):860–864, 2010. p. 175
- [White1980] H. White. A heteroskedasticity-consistent covariance matrix estimator and a direct test for heteroskedasticity. *Econometrica*, 48(4):817–838, 1980. p. 182
- [Yoshie2004] A. Yoshie, T. and Scherer, J. Hendrickson, G. Khitrova, H. M. Gibbs, G. Rupper, C. Ell, O. B. Shchekin & D. G. Deppe. Vacuum Rabi splitting with a single quantum dot in a photonic crystal nanocavity. *Nature*, 432:200–203, 2004. p. 10

Résumé

En régime de couplage fort lumière-matière, les microcavités de semiconducteurs contenant des puits quantiques abritent des quasi-particules appelées exciton-polaritons de microcavité. Leur caractère hybride mi-électronique, mi-photonique, leur confère des propriétés optiques non-linéaires remarquables. Nous nous intéressons dans cette thèse à des microcavités structurées qui permettent la coexistence de branches polaritoniques de symétrie et d'énergie différenciées. Une microcavité gravée en rubans de quelques micromètres de large est d'abord étudiée. Le confinement latéral lève la dégénérescence entre les modes polarisés parallèlement et orthogonalement à la direction du ruban. Nous montrons que ce dédoublement résulte de contraintes structurales intrinsèques, de sorte que son amplitude peut être décidée dès la conception du dispositif. Nous nous intéressons ensuite à une microcavité double. En régime de diffusion Rayleigh élastique, le dédoublement TE-TM conduit à une séparation spatiale et angulaire des polaritons de pseudo-spins différents. Nous montrons que ce phénomène, appelé "effet Hall optique de spin" peut être contrôlé par un faisceau de pompe intense. Dans le régime d'oscillation paramétrique optique, la lumière s'auto-organise pour former un motif dans le champ lointain. Les règles de sélection concernant l'orientation et la polarisation de ces motifs sont explorées dans le régime d'amplification paramétrique optique. Ces études ouvrent la voie de la conception de "dispositifs de microphares" (capables d'orienter continûment la lumière par un simple contrôle en polarisation) et d'interrupteurs tout-optique ultra-rapides.

Mots Clés

exciton-polaritons, pseudo-spin, microfil, motif, interrupteur optique, oscillation paramétrique optique

Abstract

Semiconductor microcavities with embedded quantum wells in the strong light-matter coupling regime host quasi-particles called microcavity exciton-polaritons. Their hybrid nature, half-electronic, half-photon, brings about remarkable nonlinear optical properties. In this work, we focus on microcavities that are structured to enable the coexistence of polaritonic branches with various symmetries and energies. First, a microcavity etched to form micrometers-wide wires is studied. The lateral confinement lifts the degeneracy between the modes which are polarized parallel and orthogonal to the wire direction. We show that this splitting results from built-in constraints which make a precise engineering of the splitting magnitude possible. We then focus on a double microcavity. In the elastic Rayleigh scattering regime, the TE-TM splitting induces a spatial and angular separation of polaritons with different pseudo-spins. We show that this phenomenon, called "Optical Spin Hall Effect", can be controlled by a strong optical pump beam. In the regime of Optical Parametric Oscillation, the light self-organizes to form patterns in the far field. The selection rules for the orientation and polarization of these patterns are explored in the regime of Optical Parametric Amplification. These studies pave the way for the realization of microscopic "lighthouse" devices (able to continuously orientate the light by a simple polarization control) and ultrafast all-optical switches.

Keywords

exciton-polaritons, pseudo-spin, microwire, pattern, optical switch, optical parametric oscillation